Data-driven modelling and control of plasma current profile and kinetic parameters in advanced tokamak scenarios

Sen Wang

UNIVERSITÉ GRENOBLE ALPES

THÈSE

pour obtenir le grade de

DOCTEUR DE LA COMMUNAUTÉ UNIVERSITÉ GRENOBLE ALPES

Spécialité : **Automatique et Productique**

Arrêté ministériel : 25 mai 2016

Présentée par
Sen WANG

Thèse dirigée par **Emmanuel WITRANT** et
Didier MOREAU
préparée au sein du
GIPSA-Lab
dans **l'école doctorale Electronique, Electrotechnique, Automatique, Traitement du Signal (EEATS)**

Data-driven modelling and control of plasma current profile and kinetic parameters in advanced tokamak plasmas

Thèse soutenue publiquement le **16/03/2021**,
devant le jury composé de:

Mazen ALAMIR
Directeur de Recherche CNRS, Université Grenoble Alpes,
Examinateur, Présidente du jury
Marco DE BAAR
Professeur, Technische Universiteit Eindhoven, Rapporteur
Angelo ALESSANDRI
Professeur Associé, Università di Genova, Rapporteur
Federico FELICI
Collaborateur Scientifique, École Polytechnique Fédérale de Lausanne,
Examinateur
Emmanuel WITRANT
Professeur, Université Grenoble Alpes, Directeur de thèse
Didier MOREAU
Ingénieur de Recherche HDR, CEA Cadarache, Co-Encadrant de thèse

UNIVERSITÉ GRENOBLE ALPES

ÉCOLE DOCTORALE EEATS

Electronique, Electrotechnique, Automatique, Traitement du Signal

T H È S E

pour obtenir le titre de

docteur en automatique

de l'Université Grenoble Alpes

Mention : Automatique et Productique

Présentée et soutenue par

Sen WANG

Data-driven modelling and control of plasma current profile and kinetic parameters in advanced tokamak plasmas

Thèse dirigée par Emmanuel WITRANT et Didier MOREAU

préparée au laboratoire GIPSA-Lab

soutenue le 16 Mars 2021

Jury :

Rapporteurs :	Marco DE BAAR	-	Technische Universiteit Eindhoven
	Angelo ALESSANDRI	-	Università di Genova
Directeur :	Emmanuel WITRANT	-	Université Grenoble Alpes
Encadrant :	Didier MOREAU	-	CEA Cadarache
Président :	Mazen ALAMIR	-	Université Grenoble Alpes
Examinateur :	Federico FELICI	-	École Polytechnique Fédérale de Lausanne

Contents

List of Figures

List of Tables

Résumé de la thèse

Contributions

La thèse est consacrée au contrôle du profil de courant et des paramètres cinétiques du plasma dans des scénarios avancés de tokamak en utilisant des modèles pilotés par les données. Le contrôle simultané du profil de courant et des paramètres cinétiques est un défi pour plusieurs raisons:

• Une série d'instabilités magnétohydrodynamiques (MHD) et de microturbulences existent généralement à différents endroits et dans différentes phases des plasmas de tokamak, ce qui peut détériorer le confinement du plasma et même entraîner des perturbations du plasma.

• Les sources d'entraînement et de dépôt de puissance qui régissent l'évolution du profil de courant et des paramètres cinétiques du plasma sont intrinsèquement non linéaires et variables dans le temps, et sont difficiles à caractériser.

• Le nombre d'actionneurs de contrôle disponibles pour le contrôle du profil est limité, ce qui implique que la région de contrôle attractive des profils est restreinte.

• Il existe une série d'incertitudes liées au plasma pendant le processus de contrôle, notamment les dérives des paramètres du plasma dues aux instabilités MHD, aux impuretés et à la turbulence, les erreurs de mesure et d'estimation et les retards.

Les principales contributions de cette thèse peuvent être résumées comme suit:

• Modélisation et simulation de décharges plasma de tokamak en mode H et en régime permanent sur EAST à l'aide du code METIS;

• Identification d'un modèle d'espace d'état non linéaire de la dynamique essentielle du plasma en utilisant à la fois les approches du domaine temporel et du domaine fréquentiel;

• Le développement d'un schéma de contrôle robuste décentralisé et multifonctionnel $\mathcal{H}_\infty$ pour le contrôle simultané du profil du facteur de sécurité et de β_p en utilisant le modèle piloté par les données à deux échelles temporelles identifié à partir de simulations METIS étendues;

• Développement, évaluation et comparaison de trois techniques alternatives de commande

robuste, à savoir la commande robuste $\mathcal{H}_\infty$, la commande intégrale linéaire quadratique et la commande par modèle interne, à l'aide de simulations METIS étendues et d'expériences en boucle fermée sur le tokamak EAST;

• Utilisation des approches de recherche d'extremum basées sur Newton pour l'optimisation en ligne adaptative en temps réel des paramètres cinétiques sur les tokamaks EAST et ITER;

• Application du cadre de commande adaptative à référence de modèle à la commande magnétique et cinétique simultanée dans des scénarios de tokamak avancés;

• Conception du schéma de commande prédictive de modèle sans décalage pour le contrôle simultané du profil de courant du plasma et des paramètres cinétiques sur EAST;

• Test des algorithmes de contrôle à l'aide du simulateur non linéaire METIS;

• Mise en oeuvre des algorithmes de contrôle dans le système de contrôle du plasma (PCS) de EAST [Xiao et al., 2008] et réalisation d'expériences en boucle fermée dans des scénarios opérationnels en mode H et en régime permanent pour valider les algorithmes de contrôle.

Aperçu de la thèse

Ce chapitre a présenté le concept de base de la fusion thermonucléaire, les tokamaks, les scénarios opérationnels avancés et le contrôle du plasma des tokamaks. Nous avons également introduit les sujets de la thèse, les réalisations antérieures dans cette discipline et les contributions majeures de la thèse. Le reste de la thèse est organisé comme suit:

• Le chapitre 2 présente la modélisation du transport dans le plasma du tokamak et l'identification non linéaire de la dynamique essentielle du plasma pour la conception du contrôle. Nous décrivons la modélisation de la diffusion du courant dans le plasma, du transport de chaleur, du transport de quantité de mouvement et des évolutions de la densité du plasma. Ils constituent des sources importantes d'un outil intégré rapide de modélisation de tokamak, à savoir le code METIS. Même si les modèles de premier principe décrits dans ce chapitre présentent une description fluide simple du transport du plasma dans les tokamaks, la complexité des modèles rend la conception et l'analyse du contrôle non triviales. Par conséquent, dans la deuxième partie du chapitre, nous proposons deux nouvelles approches d'identification non linéaire pour extraire la dynamique essentielle du plasma à partir de la simulation et des données expérimentales. La première approche combine la technique d'identification du sous-espace temporel avec l'identification itérative linéaire et non linéaire de l'erreur de sortie. Elle conduit à l'identification d'un modèle de réponse non linéaire à l'espace d'état du plasma qui présente une structure de modèle beaucoup plus simple. La deuxième approche est considérée comme une approche double de la première. Elle traite les données de simulation/expérimentation dans le domaine fréquentiel en combinant la technique du sous-espace fréquentiel et les techniques d'identification itérative linéaire et non linéaire des erreurs en sortie. Des exemples d'application sur le tokamak EAST utilisant à la fois des données de simulation et des données expérimentales sont fournis pour démontrer la validité des approches

d'identification proposées.

Le chapitre 3 présente des algorithmes de contrôle robuste pour le suivi du profil du courant plasma et des paramètres cinétiques. Ce chapitre est divisé en deux parties, la première se concentrant sur le contrôle robuste décentralisé du profil q et du paramètre β_p à l'aide d'un modèle à deux échelles temporelles piloté par les données. Des procédures de conception systématiques sont fournies et des simulations METIS approfondies sur EAST démontrent la performance et la robustesse du schéma de contrôle robuste proposé. Dans la deuxième partie, nous employons trois stratégies de commande robuste, à savoir la commande robuste $\mathcal{H}_\infty$, la commande linéaire-quadratique-intégrale et la commande par modèle interne, pour la commande du profil q et de β_p et nous effectuons des études comparatives. Des simulations et des expériences dans des scénarios de régime permanent en mode H sont effectuées pour évaluer, comparer et discuter les performances et la robustesse de ces trois techniques de contrôle.

Le chapitre 4 présente des algorithmes de contrôle adaptatif pour le suivi du profil de courant du plasma et des paramètres cinétiques. Les inadéquations entre le modèle piloté par les données utilisé pour la conception de la commande et la dynamique réelle du plasma sont inévitables, et il existe des perturbations imprévisibles qui peuvent accroître les inadéquations du modèle. Ce chapitre présente donc une idée alternative pour compenser les inadéquations du modèle par l'adaptation des paramètres. Nous explorons d'abord la stratégie de contrôle adaptatif sans modèle, c'est-à-dire le contrôle de recherche d'extremum basé sur Newton, pour le contrôle cinétique des plasmas des tokamaks avancés sur EAST et ITER. La validité de la commande est confirmée dans les simulations METIS en boucle fermée. Deuxièmement, les schémas de commande adaptative basés sur le modèle sont proposés, impliquant la commande adaptative à référence de modèle dans les modes direct et indirect. De nombreuses simulations METIS non linéaires en boucle fermée sont fournies pour montrer l'efficacité des algorithmes de contrôle adaptatif proposés.

Le chapitre 5 présente un algorithme de contrôle alternatif, c'est-à-dire un contrôle prédictif de modèle (MPC) sans décalage pour le profil de courant et les paramètres cinétiques dans des scénarios avancés de plasma de tokamak. L'algorithme de contrôle permet de combiner le MPC sans offset avec le modèle linéaire à deux échelles temporelles piloté par les données afin de garantir une erreur de suivi nulle en régime permanent. Le contrôle MPC sans offset consiste en un observateur Luenberger proportionnel-intégral pour estimer les états et les perturbations de sortie qui sont transmis au contrôleur MPC pour l'optimisation quadratique. Les simulations et les expériences confirment l'efficacité de l'algorithme de contrôle proposé.

Dans le chapitre 6, nous tirons les conclusions de la thèse et fournissons des perspectives pour les recherches futures.

Chapter 1

Introduction

Contents

1.1 Nuclear energy and thermonuclear fusion

With the development of industry, economy and human society, the demand for renewable, environmentally friendly and sustainable energies is increasing [MacKay, 2008]. Solar, wind, hydro and geothermal power are among these types of energies that can be exploited for electricity production. However, the intrinsic disadvantages of the utilization of these energy sources may restrict their widespread application [Manwell et al., 2010, Kalogirou, 2013, Dickson and Fanelli, 2013]. First, the exploitation of these energy sources strongly relies on their availability, which may constitute unstable energy sources influenced by the wheather and climate changes. Second, the installation of the renewable energy devices is constrained by the locations where the sources should be plentiful, which may be far away from the cities and consumers. Third, the power density generated from these sources such as the sunlight and wind may not be sufficiently intense to support the numerous consumers.

These limits on the renewable energies motivate us to focus on nuclear energy. Power generated from nuclear fission reactions has been utilized for electricity production for many years, which benefits from the intense power density, controllable plant locations, no greenhouse gas

emissions as well as tiny effects from the weather and climate [Marques, 2010]. However, the apparent disadvantages include the proliferation issues, the risks of nuclear safety events and the long-lasting nuclear wastes harmful to the environment [Van der Zwaan, 2008]. In addition, the primary fuels for nuclear fission reactions are confined by their total reserve quantity and cannot be re-generated on Earth, which makes the exploitation of nuclear fission energy not sustainable. Inspired by stars like the Sun, an alternative source of nuclear energy can be derived from nuclear fusion reactions [McCracken et al., 2005]. Therefore, in the search of the clean and safe energy sources, a great effort has been devoted to the development of controlled thermonuclear fusion. In contrast to nuclear fission, nuclear fusion does not produce long-lasting nuclear wastes that are harmful to the environment; meanwhile, the nuclear fusion fuels on Earth are more abundant which can assist in producing sufficient energies for humanity for thousands of years [Freidberg, 2008, McCracken et al., 2005]. However, the construction of a nuclear fusion power plant is extremely problematic, which involves various physical and engineering challenges. Before elaborating the challenges, we briefly describe the physics principles for nuclear fusion.

Among a series of nuclear fusion reactions, the most easily accessible one corresponding to the largest nuclear reaction cross-section occurs between the nuclei of deuterium D and tritium T, which are isotopes of hydrogen. Under certain condition, the nuclei of D and T can fuse and yield a helium nucleus and a neutron. The $D-T$ reaction [Freidberg, 2008, Wesson and Campbell, 2011] can be concretely expressed as:

$$ {}^{2}_{1}\mathrm{D} + {}^{3}_{1}\mathrm{T} \rightarrow {}^{4}_{2}\mathrm{He}(3.5\mathrm{MeV}) + {}^{1}_{0}\mathrm{n}(14.1\mathrm{MeV}) \tag{1.1} $$

where He represents a helium nucleus, while n denotes a neutron. Each reaction produces 17.6 MeV of energy, with 3.5 MeV on the helium nucleus and 14.1 MeV on the neutron. The deuterium is physically stable and abundant in nature, which can easily be extracted from sea water, while the tritium is physically stable and does not appear in nature but it is a product of the nuclear reactions between Lithium and a neutron. Fortunately, Lithium is abundant on Earth and neutrons can be produced simply through nuclear reactions.

In order to achieve nuclear fusion, the nuclei of D and T should overcome the Coulomb barrier (the repulsive forces between two positively charged particles), which requires the nuclei possessing sufficiently high kinetic energy (temperatures), typically at 20 keV. This high level of temperature fully ionizes the fuels D and T to exhibit a state with the quasi-equally distributed positive and negative particles defined as plasma state, implying that the fusion reaction must occur in the plasmas. An important concept for fusion reactions is called ignition, which defines a status where the fusion reactions can be self-sustained [Wesson and Campbell, 2011]. The condition to reach the ignition is provided by the fusion triple product criterion [Wesson and Campbell, 2011, Freidberg, 2008]. More precisely, it requires the triple product of the particle density n, temperature T and energy confinement time τ_E to exceed a critical value as:

$$ nT\tau_E \geq 3 \times 10^{21} \mathrm{m}^{-3}\mathrm{keV\ s} \tag{1.2} $$

where n is in m^{-3} and T is in keV. τ_E, defined as the ratio between the plasma thermal energy E_{th} and the loss power P_{loss}, quantifies the confinement performance in seconds.

There are three possible ways to achieve the ignition condition and realize self-sustained nuclear fusion reactions, i.e., gravitational confinement, inertial confinement, and magnetic confinement. Gravitational confinement [Pfalzner, 2006] utilizes the gravitational force to overcome the Coulomb barrier: this can only exist in the stars like the Sun. The basic idea of inertial confinement is that a rapid pulse of energy is directed onto the surface of a fuel pellet leading to the pellet implosion, thus generating the high densities and temperatures required for fusion [Velarde et al., 1992]. The energy confinement time is thus allowed to be relatively small. Magnetic confinement [Braams and Stott, 2002] is realized by confining the charged particles, such as D and T, with strong magnetic fields in a container and heating the particles to reach the required density, temperature and energy confinement time such that the ignition occurs. There are various magnetic configurations, for example, the tokamak [Wesson and Campbell, 2011], the stellarator [Wakatani, 1998] and the reversed field pinch [Bodin and Newton, 1980], among which the tokamak configuration is the most promising one.

1.2 Tokamaks and advanced tokamak scenarios

The name of tokamak comes from the Russian acronym, TOroidal'naya KAmera s MAgnitnymi Katushkami, which means toroidal chamber with magnetic coils [Wesson and Campbell, 2011]. The tokamak device was first invented by the Soviet physicists Andrei Sakharov and Igor Tamm in the late 1950s [Azizov, 2012]. In contrast to other magnetic fusion configurations, the evident merit of the tokamak device stems from the enhanced stability provided by its larger toroidal magnetic field [Wesson and Campbell, 2011]. The tokamak has therefore been operated to achieve the highest value of the triple product $nT\tau_E$ among all the magnetic fusion configurations and it is believed to be the most promising configuration for nuclear fusion reactors that can achieve commercial eletricity production [Wesson and Campbell, 2011].

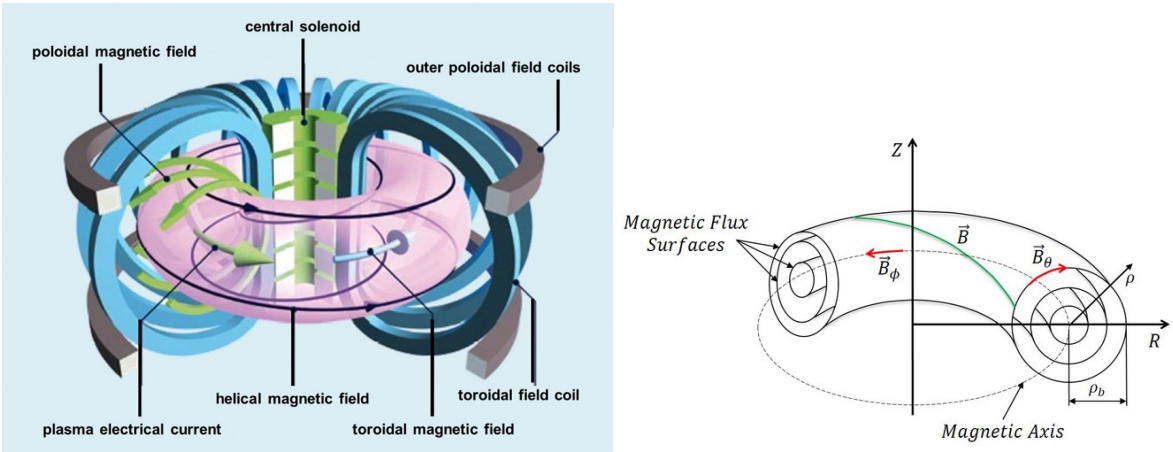

(a) Layout of a tokamak(Image source: EFDA). (b) Magnetic field topology in a tokamak (Image source: [Blanken et al., 2019]).

Figure 1.1: Layout of a tokamak and its nested magnetic field topology.

A tokamak is a toroidal plasma confinement system with its layout as shown in Fig. 1.1(a).

Table 1.1: Main parameters for the EAST and ITER tokamak.

	EAST	ITER
major radius [m]	1.8	6.2
minor radius [m]	0.4	2.0
plasma current [MA]	1	15
toroidal magnetic field [T]	3.5	5.3
EC [MW]	3.8	20
NBI [MW]	8	33
ICRH [MW]	3	20
LHCD [MW]	3.5	-

The plasma is contained in a toroidal vacuum vessel surrounded by toroidal and poloidal field coils. The principal magnetic field is generated by the toroidal field coil currents, though the toroidal field alone is not sufficient to guarantee plasma confinement. A poloidal magnetic field is therefore required to balance the plasma pressure and maintain an equilibrium. Fortunately, the poloidal field is primarily produced by the plasma current itself, which flows in the toroidal direction. The plasma current can be induced by varying the primary transformer circuit current, though fully non-inductive plasma current can be obtained by using only auxiliary current drive sources. The combination of the toroidal and poloidal magnetic fields give rise to the helical magnetic field lines (See Fig. 1.1(b)). The outer poloidal field coils can be leveraged to control plasma position, shape and vertical instability. In order to improve the plasma performance and stability, auxiliary heating and current drive systems are employed to inject neutral beams and launch electromagnetic waves into the plasma bulk. The commonly used heating and current drive systems comprise the neutral beam injection (NBI), electron cyclotron heating & current drive (ECH/ECCD), ion cyclotron resonance heating (ICRH) and lower hybrid current drive (LHCD).

There are various tokamaks being operated in the globe, including JET, DIII-D, ASDEX Upgrade, TCV, WEST [Bucalossi et al., 2014], EAST [Yuanxi et al., 2006] (Fig. 1.2(a)), NSTX [Ono et al., 2000] and KSTAR [Lee et al., 2001]. Significant progress has been made on different research topics in recent years, for example, magnetohydrodynamic instabilities, power exhausts, impurities, snowflake divertor, wall conditioning and advanced tokamak operation. It is noticable that the feasibility of the nuclear fusion production has been experimentally demonstrated in the JET and TFTR tokamaks [Wesson and Campbell, 2011]. At present, the largest tokamak, i.e., the international thermonuclear experimental reactor (ITER) (See Fig. 2.2(b)), is being constructed in southern France, and aims at the first plasma in 2025 [Walker et al., 2020]. Its objective is to demonstrate the scientific and technological feasibility of fusion energy for commercial energy production and to test technologies for a demonstration fusion power plant [Rebut et al., 1995]. The present thesis is dedicated to the investigation of plasma control with examples on two superconducting tokamaks, EAST and ITER, whose main parameters are listed in Table 1.1.

In order to achieve a fusion burn on ITER, the advanced tokamak scenarios charater-

ized by the high-pressure high-performance high-bootstrap current plasma are believed to be crucial [Joffrin, 2007]. There are two typical advanced tokamak scenarios: the steady-state scenario and the hybrid scenario. First, the steady-state scenario is defined as a scenario whose plasma current is generated fully non-inductively by additional current drive systems such as NBI, ECCD, LHCD with a large amount of bootstrap current fraction ($\sim 50\%$). One example of the steady-state scenario on ITER [Joffrin, 2007] is described as follows: the plasma current is at 9 MA with a broad q-profile charaterized by low magnetic shear, the edge safety factor $q_{95} = 5$, the normalized plasma pressure parameter $\beta_N \sim 2.9$, the H-mode enhancement factor is over 1.6, and the plasma density reaches 0.8 of the Greenwald value. This scenario can generate a total power of 350 MW, which results in the fusion gain factor of $Q = 5$. Second, the hybrid scenaro is defined as a scenario whose plasma current is primarily provided by the external current drive systems and the self-generated bootstrap current, with a small fraction of Ohmic current induced by the magnetic flux swing in the tokamak central solenoid. One example of the hybrid scenario on ITER [Green et al., 2003] is depicted as: plasma current is approximately at 13 MA, $q_{95} = 4$, $\beta_N \sim 2.0 - 2.3$, the H-factor is at 1.0 and $f_G = 0.85$ to produce the power of 350-500 MW with $Q = 5$. Advanced tokamak scenarios have already been explored in existing tokamaks [Challis, 2004, Petty et al., 2017, Gong et al., 2019, Bock et al., 2017]. It should be mentioned that the achievement and sustainment of advanced tokamak scenarios are not straightforward because there are many disturbing phenomena that can potentially degrade the plasma confinement, for example, the neoclassical tearing modes, edge localized modes and high-Z impurities. The active feedback control of essential plasma parameters/profiles can therefore facilitate the reproducibility of the advanced tokamak scenarios.

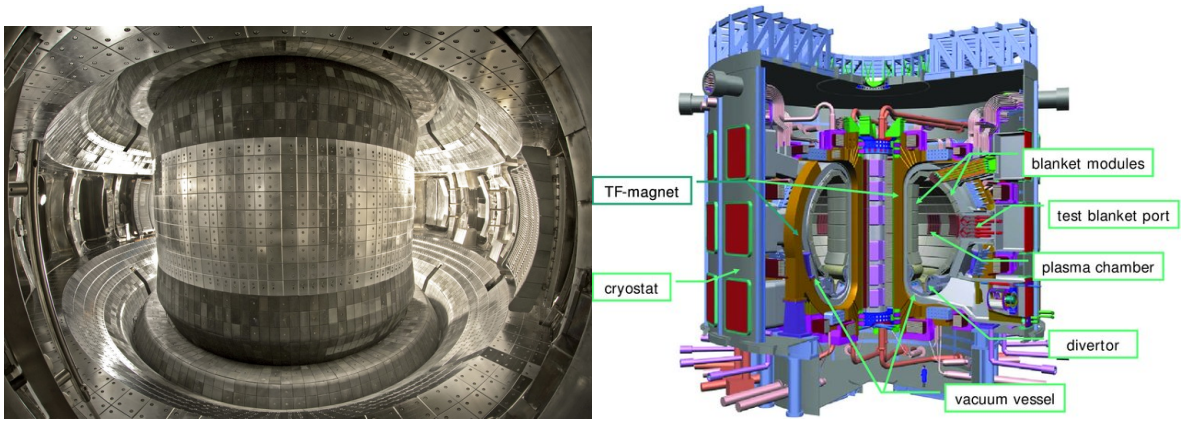

(a) EAST (b) ITER

Figure 1.2: (a) The inner view of the EAST tokamak and (b) the cutway diagram of the ITER tokamak.

1.3 Tokamak plasma control

In this section, we attempt to sketch a concise map in the tokamak plasma control field. In tokamak plasmas, there are many parameters and physical activities that should be properly controlled such that its operation can last. We can basically divide tokamak plasma control problems into the following categories:

- axisymmetric magnetic control: plasma current, position and shape control.

- magnetic and kinetic profile control: plasma current profile, density profile, toroidal rotation profile and temperature profile control.

- magnetohydrodynamic (MHD) control: sawtooth control, neoclassical tearing mode (NTM) control, resistive wall mode (RWM) control, error field control and edge localized mode (ELM) control.

- detachment, power exhaust and radiation power control.

Axisymmetric magnetic control refers to the control of plasma position and shape in the poloidal plane. The objective is to confine the plasma in a specific position with the desired magnetic geometry (plasma shape) by adjusting the poloidal field coil currents. This type of control has been extensively studied and is now mature in the tokamak plasma control community. Assuring the good magnetic control performance is vital to avoid the contact of the plasma with the surrounding walls and the concerntration of impurities from the wall materials in plasmas [Walker et al., 2020]. The control of plasma shape can also facilitate the plasma confinement and power exhaust. In [Huang et al., 2018], it is confirmed that the negative triangularity can lead to a substantial reduction of turbulence amplitude, as well as of the spectral index and correlation length, consistent with the beneficial effect on energy confinement. In [Labit et al., 2019], the magnetic configuration featured by a double null (DN), can lead to a reduction of the magnetic shear in the extreme vicinity of the magnetic separatrix, which is a necessary condition for small ELM regimes with high confinement. In [Ryutov et al., 2012], it is argued that the snowflake divertor configuration can potentially reduce both steady-state and intermittent heat loads on the divertor plates.

Magnetic and kinetic profile control comprise the control of plasma current, density, temperature and rotational profiles. The active control of these profiles is significant because they are intimately associated with the plasma confinement and performance charaterized by the energy confinement time increase, the enhanced MHD stability and the growth of the bootstrap current fraction [Walker et al., 2020]. Due to its significance, extensive studies have been conducted in different tokamaks to demonstrate the effectiveness of profile control schemes in different operational scenarios. The control actuators involve the co-current/counter-current NBI systems, the LHCD systems, the ICRH systems, the ECH/ECCD systems. This thesis is dedicated to the control of the plasma current profile and kinetic parameters on EAST and ITER.

Magnetohydrodynamic instability control refers to the active control of a broad class of

MHD instabilities in tokamak plasmas. A typical example is the real-time correction of the error fields caused by the non-axisymmetric magnetic fields. The external non-axisymmetric magnetic coil currents can be adjusted in real-time [Lanctot et al., 2016] to compensate the error fields. When the safety factor is smaller than 1, sawtooth crashes occur, which manifest themselves as a periodic collape of the pressure in the plasma core [Walker et al., 2020]. When the safety factor has rational values such as 3/2 and 5/2 on some magnetic flux surfaces, NTMs appear and grow around these flux surfaces. The period and amplitude of sawtooth crashes and NTMs can be controlled in real-time by utilizing localized current drive ECCD [Paley et al., 2009,Humphreys et al., 2006, Wehner and Schuster, 2012,Park et al., 2017,Kong et al., 2019].

Detachment, power exhaust, and radiation power control concerns the control of heat fluxes released by the plasma bulk. The power exhaust to the divertor target can be controlled by plasma shaping [Ryutov et al., 2012, Piras et al., 2009, Soukhanovskii et al., 2012]. An alternative strategy is to seed impurities, which can increase the fraction of the radiation power such that the heat loads onto the divertor can be relieved [Kallenbach et al., 2005,Kallenbach et al., 2010,Kallenbach et al., 2015, Vijvers et al., 2014].

1.4 Problem statement and prior works

The thesis aims at the feedback control of the plasma current profile and kinetic parameters in advanced tokamak scenarios using data-driven models. The simultaneous control of current profile and kinetic parameters is challenging for several reasons:

• A series of MHD instabilities and microturbulence commonly exist in various locations and phases of tokamak plasmas that may deteriorate plasma confinement and even lead to plasma disruptions [Wesson and Campbell, 2011].

• The current drive and power deposition sources that govern the evolutions of the plasma current profile and kinetic parameters are intrinsically nonlinear and time-varying, and are difficult to characterize.

• The number of available control actuators for profile control is limited, implying that the attractive region of profile control is restrictive.

• A variety of plasma uncertainties may exist during the control process, including plasma parameter drifts due to MHD instabilities, impurities and turbulence, measurement and estimation errors, and time delays.

Various control schemes for plasma profile control have been pursued both numerically and experimentally on different tokamaks, for example, DIII-D [Moreau et al., 2013,Barton et al., 2015b,Schuster et al., 2017,Boyer et al., 2014,Barton et al., 2012], NSTX-U [Goumiri et al., 2016, Goumiri et al., 2017, Boyer et al., 2015], TCV [Maljaars et al., 2015, Maljaars et al., 2017,Vu et al., 2016,Mavkov et al., 2018,Mavkov et al., 2017a] and JET [Moreau et al., 2008,Laborde et al., 2004,Moreau et al., 2003]. Many of the control schemes are based on the

first-principles plasma models [Witrant et al., 2007], while others are synthesized by using data-driven models identified from dedicated experimental and/or simulation data. In this thesis, linear data-driven models are used for feedback control design because we advert that given an equilibrium we wish to control the plasma, an identified data-based model is more reliable than the transport physics, especially for high confinement plasma, as their dynamics cannot be fully predicted yet. First-principle-based models appear to be more difficult to generally and precisely describe the multi-scale plasma dynamics in advanced plasma scenarios, especially on the fast timescale kinetic evolutions. In view of these, [Moreau et al., 2008, Moreau et al., 2011, Moreau et al., 2015] proposed a semi-empirical data-driven modelling approach that depicts the response of magnetic and kinetic profiles to the variations of the heating and current drive (H&CD) actuators with a linear two-time-scale model structure arising from the first-order singular perturbation expansion of the MHD equations governing plasma dynamics. More precisely, a black-box linear two-time-scale state-space model structure has first been proposed in [Moreau et al., 2008] to describe the plasma magnetic and kinetic responses for feedback control design on JET. The similar technique is extrapolated to the DIII-D and JT-60 tokamaks using the experimental data [Moreau et al., 2011]. Identification of linear state-space models for plasma poloidal magnetic flux profile and the electron temperature profile has been presented in [Mavkov et al., 2017b] using a time-domain approach. In contrast to the existing works regarding plasma model identification for profile control, we extend the plasma model structure into a nonlinear state-space form, which is anticipated to approximate the plasma dynamics with enhanced precision because the evolution of plasma current drive, power deposition, heat diffusivities and bootstrap current are intrinsically nonlinear. Two alternative nonlinear identification approaches, handling data in time-domain and frequency-domain separately, are thus investigated.

The robust control strategies presented in the thesis are all synthesized from linear data-driven models identified from sampled simulation/experimental data in advanced tokamak scenarios. The robust synthesis for profile control using first-principle-driven models has been proposed in [Barton et al., 2012] experimentally on the DIII-D tokamak. The extrapolation of the similar technique to the ITER profile control simulations is presented in [Barton et al., 2015a]. Linear quadratic integral (LQI) control based on a two-time-scale data-driven model was investigated in [Moreau et al., 2008,Moreau et al., 2015] and extended to the ITER profile control simulations in [Liu et al., 2012]. Data-driven models extracted from the TRANSP simulations are used to design an LQI controller for tracking of β_N, I_p and q_0 [Boyer et al., 2017].The extension of LQI to incorporating the feedforward and anti-windup is presented in [Boyer et al., 2019] for the simultaneous control of the stored energy and the toroidal rotation on DIII-D experimentally. In contrast to the existing works, we first separate the two-time-scale data-driven model into three local models, i.e. fast kinetic model, slow kinetic model and magnetic model and then provide a systematic multi-functional robust synthesis approach using linear matrix inequalities (LMIs). In addition, we perform the comparative studies on the control performance of three linear robust control schemes, i.e., $\mathcal{H}_\infty$ robust control, the LQI control and the internal model control (IMC). The comparative study can provide some indications on the pros and cons of each robust controllers, which may be valuable for the robust profile control in advanced tokamak scenarios on ITER.

Evidently, there are some restrictions on the use of linear data-driven models for control. First, the data-driven models rely on the transport, current drive and power deposition models used in simulations and depend on the essential plasma parameters, for instance, plasma density and impurities in tokamak experiments. These can bring a lot of model uncertainties. In this regard, we provide adaptive control schemes in which the manipulated inputs are adaptively updated based on the real-time measured inputs and outputs. Two categories of adaptive controllers are attempted, i.e., the model-free extremum-seeking control (ESC) and the model reference adaptive control (MRAC). Up to our best knowledge, ESC has already been applied to the sawtooth period control [Paley et al., 2009, Bolder et al., 2012], NTM control [Wehner and Schuster, 2012] and error field control [Lanctot et al., 2016]. Nonetheless, its extended version, i.e., the Newton-based ESC, has not yet been studied. The MRAC control in its direct and indirect versions [Ioannou and Sun, 1996, Tao, 2014] are both taken into account in the present thesis, which is novel for the tokamak plasma control community.

As an alternate control strategy, the model predictive control (MPC) of q-profile has already been investigated in [Maljaars et al., 2015, Maljaars et al., 2017] on ITER and TCV using the first-principle-driven models. The offset-free MPC has been proposed in the control community [Borrelli and Morari, 2007, Maeder et al., 2009, Maeder and Morari, 2010], which is proved more powerful than the standard MPC for the control of uncertain linear systems. In this study, the offset-free MPC is combined with the two-time-scale data-driven model for the simultaneous control of q-profile and the poloidal plasma pressure parameter β_p. Both nonlinear simulations and experiments on the EAST tokamak confirm the effectiveness of the proposed approach. We remark that, contrary to the other control schemes proposed in the thesis, the major disadvantage of the MPC scheme lies in the large computation time at each control cycle [Maljaars et al., 2017].

1.5 Achievements

The main achievements of the thesis are summarised as follows:

• modelling and simulation of H-mode steady-state tokamak plasma discharges on EAST and ITER using the METIS code [Artaud et al., 2018];

• performing nonlinear state-space model identification of essential plasma dynamics on EAST and ITER using both the time-domain and frequency-domain approaches;

• developing a decentralized multi-functional $\mathcal{H}_\infty$ robust control scheme for the simultaneous control of q-profile and β_p using a two-time-scale data-driven model identified from extensive METIS simulations;

• developing, evaluating and comparing three linear robust control techniques, i.e., the $\mathcal{H}_\infty$ robust control, the LQI control and the IMC control, with extensive METIS simulations and closed-loop experiments on EAST;

• using the Newton-based ESC for real-time adaptive online optimization of kinetic pa-

rameters on EAST and ITER;

• applying the MRAC schemes to the magnetic and kinetic control in advanced tokamak scenarios on EAST;

• designing the offset-free MPC scheme for the simultaneous control of q-profile and β_p on EAST;

• testing the control algorithms using the METIS plasma simulator;

• implementing the control algorithms into the EAST plasma control system (PCS) [Xiao et al., 2008] and validate them by performing closed-loop experiments in an H-mode steady-state plasma scenario on the EAST tokamak.

1.6 List of related publications

Journal Articles

- S. Wang, E. Witrant, D. Moreau. Robust control of q-profile and β_p using data-driven models on EAST. Fusion Engineering and Design [Wang et al., 2020].

- S. Wang, E. Witrant, D. Moreau, Y. Huang, et al. Identification of nonlinear plasma response models for real-time kinetic control in advanced tokamak scenarios. (submitted to Physics of Plasmas).

- S. Wang, D. Moreau, E. Witrant, et al. Robust real-time feedback algorithms in advanced tokamak scenarios. (submitted to Plasma Physics and Controlled Fusion).

International Conference Papers

- S. Wang, D. Moreau, J.P. Qian, E. Witrant, et al. Real-time control of the internal inductance and poloidal beta parameters in H-mode steady-state scenarios on EAST. The 47th European Physical Society Conference on Plasma Physics, 2021, Sitges, Spain.

- D. Moreau, S. Wang, J.P. Qian, et al. Model-predictive kinetic control experiments on EAST. The 28th IAEA Fusion Energy Conference, 2021, Nice, France.

- D. Moreau, J.P. Qian, ... (S. Wang), et al. Model-predictive kinetic control for steady state plasma operation scenarios on EAST. The 27th IAEA on Fusion Energy Conference, 2018, Gandhinagar, India.

1.7 Outline of the Thesis

This chapter has presented the basic concept of thermonuclear fusion, tokamaks, advanced operational scenarios and tokamak plasma control. The thesis topics, prior achievements in the discipline and major contributions of the thesis are also introduced. The remainder of the thesis is organized as follows:

• Chapter 2 presents the modelling of tokamak plasma transport and nonlinear identification of essential plasma dynamics for control. We describe the modelling of plasma current diffusion, heat transport, momentum transport, and plasma density evolutions, which constitute a major part of the METIS code. Even though the first-principles models described in this chapter offer a simple fluid description of tokamak plasma transport, the complexity of the models still makes the control design and analysis non-trivial. Therefore, in the second part of the chapter, we propose two novel nonlinear identification approaches to approximate the essential plasma dynamics from simulation and experimental data in tokamaks. The first approach combines the time-domain subspace identification technique with nonlinear iterative predition-error identification, resulting in a linear-time-invariant (LTI) nonlinear polynomial state-space plasma dynamic model. The second approach, as a dual technique, handles the simulation/experimental data in the frequency-domain using the combination of the frequency-domain subspace technique and the nonlinear iterative predition-error techniques. Application examples on the EAST tokamak using both simulation and experimental data are provided to demonstrate the validity of the proposed identification approaches.

• Chapter 3 presents robust control algorithms for the tracking of q-profile and kinetic parameters. This chapter is divided into two parts, where the first one focusses on the decentralized $\mathcal{H}_\infty$ robust control of q-profile and β_p using a two-time-scale data-driven model. Systematic design procedures are provided and extensive METIS simulations on EAST demonstrate the performance and robustness of the proposed robust control scheme. In the second part, we develop three linear robust controllers, i.e., $\mathcal{H}_\infty$ robust control, the LQI control, and the IMC control for tracking of plasma kinetic parameters, with a cascade inner control loop for actuation tracking. Both simulation and experiments in H-mode steady-state scenarios are carried out to evaluate, compare and discuss the performance and robustness of each control techniques.

• Chapter 4 presents adaptive control algorithms for the tracking of the plasma kinetic parameters. The model mismatches between the data-driven model and the tokamak plasma dynamics are inevitable, and there are unpredictable disturbances that is likely to enlarge these model mistmatches. An alternative idea is to compensate the model mismatches with the real-time parameter adaptation, as described in this chapter. We first explore the model-free adaptive control strategy, i.e., the Newton-based ESC, for the kinetic optimization in advanced tokamak plasmas on EAST and ITER. The validity is confirmed in the closed-loop METIS simulations. Secondly, the model-based MRAC schemes are proposed, involving both the single-input single-output (SISO) case and the multiple-input multiple-output (MIMO) case. Extensive nonlinear closed-loop METIS simulations are provided to show the effectiveness of the proposed MRAC algorithms.

• Chapter 5 presents the offset-free MPC for q-profile and β_p in advanced tokamak scenarios. The control algorithm allows for the combination of the offset-free MPC with a linear two-time-scale data-driven model to acquire the zero steady-state tracking zero. The offset-free MPC consists of a proportional-integral (PI) Luenberger observer to estimate states and output disturbances which are then fed to the MPC controller for quadratic optimization. Both simulations and experiments confirm the effectiveness of the proposed control algorithm.

• In Chapter 6, we draw the conclusions of the thesis and provide perspectives for the future research.

Chapter 2

Tokamak Plasma Modelling and Identification

Contents

The modelling of tokamak plasma transport is a broad subject in the field of nuclear fusion, which spreads from single fluid modelling to comprehensive gyro-kinetic modelling [Fasoli et al., 2016]. In this chapter, we are interested in introducing a single fluid modelling, i.e., the minute embedded tokamak integrated simulator (METIS) suite [Artaud et al., 2018], of essential tokamak plasma transport dynamics, comprising plasma current diffusion, thermal transport, momentum transport and assumptions for density profile evolutions, and make use of this modelling tool to simulate H-mode high-performance plasma discharges on the EAST and ITER tokamaks. The METIS suite is an integrated tokamak modelling tool aiming

at the fast full tokamak plasma analyses and predictions. It combines 0D scaling laws for normalised heat and particle transport with 1D current diffusion modelling and 2D equilibria [Artaud et al., 2018], which is built on a simplification paradigm of the plasma transport problem, and METIS allows for plasma scenario simulations in around 1 minute computation time, even for full ITER discharges with the pulse duration at $\sim$ 1000 s. Even though the METIS modelling appears to be simple, the objective of this code is to precisely describe the plasma profile dynamics in the timescale of the energy confinement time. It has been demonstrated to be capable of simulating the plasma profiles in H-mode high-performance plasma scenarios on different tokamaks and to be suitable for the shot-to-shot experimental scenario analyses as well as controller performance assessments [Nilsson et al., 2013, Moreau et al., 2013,Litaudon et al., 2013]. In the thesis, METIS is used as a tokamak plasma simulator that allows for the plasma discharge simulations on EAST and ITER and manifests itself as a testbed to evaluate the effectiveness and validity of the proposed model identification and feedback control strategies.

Achievement and reproducibility of high-performance steady-state plasma scenarios are essential for the current and next-generation tokamak plasma operation, which can greatly benefit from precise control of crucial plasma parameters such as the plasma safety factor and rotational velocity [Ferron et al., 2006]. In order to control these parameters, the most direct and tractable way is to use the model-free proportional-integral-derivative (PID) control [Åström et al., 2006, Landau and Zito, 2007], which has been widely applied to industrial controls due to its simple implementation and attractive control performance. However, in the absence of a plasma dynamics model, the trial and error tuning of the PID parameters may take an extra amount of experimental time that is likely to cause undesirable plasma behaviour. Therefore, to improve the control efficiency and reliability, a straightforward treatment is to first develop a control-oriented plasma response model that appropriately depicts plasma response dynamics in a reduced-order model, based on which a feedback controller can then be synthesized.

There are two categories of techniques to build control-oriented plasma response models. The first category is named the first-principle-driven model that can be simplified from nonlinear partial-differential-equations (PDEs) governing the plasma transport evolutions by a set of assumptions and simplication procedures [Witrant et al., 2007, Ou et al., 2007, Barton et al., 2012], for example, linearization and spatial discretization. The second category resorts to system identification methodologies [Moreau et al., 2008,Moreau et al., 2013], which extract black-box plasma response models from the observed input-output data by assuming a stationary model structure. Ideally, first-principle-driven models are preferred because they should have a universal domain of validity. However, the physical understanding of plasma transport and wave-plasma interaction in high-performance tokamak plasmas has not been fully clarified such that many essential physical parameters can merely be estimated empirically via scaling laws [Artaud et al., 2010, Artaud et al., 2018] and the parameter uncertainties are very difficult to be characterized and evaluated. Furthermore, in order to derive first-principle-driven models that are suitable for plasma control, an important fraction of physical fidelity may be lost during the simplication process. Therefore, this chapter is dedicated to extracting control-oriented plasma response models from sophisticated nonlinear plasma simulation data

and experimental data using a uniform system identification methodology.

The use of data-driven models for plasma current profile and kinetic control has already been studied. Initial works comprise the PID design using data-driven-based transfer function modelling of the plasma response dynamics for q-profile control on JET [Moreau et al., 2003, Joffrin et al., 2003, Mazon et al., 2003]. Data-driven plasma response models that describe the coupled dynamics of magnetic and kinetic plasma evolutions using the singular perturbation theory are systematically investigated in [Moreau et al., 2008], and its validity is further confirmed by applying the system identification methodology considered in [Moreau et al., 2008] to different tokamaks [Moreau et al., 2011]. In [Kim and Lister, 2012], static models for the response of the variations of plasma current profile and electron temperature profile with respect to those of auxiliary heating & current drive (H&CD) powers are identified online via the least-squares method based on which the feedback control actuations are computed and updated adaptively. Extensive nonlinear simulations on ITER with the CRONOS code [Artaud et al., 2010] have demonstrated the effectiveness of the static data-driven models for the feedback control design. In [Mavkov et al., 2017b], a systematic procedure is proposed to identify the coupled dynamics of the poloidal magnetic fluxes and the electron temperature profile on DIII-D using the noise-free METIS simulation data in a lumped way. It assumes a LTI state-space model structure, initializes the model with a time-domain subspace method, namely multivariable output-error state-space (MOESP) identification [Verhaegen and Verdult, 2007], and refines the model using the output-error identification technique [Verhaegen and Verdult, 2007]. Comparisons of the model-simulated output data with the corresponding output from nonlinear METIS simulations have shown the effectiveness of the identification procedure. However, the derived LTI state-space models were restricted to small output space dimensions to describe the plasma parameters profiles and have not been further employed for control design and evaluations.

System identification is a subject to build mathematical models of dynamic systems from observed input–output data, which is filled with numerous classes of techniques depending on the identified model structures, e.g. linear, nonlinear, hybrid and non-parametric [Ljung, 2010]. Interested readers are referred to [Ljung, 2010, Noël and Kerschen, 2017] for a review of this subject and to [Ljung and Söderström, 1983, Verhaegen and Verdult, 2007, Lennart, 1999] for reference textbooks. Since the objective of the thesis is to identify black-box models with a stationary model structure, e.g. a state-space model, for advanced control designs, we restrict our efforts to the topic of the black-box state-space model identification. In the literature, there are two major classes of state-space identification methods, i.e. the subspace methods and the prediction-error method (PEM) [Ljung, 2010, Yu et al., 2019]. The subspace methods are based on the fact that system matrices of the black-box state-space models can be related to certain subspaces of the structured block Hankel matrices filled with the observed input-output data [Verhaegen and Verdult, 2007]. One merit of this class of methods is that the identification is non-iterative. In order to handle the measurement noise, instrumental variables can be involved [Verhaegen and Verdult, 2007]. The idea of the prediction-error method is to minimize a cost functional defined as a mean squared prediction error between the sampled output and the one-step-ahead model prediction to obtain the optimal system model matrices. This method is iterative. The benefit of the PEM method is that it has the

best possible asymptotic accuracy. However, local minimum can often be obtained, implying its sensitivity to initial parameter estimate [Yu et al., 2019]. Combining the subspace method and PEM can naturally accumulate their advantages and compensate their limitations, which have already been confirmed in [Verhaegen and Verdult, 2007] and applied to the LTI state-space identification in tokamak plasmas using noise-free simulation data [Mavkov et al., 2017b].

In this chapter, we are dedicated to unifying the two classes of identification methods to both simulation (noise-free) and experimental (noise-corrupted) data in advanced tokamak plasma scenarios on EAST and ITER. A nonlinear model identification scheme for magnetic and kinetic parameter control is proposed using a combination of the subspace and PEM identification techniques, which aims to capture the dominant linear plasma response dynamics as well as certain nonlinearities caused by, for instance, the bootstrap effects or plasma-wave interaction. We consider the plasma dynamics to be a black-box polynomial nonlinear state-space (PNLSS) system. The objective is to identify an optimal model that approximates the plasma dynamics maximally in a prescribed model structure using the observed input-output measurements. Motivated by [Paduart et al., 2010, Mavkov et al., 2017b], we divide the nonlinear identification process into two stages: first, a combination of the subspace and PEM techniques are employed to identify the dominant linear plasma responses of magnetic and kinetic parameters with respect to control actuations, and the linear identification problem is addressed both in time-domain and frequency-domain. Second, initializing the PNLSS model with the derived linear state-space (LSS) model, a prediction-error method is applied to identify the nonlinear terms while refining the linear model matrices. The drawback of the PNLSS model is that the number of estimated nonlinear parameters increases substantially with the growth of the polynomial degree, which motivates us to utilize a decoupling technique to describe them in a parsimonious representation [Dreesen et al., 2015].

The *major contributions* of this chapter are outlined as follows:

- Single fluid modelling of plasma transport dynamics for plasma discharge simulations on EAST and ITER using the METIS code.
- Development of a systematic identification procedure for a linear state-space plasma model from simulation/experimental data in advanced tokamak plasma scenarios using both time- and frequency-domain identification approaches.
- Development of a systematic identification procedure for a nonlinear plasma response model based on the derived linear model to characterize nonlinear plasma dynamics.
- Validation of the effectiveness of the proposed identification procedures via comparisons of the model-predicted results with the associated simulation/experimental data on EAST and ITER.

In the remainder of this chapter, Section 2.1 presents the single fluid METIS modelling of the plasma current density diffusion, thermal transport, momentum transport and electron and ion density profiles on the EAST and ITER tokamaks, with the important variable definitions listed in Table 2.1. In Section 2.2, we formulate the model identification problem, propose

a nonlinear model structure, outline the identification procedure and provide guidelines to preprocess the observed data for model identification. The identification of the linear plasma dynamics is addressed using both time-domain and frequency-domain approaches. Furthermore, it is arranged to describe a PNLSS plasma model identification algorithm to characterize the nonlinear plasma dynamics. Identification results from both simulation and experimental data are presented to demonstrate the effectiveness of the proposed identification algorithms. We subsequently make a summary of the chapter and suggest possible improvements.

2.1 Tokamak plasma modelling: a single fluid description

In this section, we describe the single fluid modelling of tokamak plasma dynamics on the timescale of the energy confinement time with the METIS code, and present the reference scenario simulations in H-mode steady-state scenarios on EAST and ITER.

2.1.1 Current density diffusion

The plasma current diffusion can be expressed in terms of the poloidal magnetic flux Ψ as in [Artaud et al., 2018]:

$$\frac{\partial \Psi}{\partial t} = \alpha_1(t,\rho)\frac{\partial^2 \Psi}{\partial^2 \rho} + \alpha_2(t,\rho)\frac{\partial \Psi}{\partial \rho} + \alpha_3(t,\rho) j_{ni} \tag{2.1}$$

where

$$\alpha_1(t,\rho) = \frac{\langle \frac{|\bigtriangledown \rho|^2}{R^2} \rangle}{\mu_0 \sigma_{||} \rho_m^2 \langle \frac{1}{R^2} \rangle} \tag{2.2}$$

$$\alpha_2(t,\rho) = \frac{\langle \frac{|\bigtriangledown \rho|^2}{R^2} \rangle}{\mu_0 \sigma_{||} \rho_m^2 \langle \frac{1}{R^2} \rangle} \frac{\partial}{\partial \rho} \left[\ln \left(\frac{\frac{\partial V}{\partial \rho} \langle \frac{|\bigtriangledown \rho|^2}{R^2} \rangle}{F} \right) \right] + \frac{d\rho_m}{dt} + \frac{\rho}{2B_0} \frac{dB_0}{dt} \tag{2.3}$$

$$\alpha_3(t,\rho) = \frac{B_0}{\sigma_{||} F \langle \frac{1}{R^2} \rangle} \tag{2.4}$$

Here, $\sigma_{||}$ represents the parallel conductivity, F is the diamagnetic function, j_{ni} indicates the non-inductive current density sources, R the major radius, μ_0 the magnetic permeability of free space, ρ_m the radius at the last closed flux surfaces, ρ is a normalized flux surface average radius, i.e. $\rho = \frac{1}{\rho_m}\sqrt{\frac{\Phi}{\pi B_0}}$, where B_0 is the vacuum magnetic field at the major radius R_0, Φ being the toroidal magnetic flux. The notation $\langle\rangle$ is an identifier indicating a flux surface average. The neoclassical electrical conductivity $\sigma_{||}$ is computed as [Sauter et al., 1999]:

$$\sigma_{||} = c_{neo}(\rho) k_{spitzer}(\rho) \frac{T_e(t,\rho)^{\frac{3}{2}}}{Z_{eff}(t,\rho)} \tag{2.5}$$

where $c_{neo}(\rho)$ is the neoclassical correction profile, $k_{spitzer}(\rho)$ the constant Spitzer coefficient profile, $T_e(t,\rho)$ the electron temperature profile, and $Z_{eff}(t,\rho)$ the effective charge profile.

Table 2.1: Parameter definition.

Variables	Description	Units
ψ	poloidal magnetic flux profile	$T \cdot m^2$
W_{th}	thermal energy	J
j_{ni}	noninductive current density	$A \cdot m^{-2}$
σ	parallel conductivity	$\Omega^{-1} \cdot m^{-1}$
μ_0	permeability of free space: $4\pi \times 10^{-7}$	$H \cdot m^{-1}$
τ_E	energy confinement time	s
P_{loss}	loss power	W
Q_e	electron heat flux	W
Q_i	ion heat flux	W
T_e	electron temperature profile	eV
T_i	ion temperature profile	eV
n_e	electron density profile	m^{-3}
n_i	ion density profile	m^{-3}
χ_e	electron diffusivity	$m^2 \cdot s^{-1}$
χ_i	ion diffusivity	$m^2 \cdot s^{-1}$
P_{aux}	auxiliary power	W
P_α	α particle power due to fusion reaction	W
P_{brem}	Bremstranglur radiation power	W
P_{cyclo}	cyclotron radiation power	W
P_{rad}	line radiation power	W
Z_{eff}	effective charge number	A.U.
F	diamagnetic function	$T \cdot m$
ρ	surface average normalized radius	A.U.
$\langle \sigma \upsilon \rangle_{T(d,n)He_4}$	D-T nuclear reaction cross section	m^{-2}
n_D	deuteurium density profile	m^{-3}
n_T	tritium density profile	m^{-3}
e	unit electron charge	C
P_{NBI1}	the first neutral beam power	W
P_{NBI2}	the second neural beam power	W
P_{ECRH1}	the first electron cyclotron resonance heating power	W
P_{ECRH2}	the second electron cyclotron resonance heating power	W
P_{ICRH}	the ion cyclotron resonance heating power	W
q	safety factor profile	A.U.
ι	inverse safety factor profile	A.U.

The non-inductive current density comprises self-generated bootstrap current density j_{boot} and the auxiliary driven current density j_{auxi}, of which j_{boot} is calculated as [Sauter et al., 1999]:

$$j_{boot} = \frac{k_{boot}}{\partial\Psi/\partial\rho}\left[L_{31}\frac{\partial n_e}{\partial\rho}T_e + (L_{31} + R_{pe}L_{32} + (1-R_{pe})L_{34})\frac{\partial T_e}{\partial\rho}n_e\right] \tag{2.6}$$

Here $k_{boot}, L_{31}, L_{32}, L_{34}$ are coefficients that depend on the magnetic configuration of a plasma equilibrium and R_{pe} is the ratio between electron and total pressures, i.e. $R_{pe} = p_e/p$ the ratio between electron p_e and total pressure p. The auxiliary current density j_{auxi} is decomposed as:

$$j_{auxi} = \sum_{n=1}^{n_{NBI}} j_{NBI,n} + \sum_{n=1}^{n_{EC}} j_{EC,n} + \sum_{n=1}^{n_{IC}} j_{IC,n} + \sum_{n=1}^{n_{LH}} j_{LH,n} \tag{2.7}$$

where $n_{NBI}, n_{EC}, n_{IC}, n_{LH}$ are respectively the number of actuators of the neutral beam injection (NBI) system, the electron cyclotron (EC) current drive system, the ion cyclotron (IC) current drive system and the lower hybrid (LH) current drive system. $j_{NBI,n}$,$j_{EC,n}$,$j_{IC,n}$,$j_{LH,n}$ are the non-inductive current density profiles driven by the n^{th} NBI, n^{th} EC, n^{th} IC and n^{th} LH systems, respectively.

The total current density driven by the n^{th} NBI injector $j^{total}_{NBI,n}$ is computed by an analytical solution of the Fokker-Planck equation [Wesson and Campbell, 2011] in which both trapping effects and energy diffusion are neglected:

$$j^{total}_{NBI,n} = \frac{p_{NBI,n}(\rho)e}{E_b}\tau^s_{NBI,n}\xi_b\left(\frac{v^3_{0,n} + v^3_{c,n}}{v^3_{0,n}}^{\frac{2v^3_{\gamma,n}}{3v^3_{c,n}}}\right)\int_0^{\frac{v_{0,n}}{v_{c,n}}}\left(\frac{z^3}{z^3+1}\right)^{\frac{2v^3_{\gamma,n}}{3v^3_{c,n}}+1}dz \tag{2.8}$$

where $p_{NBI,n}(\rho)$ is the n^{th} NBI power deposition profile, $\tau^s_{NBI,n}$ the n^{th} NBI slowing down time, $v_{c,n}$ and $v_{\gamma,n}$ are the critical velocities for the n^{th} NBI injector and $v_{0,n}$ the fast ion initial velocity for the n^{th} NBI injector. The electron back-current $j^{back}_{NBI,n}$ is computed following the formulation in [Lin-Liu and Hinton, 1997], which is then subtracted from the total NBI current to obtain the driven current density due to the NBI injections, i.e. $j_{NBI,n} = j^{total}_{NBI,n} - j^{back}_{NBI,n}$.

The total current driven by the n^{th} EC system is computed as [Krivenski et al., 1985]:

$$I_{EC,n}(t) = \frac{s_{EC,n}\Gamma_{LH,EC}\eta_{EC,n}(t)P_{EC,n}(t)}{n_e(t, x_{EC,n}(t))R_{ref}(t)} \tag{2.9}$$

where $s_{EC,n}$ is the direction of the wave injection for the n^{th} EC system, i.e. $s_{EC,n} = 1$ for the co-current wave injection, $s_{EC,n} = -1$ for counter-current injection. $\Gamma_{LH,EC}$ is the synergy factor between the EC and the LH systems. $P_{EC,n}(t)$ is the total deposited power of the n^{th} EC system, $x_{EC,n}(t)$ is the maximum power deposition position of the n^{th} EC system, $n_e(t, x_{EC,n}(t))$ the electron density at $x_{EC,n}(t)$. The EC current efficiency is $\eta_{EC,n} = \frac{\gamma_n}{5+Z_{eff}}$, where Z_{eff} is the effective charge number and γ_n is computed as [Krivenski et al., 1985]:

$$\gamma_n = \left(1 + \frac{100}{\frac{T_e(t,x_{EC,n})}{10^3}}\left[1 - \left(1 + \frac{5+Z_{eff}}{3(1+Z_{eff})}(\sqrt{2}u_{t,n})^{\frac{5+Z_{eff}}{1+Z_{eff}}}\right)\right]\right)^{-1} \tag{2.10}$$

where

$$\mu_{t,n} = \sqrt{\frac{a_{ref} x_{EC,n}(1+\cos(\theta_{pol}))}{R_{ref} + a_{ref} x_{EC,n}\cos(\theta_{pol})}} \tag{2.11}$$

Here $T_e(t, x_{EC,n})$ is the electron temperature at the power deposition position of the n^{th} EC system $x_{EC,n}$. a_{ref} is the small radius while R_{ref} denotes the major radius. θ_{pol} represents the poloidal angle of the n^{th} EC system. We assume that the current density driven by the n^{th} EC system $j_{EC,n}(t,\rho) = k_{j_{EC},n}(t) p_{EC,n}(\rho)$, where $p_{EC,n}(\rho)$ is the power deposition shape for the n^{th} EC system, which is a Gaussian curve with the width $\delta_{EC,n}$ at the location $x_{EC,n}$. $k_{j_{EC},n}(t)$ is time-varying and computed as:

$$k_{j_{EC},n}(t) = \frac{I_{EC,n}(t)}{\rho_m \int_0^1 p_{EC,n}(\rho) V'(t,\rho) d\rho} \tag{2.12}$$

Where $I_{EC,n}$ is the total EC-driven current for the n^{th} EC wave launcher.

The total driven current by the n^{th} IC system is computed as [Artaud et al., 2018]:

$$I_{IC,n}(t) = \frac{s_{IC,n} P_{IC,n}(t) \eta_{IC,n}(t)}{R_{ref} \frac{n_e(t,\rho=0)}{10^{20}}} \tag{2.13}$$

where $s_{IC,n}(t)$ is the direction of the n^{th} IC wave injection, i.e. $s_{IC,n} = 1$ for co-current injection, while $s_{IC,n} = -1$ for counter-current injection. $P_{IC,n}(t)$ is the total power deposition from the n^{th} IC system. $\eta_{IC,n}(t)$ is the current drive efficiency for the n^{th} IC system. $n_e(t, \rho = 0)$ is the electron density at the magnetic axis. It is assumed that the driven current density by the n^{th} IC system is $j_{IC,n}(t,\rho) = k_{j_{IC},n}(t) j_{IC,n}^{shape}(t,\rho)$, where the driven current density shape for the n^{th} IC system is expressed as:

$$j_{IC,n}^{shape}(\rho)(t,\rho) = \frac{n_e(t,\rho) T_e(t,\rho) \sigma_{||}}{B_{out}(t,\rho)^3 V'(t,\rho)} \tag{2.14}$$

$n_e(t,\rho)$ and $T_e(t,\rho)$ are respectively the electron density and temperature profiles. $\sigma_{||}$ is the parallel electron conductivity. The normalized coefficient $k_{j_{IC},n}(t)$ is computed as [Artaud et al., 2018]:

$$k_{j_{IC},n}(t) = \frac{I_{IC,n}(t)}{\rho_m \int_0^1 j_{EC,n}^{shape}(t,\rho) V'(t,\rho) d\rho} \tag{2.15}$$

where $I_{IC,n}(t)$ is the n^{th} IC-driven current.

The total current density driven by the n^{th} LH system is expressed as:

$$j_{LH,n}(t,\rho) = \eta_{LH,n}(t,\rho) \frac{P_{LH,n}(t,\rho)}{n_e(t,\rho)} \frac{1 - \epsilon^{\frac{5+Z_{eff}(t,\rho)}{2(1+Z_{eff}(t,\rho))}}}{5 + Z_{eff}(t,\rho)} \tag{2.16}$$

where $n_e(t,\rho)$ is the electron density profile. $Z_{eff}(t,\rho)$ is the effective charge profile. $P_{LH,n}(t,\rho)$ is the local power deposition profile for the n^{th} LH system. $\eta_{LH,n}$ is the current drive efficiency for the n^{th} LH system [Fisch, 1978].

2.1.2 Thermal transport

Even though many efforts have been made in tokamak fusion research, the modelling of the heat transport in the core of tokamak plasmas features large uncertainties. In order to simultaneously capture important physics characteristics for heat transport and minimize the computational time, a mixed 0D-1D approach is adopted in two steps by separating the temporal and spatial dimensions [Artaud et al., 2018].

In the first step, the total plasma thermal energy W_{th} is calculated by a first-order ordinary differential equation (ODE) as:

$$\frac{dW_{th}}{dt} = -\frac{W_{th}}{\tau_E} + P_{heat} - P_{rad} \tag{2.17}$$

where τ_E is the energy confinement time in second, which, in tokamaks, is most commonly expressed with the help of a scaling law. For H-mode plasmas, the scaling law ITERH-98P(y,2) is applied, while for L-mode the scaling law ITERL-96 (th) is used. P_{heat} and P_{rad} are the total heating and radiation powers respectively, which can be expressed as:

$$P_{heat} - P_{rad} = P_{ohm} + P_{auxi} + P_{\alpha} - P_{brem} - P_{cyclo} - f_{line}P_{line} \tag{2.18}$$

Here, P_{ohm} is the ohmic power, P_{auxi} represents the auxiliary deposited power, which is given by $P_{auxi} = \sum_{n=1}^{n_{NBI}} P_{NBI,n} + \sum_{n=1}^{n_{EC}} P_{EC,n} + \sum_{n=1}^{n_{IC}} P_{IC,n}$. P_{α} is the total power arising from generated α particles due to D-T reactions, which is derived as $P_{\alpha} = \int_0^1 p_{\alpha,th}(t,\rho)d\rho$, where $p_{\alpha,th}(t,\rho)$ is the α power density profile, and is computed as:

$$p_{\alpha,th}(t,\rho) = eE_{\alpha,T(d,n)He_4} n_D(t,\rho) n_T(t,\rho) \langle \sigma\upsilon \rangle_{T(d,n)He_4}[T_i(t,\rho)] \tag{2.19}$$

Here $E_{\alpha,T(d,n)He_4} = 3.6$ MeV, e is the unit of electric charge, n_D and n_T are respectively the deuterium and tritium density profiles. $\langle \sigma\upsilon \rangle_{T(d,n)He_4}[T_i(t,\rho)]$ is the D-T fusion reaction cross section [Bosch and Hale, 1992] which is closely related to the ion temperature profile $T_i(t,\rho)$.

P_{brem}, P_{cyclo} and P_{rad} are respectively the total power radiated by thermal Bremsstrahlung, cyclotron and line radiation, of which P_{brem} is calculated as:

$$P_{brem}(t) = \rho_m \int_0^1 p_{brem}(t,\rho) V' dx \tag{2.20}$$

where $p_{brem}(t,\rho)$ is the Bremsstrahlung radiation power density [Rybicki and Lightman, 2008]:

$$p_{brem}(t,x) = 4.8562 \times 10^3 \frac{n_e(t,\rho)}{10^{20}} \sqrt{\frac{T_e(t,\rho)}{10^3}} \sum_{k=j} C_{gaunt}(T_e(t,\rho), Z_k) Z_k^2 \frac{n_k(t,\rho)}{10^{20}} \tag{2.21}$$

where $n_e(t,\rho)$ is the electron density profile, while $T_e(t,\rho)$ represents the electron temperature profile. $C_{gaunt}(T_e(t,\rho), Z_k)$ is the Gaunt factor [Matthews et al., 1999] while Z_k and $n_k(t,\rho)$ are the charge number and density for the k^{th} ion species, respectively.

The cyclotron radiation is modelled as [Albajar et al., 2001]:

$$P_{cyclo} = 0.0384(1-r_w)^{1/2} Ra^{1.38} \kappa^{0.79} B_t^{2.62} n_{e,c}^{0.38} T_{e,c}(16+T_{e,c})^{2.61} \\ (1+0.12\frac{T_{e,c}}{P_{a,c}^{0.14}})^{-1.51} K(\alpha_n, \alpha_T, \beta_T) G(\frac{R_{ref}}{a_{ref}}) \quad (2.22)$$

where $G(\frac{R_{ref}}{a_{ref}}) = 0.93\left(1+0.85e^{-0.82\frac{R_{ref}}{a_{ref}}}\right)$, where R_{ref} and a_{ref} are respectively the major radius and minor radius.$K(\alpha_n, \alpha_T, \beta_T) = (\alpha_n + 3.87\alpha_T + 1.46)^{-0.79}(1.98+\alpha_T)^{1.36}\beta_T^{2.14}(\beta_T^{1.53} + 1.87\alpha_T - 0.16)^{-1.33}$. α_T and β_T are determined from the best fit to the electron temperature profile. $P_{a,c} = 6.04\times10^3 \frac{an_{e,c}}{B_t}$. $n_{e,c} = \frac{n_e(t,\rho=0)}{10^{20}}$ the central electron density, $T_{e,c} = \frac{T_e(t,\rho=0)}{10^3}$ the central electron temperature, and ω_{ref} is the effective wall reflection coefficient for cyclotron radiation.

To derive the line radiation power, we first compute the combined radiation power due to both bremsstrahlung and line radiation, which is $P_{rad} = \rho_m \int_0^1 p_{rad}(t,\rho)V'd\rho$, where $p_{rad}(t,\rho)$ is the combined radiation power density due to both Bremsstrahlung and line radiation, which is modelled as:

$$p_{rad}(t,\rho) = n_e(t,\rho) \sum_{k\in species} l(Z_k, T_e(t,\rho))T_i(t,\rho) \quad (2.23)$$

Here, $l(Z_k, T_e(t,\rho))$ is the cooling rate based on the ADAS database [Summers and O'Mullane, 2011]. The line radiation power is then expressed as $P_{line} = P_{rad} - P_{brem}$. $f_{line} \in [0,1]$ is an ad hoc coefficient.

The second step is to calculate the electron and ion temperature profile by assuming $\frac{\partial T_e(t,\rho)}{\partial t} = \frac{\partial T_i(t,\rho)}{\partial t} = 0$, we could then derive the following equations:

$$\frac{\partial T_e}{\partial \rho} = \frac{-\int_0^\rho V'Q_e(t,\rho)d\rho}{n_e(t,\rho)\chi_e(\rho)V'\langle|\bigtriangledown\rho|^2\rangle}, \frac{\partial T_i}{\partial \rho} = \frac{-\int_0^\rho V'Q_i(t,\rho)d\rho}{n_i(t,\rho)\chi_i(t,\rho)V'\langle|\bigtriangledown\rho|^2\rangle} \quad (2.24)$$

where $Q_e(t,\rho)$ and $Q_i(t,\rho)$ are respectively electron and ion power deposition profiles, and χ_e and χ_i respectively indicate the electron and ion heat diffusivity profiles. Q_e and Q_i are expressed as [Artaud et al., 2018]:

$$Q_e = \sum_{n=1}^{n_{NBI}} Q_{NBI,n}^e + \sum_{n=1}^{n_{EC}} Q_{EC,n}^e + \sum_{n=1}^{n_{IC}} Q_{IC,n}^e + \sum_{n=1}^{n_{LH}} Q_{LH,n}^e + Q_\Omega + Q_{fus}^e \\ - Q_{ei} - Q_{brem}^e - Q_{cyclo}^e - Q_{line}^e \quad (2.25)$$

$$Q_i = \sum_{n=1}^{n_{NBI}} Q_{NBI,n}^i + \sum_{n=1}^{n_{EC}} Q_{EC,n}^i + \sum_{n=1}^{n_{IC}} Q_{IC,n}^i + \sum_{n=1}^{n_{LH}} Q_{LH,n}^i + Q_\Omega + Q_{fus}^i \\ + Q_{ei} - Q_{brem}^i - Q_{cyclo}^i - Q_{line}^i \quad (2.26)$$

where $Q_{NBI,n}^e$,$Q_{EC,n}^e$,$Q_{IC,n}^e$,$Q_{LH,n}^e$ are respectively the power density profile for the n^{th} NBI, EC, IC and LH system deposited on the electrons, Q_Ω the ohmic power density, Q_{fus}^e the

fusion power density on the electrons. Q^e_{brem}, Q^e_{cyclo} and Q^e_{line} are respectively the total power radiated by thermal Bremsstrahlung, cyclotron and line transition from electrons. $Q^i_{NBI,n}$,$Q^i_{EC,n}$,$Q^i_{IC,n}$ and $Q^i_{LH,n}$ are the power density profile for the n^{th} NBI, EC, IC and LH system deposited on the ions, respectively. Q^i_{brem}, Q^i_{cyclo} and Q^i_{line} are the total power radiated by thermal Bremsstrahlung, cyclotron and line transition from ions, respectively. Q^i_{fus} the fusion power density on the ions. Q_{ei} is the equipartition power from electrons to ions.

The electron diffusivity from the magnetic axis to the pedestal top is expressed as $\chi_e(t,\rho) = \chi^0_e(t)\chi^1_e(t,\rho)$, where $\chi^0_e(t)$ is a coefficient that is used to ensure that the total thermal energy derived from equation (2.24) is consistent with the result of equation (2.17), while $\chi^1_e(t,\rho)$ is the diffusivity shape, which is modelled as $\chi^1_e(t,\rho) = 2.514\times10^{-4}\frac{|\nabla n_e T_e|}{n_e B_0}q^2$. The ion diffusivity coefficient is modelled as $\chi_i(t,\rho) = \mu_{e,i}\chi^0_e(t)\chi^1_e(\rho)$, where $\mu_{e,i}$ is a constant factor. The time-varying electron diffusivity coefficient $\chi^0_e(t)$ is derived by solving the energy conservation equation, which is expressed as [Artaud et al., 2018]:

$$\frac{3}{2}\int_0^{\rho_{ped}}(n_e\int_{\rho_{ped}}^{\rho}\frac{\partial T_e}{\partial\rho}d\rho + n_i\int_{\rho_{ped}}^{\rho}\frac{\partial T_i}{\partial\rho}d\rho)V'd\rho = W_{th} - W_{ped} \tag{2.27}$$

where ρ_{ped} is the normalized radius of the pedestal top, which is fixed at 0.95, while W_{ped} is the pedestal energy. After simple mathematical deductions, we could derive the time-varying electron diffusitivity coefficient as:

$$\chi^0_e(t) = \frac{\frac{3}{2}\int_0^1\left(n_e\int_{\rho_{ped}}^{\rho}\frac{-\int_0^\rho V'Q_e d\rho}{n_e\chi^1_e(t,\rho)V'\langle|\nabla\rho|^2\rangle}d\rho + n_i\int_{\rho_{ped}}^{\rho}\frac{-\int_0^\rho V'Q_i d\rho}{n_i\mu_{e,i}\chi^1_e(t,\rho)V'\langle|\nabla\rho|^2\rangle}d\rho\right)V'd\rho}{W_{th}-W_{ped}} \tag{2.28}$$

Then the electron and ion diffusivity coefficients can be obtained, thus the electron and ion temperature profiles are computed as:

$$T_e(t,\rho) = T_{ped,e} - \int_{\rho_{ped}}^{\rho}\frac{\int_0^\rho V'Q_e d\rho}{n_e\chi_e(t,\rho)V'\langle|\bigtriangledown\rho|^2\rangle}d\rho \tag{2.29}$$

$$T_i(t,\rho) = T_{ped,i} - \int_{\rho_{ped}}^{\rho}\frac{\int_0^\rho V'Q_e d\rho}{n_e\chi_i(t,\rho)V'\langle|\bigtriangledown\rho|^2\rangle}d\rho \tag{2.30}$$

2.1.3 Momentum transport

In this section, we present the momentum transport modelling in METIS for the nonlinear simulation study. The estimation of the toroidal rotation is performed mainly in order to account for the neutral beam injection effects and the intrinsic plasma rotation. The effects of magnetic field ripple losses, fast ion losses and fast ion momentum transport cannot be described by simple models and they are neglected in METIS. Nevertheless, the model is sufficient to characterise NBI-dominated plasmas, even for a reactor such as ITER.

The total momentum R_{tot} is defined as [Artaud et al., 2018]:

$$R_{tot} = \int_0^1\sum_{k=1}^{N_{ion}} m_p A_k n_k R v_{\phi,k} V' dx \tag{2.31}$$

where m_p represents the proton mass, A_k the number of the nucleons in the k^{th} ion species, n_k the k^{th} ion density. $v_{\phi,k}$ is the toroidal velocity of the species k, R the major radius, N_{ion} the total number of different ion species.

Analogous to the thermal energy computation, the volume-averaged toroidal angular momentum can be expressed as [Artaud et al., 2018]:

$$\frac{dR_{tot}}{dt} = -\frac{R_{tot}}{\tau_\phi} + \sum_{k=1}^{N_{NBI}} S_{\phi,NBI,k} + S_{\phi,intrinsic} + S_{\phi,RF} + S_{\phi,E_\parallel} + S_{\phi,ripple} + F_{n,0} \tag{2.32}$$

where τ_ϕ is the toroidal rotation confinement time, defined as $\tau_\phi = f_{\tau,rot}\min(\tau_E, \tau_{ii})$, and $f_{\tau,rot}$ is an adjustable factor with the order $O(1)$. τ_{ii} is the ion confinement time defined as $\tau_{ii} = \frac{e\int_0^1 n_i T_i V' dx}{\int_0^1 (Q_i + Q_{e,i}) V' dx}$, and τ_E is the plasma energy confinement time.

$S_{\phi,NBI,k}$ denotes the rotational torque from the k^{th} NBI system, which is computed as:

$$S_{\phi,NBI,k} = \sum_{k\in\{H,D,T\}} m_k \int_0^1 R_{axe}(x) \frac{P_{NBI,k}(x)}{eE_{k,0}} \sqrt{\frac{2eE_{k,0}}{m_k}} \mu_k(x) V'(x) dx \tag{2.33}$$

Here, m_k denotes the k^{th} injected species mass. R_{axe} represents the average major radius of each poloidal flux surface, $P_{NBI,k}(x)$ the power deposition profile due to the k^{th} NBI source, $\mu_k(x)$ the pitch angle profile, $E_{k,0}$ the injected energy of the k^{th} ion species, and e the electron charge.

The intrinsic torque $S_{\phi,intrinsic}$ is modelled as $S_{\phi,intrinsic} = \frac{\Gamma_\phi v_{\phi,self}}{\tau_\phi}$, where Γ_ϕ is a conversion factor between velocity and momentum, expressed as:

$$\Gamma_\phi = \frac{1}{\langle v_{\phi,shape}\rangle} \int_0^1 \sum_{k\in species} m_p A_k n_k R v_{\phi,shape} V' dx \tag{2.34}$$

$\langle v_{\phi,shape}\rangle = \frac{\int_0^1 v_{\phi,shape} V' dx}{\int_0^1 V' dx}$, where $v_{\phi,scaling}$ is the rotation velocity following the Rice scaling [Rice et al., 2007].

The toroidal torque arising from the interaction between RF waves and the plasma is given by [Eriksson and Porcelli, 2002]:

$$S_{\phi,RF} = \frac{-(2D_{LH} - 1) R_{ref} n_{n_{||,0}} P_{LH,th}}{c} - \frac{s_{EC} R_{ref} P_{EC}}{2c} \tag{2.35}$$

Here, D_{LH} is the directivity of the LH waves, and s_{EC} is a constant fixed at 0.5, R_{ref} denoting the major radius of the geometric center, c is the light velocity, $P_{LH,th}$ is the LH power absorbed by thermal electrons while P_{EC} is the total EC power, and $n_{n_{||,0}}$ is the parallel refractive index.

The toroidal torque due to the parallel electric field is modelled as [Kim et al., 1991]:

$$S_{\phi,E_{||}} = \frac{m_e}{e m_p} \frac{\Gamma_\phi}{\tau_\phi} \frac{M_{eff}}{Z_{eff}} \frac{I_\Omega + I_{runaway}}{\langle n_e\rangle S_p} \tag{2.36}$$

where M_{eff} is the plasma effective mass, I_Ω and $I_{runaway}$ are respectively the ohmic and runaway currents, $\langle n_e \rangle$ the volume-averaged electron density while S_p is the plasma poloidal cross section.

$S_{\phi,ripple}$ is the rotation torque due to ripple effects. The toroidal rotation at the plasma edge can be slowed down by the friction effects from cold neutrals, which is modelled as

$$F_{n0} = -m_p \int_0^1 \sum_{k \in H,D,T} A_k n_k \langle \sigma \upsilon \rangle_{cx} R_{axe} \upsilon_\phi n_0 V' dx \tag{2.37}$$

where n_0 is the neutral hydrogen isotope density, and $\langle \sigma \upsilon \rangle_{cx}$ denotes the charge exchange reaction cross section.

The edge toroidal rotation is calculated using a simple model that only considers the convective effect, which reads:

$$R_{rot,edge} = \frac{\sum_{k=1}^{N_{NBI}} S_{\phi,NBI,k} + S_{\phi,intrinsic} + S_{\phi,RF} + S_{\phi,E_\parallel} + S_{\phi,ripple}}{\frac{\sum_{k \in species} A_k n_k}{\sum_{k \in species} Z_k n_k} m_p n_{out} R_{ref} - F_{n,0}} \tag{2.38}$$

Here, n_{out} is the ion exchange flux through the LCFS due to interchange, cold neutrals, pellet injection and neutral beam injection. Note that the interchange component plays an important role for the ion exchange flux.

2.1.4 Plasma density profiles

Since particle sources and sinks at the plasma edge are the result of complicated recycling phenomena that depend on plasma wall interaction and are quite difficult to describe using first principle models, a simple modelling technique is used to characterize the essential features of the density profile evolution in METIS. Primary attention is given to the electron density profile evolution, which is determined by 3 parameters, i.e. the line-averaged electron density $\langle n_e \rangle(t)$ along the vertical chord crossing the plasma through the magnetic axis, the peaking factor $\upsilon_e(t) = \frac{n_{e,0}(t)}{\langle n_e \rangle(t)}$ (with $n_{e,0}(t)$ denoting the central electron density) and the electron density at the plasma edge $n_{e,a}(t)$. The peaking factor and edge electron density are computed by using scaling laws.

For L-mode plasmas, the shape of the electron density profile is modelled as [Artaud et al., 2018]:

$$n_e(t,\rho) = (n_{e,0}(t) - n_{e,a}(t))(1-\rho^2)^{\nu_n(t)} + n_{e,a}(t) \tag{2.39}$$

where $\nu_n(t)$ is defined as $\nu_n(t) = \upsilon_e(t) - 1$.

For H-mode plasmas, where an electron density pedestal is present, the electron density profile is determined by three points: the central electron density ($\rho = 0$), the electron density at the pedestal top ($\rho = 0.95$) and the edge electron density ($\rho = 1$). The electron density at the pedestal top is maximized by constraining the spatial derivative of the electron temperature profile $\frac{\partial T_e(t,\rho)}{\partial \rho} < 0$. A piecewise cubic Hermite polynomial interpolation is then used to compute the electron density profile at the other points ensuring that $\frac{\partial n_e(t,\rho)}{\partial \rho}|_{\rho=0} = 0$.

2.1.5 METIS reference scenario simulations

In this section, we present the open-loop simulations of H-mode steady-state plasma discharges on the EAST and ITER tokamaks using the METIS code.

2.1.5.1 Simulation of an H-mode steady-state plasma discharge on EAST

The EAST tokamak is a D-shaped fully superconducting divertor tokamak intended for the high-performance steady-state operation, with a major radius at 1.8 m, a minor radius at 0.4 m and the elongation of 1.5 - 2.0. The reference scenario simulated by the METIS code is a fully non-inductive upper-single-null (USN) H-mode plasma discharge, based on the shot number #62946. In this discharge, the toroidal magnetic field $B_T = 2.5$ T, the central electron density $n_{e0} \approx 3.5 \times 10^{19}$ m^{-3} and plasma current $I_p = 0.42$ MA. The discharge was obtained using LHCD (0.6 MW at 2.45 GHz and 2 MW at 4.6 GHz), 0.32 MW of ICRH at 33 MHz and 0.3 MW of ECRH at 140 GHz. The transition to H-mode occurred at 3.1 s with an H-mode enhancement factor $\mathrm{H}_{98}(y, 2) \sim 1.1$. The q-profile exhibited a small negative shear in the plasma core, with minimum q around 1.5 and $q_0 \sim 2$ on axis. The plasma profiles were retrieved from the EFIT magnetic equilibrium reconstruction code using real-time magnetic and kinetic measurements, for instance, interfero-polarimetry data from the POINT diagnostics [Liu et al., 2016b, Liu et al., 2016a, Huang et al., 2017]. The initialization of the METIS code is preset to be consistent with shot #62946 at 3.1 s. The plasma poloidal magnetic equilibrium is shown in Fig. 2.1(d) and is consistent with the real-time EFIT reconstruction at 3.1 s. The plasma density profile used in the METIS code is fitted with the equilibrium reconstruction from the same shot using the POINT diagnostics [Liu et al., 2016a]. The plasma current and density profiles are set to be consistent with the EAST experiments at the flat-top phase. The METIS transport coefficients, power and current driven models are tuned to have the internal inductance l_i and the diamagnetic energy W_{dia} consistent with the EFIT reconstructions and have the temperature and current deposition profiles consistent with the TRANSP simulations [Moreau et al., 2011]. The simulation results of the reference scenario in METIS are therefore shown in Fig. 2.1 and the electron density, temperature profiles, the current drive and power deposition profiles at 6.78 s are shown in Fig. 2.2. The total current profile is approximately equal to the non-inductive current profile with the loop voltage at -20 mV, indicating an H-mode steady-state operational scenario.

2.1.5.2 Simulation of an H-mode steady-state burning plasma discharge on ITER

The ITER tokamak is the largest superconducting divertor tokamak in the world and is under construction in southern France with the first plasma foreseen in 2025. This subsection presents the METIS simulation of an H-mode steady-state (i.e. fully non-inductive) burning plasma scenario in ITER. The magnetic equilibrium used in METIS is shown in Fig. 2.3(d), with the major and minor radius at 6.2 m and 2.0 m, respectively. The toroidal magnetic field is $B_T = 5.3$ T, central electron density, $n_{e0} \approx 6.524 \times 10^{19}$ m^{-3} , central ion temperature

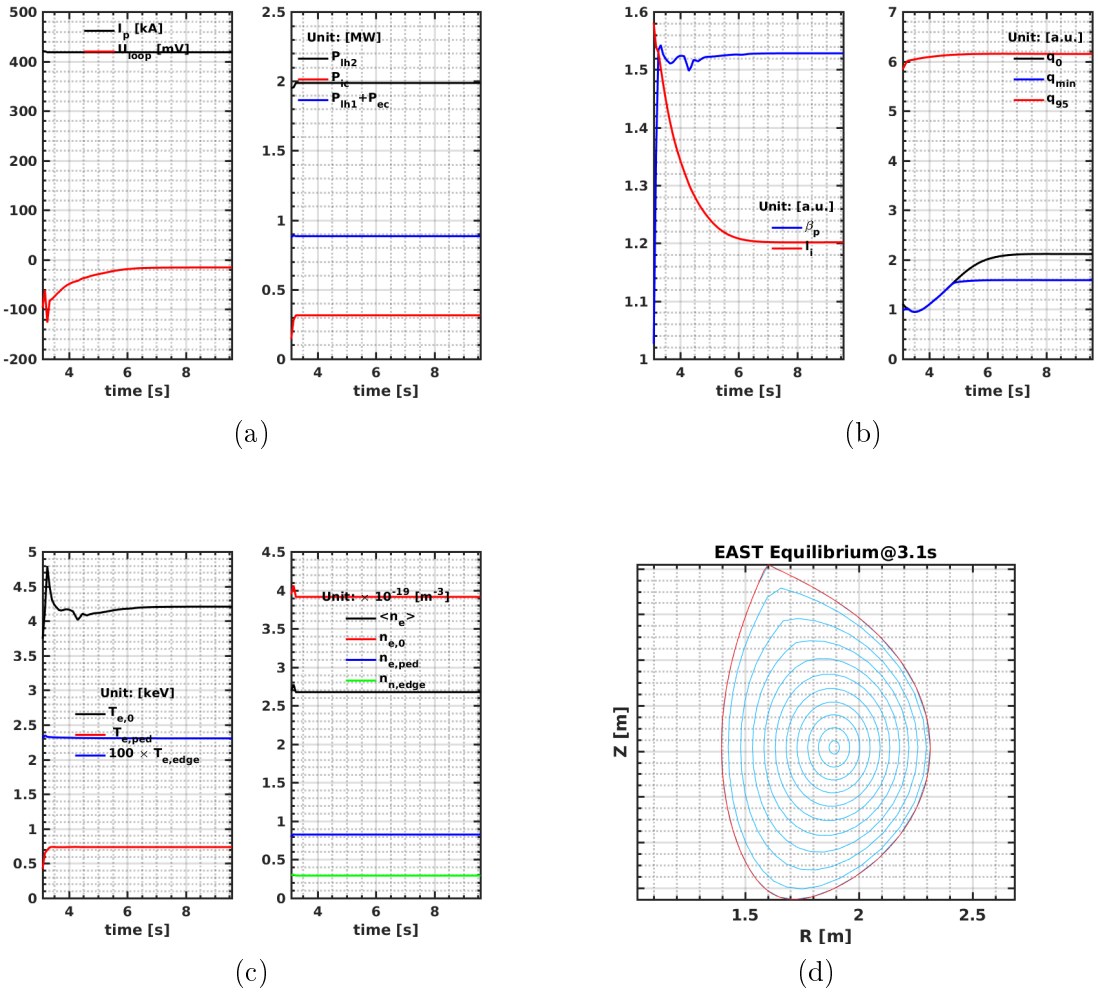

Figure 2.1: Simulation of an H-mode steady-state plasma scenario on EAST. (a) Left: time traces of plasma current and the loop voltage; Right: time traces of the auxiliary heating powers. (b) Left: time traces of plasma poloidal parameter and internal inductance; Right: time traces of the safety factors at typical points. (c) Left: time traces of electron temperatures at typical points; Right: time traces of electron densities at typical points. (d) The EAST magnetic equilibrium and flux surfaces in a poloidal cross-section at 3.1 s.

$T_{i0} \approx 40$ keV and plasma current $I_p = 9$ MA. Fig. 2.3 shows the time evolutions of important plasma parameters from the METIS simulation. The plasma scenario is obtained with 33 MW of co-current NBI, 20 MW of ECRH, 40 MW of LHCD and 20 MW of ICRH. The transition to H-mode occurs at 1.5 s with an H-factor, $H_{98(y,2)} \sim 1.5$. At the steady-state equilibrium, the poloidal plasma pressure parameter β_p, the normalized plasma pressure parameter β_n and the internal inductance l_i are respectively 2.48, 3.03 and 0.85. The q-profile is monotonic along the normalized radius, with $q_0 \sim 1.25$ on axis and $q_{95} \sim 5.6$ near the magnetic separatrix. The loop voltage is very small at around 2 mV, confirming that this scenario is an H-mode steady-state scenario. Fig. 2.4 illustrates the temperature, density profiles, the current drive

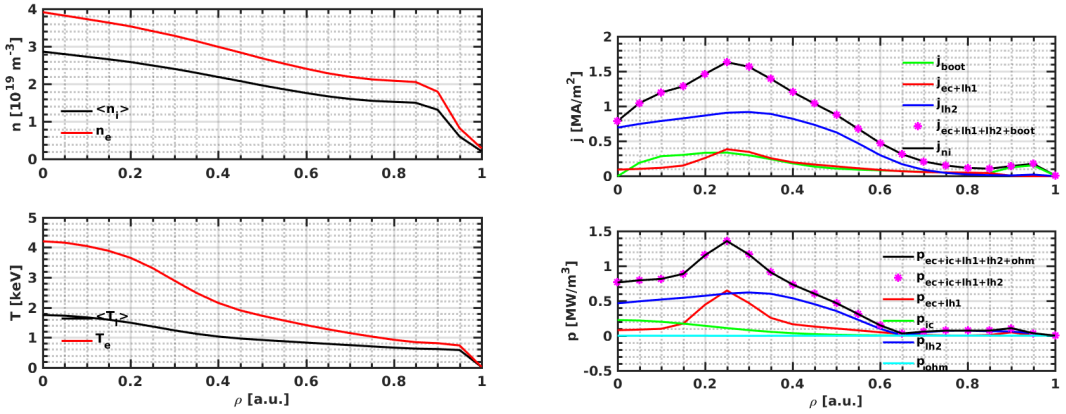

Figure 2.2: The magnetic and kinetic profiles of the reference scenario for H-mode steady-state plasma on EAST at 6.78 s. Left panels: plasma density profiles (top), and plasma temperature profiles (bottom); Right panels: plasma current drive profiles(top), and plasma deposited power profiles (bottom).

and power deposition profiles at 925.9 s. One can notice that the NBI-driven, LH-driven and bootstrap current constitute the major current fraction in the core region, while the current profile in the pedestal region near the separatrix is mainly composed of the bootstrap current. The plasma heating is primarily provided by the generated α particles from nuclear fusion reactions. The EC heating is localized at the normalized radius 0.4, while the power deposition profile of NBI, IC and LH are broader than that of EC, but much smaller than the heating from the generated α particles.

2.1.6 Conclusion of Section 2.1

In this section, the modelling of the plasma current density diffusion, thermal and momentum transport as well as density profile have been described. Simulations of H-mode steady-state plasma discharge on the EAST and ITER tokamaks via the METIS code are presented as well. It should be noted that the METIS modelling not only involves the models presented in sub-sections 2.1.2 to 2.1.4, but also involves a number of other models, for example, the scrape-off-layer (SOL) models, impurity models and MHD instability models. Since the objective of the thesis is to develop advanced identification methods using data and provide robust and adaptive solutions for the control of magnetic and kinetic parameters in advanced tokamak scenarios, the modelling details presented above are ample to assist in understanding the relevant plasma dynamics and provide the physical insights in developing effective control algorithms.

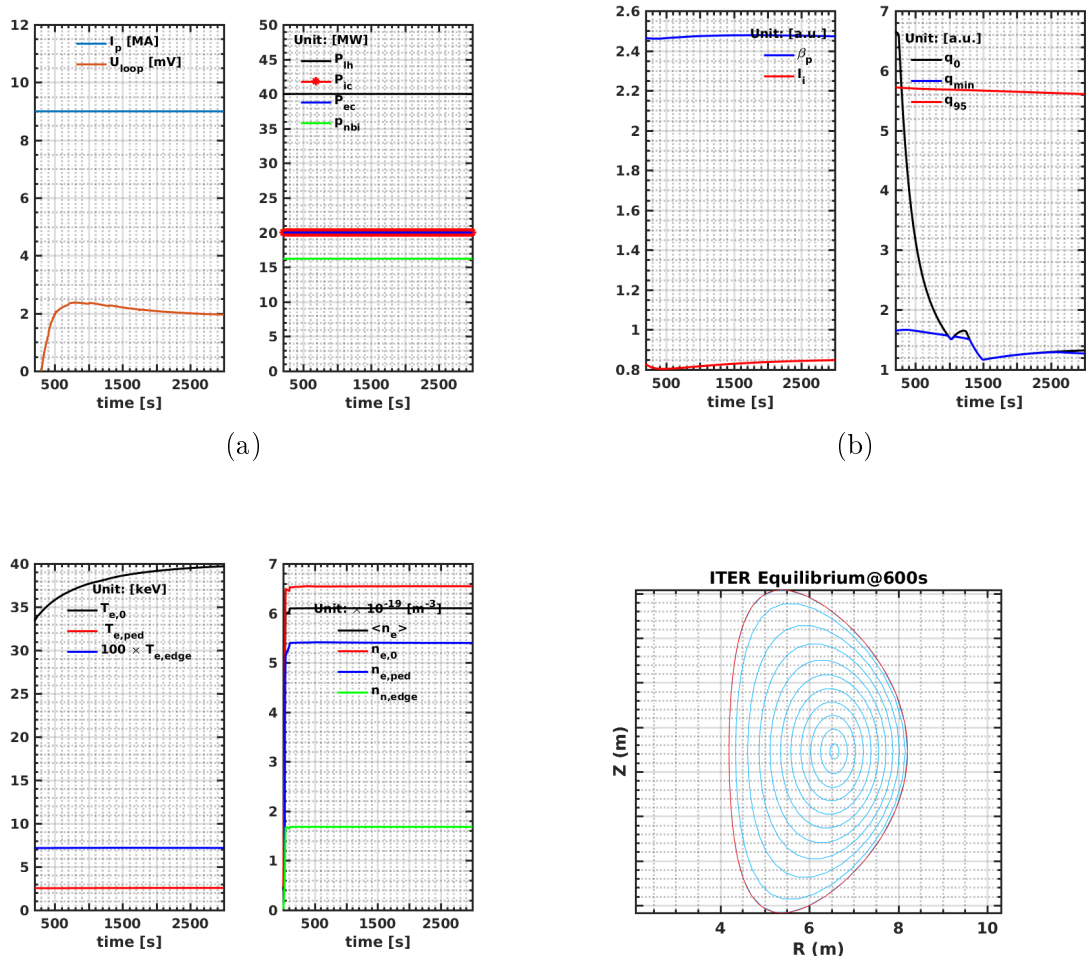

Figure 2.3: Simulation of an H-mode steady-state plasma scenario on ITER. (a) Left: time traces of plasma current and the loop voltage; Right: time traces of the auxiliary heating powers. (b) Left: time traces of plasma poloidal parameter and internal inductance; Right: time traces of the safety factors at typical points. (c) Left: time traces of electron temperatures at typical points; Right: time traces of electron densities at typical points. (d) The ITER magnetic equilibrium and flux surfaces in a poloidal cross-section at 600 s.

2.2 Identification of PNLSS plasma models

2.2.1 Model structure

Plasma magnetic and kinetic transport dynamics can be modelled as MHD fluid equations [Hinton and Hazeltine, 1976], which are intrinsically nonlinear time-varying PDEs. However, in view of model identification, it is preferable to describe plasma response models as nonlinear ordinary differential equations (ODEs), which may be obtained by discretizing the PDEs in

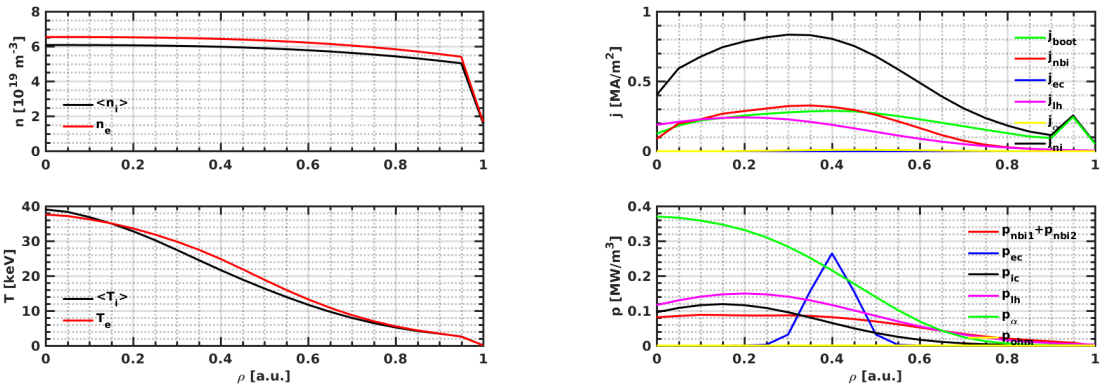

(a) (b)

Figure 2.4: The magnetic and kinetic profiles of the reference scenario for H-mode steady-state plasma on ITER at 925.9 s. Left panels: plasma density profiles (top), and plasma temperature profiles (bottom); Right panels: plasma current drive profiles(top), and plasma deposited power profiles (bottom).

the spatio-temporal domain. In this regard, the sampled input-output data from interpretative plasma simulations or tokamak plasma experiments can therefore be used for model identification. We describe the plasma dynamics in a general nonlinear discrete state-space form as:

$$\begin{aligned} x(t+1) &= f\left(x(t), u(t)\right) \\ y(t) &= g\left(x(t), u(t)\right) \end{aligned} \tag{2.40}$$

where $u(t) \in \mathbb{R}^{n_u}$ represents the model inputs at time t, $x(t) \in \mathbb{R}^{n}$ denotes the model states at time t, while $y(t) \in \mathbb{R}^{n_y}$ indicates the model outputs at time t. A more convenient model structure to characterize the combined effects from the dominant linear dynamics and the auxiliary nonlinear dynamics can be expressed as:

$$\begin{aligned} x(t+1) &= Ax(t) + Bu(t) + f_{NL}\left(x(t), u(t)\right) \\ y(t) &= Cx(t) + Du(t) + g_{NL}\left(x(t), u(t)\right) \end{aligned} \tag{2.41}$$

where $A \in \mathbb{R}^{n \times n}, B \in \mathbb{R}^{n \times n_u}, C \in \mathbb{R}^{n_y \times n}, D \in \mathbb{R}^{n_y \times n_u}$ are LSS matrices that depict the linear system dynamics. $f_{NL}\left(x(t), u(t)\right)$ and $g_{NL}\left(x(t), u(t)\right)$ are nonlinear functions of the system states $x(t)$ and inputs $u(t)$, which can be approached by a combination of nonlinear basis functions, for example, monomials, sigmoid functions, hyperbolic tangents and radial basis functions [Relan et al., 2018]. Due to the flexibility and effectiveness of monomials, we use a set of monomials as basis functions to approximate the nonlinear plasma dynamics. We define $f_{NL}\left(x(t), u(t)\right) = E\zeta(t)$ and $g_{NL}\left(x(t), u(t)\right) = F\eta(t)$, where $E \in \mathbb{R}^{n \times n_\zeta}$ and $F \in \mathbb{R}^{n_y \times n_\eta}$ are coefficients of the basis functions $\zeta(t) \in \mathbb{R}^{n_\zeta}$ and $\eta(t) \in \mathbb{R}^{n_\eta}$, respectively. Hence, the plant model can then be transformed into a more compact form as:

$$\begin{aligned} x(t+1) &= Ax(t) + Bu(t) + E\zeta(t) \\ y(t) &= Cx(t) + Du(t) + F\eta(t) \end{aligned} \tag{2.42}$$

Here, (A, B, C, D, E, F) are constant coefficient matrices to be identified, in which (A, B, C, D) describe the linear dynamics with the degree of monomials at 1, while (E, F) depict the nonlinear dynamics with the degree of monomials greater than 1. $\zeta(t)$ and $\eta(t)$ contain nonlinear monomials in $x(t)$ and $u(t)$ of degree 2 up to a threshold degree l (design parameter).

Specifically, $\zeta(t)$ and $\eta(t)$ are formed by all possible products of the input and state variables raised to l. For example, define $\zeta_{l_u^1,..,l_u^{n_u},l_x^1,...l_x^n}$ as one element of $\zeta(t)$, it can be expressed as:

$$\begin{aligned} \zeta_{l_u^1,..,l_u^{n_u},l_x^1,...,l_x^n} &= \Pi_{i=1}^{n_u} u_i^{l_u^i} \Pi_{j=1}^{n} x_j^{l_x^j} \\ \text{s.t.} \sum_{i=1}^{n_u} l_u^i + \sum_{j=1}^{n} l_x^j &\in \{2, 3, ..., l\}, l_u^i \in \mathbb{N}, l_x^j \in \mathbb{N} \end{aligned} \tag{2.43}$$

where l_u^i is the degree of the i-th element of $u(t)$, while l_x^j represents the degree of the j-th element of $x(t)$. The merits of using polynomial expansions are twofold: to set universal approximation properties and to be amenable for multivariate extensions.

Let us define the concatenation of the input and state variables as:

$$\upsilon = [u_1(t), u_2(t), ..., u_{n_u}(t), x_1(t), x_2(t), ..., x_n(t)]^T \tag{2.44}$$

where $\upsilon \in \mathbb{R}^{n_u+n}$. Combining equations (2.43) and (2.44), the total number of elements for $\zeta(t)$, i.e. n_ζ, can be calculated as

$$n_\zeta = \left[\binom{n_u + n + l}{l} - (n_u + n) - 1 \right] (n_u + n) \tag{2.45}$$

We choose the same set of basis functions to approximate nonlinear output dynamics, thus $\eta(t) = \zeta(t)$ and $n_\eta = n_\zeta$. According to equation (2.45), we find that the number of estimated parameters for nonlinear components rely on the number of states, inputs and the threshold degree. For a high-order system, the value of n_ζ and n_η can be extremely large, which may cause identifiability problem. As suggested in [Paduart et al., 2012], to keep the number of the estimated nonlinear parameters under control, it is practical to restrict the threshold degree at 3 and to optionally eliminate the model inputs from the nonlinear combinations.

2.2.2 Identification procedure

The procedure to identify a PNLSS plasma model as expressed in equation (2.42) for control from sampled input-output data is illustrated in Fig. 2.5. First, we determine the identification objective, including the model inputs and outputs. The model inputs are the selected auxiliary heating & current drive powers. For different applications, the model inputs are allowed to be different. They comprise the neutral beam injection power P_{NBI}, the electron cyclotron heating power P_{EC}, the ion cyclotron resonance heating power P_{IC} and the lower hybrid current drive power P_{LH}. The model outputs are the selected magnetic and kinetic parameters including the poloidal pressure parameter β_p, the normalized pressure parameter β_n, the

average toroidal rotation angular speed ω_ϕ, the α particle power P_α, the central rotational transform ι_0 and the central electron temperature $T_{e,0}$. Likewise, for different applications, the model outputs are permitted to vary depending on the availability of these variables.

Once the model inputs and outputs are determined, the desired input waveforms in terms of the pseudorandom binary sequences (PRBS) and chirping signals are designed to excite the dominant plasma dynamics and then implemented into a tokamak plasma simulator or PCS. Subsequently, we perform the identification experiments either with a plasma simulator or a tokamak device. For the case of real tokamak plasma identification experiments, the model inputs are forced to track the desired input waveforms, which may necessitate a feedback controller. In addition, the model inputs and outputs should either be directly measured by tokamak plasma sensors, e.g. the electron temperature from the Thomson scattering diagnostic, or be estimated by the kinetic-magnetic equilibrium reconstruction code [Lao et al., 1985, Ferron et al., 1998]. In this thesis, we focus on the technical problems of the identification procedure, including how to preprocess the sampled input-output data for identification, how to identify LSS models and how to derive a PNLSS plasma response model, which are summarised in the red frames in Fig. 2.5.

The major steps of the identification process are described below:

Data-preprocessing The measured inputs and outputs from the experiments are first selected and merged into an input and output dataset, respectively. The datasets are then handled by a lowpass filter with the same time constant to remove the measurement noise. Then the means of the input and output datasets are removed before normalizing them into the domain of [-1,1] [Ljung, 1995]. The new input-output data are divided into three sets: identification dataset for model identification, selection dataset to select an optimal model and testing dataset to evaluate the predictive performance of the selected model.

Linear model identification Two LSS model identification approaches are introduced, in which the first one handles the identification dataset in the time domain while the second analyze it in the frequency domain.

Time-domain approach: First, determine the linear system order and obtain an initial guess of the LSS model using the time-domain subspace identification technique. In particular, the input-output data sequences are stacked into a block Hankel matrix, which is analyzed via the RQ factorization and the singular value decomposition (SVD) to determine the order of the linear system. The system matrices A and C are then estimated up to a similarity transformation [Verhaegen and Verdult, 2007], while B and D are calculated by solving a least-squares problem. Second, nonlinear Levenberg-Marquardt (LM) [Marquardt, 1963] optimization of a cost function that penalizes the prediction errors, between the linear model estimates and the associated outputs, is adopted to improve the linear model accuracy.

Frequency-domain approach: First, non-parametric estimate of the frequency response functions (FRF) of the identification dataset is derived based on the local polynomial method

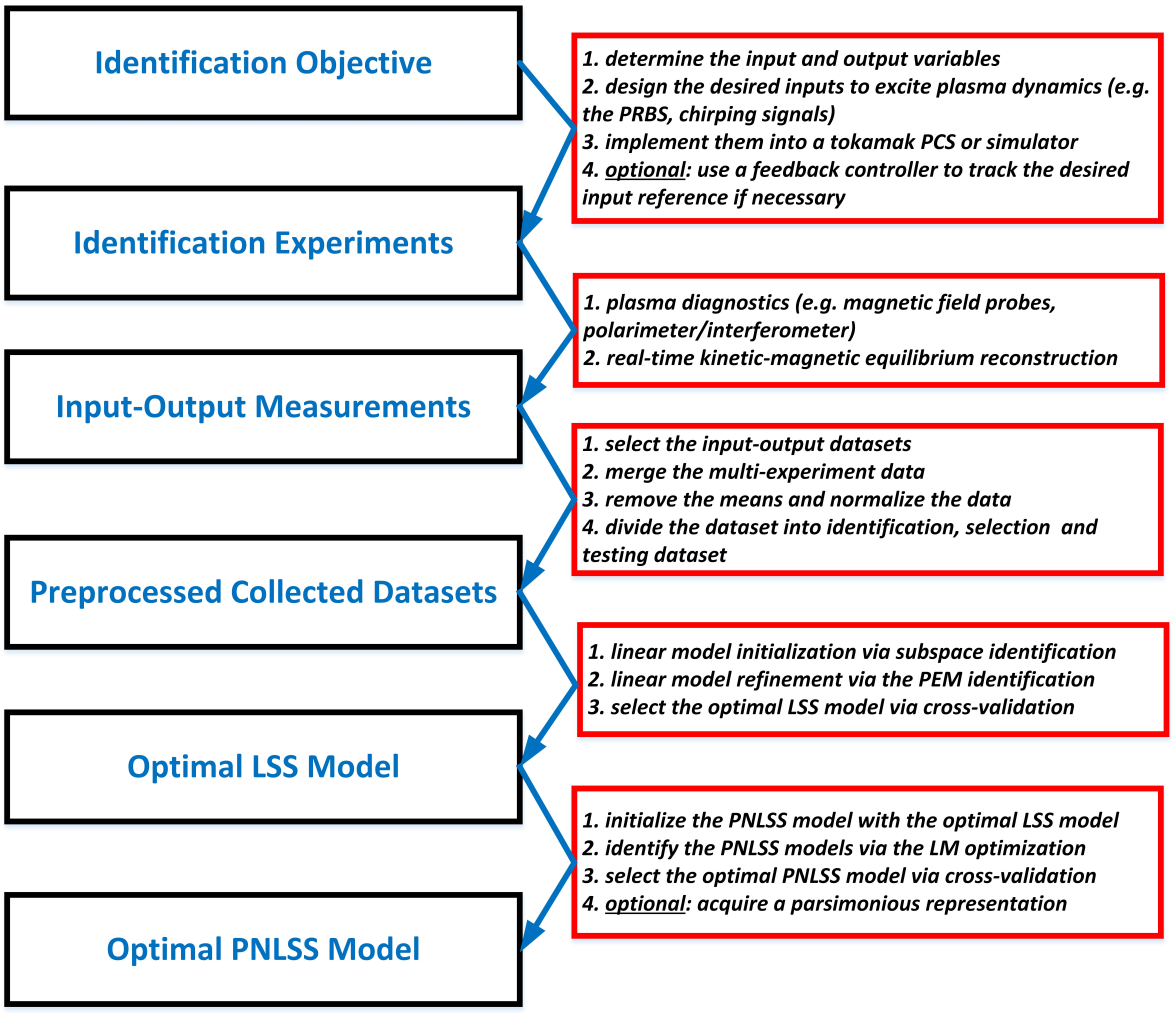

Figure 2.5: Schematic of the PNLSS plasma model identification procedure.

(LPM) [Pintelon et al., 2010]. Second, approximating plasma dynamics using an LSS model structure regardless of the nonlinear terms in equation (41), the weighted mean square deviation, between the nonparametric FRF and the FRF of the LSS model, is minimized to estimate an optimal LSS model using the frequency-domain subspace identification technique [Pintelon and Schoukens, 2012]. Third, the model estimates of (A, B, C, D) are further optimized to improve the model accuracy in the frequency domain.

PNLSS model identification The LM optimization technique is used to estimate the PNLSS plasma model coefficients, specifically the system matrices (A, B, C, D, E, F) and the initial states $v(t_0)$, where t_0 represents the initial time used for the identification. First, assuming $E = 0$, $F = 0$ and $v(t_0) = 0$, the nonlinear model is initialized with the optimal LSS model (A, B, C, D). Second, a cost function that defines the weighted mean square deviation, between the modelled and measured output spectra, is minimized via the LM algorithm such that both the system matrices of the PNLSS model and the initial conditions can be optimally

approximated. Third, derive a parsimonious representation of the PNLSS plasma response model [Relan et al., 2018], as described in section 2.4.

Model selection and evaluation Assess the predictive performance of the identified PNLSS models and select an optimal one. The selection dataset is used to determine the optimal PNLSS model. The effectiveness of the model identification algorithm is evaluated by examining the root-mean-square (RMS) errors between model estimates from each PNLSS model candidates and the output measurements. The final chosen model should pass the cross-validation test and exhibit the lowest RMS error. The optimal PNLSS model is then used to predict the model outputs in the testing dataset and the predictive performance is further examined.

2.2.2.1 Data-preprocessing for plasma model identification

The collected data from simulations/experiments are not likely to be in shape for immediate use in an identification algorithm [Ljung, 1995]. For experimental application on EAST, the experimental measurements can intrinsically involve noise, which generally appears in the high-frequency domain beyond the bandwidth of the dominant plasma dynamics. Prefiltering the input and output data via a lowpass filter $L(s) = \frac{1}{\tau_f s+1}$ is therefore adopted where τ_f is a small time constant, typically at 0.003 s. Prefiltering does not change the input-output relation for a linear system in the frequency domain of interest while it can improve the identification performance in the range of the dominant plasma dynamics [Ljung, 1995].

Due to the pulse duration limit in tokamak plasma discharges, the identification dataset may need to contain the input-output measurements from many independent simulations and/or experiments. In addition, there are a number of phases in a tokamak plasma discharge, where the kinetic control is preferably scheduled from the early flat-top phase to the end of the flat-top phase. Therefore, it is naturally beneficial to select the dedicated simulation/experimental data in the flat-top phase and merge them into the input-output datasets. Assume that there are m merged plasma discharges, where each discharge has the number of samplings at N_i, the input-output dataset can thus be expressed as:

$$\begin{aligned} U(k) &= \left[U_1(k_1), U_2(k_2), \ldots, U_m(k_m)\right], Y(k) = \left[Y_1(k_1), Y_2(k_2), \ldots, Y_m(k_m)\right] \\ k_i &= 1, 2, \ldots, N_i, i = 1, 2, \ldots, m; k = 1, 2, \ldots, N, N = \sum_{i=1}^{m} N_i \end{aligned} \tag{2.46}$$

where N is the total number of sampling points, $U(k)$ and $Y(k)$ represent the input and output vectors at the sampling time k, respectively. $U_i(k_i)$ and $Y_i(k_i)$ represent the input and output vectors of the i-th plasma discharge at the sampling time k_i, respectively.

In practice, the input-output measurements are collected and recorded in physical units, the levels of which can be quite arbitrary. For example, the typical average toroidal rotation is of the order of 10^4 rad/s, while β_n is of the order of 10^{-2}. It is beneficial to subtract sample

means $(\langle U\rangle, \langle Y\rangle)$ from the input-output datasets and normalize them with the maximum allowed variations (U_{norm}, Y_{norm}) in each input-output channel as:

$$\mathcal{U}(k) = \frac{U(k) - \langle U\rangle}{U_{norm}}, \mathcal{Y}(k) = \frac{Y(k) - \langle Y\rangle}{Y_{norm}}, k = 1, 2, ..., N \tag{2.47}$$

where $\langle U\rangle$ and $\langle Y\rangle$ are the mean vector of the inputs and measured outputs. $\mathcal{U}(k)$ and $\mathcal{Y}(k)$ are, respectively, input and output deviations from the operating point $(\langle U\rangle, \langle Y\rangle)$. U_{norm} and Y_{norm} are defined as the maximum and minimum input and output values in the collected dataset, respectively.

Subsequently, the new input-output datasets are divided into three subsets as:

$$\begin{aligned}
(\mathcal{U}_{id}(k_{id}), \mathcal{Y}_{id}(k_{id})) &= (\mathcal{U}(k_a), \mathcal{Y}(k_a)) \\
(\mathcal{U}_{sel}(k_{sel}), \mathcal{Y}_{sel}(k_{sel})) &= (\mathcal{U}(k_b), \mathcal{Y}(k_b)) \\
(\mathcal{U}_{test}(k_{test}), \mathcal{Y}_{test}(k_{test})) &= (\mathcal{U}(k_c), \mathcal{Y}(k_c)) \\
k_{id} &= 1, 2, \ldots, N_{id}, k_a = 1, 2, \ldots, N_{id} \\
k_{sel} &= 1, 2, \ldots, N_{sel}, k_b = N_{id} + 1, \ldots, N_{id} + N_{sel} \\
k_{test} &= 1, 2, \ldots, N_{test}, k_c = N_{id} + N_{sel} + 1, \ldots, N \\
N &= N_{id} + N_{sel} + N_{test}
\end{aligned} \tag{2.48}$$

where N_{id}, N_{sel} and N_{test} are respectively the number of samplings for model identification, selection and testing. $(\mathcal{U}_{id}(k_{id}), \mathcal{Y}_{id}(k_{id}))$, $(\mathcal{U}_{sel}(k_{sel}), \mathcal{Y}_{sel}(k_{sel}))$ and $(\mathcal{U}_{test}(k_{test}), \mathcal{Y}_{test}(k_{test}))$ represent the dataset for model identification, selection and testing, respectively.

2.2.3 Identification of the linear plasma dynamics

In this section, the linear plasma dynamics is identified using a combination of subspace and PEM techniques. The objective is to identify the system matrices (A, B, C, D) in equation (2.41) using the identification dataset $(\mathcal{U}_{id}(k_{id}), \mathcal{Y}_{id}(k_{id})), k_{id} = 1, 2, \ldots, N_{id}$. Two alternative approaches that take into account the problem in the time- and frequency-domain are investigated in parallel.

2.2.3.1 A time-domain approach

Time-domain subspace identification The time-domain subspace identification technique is employed to identify a linear state-space model. The idea of the subspace identification is that the system matrices of the signal-generating state-space model is associated with certain subspaces of the structured block Hankel matrix filled with the input-output data [Verhaegen and Verdult, 2007]. Subspace identification is a non-iterative identification technique which does not require any parameterization, and it can also assist in determining the system order. Its linear parameter-varying extensions can be found in [Verdult and Verhaegen, 2002, Verdult and Verhaegen, 2005]. The multiple-input multiple-output (MIMO)

subspace identification of the discrete linear time-invariant (LTI) state-space system matrices is considered, regardless of the nonlinear terms. The state-space model structure reads:

$$\begin{aligned} X(t+1) &= AX(t) + B\mathcal{U}_{id}(t) \\ \mathcal{Y}_{id}(t) &= CX(t) + D\mathcal{U}_{id}(t) \end{aligned} \tag{2.49}$$

where $A \in \mathbb{R}^{n\times n}, B \in \mathbb{R}^{n\times n_u}, C \in \mathbb{R}^{n_y\times n}, D \in \mathbb{R}^{n_y\times n_u}$ are the linear system matrices to be estimated. n is the order of the linear system to be determined, and $X(t) \in \mathbb{R}^n$ represents a state vector. n_u and n_y are the number of model inputs and outputs, respectively.

We first construct input and output block Hankel matrices using the pre-processed identification data set as

$$\begin{aligned} \mathcal{U}_{1,s,N} &= \begin{bmatrix} \mathcal{U}_{id}(1) & \mathcal{U}_{id}(2) & \dots & \mathcal{U}_{id}(N_{id}-s+1) \\ \mathcal{U}_{id}(2) & \mathcal{U}_{id}(3) & \dots & \mathcal{U}_{id}(N_{id}-s+2) \\ \vdots & \vdots & \ddots & \vdots \\ \mathcal{U}_{id}(s) & \mathcal{U}_{id}(s+1) & \dots & \mathcal{U}_{id}(N_{id}) \end{bmatrix} \\ \mathcal{Y}_{1,s,N} &= \begin{bmatrix} \mathcal{Y}_{id}(1) & \mathcal{Y}_{id}(2) & \dots & \mathcal{Y}_{id}(N_{id}-s+1) \\ \mathcal{Y}_{id}(2) & \mathcal{Y}_{id}(3) & \dots & \mathcal{Y}_{id}(N_{id}-s+2) \\ \vdots & \vdots & \ddots & \vdots \\ \mathcal{Y}_{id}(s) & \mathcal{Y}_{id}(s+1) & \dots & \mathcal{Y}_{id}(N_{id}) \end{bmatrix} \end{aligned} \tag{2.50}$$

where s is an arbitrary positive integer, greater than the system order n, but much smaller than N_{id}. Using equation (2.49), we can derive an equation which relates the input and output block Hankel matrices with the system matrices as

$$\mathcal{Y}_{1,s,N_{id}} = \mathcal{O}_s X_{1,N_{id}} + \mathcal{T}_s \mathcal{U}_{1,s,N_{id}} \tag{2.51}$$

where

$$\begin{aligned} \mathcal{O}_s &= \begin{bmatrix} C \\ CA \\ CA^2 \\ \vdots \\ CA^{s-1} \end{bmatrix}, \mathcal{T}_s = \begin{bmatrix} D & 0 & 0 & \dots & 0 \\ CB & D & 0 & \dots & 0 \\ CAB & CB & D & \dots & 0 \\ \vdots & \vdots & \ddots & \ddots & 0 \\ CA^{s-2}B & CA^{s-3}B & \dots & CB & D \end{bmatrix}, \\ X_{1,N_{id}} &= \begin{bmatrix} X(1) & X(2) & \dots & X(N_{id}) \end{bmatrix} \end{aligned} \tag{2.52}$$

where $\mathcal{O}_s \in \mathbb{R}^{n_y s\times n}$ is the extended observability matrix containing A and C, while $\mathcal{T}_s \in \mathbb{R}^{n_y s\times n_u s}$ comprises A, B and C. One idea of estimating A and C up to a similarity transformation is to cancel the term $\mathcal{T}_s\mathcal{U}_{1,s,N_{id}}$ by post-multiplying an orthogonal matrix of $\mathcal{U}_{1,s,N_{id}}$, i.e. $\Pi^{\perp}_{\mathcal{U}_{1,s,N_{id}}} = I_{N_{id}} - \mathcal{U}^T_{1,s,N_{id}} \left(\mathcal{U}_{1,s,N_{id}}\mathcal{U}^T_{1,s,N_{id}}\right)^{-1} \mathcal{U}_{1,s,N_{id}}$, and then exploit the column space of $\mathcal{Y}_{1,s,N}\Pi^{\perp}_{\mathcal{U}_{1,s,N}}$. A more computationally efficient technique is to concatenate the input and output block Hankel matrices and perform the RQ factorization as

$$\begin{bmatrix} \mathcal{U}_{1,s,N} \\ \mathcal{Y}_{1,s,N} \end{bmatrix} = \begin{bmatrix} R_{11} & 0 & 0 \\ R_{21} & R_{22} & 0 \end{bmatrix} \begin{bmatrix} Q_1 \\ Q_2 \\ Q_3 \end{bmatrix} \tag{2.53}$$

where $R_{11} \in \mathbb{R}^{n_u s \times n_u s}$, $R_{21} \in \mathbb{R}^{n_y s \times n_u s}, R_{22} \in \mathbb{R}^{n_y s \times n_y s}$, $Q_1 \in \mathbb{R}^{n_u s \times N_{id}}$, $Q_2 \in \mathbb{R}^{n_y s \times N_{id}}$. Given the factorization in equation (2.53), we have $\mathcal{Y}_{1,s,N}\Pi^{\perp}_{\mathcal{U}_{1,s,N}} = R_{22}Q_{22}$ (See Lemma 9.2 in [Verhaegen and Verdult, 2007]). By assuming that the rank of $\begin{bmatrix} X_{1,N_{id}} \\ U_{1,s,N_{id}} \end{bmatrix}$ equals $(n+n_u s)$, we can further obtain the relation: range$(\mathcal{O}_s)$ = range(R_{22}), where the symbol 'range()' denotes the column space of a matrix (See Theorem 1 in [Verhaegen and Verdult, 2007]). It implies that the estimates of A and C up to the similarity transformation can be extracted directly from the low dimensional matrix R_{22}.

The column space of the extended observability matrix is examined by performing SVD on R_{22} as $R_{22} = W\Sigma V^T$, we may sort out the dominant subspace of linear dynamics by truncating the subspace corresponding to the small singular values. In this regard, we impose the singular value decomposition on R_{22} as

$$R_{22} = \begin{bmatrix} W_1 & W_2 \end{bmatrix} \begin{bmatrix} \Sigma_1 & 0 \\ 0 & \Sigma_2 \end{bmatrix} \begin{bmatrix} V_1 & V_2 \end{bmatrix}^T \simeq W_1 \Sigma_1 V_1^T \tag{2.54}$$

where $W_1 \in \mathbb{R}^{n_y s \times n}, W_2 \in \mathbb{R}^{n_y s \times (n_y s - n)}, \Sigma_1 \in \mathbb{R}^{n \times n}, \Sigma_2 \in \mathbb{R}^{(n_y s - n) \times (n_y s - n)}$, $V_1 \in \mathbb{R}^{n_y s \times n}, V_2 \in \mathbb{R}^{n_y s \times (n_y s - n)}$, where the order of the system model is specified by n. The estimate of A and C can be obtained by examining the left singular vector space W_1. Obviously, $C = W_1(1 : n_y, :)$. We define $\Upsilon_0 = W_1(1 : n_y(s-1), :)$ and $\Upsilon_1 = W_1(n_y + 1 : n_y s, :)$. Defining $M \in \mathbb{R}^{n \times n}, N \in \mathbb{R}^{n \times n}, A = MN^{-1}$, A can be obtained by performing a constrained optimization by minimizing a cost function:

$$\begin{aligned} V_{\mathrm{TL1}}(A) =& \parallel \Upsilon_1 N - \Upsilon_0 M \parallel_F \\ \text{subject to: } & \delta \otimes N + \beta \otimes M + \beta^T \otimes M^T \geq 0 \\ & N^T = N > 0, \beta = \begin{bmatrix} 0 & 1 \\ -1 & 0 \end{bmatrix} \end{aligned} \tag{2.55}$$

where δ is a small number that limits the imaginary part of the poles of A. The symbol $\|\|_F$ is the Frobenius matrix norm, where $\otimes$ denotes a Kronecker product.

In order to calculate B, D and the initial states $X(1)$, we parameterize the input-output equation as:

$$y(k) = \phi(k)^T \theta \tag{2.56}$$

where

$$\begin{aligned} \phi &= \begin{bmatrix} CA^k & \sum_{i=0}^{k-1} u(i)^T \otimes CA^{k-i-1} & u^T \otimes I_q \end{bmatrix} \\ \theta &= \begin{bmatrix} X(1)^T & vec(B)^T & vec(D)^T & \end{bmatrix}^T \end{aligned}$$

where the symbol $vec()$ denotes a vector constructed by stacking the columns of a matrix on top of each other. Hence, $X(1)$, B and D are derived by minimizing the cost function

$$V_{\mathrm{TL2}} = \min_{\theta} \sum_{k=1}^{N_{id}} \parallel y(k) - \phi(k)^T \theta \parallel_2^2 \tag{2.57}$$

Prediction-error identification A linear state-space model identified from the identification dataset via the time-domain subspace method can provide an initial guess on the linear plasma response dynamics. The model can be further refined by involving a nonlinear iterative optimization routine [Ljung, 1995]. we define the parameter vector $\theta_L = \left[vec(A)^T, vec(B)^T, vec(C)^T, vec(D)^T\right]^T$. The parameter vector can be estimated by optimizing the cost function as:

$$V_{\mathrm{TL3}} = \min \sum_{k=1}^{N_{id}} \parallel y(k) - \hat{y}(u(k), \theta_L) \parallel_2^2 \tag{2.58}$$

where θ_L is initialized with the model derived from the subspace identification. The parameters θ_L are estimated by minimizing the cost function V_{TS3} using the LM optimization method. This method is essentially a mixture of the gradient-descent and Gauss-Newton methods and a trade-off factor λ is used to determine its characteristic. More precisely, when $\lambda \to \infty$, the LM algorithm tends to behave like a gradient-descent method, when $\lambda \to 0$, the LM algorithm gradually exhibits the feature of the Gauss-Newton method. The gradient-descent method is more robust than the Gauss-Newton algorithm if the parameter estimate is far away from the local minimum, while the Gauss-Newton converges much faster than the gradient-descent method when the parameter estimate approaches the local minimum. The LM algorithm can therefore accumulate the advantages of these two optimization algorithms in one optimization setup. Iterative LM optimization results in a set of refined system matrices as $(A^*_{TL}, B^*_{TL}, C^*_{TL}, D^*_{TL})$.

2.2.3.2 A frequency-domain approach

A frequency-domain approach, as an alternate method, is applied to identify an LSS model. The best linear approximation (BLA) of plasma response dynamics is first introduced via LPM [Pintelon et al., 2010]. Then the frequency-domain subspace method is used to extract an LSS model consistent with the non-parametric BLA estimate, which is further refined using the LM optimization algorithm.

Non-parametric BLA The BLA of plasma dynamics refers to the best approximation of the measured output in a given model set $\mathbb{G}$ in a least-squares sense, expressed as:

$$\hat{G}_{BLA}(k) = \arg \min_{G(k)\in\mathbb{G}} E_u\{\parallel Y(k) - G(k)U(k) \parallel_2^2\} \tag{2.59}$$

where $\hat{G}_{BLA}(k)$ represents the estimate of the FRF of the BLA, $Y(k)$ and $U(k)$ denote the discrete Fourier spectra of the output and the input at the frequency line k, respectively. $G(k)$ indicates the FRF of a linear system in $\mathbb{G}$. E_u is an average of the frequency bandwidth of interest.

Parametric BLA With the given non-parametric estimate $\hat{G}_{BLA}$, we subsequently identify a linear parametric model, estimated by the frequency-domain subspace method [McKelvey

et al., 1996]. The model fitting quality is evaluated by a weighted least-squares cost function as:

$$V_{FL1} = \sum_{k=1}^{n_f} \epsilon_{FL1}^H(k) W_{FL1}(k) \epsilon_{FL1}(k), \epsilon_{FL1}(k) = \hat{G}_{BLA}(k) - \hat{G}_{FL1}(A,B,C,D,k) \tag{2.60}$$

where n_f represents the number of processed frequency lines, and $W_{FL1}(k)$ denotes the weighting matrix, while the superscript H is a symbol of the Hermitian transpose. $\epsilon_{FL1}(k)$ denotes the deviation between the non-parametric FRF estimate $\hat{G}_{BLA}(k)$ and the parametric model estimate $\hat{G}_{FL1}(A,B,C,D,k)$, given by:

$$\hat{G}_{FL1}(A,B,C,D,k) = C(z_k I_n - A)^{-1} B + D, z_k = e^{j\frac{2\pi k}{N_{id}}} \tag{2.61}$$

where (A,B,C,D) are model parameters to be estimated, and z_k is a z-transform variable, while n represents the optimal model order (free parameter). Using the non-iterative subspace identification, we therefore derive a parametric model with the system matrices as $\hat{M}_{FL1}^* = (A_{FL1}^*, B_{FL1}^*, C_{FL1}^*, D_{FL1}^*)$ with an optimal model order at n^*.

Prediction-error identification To improve the fitting accuracy, an iterative LM optimisation method is utilized, whose cost function is expressed as:

$$\begin{aligned} V_{FL2} &= \sum_{k=1}^{n_f} \epsilon_{FL2}^H(k) W_{PI}(k) \epsilon_{FL2}(k) \\ \epsilon_{FL2}(k) &= \text{vec}\left(\hat{G}_{BLA}(k) - \hat{G}_{FL2}(A,B,C,D,k)\right) \\ \hat{G}_{FL2}(A,B,C,D,k)|_{i=0} &= \hat{G}_{FL1}(A_{FL1}^*, B_{FL1}^*, C_{FL1}^*, D_{FL1}^*, k) \end{aligned} \tag{2.62}$$

where V_{FL2} and $\epsilon_{FL2}(k)$ are the cost function and model prediction error, respectively. $W_{FL2}(k)$ represents the weighting matrix at the frequency line k. The initial guess of $\hat{G}_{FL2}(A,B,C,D,k)|_{i=0}$ is assumed to be the one obtained via the frequency-domain subspace method. The nonlinear optimization requires the calculation of the Jacobian of the model error $\epsilon_{FL2}(k)$ with respect to the model parameters as

$$\begin{aligned} \frac{\partial \epsilon(k)}{A_{ij}} &= \text{vec}\left(C(z_k I_{n^*} - A)^{-1} I_{ij}^{n^* \times n^*} C(z_k I_{n^*} - A)^{-1} B\right) \\ \frac{\partial \epsilon(k)}{B_{ij}} &= \text{vec}\left(C(z_k I_{n^*} - A)^{-1} I_{ij}^{n^* \times n_u}\right) \\ \frac{\partial \epsilon(k)}{C_{ij}} &= \text{vec}\left(I_{ij}^{n_y \times n^*} C(z_k I_{n^*} - A)^{-1} B\right) \\ \frac{\partial \epsilon(k)}{D_{ij}} &= \text{vec}\left(I_{ij}^{n_y \times n_u}\right) \end{aligned} \tag{2.63}$$

where $I_{ij}^{m \times n} \in \mathbb{R}^{m \times n}$ represents a matrix with the (i,j) element at 1 and all the other elements at 0. Using the LM optimization, an optimal discrete LSS model, denoted as $(A_{FL}^*, B_{FL}^*, C_{FL}^*, D_{FL}^*)$, is therefore identified such that V_{FL2} can be driven to a good local minimum or a global minimum. The optimal discrete LSS model can be further transformed into a continuous one for control design or predictive simulations.

2.2.4 Identification of the nonlinear plasma dynamics

In this section, a PNLSS plasma model is identified based on an optimal LSS model, either derived from the time-domain approach or from the frequency-domain approach. Next, a parsimonious representation of the PNLSS model is obtained by using the canonical polyadic decomposition (CPD) technique [Dreesen et al., 2015].

2.2.4.1 Identification of a PNLSS plasma model

In advanced tokamak scenarios, the response of magnetic and kinetic parameters with respect to additional heating powers may exhibit nonlinear behaviours. In this regard, it is necessary to identify the nonlinear terms E and F in equation (2.42) such that nonlinear dynamics can be captured. First, we initialize the nonlinear (NL) model $(A_{NL}, B_{NL}, C_{NL}, D_{NL}, E_{NL}, F_{NL})$ with an optimal LSS model plus the null nonlinear terms as $(A_p^*, B_p^*, C_p^*, D_p^*, 0_{n\times n_\zeta}, 0_{n\times n_\eta}), p \in \{TL, FL\}$, which is parameterized as:

$$\theta_{NL} = \left[vec(A_{NL})^T, vec(B_{NL})^T, vec(C_{NL})^T, vec(D_{NL})^T, vec(E_{NL})^T, vec(F_{NL})^T\right] \tag{2.64}$$

The vector θ_{NL} is then estimated by minimizing the weighted cost function that penalizes the output errors as:

$$V_{NL}(\theta_{NL}) = \sum_{k=1}^{n_f} E_{NL}^H(k) W_{NL}(k) E_{NL}(k) \tag{2.65}$$

with respect to θ_{NL}. $W_{NL}(k)$ denotes the user-defined frequency domain weighting matrix, through which one can weigh the importance of the frequency bandwidth. Typically, this matrix is prescribed as the inverse covariance matrix of the output. The output error is defined as $E_{NL} = Y_{MEA}(k) - Y_{NL}(k, \theta_{NL})$, where $Y_{MEA}(k)$ and $Y_{NL}(k)$ are the discrete Fourier spectra of the measured (MEA) and NL model-simulated outputs, respectively. The optimal model parameter vector θ_{NL}^* is optimized as:

$$\theta_{NL}^* = \arg\min_{\theta_{NL}} V_{NL}(\theta_{NL}) \tag{2.66}$$

Analogous to the linear cases, the LM algorithm is used to optimize θ_{NL}, which requires the computation of the Jacobian of the output prediction error with respect to the model parameters:

$$\frac{\partial E(k)}{\partial \theta_{NL}} = \frac{\partial Y_{NL}(k, \theta_{NL})}{\partial \theta_{NL}} \tag{2.67}$$

As mentioned in [Paduart et al., 2010, Paduart et al., 2012], the explicit calculation of $\frac{\partial E(k)}{\partial \theta_{NL}}$ in the frequency domain is not practical. Hence, an implicit technique is adopted: we first compute these terms in the time-domain, which are then transformed into the frequency domain via discrete Fourier transform (DFT) for optimization.

2.2.4.2 Parsimonious representation of the PNLSS plasma model

Although the standard PNLSS modelling is potential to approximate nonlinear plasma dynamics, its obvious drawback is that the model parameter number grows substantially with the increase of polynomial degree and the number of states and inputs. The significant growth of the parameter number may result in identifiability issues and over-fitting [Relan et al., 2018]. Inspired by [Relan et al., 2018], we adopt a decoupling method that calculates the decoupled representation of the multivariate polynomials via the CPD of a tensor containing Jacobians for a set of samplings. The idea of the decoupling method is that a multivariate polynomial vector function is decomposed into a linear transformation V, followed by a set of parallel univariate polynomials g_1, g_2, g_r, and another linear transformation W, which therefore removes insignificant cross-terms in the multivariate polynomials.

Let us consider the nonlinear terms in the PNLSS model jointly as:

$$h(\upsilon(t)) = \begin{bmatrix} E\zeta(\upsilon(t)) \\ F\eta(\upsilon(t)) \end{bmatrix}, \upsilon(t) = [x(t)^T, u(t)^T]^T \in \mathbb{R}^{n+n_u} \tag{2.68}$$

The aim of the decoupling algorithm is to transform equation (2.68) into a form

$$h((\upsilon(t)) = W\alpha\left(V^T\upsilon(t)\right), W = \begin{bmatrix} W_x \\ W_y \end{bmatrix} \tag{2.69}$$

where $V \in \mathbb{R}^{(n+n_u)\times r}$ and $W \in \mathbb{R}^{(n+n_y)\times r}$ are two constant mapping matrices. In particular, denoting $\underline{\upsilon} = V^T\upsilon(t)$, V maps the joint vector of states and inputs $\upsilon(t)$ into a new coordinate $\underline{\upsilon}(t) \in \mathbb{R}^r$ with the reduced dimension r. In the new coordinate, the univariate functions $\alpha_i(\underline{\upsilon}_i), i = 1, 2, ..., r$ are able to operate on the variables $\underline{\upsilon}_i, i = 1, 2, ..., r$ separately, where $\underline{\upsilon}_i$ and α_i denote the i-th element of the vector $\underline{\upsilon}$ and the polynomial functions $\alpha(\underline{\upsilon}(t))$. The mapping matrix W then transforms the results of the univariate functions into the nonlinear terms consistently with the process and output equations in the PNLSS model. Specifically, W_x relates the process nonlinear term $E\zeta(\upsilon(t))$ with $\alpha(\underline{\upsilon}(t))$, while W_y links the output nonlinear term $F\eta(\upsilon(t))$ to $\alpha(\underline{\upsilon}(t))$.

In order to calculate the mapping matrices W and V as well as the univariate polynomial functions $\alpha_i(\upsilon), i = 1, 2, ..., r$, we first calculate the Jacobians of $h(\upsilon(t))$ with respect to υ at a set of sampling points $k = 1, 2, ..., N_s$ as:

$$J_{i,j,k} = \frac{\partial h_i(\upsilon_j^k)}{\partial \upsilon_j^k}, i = 1, 2, ..., (n + n_y), j = 1, 2, ..., (n + n_u), k = 1, 2, ..., N_{id} \tag{2.70}$$

where $\upsilon_j^k \in \mathbb{R}^{n+n_u}$ denotes the j-th element of υ at the sampling point k. Subsequently, we accumulate all the Jacobians into a tensor bank with the dimension at $(n+n_y)\times(n+n_u)\times N_{id}$. Performing the CPD decomposition, the Jacobians can thus be truncated into a form as:

$$J_{i,j,k} = \sum_{q=1}^{r} w_{iq}\upsilon_{jq}\chi_{kq} \tag{2.71}$$

where $W = [w_{iq}]_{(n+n_y)\times r}$ and $V = [v_{jq}]_{(n+n_u)\times(r)}$ are computed easily. The univariate polynomial functions are calculated by following the Lemma.

Lemma 1. *[Dreesen et al., 2015] The first-order derivatives of the parameterization* (69) *are given by* $J(u) = W\,diag(g_i'(v_i^T u))V^T$, *where* $g_i'(v_i^T u)$. *Therefore, we have the relation* $\chi_{kq} = g_q'(\upsilon_q^k)$.

We define the univariate polynomial functions as $\alpha_q'(\underline{\upsilon}_q) = c_{q,1}'\underline{\upsilon}_q + c_{q,2}'\underline{\upsilon}_q^2 + ... + c_{q,2}'\underline{\upsilon}_q^{d-1}$, where d is the order of the univariate polynomials $\alpha_q(\underline{\upsilon}_q)$. For the i-th branch $g_q'(\underline{\upsilon}_q)$, the coefficients are simply derived by polynomial fitting as:

$$\begin{bmatrix} (\underline{\upsilon}_q^1)^1 & (\underline{\upsilon}_q^1)^2 & ... & (\underline{\upsilon}_q^1)^{d-1} \\ (\underline{\upsilon}_q^2)^1 & (\underline{\upsilon}_q^2)^2 & ... & (\underline{\upsilon}_q^2)^{d-1} \\ ... & & & \\ (\underline{\upsilon}_q^{N_s})^1 & (\underline{\upsilon}_q^{N_s})^2 & ... & (\underline{\upsilon}_q^{N_s})^{d-1} \end{bmatrix} \begin{bmatrix} c_{q,1}' \\ c_{q,2}' \\ ... \\ c_{q,d-1}' \end{bmatrix} = \begin{bmatrix} \chi_{1q} \\ \chi_{2q} \\ ... \\ \chi_{N_s,q} \end{bmatrix} \tag{2.72}$$

where $(\underline{\upsilon}_q^k)^p$ represents the q-th element of the vector $\underline{\upsilon}$ at the sampling point k to the p-th power. Once the derivative of univariate functions $\alpha_q'(\underline{\upsilon}_q)$ are fitted, the univariate functions are consequently obtained as $\alpha_q(\underline{\upsilon}_q) = \int_0^{\underline{\upsilon}_q} \alpha_q'(\underline{\upsilon}_q) d\underline{\upsilon}_q$.

2.2.5 Identification results

In this section, the nonlinear model identification scheme described above is applied to identifying PNLSS plasma models. The identification performance is extensively evaluated, compared and discussed through simulations and/or experiments on the EAST and ITER tokamaks. Specifically, we compare the model predicted outputs with the outputs sampled from METIS simulations or experiments and introduce the RMS error to quantify the identification performance, which reads:

$$e_{RMS} = \sqrt{\frac{1}{N_t}\sum_{t=1}^{N_t}\left(y(t) - y_{mod}(t)\right)^2} \tag{2.73}$$

where y_{mod} represent the model-predicted outputs, while $y(t)$ denotes the original outputs, either from METIS simulations or from the EFIT reconstructions [Huang et al., 2017] in tokamak plasma experiments. N_t is the total number of sampling points in $y(t)$.

2.2.5.1 Identification results from METIS simulations on EAST

In the first case, the noise-free data generated from the nonlinear plasma simulator METIS in an H-mode steady-state plasma discharge on the EAST tokamak, i.e. shot #62946, is collected to identify LSS and PNLSS models. The key plasma parameters for the discharge simulation are described in Section 1.4 and the METIS tuning procedure for advanced tokamak plasma discharge simulations is referred to [Moreau et al., 2013]. Our objective is to identify

the responses of β_p (poloidal plasma pressure parameter), β_n (normalized plasma pressure parameter), $T_{e,0}$ (the central electron temperature), ω_ϕ (the average toroidal rotation angular speed) and ι_0 (the central rotational transform) with respect to the heating powers of ICRH at 33 MHz and of LHCD at 4.6 GHz. In order to excite the dominant plasma eigenmodes, five dedicated METIS simulations are performed, among which two heating powers are modulated using PRBS waveforms [Ljung, 1995, Landau and Zito, 2007], while all the other METIS simulation setup remain unchanged. As shown in Fig. 2.6(f), the ICRH power varies in the range 0 MW-1.5 MW while the LHCD power is limited to the interval 0.85 MW-2.6 MW. The measurements of both the control actuations and the plasma parameters of interest are taken with the sampling time at 0.02 s, and the pulse duration for each simulations vary between 15 and 20 s. Accounting for the plasma dynamics in the flat-top phase, the control inputs and measurements in the interval 4-15 s of each simulation are selected as datasets for model identification, selection and testing. Five selected datasets are first merged and then divided into three subsets, with one half used for identification (See the upper panel in Fig. 2.6(f)), a quarter for model selection (See the left bottom panel in Fig. 2.6(f)) and the remaining for predictive tests (See the right bottom panel in Fig. 1(f)). The green dashed lines denote the starting/ending sampling of each selected numerical shots. For convenience, we label TD as the time-domain approach, while denoting FD as the frequency-domain approach.

With the identification dataset, an LSS plasma model of order 4 is identified by the TD approach, and the characteristic time constants are 0.6019 s, 0.0597 s, 0.005 s. The model-simulated outputs from the TD approach are compared with the corresponding METIS simulation outputs in Fig. 2.6, indicating that the TD-LSS and TD-PNLSS model predictions are consistent with the METIS simulations in both identification, selection and testing phases. In contrast to the TD-LSS model, it is found that enhanced identification performance has been obtained with the TD-PNLSS model for all the outputs. More specifically, the RMS errors of β_p, β_n and ω_ϕ decrease from 0.1134, 0.0823, 0.5362 to 0.0762, 0.0556 and 0.4036 in the testing phase, respectively. The underlying reason is that the TD-PNLSS model involves two nonlinear polynomial terms in both the process and output equations for nonlinear dynamics accommodation.

Compared with the TD approach, the FD approach cannot identify an appropriate LSS using the given identification dataset, as listed in Table 2.2, perhaps because the linear couplings are more difficult to be captured by the FD approach in the MIMO setup. The RMS errors for all the output variables are around twice larger than those corresponding to the TD-LSS model. Nonetheless, initializing the PNLSS model with the identified FD-LSS model, significant model prediction error reduction has been achieved with the FD-PNLSS model, whose RMS errors in all the output variables are comparable to those obtained by the TD-LSS model, but not as small as those predicted by the TD-PNLSS model due to improper model initialization.

To sum up, the identification results have shown that both the TD-LSS, TD-PNLSS and FD-PNLSS models can properly describe the responses of plasma parameters β_p, β_n, $T_{e,0}$, ω_ϕ, and ι_0 with respect to the ICRH power at 33MHz and the LHCD power at 4.6GHz in a broad frequency bandwidth. The enhanced identification performance has been demonstrated by

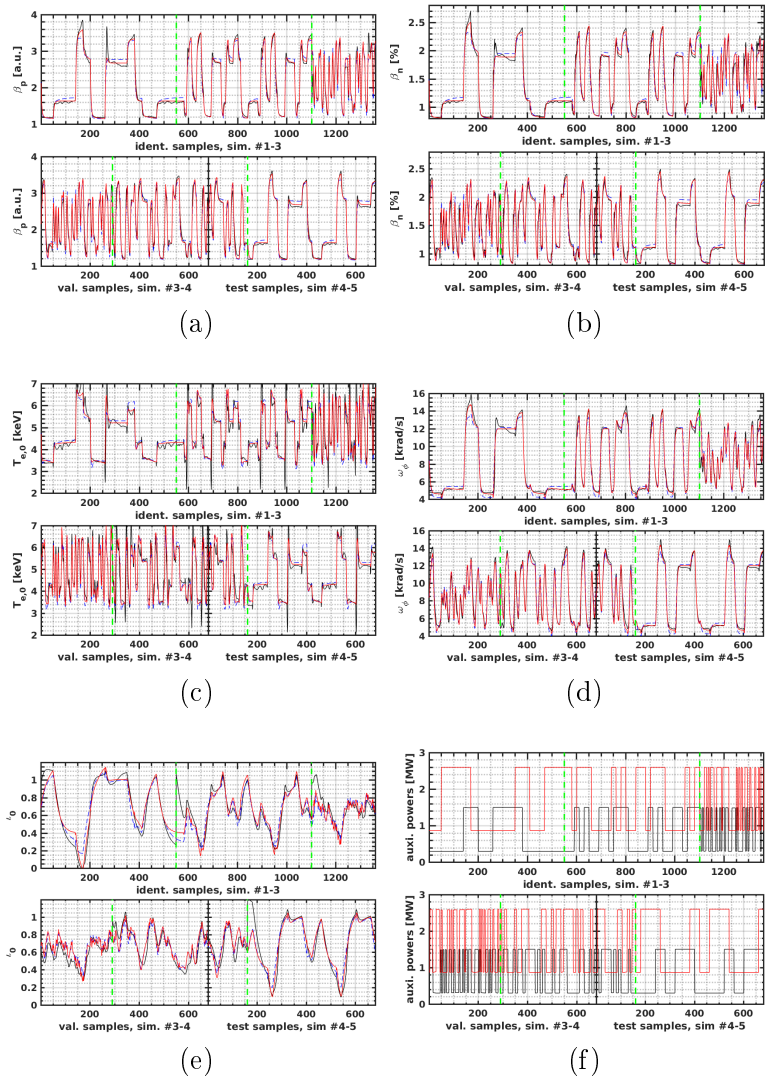

Figure 2.6: Comparison of the model-predicted outputs and the outputs generated from METIS simulations on EAST. Upper panels of (a)-(e): comparison of the TD-LSS predictions (blue dashed), the TD-PNLSS predictions (red) and the METIS simulation outputs (black) of (a) β_p ,(b) β_n,(c) $T_{e,0}$,(d) ω_ϕ (e) ι_0 in the identification data set. Bottom panels of (a)-(e): comparison of the TD-LSS predictions (blue dashed), the TD-PNLSS predictions (red) and the METIS simulation outputs (black) of (a) β_p ,(b) β_n,(c) $T_{e,0}$,(d) ω_ϕ,(e) ι_0 in the validation (left half) and testing (right half) data set. Upper panel of (f) Time traces of the ICRH power (black) and LHCD power (red) in the identification data set; Bottom panel of (f): Time traces of the ICRH power (black) and LHCD power (red) in the validation (left half) and testing (right half) data set. The green dashed lines separate different METIS simulation shots.

involving nonlinear polynomial terms at both the state and output equations. In addition, good LSS initialization is proved beneficial to the identification performance of the generated PNLSS model.

Table 2.2: Comparison of the RMS errors from METIS simulations on EAST.

	Option	TD-LSS	TD-PNLSS	FD-LSS	FD-PNLSS
	No. of parameters	54	747	54	747
β_p	model iden.	0.1529	0.1138	0.5740	0.1394
[a.u.]	model val.	0.1497	0.1313	0.5630	0.2153
	model test	0.1134	0.0762	0.5671	0.1205
β_n	model iden.	0.1049	0.0763	0.3752	0.0723
[%]	model val.	0.1181	0.0983	0.3466	0.1208
	model test	0.0823	0.0556	0.3723	0.0683
$T_{e,0}$	model iden.	0.5120	0.4392	1.0388	0.4841
[keV]	model val.	0.4959	0.4251	1.1325	0.6273
	model test	0.3853	0.3230	0.9544	0.4064
ω_ϕ	model iden.	0.7191	0.5522	2.1946	0.6359
[krad/s]	model val.	0.8428	0.7736	2.1307	1.0908
	model test	0.5362	0.4036	2.1600	0.6383
ι_0	model iden.	0.1222	0.1029	0.2906	0.1349
[a.u.]	model val.	0.0834	0.0804	0.1844	0.1815
	model test	0.1193	0.1123	0.3031	0.1567

2.2.5.2 Identification results from H-mode plasma experiments on EAST

In the experimental case, the noise-corrupted data obtained from the EAST experiments are used for plasma model identification. The reference plasma discharge has the toroidal field at 2.5 T, the central electron density at around 4.2×10^{19} m^{-3}, the plasma current at 350 kA and the central electron temperature at around 4 keV. The LHCD power was injected at 2.45 GHz during the plasma current ramp-up phase, specifically 0.6 MW in the period [0.95, 2.25] s. In addition, 0.9 MW of ECRH power was injected during the current flat-top phase (in the time interval [1.98, 7.91] s), from two gyrotrons at 140 GHz. The LHCD power at 4.6 GHz varies in the range of 1.0-2.5 MW. The ICRH system was not available during the whole experiments. Simple internal model control with proportional integral (SIMC PI) [Skogestad and Postlethwaite, 2007] was used to track the desired 4.6 GHz LHCD power modulations in the current flattop phase. The objective here is to identify the responses of β_p, β_n, li and ι_0 with respect to the LHCD power at 4.6 GHz. Two identification experiments have been performed by modulating the LHCD power in the PRBS (shot #93298) and chirping (shot #93297) waveforms, respectively. The LHCD power coupled to the plasma was measured as shown in Fig. 2.7. The magnetic and kinetic parameters of interest are estimated by the GPU-accelerated EFIT reconstruction code, i.e. P-EFIT [Huang et al., 2017], taking into account a large number of magnetic and kinetic measurements, whose estimates are considered as experimental measurements. All the input-output measurements are taken with the sampling time at 1 ms, and the pulse durations for shot #93297 and #93298 are about 9.0 s, including plasma ramp-down phase. The input-output measurements of shot #93298 in the period [3.5, 7]s are chosen for model identification, while the input-output measurements of shot #93297

in the intervals 3.5-5.25 s and 5.25-7 s are used for model selection and testing, respectively. A lowpass filter with the time constant at 0.003 s was used to remove the measurement noise.

Both the TD and FD approaches are used for model identification. The model-simulated outputs from the TD-LSS, TD-PNLSS, FD-LSS and FD-PNLSS models are compared with the EFIT estimates in the identification dataset, as illustrated in Fig. 2.8. It is found that the evolutions of β_p and β_n predicted by TD-LSS and TD-PNLSS models match the P-EFIT estimates satisfactorily, with the RMS errors at 0.0217 and 0.0184, respectively (See Table 2.3). Obviously, enhanced identification performance has been obtained by the PNLSS model. The TD-LSS and TD-PNLSS models can both predict the evolution of li and ι_0 at a reasonable level, but the fitting errors exhibit a linear downward drift, due to the poloidal magnetic measurement faults at the plasma boundary. This disturbance caused ι_0 and li to drift linearly at the rate of -0.01 s^{-1}. Nonetheless, the PNLSS model shows better identification performance compared to the LSS model in the identification dataset. The identified TD-LSS and TD-PNLSS models are then tested in shot #93297. As illustrated in Fig. 2.9, the TD-LSS and TD-PNLSS models can simulate the evolutions of β_p and β_n fairly well, with the RMS errors at 0.0245 and 0.0176 for the TD-PNLSS model. For li and ι_0, a drift with the rate at -0.01 s^{-1} happens similarly in shot #93297. In addition to that, an offset of 0.02 for li and ι_0 are observed, which are attributed to the difference between the plasma density evolution in shot #93298 (steady at 4.2×10^{19} m^{-3}) and in shot #93297, where the density control was poor for $t < 4$ s, with a final steady density of 3.7×10^{19} m^{-3} for $t > 4$ s.

Table 2.3 shows the comparison of the RMS errors among the four identified models. In this case, the TD-LSS model still outperforms the FD-LSS model in all the RMS errors, suggesting that it may be preferable to apply the TD approach for linear model identification if the control inputs are designed as PRBS signals. However, the predictive performance of the FD-PNLSS model slightly outperforms that of the FD-PNLSS model in β_p and β_n thanks to better PNLSS model optimization. It should be remarked that the TD-PNLSS model shows comparable predictive performance with the FD-PNLSS model in this case primarily because the FD identification method is more effective in the single input setup.

To sum up, the identification results have demonstrated that the proposed identification scheme can successfully extract linear and nonlinear models describing the responses of plasma kinetic parameters with respect to the variations of the LHCD power from dedicated experimental data. Furthermore, enhanced identification performance has been obtained by the PNLSS models with respect to the LSS models. It is evident that the disturbances in li and ι_0 are not solely dependent on the variations of the LHCD power at 4.6 GHz. Hence, the disturbance dynamics cannot be modelled directly using the available inputs and outputs, even involving polynomial nonlinear model expansions. Nevertheless, these disturbances are the combination of constant and linear drifts, whose values are predictable and possibly linked, for instance, to the plasma density evolution.

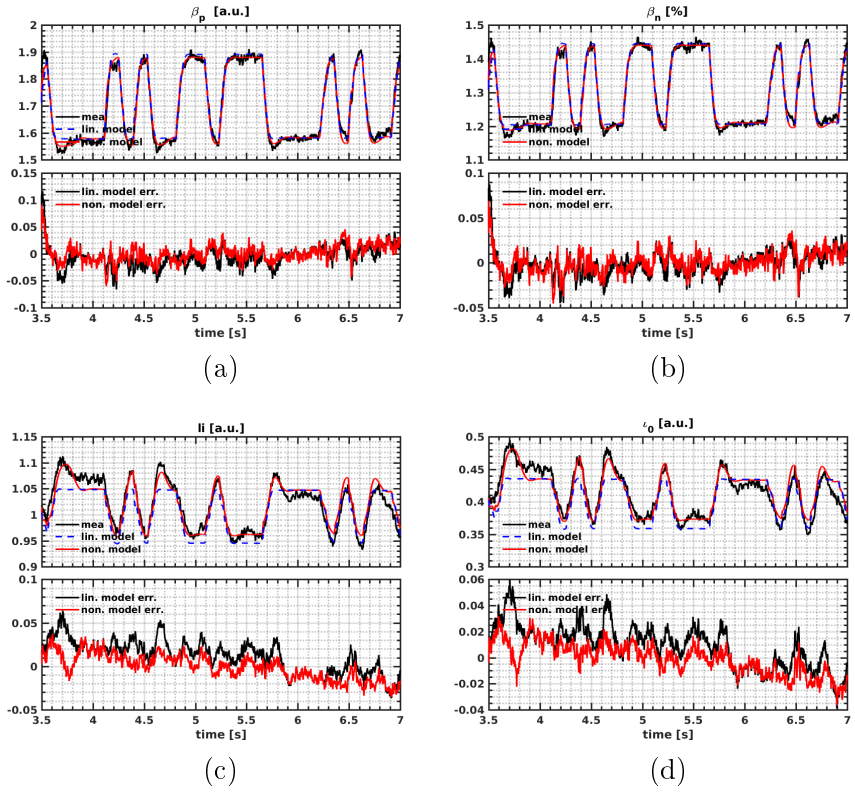

Figure 2.7: Comparison of the model-predicted outputs and the measured outputs in EAST shot #93298 (identification data set). Upper panels of (a)-(d): comparison of the TD-LSS predictions (blue dashed), the TD-PNLSS predictions (red) and the EFIT estimates (black) of (a) β_p ,(b) β_n,(c) li ,(d) ι_0. Bottom panels of (a)-(d): the predictive errors of (a) β_p ,(b) β_n,(c) li ,(d) ι_0 by the TD-LSS model (black) and the TD-PNLSS model (red).

2.2.5.3 Identification results from METIS simulations on ITER

In the third case, the proposed identification scheme is extrapolated to the noise-free data sampled from METIS simulations of H-mode steady-state burning plasma scenarios on the ITER tokamak. The key plasma parameters configured for METIS simulations are illustrated in Section 1.4. The objective now is to identify the responses of β_p, β_n, ω_ϕ and P_α (the α particle power generated from D-T fusion reactions) with respect to the co-current neutral beam injection power P_{NBI}. Analogously, we design the P_{NBI} references in PRBS waveforms to excite the dominant plasma eigenmodes governing kinetic evolutions. More precisely, two dedicated METIS simulations are performed, whilst the other parameters for METIS setup are kept unchanged. The co-current NBI power is limited to the interval of 5-16.5 MW. The sampling time is fixed at 1 s, and the pulse duration for each simulations is over 2800 s. The control input and output measurements in the period 1000-2500 s are chosen as datasets for model identification, selection and testing. Similarly, the selected datasets are first merged and then divided into three subsets, with one half for model identification, a quarter for model selection and the rest for model testing.

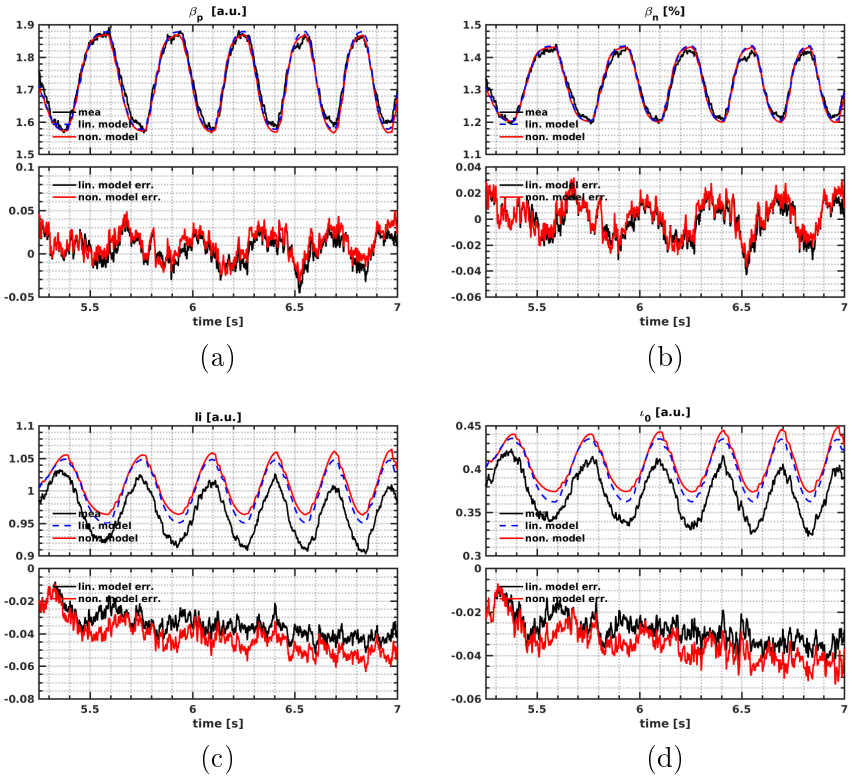

Figure 2.8: Comparison of the model-predicted outputs and the measured outputs in EAST shot #93297 (testing data set). Upper panels of (a)-(d): comparison of the TD-LSS predictions (blue dashed), the TD-PNLSS predictions (red) and the EFIT estimates (black) of (a) β_p ,(b) β_n,(c) li ,(d) ι_0. Bottom panels of (a)-(d): comparison of the predictive errors of (a) β_p ,(b) β_n,(c) li ,(d) ι_0 by the TD-LSS model (black) and the TD-PNLSS model (red).

Both the TD and FD approaches are used to identify the LSS and PNLSS models. The outputs predicted by the FD-LSS and FD-PNLSS models are compared with the METIS simulated outputs as depicted in Fig. 2.10, showing that the FD-LSS and FD-PNLSS models can both successfully predict kinetic responses under the perturbation of P_{NBI}. The RMS errors corresponding to all the identified models are listed in Table 2.4, which demonstrates that the PNLSS models are able to predict plasma kinetic evolutions with more precision than the LSS models. In contrast to EAST identification results, the FD-LSS model now achieves smaller RMS errors than the TD-LSS model in β_p and β_n since in this case we involve only one control input, where the FD approach turns out to be effective. When moving onto model selection and testing datasets, it is confirmed that the FD-LSS model has a high accuracy of predictive performance, and the FD-PNLSS model acquires much smaller RMS errors than those corresponding to the TD-PNLSS model, thanks to the enhanced model initialization and the single control input setup.

Table 2.3: Comparison of the RMS errors from experiments on EAST.

	Option	TD-LSS	TD-PNLSS	FD-LSS	FD-PNLSS
	No. of parameters	40	440	40	440
β_p	model iden.	0.0217	0.0184	0.0386	0.0153
[a.u.]	model val.	0.0254	0.0245	0.0372	0.0278
	model test	0.0193	0.0188	0.0272	0.0145
β_n	model iden.	0.0154	0.0138	0.0313	0.0117
[%]	model val.	0.0187	0.0176	0.0293	0.0213
	model test	0.0153	0.0137	0.0231	0.0138
li	model iden.	0.0212	0.0142	0.0243	0.0125
[a.u.]	model val.	0.0255	0.0226	0.0268	0.0267
	model test	0.0362	0.0433	0.0366	0.0373
ι_0	model iden.	0.0181	0.0123	0.0234	0.0110
[a.u.]	model val.	0.0214	0.0192	0.0245	0.0227
	model test	0.0298	0.0357	0.0322	0.0313

Table 2.4: Comparison of the RMS errors from METIS simulations on ITER.

	Option	TD-LSS	TD-PNLSS	FD-LSS	FD-PNLSS
	No. of parameters	40	440	40	440
β_p	model iden.	0.0140	0.0033	0.0183	0.0098
[a.u.]	model val.	0.0185	0.0127	0.0138	0.0047
	model test	0.0214	0.0269	0.0110	0.0101
β_n	model iden.	0.0223	0.0034	0.0138	0.0105
[%]	model val.	0.0219	0.0164	0.0087	0.0055
	model test	0.0268	0.0328	0.0085	0.0114
ω_ϕ	model iden.	0.0710	0.0358	0.2318	0.0622
[krad/s]	model val.	0.0909	0.1389	0.2220	0.0605
	model test	0.0963	0.1658	0.2541	0.0721
P_α	model iden.	0.6548	0.1180	0.6117	0.2299
[MW]	model val.	0.3680	0.3422	0.6060	0.1859
	model test	0.4121	0.4165	0.4669	0.1756

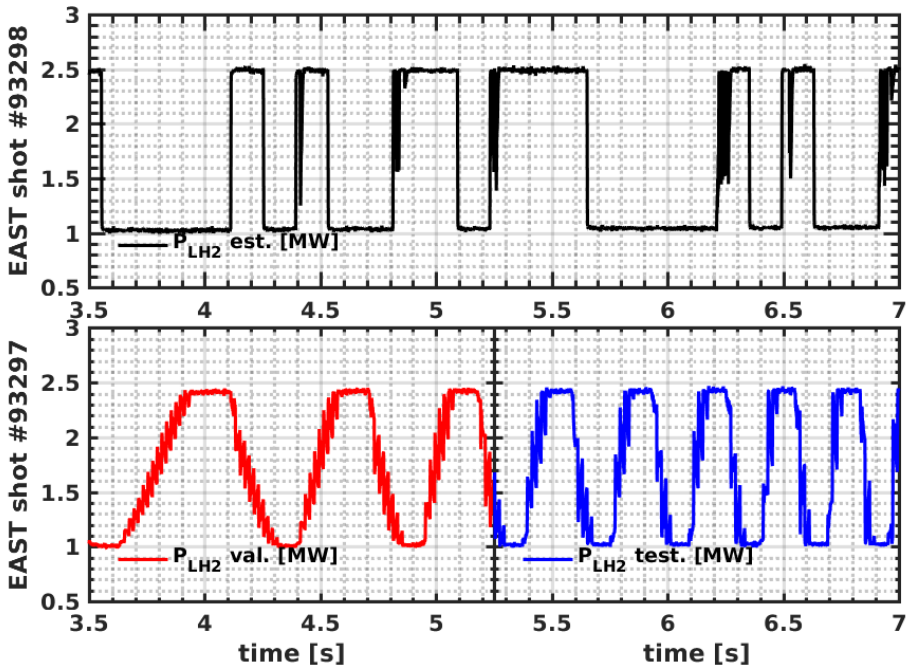

Figure 2.9: Time traces of the coupled lower hybrid current drive system power at 4.6GHz in shots #93297 and #93298 on EAST. In both shots, the data in the time interval [3.5, 7.0]s are selected and merged. In particular, the data (black) in shot #93298 is used for model identification, and the data (red) in the interval [3.5,5.25]s of the shot #93297 are arranged for model validation, while the data (blue) in the interval [5.25,7]s of the same shot are utilized for model testing.

2.2.5.4 Discussion

In contrast to other model structures such as LSS models and neural networks, there are a number of advantages to use the PNLSS model structure for plasma dynamics approximation. First, the PNLSS model structure takes into account the dominant linear dynamics in conjunction with moderate nonlinearities, which can thus deliver enhanced predictive performance with respect to the LSS models. Second, the identification scheme has no difficult parameter setup, e.g., the number of neurons. Third, the PNLSS model identification scheme is systematic and general, and it can be easily extrapolated to data-driven modelling in different tokamaks, including both simulations and experiments.

However, it should be mentioned that there are a few restrictions on the use of this identification scheme. First, the PNLSS model structure is more suitable to approximate low-order systems, whose order is typically less than 10. For high-order systems, the number of estimated model parameters in nonlinear terms grow substantially, likely to cause identifiability issues. However, it is possible to overcome this problem by tweaking the estimated model parameters. For instance, the monomials in the polynomial expansion can be constrained to certain inputs and states that play an important role in causing nonlinearities. The second

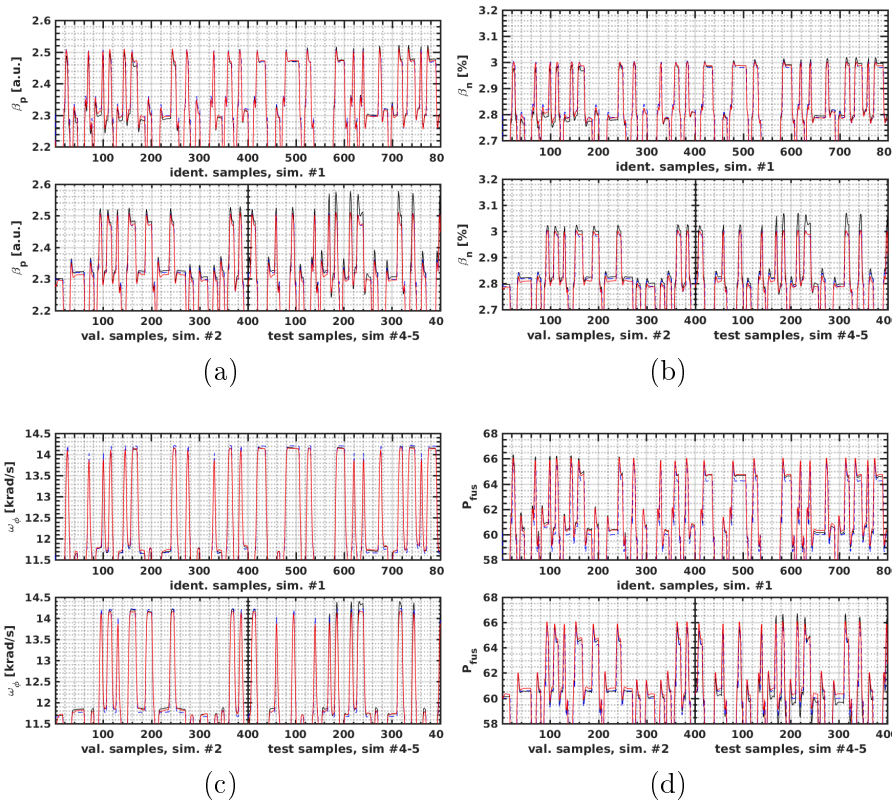

Figure 2.10: Comparison of the model-predicted outputs and the outputs generated from METIS simulations on ITER. Upper panels of (a)-(d): comparison of the FD-LSS predictions (blue dashed), the FD-PNLSS predictions (red) and the METIS simulation outputs (black) of (a) β_p ,(b) β_n,(c) ω_ϕ ,(d) P_α in the identification data set. Bottom panels of (a)-(d): comparison of the FD-LSS predictions (blue dashed), the FD-PNLSS predictions (red) and the METIS simulation outputs (black) of (a) β_p ,(b) β_n,(c) ω_ϕ ,(d) P_α in the validation (left half) and testing (right half) data set. The green dashed lines separate different METIS simulation shots.

restriction is that, due to the use of PEM for model refinement, the optimization may result in a local minimum instead of a global one, but this is a common issue for nonlinear system identification.

2.2.6 Conclusion of Section 2.2

In this section, the identification of PNLSS plasma model, as a natural extension of LSS model identification, has been investigated using a combination of subspace and PEM identification techniques. In contrast to prior works [Mavkov et al., 2017b, Moreau et al., 2008], two alternative LSS identification approaches handling data in both frequency-domain and time-domain have been presented to identify the LSS models for plasma control. Up to the

best of our knowledge, the PNLSS model identification scheme has, for the first time, been applied to describing the dynamics of plasma kinetic parameters in tokamaks. The identification methodology proposed in this chapter is systematic, general and powerful, and can be easily adapted to data-driven modelling of other tokamak plasma parameters or profiles for control, especially for those problems where the first-principles-driven modelling fails or proves difficult but where the input-output measurements are abundant. One potential topic for future investigations is that plasma nonlinearities can be characterized by other types of basis functions, for example, radial basis functions, wavelets, hyperbolic tangents. One may find an optimal set of basis functions that can achieve the optimal predictive performance in characterzing tokamak plasma nonlinearities by conducting further studies.

2.3 Summary of Chapter 2

In this chapter, the single fluid modelling of tokamak plasma transport using the METIS code has been described, with applications to H-mode steady-state plasma discharge simulations on the EAST and ITER tokamaks. In order to control plasma kinetic parameters in H-mode steady-state tokamak scenarios, a nonlinear model identification scheme has been proposed based on the subspace and prediction-error methods. This identification scheme has been applied to both simulated and experimental data on the EAST and ITER tokamaks, whose effectiveness and validity have been demonstrated. The following chapters will present robust, adaptive and model predictive control strategies using linear data-driven models to support advanced tokamak plasma operation and greatly improve the reproducibility of high performance high bootstrap current plasma discharges.

Chapter 3

Linear Robust Control

Contents

One of the main challenges for the tokamak plasma operation is to achieve and maintain advanced scenarios with high plasma pressures and temperatures such that a high gain nuclear fusion burn can be sustained [Wesson and Campbell, 2011]. However, since a series of MHD instabilities and microturbulence commonly exist in various locations and phases of tokamak plasmas that are likely to deteriorate plasma confinement and even lead to disruptions [Wesson and Campbell, 2011], it is demanding to deliver and sustain advanced tokamak plasma scenarios without active feedback control. Among the numerous tokamak plasma parameters, the safety factor q, defined as the rate of change of toroidal magnetic flux (Φ) with poloidal magnetic flux (Ψ), i.e. $q = -\frac{d\Phi}{d\Psi}$, is a particularly important parameter whose shape and magnitude are directly associated with some deleterious MHD events and micro-instabilities [Kessel et al., 1994, Humphreys et al., 2015]. For instance, sawtooth crashes occur in the region where the plasma safety factor is less than 1 [Denton et al., 1986]; neoclassical tearing modes (NTMs) appear and grow around plasma flux surfaces where the safety factor

exhibits rational values [Westerhof et al., 2002]. Moreover, it is inferred that the negative central magnetic shear ($s = \frac{r}{q}\frac{\partial q}{\partial r}$) is a key stabilizing factor to reduce turbulence transport in the pressure gradient region, thus supporting the formation of ion/electron internal transport barriers (i/eITBs) [Wolf, 2002, Ida and Fujita, 2018]. In view of multiple timescales involved in plasma dynamics, simultaneous control of the q-profile and kinetic parameters (e.g. the stored energy, W, the normalized pressure parameter, β_N, or the poloidal pressure parameter, β_p) is preferred to the control of q-profile alone [Moreau et al., 2013, Barton et al., 2015a]. Therefore, in the first part of the chapter, simultaneous control of q-profile and β_p is numerically investigated. β_p is a ratio between the total plasma kinetic energy and the energy stored in the poloidal magnetic field, expressed as $\beta_p = \frac{4W(1+\kappa^2)}{3\mu_0 aRI_p^2}$, where W represents the plasma kinetic energy, κ the elongation, μ_0 the magnetic permeability in vacuum space, a the minor radius, R the major radius, I_p plasma current. The active control of kinetic parameters such as β_p, the average rotational velocity (ω_ϕ) and the α particle power generated from nuclear fusion reactions should occur in a much faster timescale than magnetic control, e.g. q-profile control. These kinetic parameters are intimately related to fast timescale kinetic evolutions that are much easier to suffer from nonlinear disturbing effects, which, however, provides a prerequisite for effective magnetic control. In the second part of the chapter, the active control of plasma kinetic parameters based on linear data-driven models in advanced tokamak plasma scenarios is pursued.

Various control schemes have been proposed for tailoring plasma magnetic and kinetic parameters, a majority of which are based on control-oriented plasma response models, either in terms of PDEs or ODEs, either using first-principle-driven (FPD) models or data-driven (DD) models. Those control schemes are then verified numerically and/or experimentally in some region of attraction in certain tokamak plasma scenarios. For instance, the proposed control techniques comprise simple PID control [Moreau et al., 2003], LQI control [Boyer et al., 2013, Moreau et al., 2008], $\mathcal{H}_\infty$ robust control [Barton et al., 2012, Barton et al., 2015a, Barton et al., 2015b], MPC [Maljaars et al., 2015, Maljaars et al., 2017], passivity-based control [VU et al., 2014, Vu et al., 2016, Vu et al., 2017], Lyapunov-based control [Argomedo et al., 2013, Mavkov et al., 2018], backstepping control [Boyer et al., 2014], sliding mode control [Gaye et al., 2011] and adaptive control [Kim and Lister, 2012]. More precisely, in [Moreau et al., 2003], a simple PID controller is designed to control the central safety factor using the lower hybrid waves on JET. In [Boyer et al., 2013], an LQI optimal controller is combined with nonlinear input transformation to ensure the minimum weighted norm of tracking errors and control efforts in L-mode plasmas on DIII-D. In [Maljaars et al., 2017], a model-predictive controller is employed to track q-profile and plasma β that accounts for the time-varying operational and physics limits and tested experimentally in L-mode plasmas on TCV. In [Vu et al., 2017], the interconnection and damping-assignment passivity-based control (IDA-PBC) is developed and evaluated experimentally in L-mode plasmas on TCV. In [Mavkov et al., 2018], a Lyapunov-based q-profile controller combined with SIMC PI for β_p is validated both numerically and experimentally in a TCV L-mode plasma. In [Boyer et al., 2014], an adaptive backstepping feedback control technique is proposed for a DIII-D L-mode plasma. In [Gaye et al., 2011], a sliding model controller for a Tore Supra plasma is developed and evaluated via nonlinear closed-loop METIS [Artaud et al., 2018] simulations. In [Kim and Lister, 2012],

static models of the current density and electron temperature profiles are identified in real-time, which are then used to compute the control actuations, and the static adaptive feedback controller is numerically assessed via CRONOS [Artaud et al., 2010] simulations for ITER hybrid scenarios.

In contrast to the existing works, the objective of the chapter is to provide *systematic, practical, effective and robust control strategies* for plasma magnetic and kinetic parameters *in advanced tokamak plasma scenarios* using *linear data-driven models*. We advert that modelling the current profile, momentum and thermal transport in advanced tokamak scenarios for control using the FPD models is not as straightforward as in L-mode scenarios due to different levels of plasma disturbances arising from, for instance, plasma-wave interactions, bootstrap current effects, MHD instabilities, microturbulence and impurity effects [Wesson and Campbell, 2011, Fasoli et al., 2016]. Therefore, we utilize linear models identified from the sampled input and output measurements in an interesting plasma scenario, e.g. H-mode steady-state operational scenario, via system identification methodologies [Ljung and Söderström, 1983, Moreau et al., 2008] for controller design. Since the plasma transport dynamics is intrinsically nonlinear, it necessitates the data-driven model-based controllers to be sufficiently robust against model mismatches and parameter uncertainties. Hence, we devote ourselves primarily to developing a controller that retrieves the most appropriate information from the data-driven models while acquiring good control performance and reasonable robustness against various engineering constraints. The chapter is divided into two parts: the first part shows a decentralized data-driven model-based robust control scheme by combining the multivariate $\mathcal{H}_\infty$ norm optimal control with the singular perturbation theory and demonstrates its effectiveness in both control performance and robustness via extensive nonlinear closed-loop simulations for an EAST H-mode steady-state scenario with the METIS code [Artaud et al., 2018]. The second part reports comparative studies of plasma kinetic control in advanced tokamak scenarios on EAST, comprising both simulations and experiments, where four alternative controllers are considered.

The *main contributions* of the chapter are summarized as follows:

- Developing a decentralized robust control scheme for q-profile and β_p in advanced tokamak scenarios based on a two-time-scale data-driven model by solving LMIs, and provide beneficial control implementation techniques to handle engineering restrictions in tokamak plasma experiments such as time-delays, power saturations, constrained attractive control region and control switching.

- Developing four optional kinetic control strategies, namely the $\mathcal{H}_\infty$ robust control, LQI and IMC, for essential kinetic parameters in advanced tokamak scenarios using LSS models and involve a cascade actuator controller to enable the enhanced tracking of control actuations.

- Evaluating the effectiveness of the decentralized $\mathcal{H}_\infty$ robust control scheme through METIS simulations on EAST; assessing and comparing the performance of the two-layer cascade kinetic control scheme through nonlinear METIS simulations on EAST.

- Implementing the two-layer cascade kinetic control scheme into the EAST PCS using the embedded MATLAB coder (EMC) toolbox and experimentally validating the effectiveness in a typical H-mode plasma scenario on the EAST tokamak.

The rest of the chapter is organized as follows: Section 1 presents the decentralized $\mathcal{H}_\infty$ robust control scheme for q-profile and β_p in advanced tokamak scenarios based on a two-time-scale data-driven model, whose effectiveness is confirmed by extensive nonlinear METIS simulations on EAST. In Section 2, we develop a two-layer cascade kinetic control scheme containing four alternative kinetic controllers and SIMC PI actuator controllers for advanced tokamak plasma operation based on LSS models, whose validity is evaluated, discussed and compared both numerically and experimentally on the EAST tokamak. Consequently, we draw the conclusion of the chapter and outline possible extensions.

3.1 Decentralized robust control of q-profile and β_p

In this section, a novel $\mathcal{H}_\infty$ robust feedback controller for q-profile and poloidal plasma pressure parameter has been developed using a two-time-scale data-driven model. Due to the simplicity and robustness properties, the $\mathcal{H}_\infty$ optimal control technique has been applied to various tokamak plasma control problems. In [Barton et al., 2012, Barton et al., 2015b], an $\mathcal{H}_\infty$ optimal controller combined with a feedforward optimizer synthesized from FPD models has been applied to track the trajectories of the poloidal flux gradient profile in L-mode and H-mode plasma scenarios on DIII-D experimentally. In [Nouailletas et al., 2014], a robust PI control technique using DD models is employed to stabilize the vertical instability on the WEST tokamak numerically. In [Nouailletas et al., 2019], the similar technique has been extended to control the poloidal field coil currents, plasma position and shape parameters on WEST experimentally. In [Blanken et al., 2019], the plasma electron density is successfully controlled by using $\mathcal{H}_\infty$ robust synthesis on ASDEX-Upgrade and TCV. Next, a two-time-scale plasma dynamic model for q-profile and β_p is briefly described. Subsequently, a decentralized $\mathcal{H}_\infty$ feedback controller is synthesized from the model and beneficial control implementation techniques are presented. Afterwards, extensive nonlinear closed-loop METIS simulations are conducted to numerically evaluate the effectiveness of the control scheme on EAST. Consequently, we draw conclusions and suggest possible extensions.

3.1.1 Two-time-scale plasma model

In tokamak plasmas, there are multiple time scales in which various parameters/profiles evolve [Wesson and Campbell, 2011]. Specifically, the inversed safety factor profile has much slower dynamics than plasma pressure in medium-sized (e.g. EAST) and large (e.g. ITER) tokamaks. By virtue of this, we describe the coupled dynamics of ι, defined as an inverse of the safety factor q, and β_p in a two-time-scale manner, linearized around a plasma equilibrium [Moreau

et al., 2008, Moreau et al., 2011, Moreau et al., 2015]. The model reads as:

$$\begin{bmatrix} \frac{\partial \Psi(x,t)}{\partial t} \\ \epsilon \frac{\partial \Xi(x,t)}{\partial t} \end{bmatrix} = \begin{bmatrix} M_{\Psi,\Psi}(x) & M_{\Psi,\Xi}(x) \\ M_{\Xi,\Psi}(x) & M_{\Xi,\Xi}(x) \end{bmatrix} \begin{bmatrix} \Psi(x,t) \\ \Xi(x,t) \end{bmatrix} + \begin{bmatrix} M_{\Psi,U}(x) \\ M_{\Xi,U}(x) \end{bmatrix} U(t) \tag{3.1}$$

where x, namely the flux-averaged normalized radius, is defined as $(\Phi/\Phi_{max})^{1/2}$, in which $\Phi(x)$ is the toroidal magnetic flux within a given flux surface, and Φ_{max} is the maximum value at the last closed flux surface (LCFS). $\Psi(x,t)$ represents the poloidal magnetic flux minus its value at the plasma boundary, while $\Xi(x,t)$ a combination of kinetic parameters/profiles. $U(t)$ is a vector of actuators containing the heating and current drive powers. The constant ϵ denotes a typical value of the ratio between the kinetic and magnetic time constants, which makes the various elements of the M matrix of comparable magnitude.

In order to obtain finite dimensional variables for control design, a projection of equation (3.1) onto cubic spline basis functions is carried out. For the EAST tokamak, ϵ is typically 0.05, hence a singular perturbation approach is employed. Then the linearized PDE is transformed into a two-time-scale LSS model as described below.
Defining:

$$\Xi(t) = \Xi_S(t) + \Xi_F(t), U(t) = U_S(t) + U_F(t) \tag{3.2}$$

The slow model is:

$$\begin{aligned} \dot{\Psi}(t) =& A_S\Psi(t) + B_S U_S(t) \\ \Xi_S(t) =& C_S\Psi(t) + D_S U_S(t) \end{aligned} \tag{3.3}$$

while the fast model is:

$$\dot{\Xi}_F(t) = A_F\Xi_F(t) + B_F U_F(t) \tag{3.4}$$

where $\Xi(t)$ is a vector of kinetic variables, comprising the slow Ξ_S and fast Ξ_F components. Likewise, $U(t)$ is a vector of actuated powers with the slow part $U_S(t)$ and fast part $U_F(t)$.

The control of ι-profile motivates us to model the ι-profile dynamics. $\iota(\rho,t)$ is defined as

$$\iota(\rho,t) = -\frac{d\Psi(\rho,t)}{d\Phi(\rho,t)} = -\frac{\partial\Psi(\rho,t)}{\partial\rho}\frac{\partial\rho}{\partial\Phi(\rho,t)} = -\frac{\pi}{\Phi_{max}(t)}\left(\frac{1}{\rho}\frac{\partial\Psi(\rho,t)}{\partial\rho}\right) \tag{3.5}$$

Linearizing $\iota(\rho,t)$ around a reference profile $\iota_{ref}(\rho)$, projecting $\iota(\rho,t)$ on the cubic basis functions, we then obtain

$$\tilde{\iota}(t) = C_\iota\Psi(t), \quad \tilde{\iota}(t) = \iota(t) - \bar{\iota} \tag{3.6}$$

where $\tilde{\iota}$ are a vector of the perturbed ι profile around a reference profile $\bar{\iota}$. C_ι is a constant coefficient matrix by assuming the constant Φ_{max}, which is satisfied when the plasma shape parameters and the toroidal magnetic fields remain constant. Combining the equations (3.2), (3.3), (3.4) and (3.6), we derive the two-time-scale plasma response model that describes the ι-profile and kinetic parameter dynamics in a structural form.

In this work, the objective is to acquire the response of ι and β_p to actuated powers from the ICRH and LHCD systems for an H-mode EAST plasma at the flat-top phase, in which

ι is a vector evolving only at the magnetic timescale, uniformly distributed in 10 points, i.e. $x = 0, 0.1, 0.2, ..., 0.9$, while β_p is a scalar evolving both at the magnetic and kinetic timescales. Specifically, the model for ι and β_p is given as follows. The slow model is:

$$\begin{bmatrix} \dot{\Psi}_0(t) \\ \dot{\Psi}_1(t) \\ ... \\ \dot{\Psi}_{N-1}(t) \end{bmatrix} = A_\Psi \begin{bmatrix} \Psi_0(t) \\ \Psi_1(t) \\ ... \\ \Psi_{N-1}(t) \end{bmatrix} + B_\Psi \begin{bmatrix} U_{S,IC}(t) \\ U_{S,LH}(t) \end{bmatrix}, N = 10 \tag{3.7}$$

$$\begin{bmatrix} \iota_0(t) \\ \iota_1(t) \\ ... \\ \iota_{N-1}(t) \\ \beta_{p,S}(t) \end{bmatrix} = \begin{bmatrix} C_\iota \\ C_{\beta_{p,S}} \end{bmatrix} \begin{bmatrix} \Psi_0(t) \\ \Psi_1(t) \\ ... \\ \Psi_{N-1}(t) \end{bmatrix} + \begin{bmatrix} D_\iota \\ D_{\beta_{p,S}} \end{bmatrix} \begin{bmatrix} U_{S,IC} \\ U_{S,LH} \end{bmatrix} \tag{3.8}$$

while the fast model is:

$$\dot{\beta}_{p,F}(t) = A_{\beta_p,F}\beta_{p,F}(t) + B_{\beta_{p,F}} \begin{bmatrix} U_{F,IC} \\ U_{F,LH} \end{bmatrix} \tag{3.9}$$

and the controlled input is decomposed as:

$$\begin{bmatrix} U_{IC} \\ U_{LH} \end{bmatrix} = \begin{bmatrix} U_{S,IC} \\ U_{S,LH} \end{bmatrix} + \begin{bmatrix} U_{F,IC} \\ U_{F,LH} \end{bmatrix} \tag{3.10}$$

3.1.2 Control design

In this section, we present the robust feedback design using the two-time-scale model. First we describe the overall control scheme. Then details of the feedback synthesis are illustrated, including the control-oriented model formulation, local controllers design, the control decoupling and some remarks on controller tunings. Subsequently, we introduce beneficial control implementation techniques to guarantee the performance and robustness of the proposed controller in nonlinear closed-loop simulations and real-time tokamak plasma experiments.

In order to design a robust feedback controller that possesses sufficient freedom, available for control of ι and β_p both separately and simultaneously (with multi-function), feedback controllers with different control objectives are synthesized separately and then integrated for composite control. As depicted in Fig. 3.1, the controller is divided into two components: feedforward and feedback. The feedforward component is a simple module involving constant H&CD powers at the plasma equilibrium around which the model is linearized, and a low-pass filter with two time constants for β_p and ι respectively, to make the reference trajectories smooth. The feedback component consists of a low-pass filter, three local controllers and a decoupling module. The low-pass filter in the feedback component, with a time constant between kinetic and magnetic timescales, is designed to split the β_p estimation into the fast and slow components such that the fast one is controlled by the fast β_p controller in the kinetic timescale, while the slow one is controlled by the slow β_p controller in the magnetic timescale.

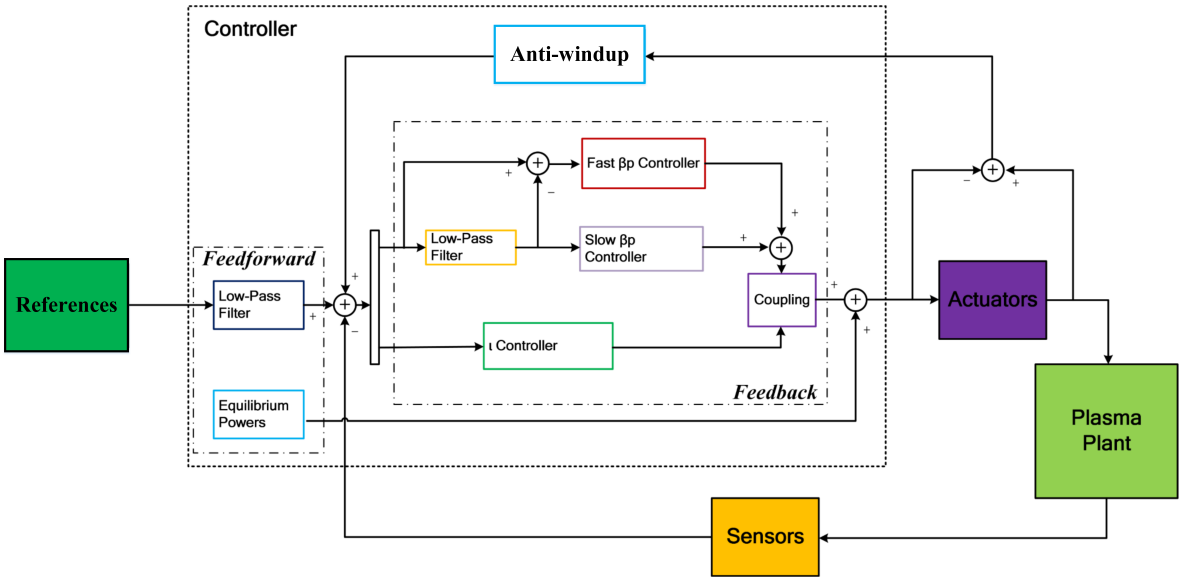

Figure 3.1: Feedback-feedforward control scheme for ι and β_p using timescales separation.

The ι controller is designed separately using the slow model for ι. The decoupling module is employed to formulate the simultaneous control of ι and β_p. The control conditioning module is involved to attenuate the negative effects from moderate actuation time delays and power saturations [Skogestad and Postlethwaite, 2007, Hanus et al., 1987].

3.1.2.1 Feedback synthesis

The feedback control objective is to minimize tracking errors from any reference inputs, attenuate the effects from system disturbances as well as involve minimum control efforts. The definition of gain for a transfer function matrix (or in terms of a state-space representation) is given by its singular values [Skogestad and Postlethwaite, 2007]. By shaping the singular values of appropriately specified transfer function matrices, the closed-loop control performance can therefore be guaranteed. As shown in Fig. 3.2(a), the plant G and the controller K interconnection is driven by the reference inputs r, output disturbances d and measurement noise n. The vector y denotes the controlled variables while u represents the controlled input. The sensitivity function is then expressed as $S = (I + GK)^{-1}$, which maps the control error e from y, r, d. The transfer function KS describes the mapping from y, r, d to u. Shaping the maximum singular value of S and KS in the frequency domain can then be transformed into minimizing the $\mathcal{H}_\infty$ norm of the integrated transfer function matrix $\begin{bmatrix} W_S S & W_{KS} KS \end{bmatrix}$, where W_S and W_{KS} are appropriately designed weighting functions for S and KS, respectively. Therefore, the feedback control synthesis problem is formulated as an $\mathcal{H}_\infty$ norm optimization problem, which is easily solved by using LMIs.

Solving the $\mathcal{H}_\infty$ norm optimization problem using LMIs We consider a general state-space model $G = (A_0, B_0, C_0, D_0)$. As shown in Fig. 3.2(b), the weighting functions $W_S =$

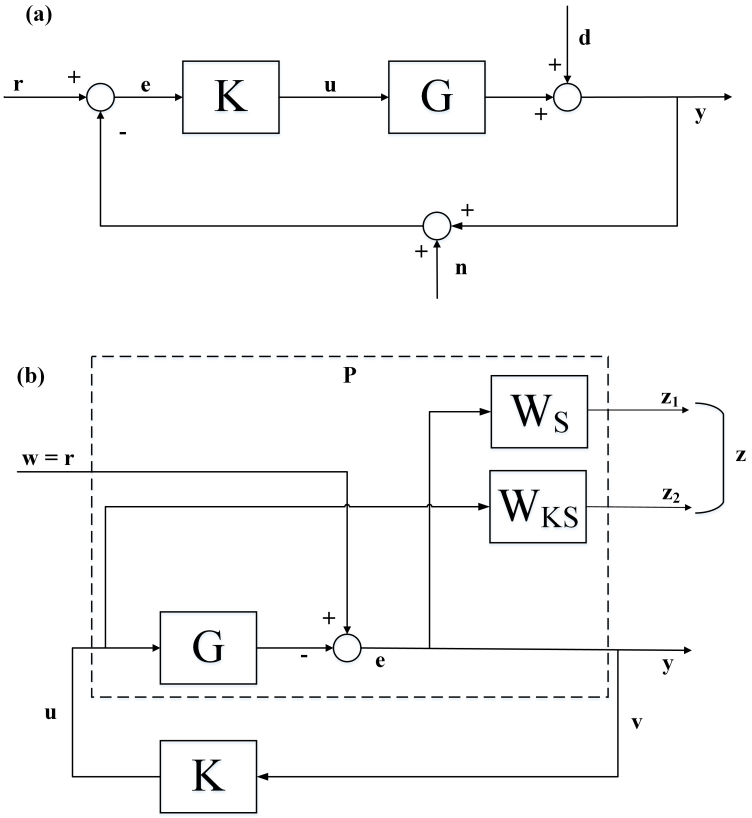

Figure 3.2: Schematic of the $\mathcal{H}_\infty$ norm feedback control formulation.

$(A_{\mathrm{S}}, B_{\mathrm{S}}, C_{\mathrm{S}}, D_{\mathrm{S}})$ and $W_{KS} = (A_{\mathrm{KS}}, B_{\mathrm{KS}}, C_{\mathrm{KS}}, D_{\mathrm{KS}})$ are respectively interconnected to the feedback control error e and the controlled input u with the combined output as z. The controller is realized as $K = (A_c, B_c, C_c, D_c)$ with the input as y and the output as u. The reference inputs r, the output disturbances y and [?] noise n are combined in the vector w. We then augment the plant model G into a generalized LTI state-space form P as:

$$\begin{bmatrix} \dot{x} \\ \hline z \\ y \end{bmatrix} = \left[\begin{array}{c|cc} A & B_1 & B_2 \\ \hline C_1 & D_{11} & D_{12} \\ C_2 & D_{21} & D_{22} \end{array}\right] \begin{bmatrix} x \\ \hline w \\ u \end{bmatrix} \tag{3.11}$$

where

$$A = \begin{bmatrix} A_0 & 0 & 0 \\ -B_{\mathrm{S}}C_0 & A_{\mathrm{S}} & 0 \\ 0 & 0 & A_{\mathrm{KS}} \end{bmatrix}, B_1 = \begin{bmatrix} 0 \\ B_{\mathrm{S}} \\ 0 \end{bmatrix}, B_2 = \begin{bmatrix} B_0 \\ -B_{\mathrm{S}}D_0 \\ B_{\mathrm{KS}} \end{bmatrix}, C_1 = \begin{bmatrix} -D_{\mathrm{S}}C_0 & C_{\mathrm{S}} & 0 \\ 0 & 0 & C_{\mathrm{KS}} \end{bmatrix}$$

$$C_2 = \begin{bmatrix} C_0 & 0 & 0 \end{bmatrix}, D_{11} = \begin{bmatrix} D_{\mathrm{S}} \\ 0 \end{bmatrix}, D_{12} = \begin{bmatrix} -D_{\mathrm{S}}D_0 \\ D_{\mathrm{KS}} \end{bmatrix}, D_{21} = 0, D_{22} = D_0$$

and x is the state vector of the plant G plus the state vector of the weighting functions W_S and W_{KS}. We assume that $x \in X \subset \mathbb{R}^n$, $z \in Z \subset \mathbb{R}^{n_z}, y \in Y \subset \mathbb{R}^{n_y}, w \in W \subset \mathbb{R}^{n_w}$ and $u \in U \subset \mathbb{R}^{n_u}$. In order to synthesize the robust feedback controller K for the plant G, the following theorem is applied.

Theorem 2. *(Scherer et al., 1997 [Scherer et al., 1997]). A dynamical output feedback controller $K : (A_c, B_c, C_c, D_c)$ with n_u outputs and n_y inputs that solves the $\mathcal{H}_\infty$ norm problem is obtained by solving the following LMIs in $(X, Y, \tilde{A}, \tilde{B}, \tilde{C}, \tilde{D})$ while minimizing γ:*

$$\begin{bmatrix} M_{11} & (*)^T & (*)^T & (*)^T \\ M_{21} & M_{22} & (*)^T & (*)^T \\ M_{31} & M_{32} & M_{33} & (*)^T \\ M_{41} & M_{42} & M_{43} & M_{44} \end{bmatrix} < 0$$
$$\begin{bmatrix} X & I_n \\ I_n & Y \end{bmatrix} > 0 \tag{3.12}$$

where

$$\begin{aligned} M_{11} =& AX + XA^T + B_2\tilde{C} + \tilde{C}^T B_2^T \\ M_{21} =& \tilde{A} + A^T + C_2^T \tilde{D}^T B_2^T \\ M_{22} =& YA + A^T Y + \tilde{B}C_2 + C_2^T \tilde{B}^T \\ M_{31} =& B_1^T + D_{21}^T \tilde{D}^T B_2^T \\ M_{32} =& B_1^T Y + D_{21}^T \tilde{B}^T; \\ M_{33} =& -\gamma I_{n_u} \\ M_{41} =& C_1 X + D_{12}\tilde{C} \\ M_{42} =& C_1 + D_{12}\tilde{D}C_2 \\ M_{43} =& D_{11} + D_{12}\tilde{D}D_{21} \\ M_{44} =& -\gamma I_{n_y} \end{aligned}$$

Then, the dynamical feedback controller K is given in the state space form with matrice coefficients:

$$\begin{aligned} D_c =& \tilde{D} \\ C_c =& (\tilde{C} - D_c C_2 X) M^{-T} \\ B_c =& N^{-1}(\tilde{B} - Y B_2 D_c) \\ A_c =& N^{-1}(\tilde{A} - YAX - YB_2 D_c C_2 X \\ & - NB_c C_2 X - YB_2 C_c M^T) M^{-T} \end{aligned} \tag{3.13}$$

where M and N are such that $MN^T = I_n - XY$.

In order to apply the above theorem to solving the $\mathcal{H}_\infty$ norm optimization problem and synthesize a robust feedback controller that satisfies the feedback control objective, the two-time-scale model derived in Section 2, i.e., equations (3.7)-(3.10), is reformulated as three

sub-models which are expressed in the state-space form as:

$$
\begin{aligned}
G_{\beta_{p,F}} &= \left[\begin{array}{c|c} A_{\beta_p,F} & B_{\beta_{p,F}} \\ \hline 1 & 0 \end{array}\right] \\
G_{\beta_{p,S}} &= \left[\begin{array}{c|c} A_{\Psi} & B_{\Psi} \\ \hline C_{\beta_{p,S}} & D_{\beta_{p,S}} \end{array}\right] \\
G_{\iota} &= \left[\begin{array}{c|c} A_{\Psi} & B_{\Psi} \\ \hline C_{\iota} & D_{\iota} \end{array}\right]
\end{aligned}
\tag{3.14}
$$

where $G_{\beta_{p,F}}$, $G_{\beta_{p,S}}$ and G_{ι} respectively represent the fast β_p model, the slow β_p model and the ι model. The three models are considered as three plants and are utilized for local controllers design.

Local controllers design In this section, we develop three local controllers for the fast and slow β_p control as well as ι control. The design procedure is illustrated in Fig. 3.3.

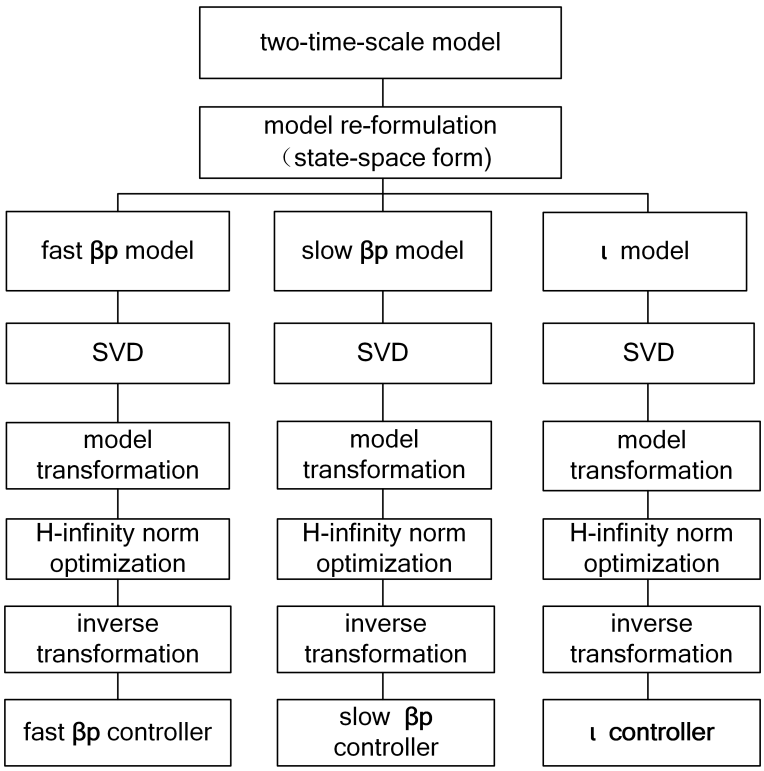

Figure 3.3: Schematic of the local controllers design.

The fast β_p controller is synthesized by shaping the mixed-sensitivity functions of the fast β_p model. Since the number of controlled variables is less than that of actuators, a singular value decomposition (SVD) technique is employed on the fast β_p model at a cut-off frequency $\omega_{c,\beta_{p,F}}$ to extract the principal output and input control channels, expressed as $G_1 = W_1 \Sigma_1 V_1^T$, where $G_1 = (\omega_{c,\beta_{p,F}} I - A_{\beta_p,F})^{-1} B_{\beta_p,F}$. The cut-off frequency $\omega_{c,\beta_{p,F}}$ represents the lower

closed-loop bandwidth for the fast β_p controller, which is set at 1 rad/s to extract the fast component of β_p. W_1 are the left singular vectors, V_1 are the right singular vectors, Σ_1 the diagonal matrix with singular values of G_1 on its diagonal. Assume the first left and right singular vectors as well as the first singular value to be $W_{1,1}$, $V_{1,1}$ and $\Sigma_{1,1}$, respectively, which represent the principal control channel for the fast β_p dynamics. Projecting $G_{\beta_{p,F}}$ onto the principal output and input control channels yields $G_{\beta_{p,F},1} = W_{1,1}G_{\beta_{p,F}}V_{1,1}\Sigma_{1,1}^{-1}$. Assume that $K_{\beta_{p,F},1}$ represents the transfer function of the controller for the plant model $G_{\beta_{p,F},1}$, and then the sensitivity function $S_{\beta_{p,F},1}$ is derived as $(1 + G_{\beta_{p,F},1}K_{\beta_{p,F},1})^{-1}$. Using the LMI optimization method, the controller $K_{\beta_{p,F},1}$ is synthesized by minimizing the $\mathcal{H}_\infty$ norm of $T_{zw,\beta_{p,F}} = \begin{bmatrix} W_{S,\beta_{p,F}}S_{\beta_{p,F},1} & W_{KS,\beta_{p,F}}K_{\beta_{p,F},1}S_{\beta_{p,F},1} \end{bmatrix}$, where $W_{S,\beta_{p,F}}$ and $W_{KS,\beta_{p,F}}$ are two weighting functions. The fast β_p controller is then obtained as $K_{\beta_F} = V_{1,1}\Sigma_{1,1}^{-1}K_{\beta_{p,F},1}W_{1,1}$.

The slow β_p controller is synthesized by shaping the mixed-sensitivity functions of the slow β_p model. Similarly, an SVD technique is performed on the slow β_p model at a cut-off frequency $\omega_{c,\beta_{p,S}} = 0$ rad/s to obtain the principal output and input control channels, expressed as $G_2 = W_2\Sigma_2V_2^T$, where $G_2 = -C_{\beta_{p,S}}A_\Psi^{-1}B_\Psi + C_{\beta_{p,S}}$. For the slow β_p controller, the lower closed-loop bandwidth is 0 rad/s, so $\omega_{c,\beta_{p,S}} = 0$ rad/s. Assume the first left and right singular vectors to be $W_{2,1}$ and $V_{2,1}$, which respectively represent the principal output and input control channel. The first singular value is $\Sigma_{2,1}$. Projecting $G_{\beta_{p,S}}$ onto the principal output and input control channels yields $G_{\beta_{p,S},1} = W_{2,1}G_{\beta_{p,S}}V_{2,1}\Sigma_{2,1}^{-1}$. Assume that $K_{\beta_{p,S},1}$ represents the transfer function of the controller for the plant $G_{\beta_{p,S},1}$, we then obtain the sensitivity function $S_{\beta_{p,S},1} = (I + G_{\beta_{p,S},1}K_{\beta_{p,S},1})^{-1}$. Using the LMI optimization method, the controller $K_{\beta_{p,S},1}$ is synthesized by minimizing the $\mathcal{H}_\infty$ norm of $T_{zw,\beta_{p,S}} = \begin{bmatrix} W_{S,\beta_{p,S}}S_{\beta_{p,S},1} & W_{KS,\beta_{p,S}}K_{\beta_{p,S},1}S_{\beta_{p,S},1} \end{bmatrix}$, where $W_{S,\beta_{p,S}}$ and $W_{KS,\beta_{p,S}}$ are two weighting functions. The slow β_p controller is then obtained as $K_{\beta_S} = V_{2,1}\Sigma_{2,1}^{-1}K_{\beta_{p,S},1}W_{2,1}$.

The ι controller is synthesized by shaping the mixed-sensitivity functions of the ι model. Similarly, an SVD technique is performed on the ι model at a cut-off frequency $\omega_{c,\iota} = 0$ rad/s to obtain the principal output and input control channels, expressed as $G_3 = W_3\Sigma_3V_3^T$, where $G_3 = -C_\iota A_\Psi^{-1}B_\Psi + C_\iota$. For the ι controller, the lower closed-loop bandwidth is 0 rad/s, so $\omega_{c,\iota} = 0$ rad/s. Assume that the first n left and right singular vectors to be $W_{3,n}$ and $V_{3,n}$, which represent the first n principal output and input control channels. The first n singular values are $\Sigma_{3,n}$. In our case, n is set at 1 because analysis shows that the second singular value is much smaller than the first one. Projecting G_ι onto the principal output and input control channels yields $G_{\iota,1} = W_{3,1}G_\iota V_{3,1}\Sigma_{3,1}^{-1}$. Assume that $K_{\iota,1}$ represents the transfer function of the controller for the plant $G_{\iota,1}$, we then obtain the sensitivity function $S_{\iota,1} = (I+G_{\iota,1}K_{\iota,1})^{-1}$. Using the LMI optimization method, the controller $K_{\iota,1}$ is synthesized by minimizing the $\mathcal{H}_\infty$ norm of $T_{zw,\iota} = \begin{bmatrix} W_{S,\iota}S_{\iota,1} & W_{KS,\iota}K_{\iota,1}S_{\iota,1} \end{bmatrix}$, where $W_{S,\iota}$ and $W_{KS,\iota}$ are two weighting functions. The ι controller is consequently obtained as $K_\iota = V_{3,1}\Sigma_{3,1}^{-1}K_{\iota,1}W_{3,1}$.

Combining the inputs for composite control In order to achieve the simultaneous control of ι and β_p, the outputs of the ι and β_p controllers should be combined to generate a set of actuated powers for the H&CD systems. Suppose that the output of the fast β_p controller, of the slow β_p controller and of the ι controller are $\vec{u}_{\beta_p,F}$, $\vec{u}_{\beta_p,S}$ and $\vec{u}_\iota$, respectively.

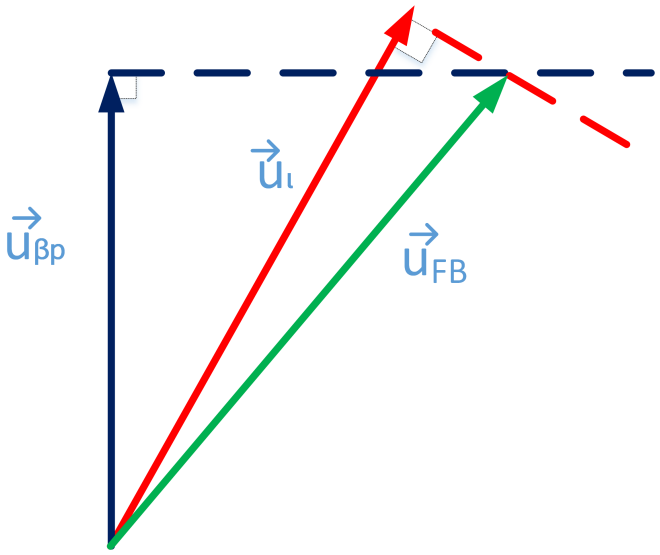

Figure 3.4: Geographic illustration

Denoting $\vec{u}_{\beta_p} = \vec{u}_{\beta_p,F} + \vec{u}_{\beta_p,S}$, the feedback controller output is expressed as:

$$\vec{u}_{FB} = (1 + \lambda_{\beta_p})\vec{u}_{\beta_p} + (1 + \lambda_\iota)\vec{u}_\iota \tag{3.15}$$

Here, λ_{β_p} and λ_ι are the coupling coefficients which ensure that the projection of $\vec{u}_{FB}$ onto the direction of $\vec{u}_{\beta_p}$ is the magnitude of $\vec{u}_{\beta_p}$ and meanwhile, the projection of $\vec{u}_{FB}$ onto the direction of $\vec{u}_\iota$ is the magnitude of $\vec{u}_\iota$. As shown in Fig. 3.4, the problem can be formulated as:

$$\vec{u}_{FB} \cdot \frac{\vec{u}_{\beta_p}}{\|\vec{u}_{\beta_p}\|} = \|\vec{u}_{\beta_p}\|, \vec{u}_{FB} \cdot \frac{\vec{u}_\iota}{\|\vec{u}_\iota\|} = \|\vec{u}_\iota\| \tag{3.16}$$

Combining equations (3.15) and (3.16), we can derive:

$$\begin{aligned} \lambda_{\beta_p}\|\vec{u}_{\beta_p}\|^2 + \lambda_\iota \vec{u}_\iota \cdot \vec{u}_{\beta_p} &= -\vec{u}_\iota \cdot \vec{u}_{\beta_p} \\ \lambda_\iota\|\vec{u}_\iota\|^2 + \lambda_{\beta_p}\vec{u}_{\beta_p} \cdot \vec{u}_\iota &= -\vec{u}_{\beta_p} \cdot \vec{u}_\iota \end{aligned} \tag{3.17}$$

Solving equations (3.17), we obtain the coupling coefficients λ_{β_p} and λ_ι as:

$$\lambda_{\beta_p} = \frac{\left(\frac{\vec{u}_\iota \cdot \vec{u}_{\beta_p}}{\|\vec{u}_\iota\|\|\vec{u}_{\beta_p}\|}\right)^2 - \frac{\vec{u}_\iota \cdot \vec{u}_{\beta_p}}{\|\vec{u}_{\beta_p}\|^2}}{1 - \left(\frac{\vec{u}_\iota \cdot \vec{u}_{\beta_p}}{\|\vec{u}_\iota\|\|\vec{u}_{\beta_p}\|}\right)^2}, \lambda_\iota = \frac{\left(\frac{\vec{u}_{\beta_p} \cdot \vec{u}_\iota}{\|\vec{u}_{\beta_p}\|\|\vec{u}_\iota\|}\right)^2 - \frac{\vec{u}_{\beta_p} \cdot \vec{u}_\iota}{\|\vec{u}_\iota\|^2}}{1 - \left(\frac{\vec{u}_{\beta_p} \cdot \vec{u}_\iota}{\|\vec{u}_{\beta_p}\|\|\vec{u}_\iota\|}\right)^2}$$

We consider the constant feedforward $\vec{u}_{FF}$ to be the steady-state powers for the plasma equilibrium around which the model is linearized. The total actuated powers for the H&CD systems are then obtained as $U = \vec{u}_{FB} + \vec{u}_{FF}$.

Table 3.1: Weighting functions for S/KS.

Option	W_S	W_{KS}
I	$\frac{\frac{s}{M}+\omega_B}{s+\omega_B A}$	1
II	$\frac{(\frac{s}{\sqrt{M_p}}+\omega_p)^2}{(s+\omega_p\sqrt{A_p})^2}$	$\frac{(\frac{s}{\sqrt{M_u}}+\omega_u)^2}{(s+\omega_u\sqrt{A_u})^2}$

Remarks on the weighting functions In this study, two options of the weighting functions W_S/W_{KS} [Skogestad and Postlethwaite, 2007, Barton et al., 2015a] are attempted to shape the $\mathcal{H}_\infty$ norm of the mixed sensitivity function S/KS, as listed in Table 3.1.

In option I, the sensitivity function S is shaped by the weighting function $W_S = \frac{\frac{s}{M}+\omega_B}{s+\omega_B A}$. We select $A << 1$ to ensure the approximate integral action with $S(0) \approx 0$ such that the tracking error can be made small and the output disturbance can be attenuated. We keep M fixed at 2 for all the controlled outputs. The desired closed-loop bandwidth ω_B are tuned by trials and errors, which is directly related to the transient performance. A large value of ω_B yields a faster response for the controlled output, but it may result in larger overshoots.

In option II, the mixed-sensitivity functions S and KS are respectively shaped by $\frac{(\frac{s}{\sqrt{M_p}}+\omega_p)^2}{(s+\omega_p\sqrt{A_p})^2}$ and $\frac{(\frac{s}{\sqrt{M_u}}+\omega_u)^2}{(s+\omega_u\sqrt{A_u})^2}$, implying more tuning parameters. The parameters M_p and M_u are associated with the high frequency behaviour, which are fixed at 2. The parameters A_p and A_u are related to the low frequency behaviour and we select them to be small for good tracking and disturbance rejection. The parameters ω_p and ω_u determine the closed-loop control bandwidth [Barton et al., 2012], which are tuned by trials and errors.

3.1.2.2 Control implementation

Setpoints selection The setpoints selection is essential for the situation where the number of outputs is larger than that of inputs, because if the setpoints are specified out of the attractive control region they should never be achieved even with the maximum/minimum allowed actuations. In this study, the ι and β_p sepoints are determined semi-empirically by nonlinear closed-loop METIS simulations such that all the setpoints are located in the attractive control region.

Control discretization and model reduction Using the $\mathcal{H}_\infty$ norm optimization approach we consequently derive a set of continuous dynamical controllers with different orders. The real-time application to plasma control requires the discretisation of these controllers. Accounting for the constraints of the equilibrium reconstruction and energy confinement time on EAST, we discretize the controller with the sampling time $T_s = 20$ ms.

For simplicity, one can further perform model reduction on these discrete controllers to remove insignificant controller dynamics and obtain their minimal realizations [Skogestad and

Postlethwaite, 2007]. After model reduction, the order of the fast β_p controller remains at 2 by using the weighting functions in option I. The initial order of the fast β_p controller (2) is equal to the sum of the order of the fast β_p model (1) and of the weighting functions (1). The slow β_p controller order substantially decreases for example by using the weighting functions in option II, from 14 to 8. The initial order of the slow β_p controller (14) is the sum of the order of the slow β_p model (10) and of the weighting functions (2+2). The order of ι controller drops from 14 to 5. The initial order of the ι controller (14) is the sum of the order of the ι model (10) and of the weighting functions $(2+2)$.

Feedforward and control initialization The control initialization is important for good control performance, because if it is not well configured, the actuations are probably saturated which may cause large overshoots, even plasma disruptions. To avoid the possibilities of potential plasma disruptions arising from improper control initialization, a feedforward in terms of discrete low-pass filters for ι and β_p is designed. The characteristic time for the ι and β_p pre-filters are respectively of the order of the resistive diffusion time $\tau_{\text{mag}} = 0.4$ s and the energy confinement time $\tau_{\text{kin}} = 0.04$ s. The feedforward trajectories are then obtained as follows in the discrete state space form:

$$\begin{aligned}\begin{bmatrix} x_\iota[k+1] \\ x_{\beta_p}[k+1] \end{bmatrix} &= \begin{bmatrix} A_{f,\iota} & 0 \\ 0 & A_{f,\beta_p} \end{bmatrix} \begin{bmatrix} x_\iota[k] \\ x_{\beta_p}[k] \end{bmatrix} + \begin{bmatrix} B_{f,\iota} & 0 \\ 0 & B_{f,\beta_p} \end{bmatrix} \begin{bmatrix} \iota_{\text{ref}}[k] \\ \beta_{\text{p,ref}}[k] \end{bmatrix} \\ \begin{bmatrix} \iota_m[k] \\ \beta_{p,m}[k] \end{bmatrix} &= \begin{bmatrix} C_{f,\iota} & 0 \\ 0 & C_{f,\beta_p} \end{bmatrix} \begin{bmatrix} x_\iota[k] \\ x_{\beta_p}[k] \end{bmatrix}\end{aligned} \tag{3.18}$$

where $\iota_{\text{ref}}[k]$ and $\beta_{\text{p,ref}}[k]$ are respectively the setpoints selected in section (3.3.1) for ι and β_p at time k, $x_\iota[k]$ and $x_{\beta_p}[k]$ the filter states at time k, while $\iota_m[k]$ and $\beta_{p,m}[k]$ respectively denote the ι and β_p reference trajectories at time k for the feedback controller to track.

To avoid undesirable bump and power saturations due to control switching [Hanus et al., 1987], the initial states of the ι and β_p filters are then computed as:

$$\begin{bmatrix} x_\iota[0] \\ x_{\beta_p}[0] \end{bmatrix} = \begin{bmatrix} C_{f,\iota} & 0 \\ 0 & C_{f,\beta_p} \end{bmatrix}^{-1} \begin{bmatrix} \iota_{\text{mea}}[0] \\ \beta_{\text{p,mea}}[0] \end{bmatrix} \tag{3.19}$$

Here we assume that k = 0 represents the starting time when the feedback controller is switched on. $\iota_{\text{mea}}[0]$ and $\beta_{\text{p,mea}}[0]$ indicate the initial measured/estimated ι and β_p respectively, which are equal to their corresponding initial setpoints $\iota_{\text{ref}}[0]$ and $\beta_{\text{p,ref}}[0]$.

Actuator dynamics In order to mimick the experimental conditions for auxiliary H&CD power actuators on EAST, actuation dynamics are considered to evaluate the performance and robustness of the feedback control algorithm. The actuation dynamics for the ICRH and LHCD are modelled separately as a first-order transfer function with time-delay:

$$G_i(s) = \frac{k_i}{\tau_i s + 1} e^{-\theta_i s}, i \in \{\text{ICRH}, \text{LHCD}\} \tag{3.20}$$

Table 3.2: ICRH and LHCD power actuator model parameters.

Actuators	τ_i [ms]	θ_i [ms]	S_m [MW]	S_r [MW$\cdot$ s $^{-1}$]
ICRH	1	[0, 60]	[0, 1.5]	[-8, 8]
LHCD	1	[0, 60]	[0, 3]	[-8, 8]

where i is an indicator for power actuators, k_i the i-th steady-state gain which is fixed at 1, τ_i the i-th characteristic time, θ_i the i-th time delay and $G_i(s)$ the transfer function for the i-th power actuator. A saturation module that accounts for both the magnitude and rate limits of ICRH and LHCD is considered. Table 3.2 lists the related parameter values, where S_m and S_r respectively denote the magnitude and rate limits allowed by the actuators.

Control conditioning and anti-windup compensation Since there is a series of dynamics in the actuated power systems, the actual delivered powers are never totally equal to the control commands requested by the controller at each time slice. However, the controller cannot automatically identify whether the commands are followed or not unless an extra closed loop is involved. In some cases, for instance, due to power saturations and time delays, the states of the controller may wind up because the plant does not respond accordingly, so that the behaviour of the system will deteriorate dramatically. To handle this problem, an anti-windup compensator is designed to keep the controller well-behaved and avoid undesirable oscillations when saturations and moderate time delays are present, which is expressed in a discrete state-space form:

$$\begin{bmatrix} x_{\mathrm{aw}}[k+1] \\ y_{\mathrm{aw,d}}[k] \end{bmatrix} = \begin{cases} \begin{bmatrix} A_{\mathrm{aw}} & B_{\mathrm{aw}} \\ C_{\mathrm{aw}} & D_{\mathrm{aw}} \end{bmatrix} \begin{bmatrix} x_{\mathrm{aw}}[k] \\ \delta u[k] \end{bmatrix} & , \text{if} \quad \delta u[k] \neq 0 \\ \begin{bmatrix} A_{\mathrm{exp}} \\ C_{\mathrm{exp}} \end{bmatrix} x_{\mathrm{aw}}[k] & , \text{if} \quad \delta u[k] = 0 \end{cases} \tag{3.21}$$

Here, $\delta u = u_a[k] - u_c[k]$, $u_a[k]$ denotes the measurements of the actuated powers and $u_c[k]$ denotes the control outputs of the controller. The system matrices $(A_{\mathrm{aw}}, B_{\mathrm{aw}}, C_{\mathrm{aw}}, D_{\mathrm{aw}})$ of the anti-windup compensator are chosen identical to the discrete form of the system matrices in the two-time-scale plasma model. $(A_{\mathrm{exp}}, C_{\mathrm{exp}})$ is a discrete state-space realization of the asymptotically stable equation $\dot{x}_{\mathrm{aw}}(t) = \lambda x_{\mathrm{aw}}(t)$, and λ is set to be -50. $y_{\mathrm{aw,d}}[k]$ is the modified reference arising from the actuation dynamics to be added to the reference trajectories for controller states conditioning in real-time. This conditioning technique can be combined with the fast and slow β_{p} controller to cope with up to 60 ms of time delays plus power saturations, which will be demonstrated in Section 4.2.

Real-time capability Testing on a computer with Intel(R) Xeon (R) CPU X5660@2.8GHz processors shows that the average computational time for one control cycle is 40.6 μs (less than the 20 ms sampling time). Considering that the current implementation of the control algorithms is based on the MATLAB/Simulink framework, the computation time for each control cycle should be further reduced when the algorithm is realized by the C/C++ code

and implemented into the EAST PCS using the embedded MATLAB coder (EMC) toolbox. Therefore, we conclude that this algorithm meets the real-time constraints.

Performance indexes The feedback control performance is evaluated based on a set of indexes that can be used to represent the control performance in different aspects. The first index is the rise time, which is defined as the total time required for the response to rise/fall from 10 % (90 %) to 90 % (10 %) of its regulation height in a specific time window. Specifically, we assume that there are N time windows for the regulation of ι and β_p in a controlled scenario, and the starting time for the ι and β_p setpoint transition remain the same. In a given time window n, the rise time of ι at $x = 0, 0.1, 0.2, ..., 0.9$ ($t_{r,\iota}(n,x)$) and β_p ($t_{r,\beta_p}(n)$) read as:

$$\begin{aligned} t_{r,\iota}(n,x) =& t(\iota_a^1(n,x)) - t(\iota_a^0(n,x)) \\ t_{r,\beta_p}(n) =& t(\beta_{p,a}^1(n)) - t(\beta_{p,a}^0(n)) \end{aligned} \tag{3.22}$$

where

$$\begin{bmatrix} \iota_a^1(n,x) & \beta_{p,a}^1(n) \\ \iota_a^0(n,x) & \beta_{p,a}^0(n) \end{bmatrix} = \begin{bmatrix} 0.1 & 0.9 \\ 0.9 & 0.1 \end{bmatrix} \begin{bmatrix} \iota_0(n,x) & \beta_{p,0}(n) \\ \iota_1(n,x) & \beta_{p,1}(n) \end{bmatrix}$$
$$n = 1, 2, .., N, \quad x = 0, 0.1, 0.2, ..., 0.9$$

Here, $\iota_0(n,x)$ and $\beta_{p,0}(n)$ are the starting setpoints of $\iota(x)$ and β_p in the time window n respectively, while $\iota_1(n,x)$ and $\beta_{p,1}(n)$ indicate the final setpoints. Likewise, $\iota_a^0(n,x)$ and $\beta_{p,a}^0(n)$ are the estimated/measured values at the 10 % of the regulation heights in a given time window n, while $\iota_a^1(n,x)$ and $\beta_{p,a}^1(n)$ are those at the 90 % of the regulation heights.

Once the rise times for ι and β_p in a time window are obtained, we can then calculate the averaged values. For ι, averaging the rise time $t_{r,\iota}(n,x)$ on n leads to the averaged rise time at each point over all the time windows, i.e. $\langle t_{r,\iota}(n,x)\rangle_n$, meanwhile averaging $t_{r,\iota}(n,x)$ on x results in the integrated rise time of ι points in different time windows, i.e. $\langle t_{r,\iota}(n,x)\rangle_x$. $\langle t_{r,\iota}\rangle$ and $\langle t_{r,\beta_p}\rangle$ are two scalars which show the comprehensive response time for ι and β_p respectively. Note that $W(x)$ is the normalized weighting matrix which represents the importance of each point. The averages are computed as:

$$\langle t_{r,\iota}\rangle = \frac{1}{10N}\sum_{x=0}^{0.9}\sum_{n=1}^{N} W(x)t_{r,\iota}(n,x), \langle t_{r,\beta_p}\rangle = \frac{1}{N}\sum_{n=1}^{N} t_{r,\beta_p}(n)$$
$$\langle t_{r,\iota}(n,x)\rangle_n = \frac{1}{N}\sum_{1}^{N} t_{r,\iota}(n,x), \langle t_{r,\iota}(n,x)\rangle_x = \frac{1}{10}\sum_{x=0}^{0.9} W(x)t_{r,\iota}(n,x)$$

The second performance index is the overshoot, defined as the maximum amount a system overshoots its final value divided by its final value, often expressed in percentage. In tokamak plasma operation, large overshoots of ι and β_p can result in undesirable MHD and kinetic instabilities, thus it is good to quantify this index to reflect the control performance. For our

problem, since ι and β_p are not the same kind of physical quantities, we define $l_{os,\iota}(n,x)$ and $l_{os,\beta_p}(n)$ respectively as the overshoot of $\iota(x)$ and β_p at a given time window n:

$$\begin{aligned} l_{os,\iota}(n,x) =& \frac{\iota_{max}(n,x) - \iota_{ss}(n,x)}{\iota_{ss}(n,x)} \times 100\% \\ l_{os,\beta_p}(n) =& \frac{\beta_{p,max}(n) - \beta_{p,ss}(n)}{\beta_{p,ss}(n)} \times 100\% \\ n =& 1,2,..,N, \quad x = 0, 0.1, 0.2, ..., 0.9 \end{aligned} \tag{3.23}$$

where $\iota_{max}(n,x)$ and $\beta_{p,max}(n)$ are the maximum values exceeding their corresponding steady state values $\iota_{ss}(n,x)$ and $\beta_{p,ss}(n)$, respectively.

With the similar technique, we can derive two scalars, i.e., $\langle l_{os,\iota} \rangle$ and $\langle l_{os,\beta_p} \rangle$ for the comprehensive evaluation of ι and β_p overshoots in the whole controlled scenario. Two partial averaged values $\langle l_{os,\iota}(n,x) \rangle_n$ and $\langle l_{os,\iota}(n,x) \rangle_x$ represent the overshoots of ι in two different aspects. The weighting matrix $W(x)$ is the same as the one for the rise time calculation.

$$\begin{aligned} \langle l_{os,\iota} \rangle =& \frac{1}{10N} \sum_{x=0}^{0.9} W(x) \sum_{n=1}^{N} l_{os,\iota}(n,x), \langle l_{os,\beta_p} \rangle = \frac{1}{N} \sum_{n=1}^{N} l_{os,\beta_p}(n) \\ \langle l_{os,\iota}(n,x) \rangle_n =& \frac{1}{N} \sum_{n=1}^{N} l_{os,\iota}(n,x), \langle l_{os,\iota}(n,x) \rangle_x = \frac{1}{10} \sum_{x=0}^{0.9} W(x) l_{os,\iota}(n,x) \end{aligned}$$

The third performance index is the relative error index, which represents the relative error of the controlled output against its setpoint. For our problem, $J_\iota[k]$ and $J_{\beta_p}[k]$ are two time-variant relative error indexes for ι and β_p respectively. These two indexes are defined as:

$$\begin{aligned} J_\iota[k] =& \frac{\delta\iota^T[k] Q \delta\iota[k]}{\iota_r^T[k] Q \iota_r[k]}, \quad \delta\iota[k] = \iota[k] - \iota_r[k] \\ J_{\beta_p}[k] =& \frac{\delta\beta_p^T[k] \delta\beta_p[k]}{\beta_{p,r}^T[k] \beta_{p,r}[k]}, \quad \delta\beta_p[k] = \beta_p[k] - \beta_{p,r}[k] \end{aligned} \tag{3.24}$$

where Q is the weighting matrix for ι, $\delta\iota$ ($\delta\beta_p$) is the error between the estimation $\iota[k]$ ($\beta_p[k]$) and the setpoint $\iota_r[k]$ ($\beta_{p,r}[k]$). Averaging them can as well attain the overall relative error indexes for ι, i.e. $\langle J_\iota \rangle$ and β_p, i.e. $\langle J_{\beta_p} \rangle$, where K is the number of samplings in the whole controlled process.

$$\langle J_\iota \rangle = \frac{1}{K} \sum_{k=1}^{K} J_\iota[k], \quad \langle J_{\beta_p} \rangle = \frac{1}{K} \sum_{k=1}^{K} J_{\beta_p}[k]$$

We do not combine them by adding these two scalars for a comprehensive representation of the control performance because we note that they may evolve in different orders, and adding them may neglect important information about control performance.

3.1.3 Simulation results

In order to evaluate the control scheme proposed in the previous section, closed-loop simulations were carried out by coupling the controller with the METIS code, which is a nonlinear plasma simulator. The two-time-scale model is identified from 20 different METIS open loop simulations with random power modulations: the details of the system identification methodology can be found in [Moreau et al., 2008, Moreau et al., 2011, Moreau et al., 2015]. The reference scenario around which the model is identified is a steady-state, fully non-inductive single-null H-mode discharge in the EAST tokamak, i.e. shot #62946, with the toroidal magnetic field $B_T = 2.5$ T, the central electron density $n_{e0} \approx 3.5 \times 10^{19}$ m^{-3} and plasma current $I_p = 0.42$ MA. The discharge was obtained using LHCD (0.6 MW at 2.45 GHz and 2 MW at 4.6 GHz), 0.32 MW of ICRH at 33 MHz and 0.3 MW of ECRH at 140 GHz. The transition to H-mode occurred at 3.1 s with an H-mode enhancement factor $\mathrm{H}_{98}(y, 2) \sim 1.1$. The q-profile exhibited a small negative shear in the plasma core, with minimum q around 1.5 and $q_0 \sim 2$ on axis. The plasma profiles were retrieved from the EFIT magnetic equilibrium reconstructions available in real-time using magnetic and kinetic measurements, for instance, interfero-polarimetry data from the POINT diagnostics [Liu et al., 2016b, Liu et al., 2016a, Huang et al., 2017].

The initialization of the METIS code is preset to be consistent with shot #62946 at 3.1 s, including plasma current, shape, magnetic fluxes, kinetic profiles and actuated powers. The plasma transport model is described in detail in [Artaud et al., 2018] and was chosen consistent with the standard ITER-EIV H-mode scaling law [Cordey et al., 2005]. With this scaling law, an H-factor of 0.99 was used in METIS simulations to fit the measured plasma energy content. This H-factor can be varied in some simulations to study the effect of model perturbations. Some other fitting parameters were chosen in order to fit the temperature profiles measured in shot #62946 and then fixed for all simulations. The LHCD model is also described in [Artaud et al., 2018]. The lower hybrid power deposition profile is based on a probabilistic ad-hoc formulation which takes into account the limits of the wave propagation domain in space and parallel wave-index and the Landau absorption criterion as a function of local plasma temperature. With the chosen parameters, the LHCD was generally deposited off-axis, which could lead to reverse magnetic shear at high power, and to the formation of electron internal transport barriers in some cases. Plasma parameters such as plasma current, geometry, densities and effective charge numbers are assumed to be regulated by dedicated controllers. The sampling time is fixed to 20 ms. The LHCD power at 2.45 GHz and the ECRH power at 140 GHz are not considered as control actuators. They are always at their reference values in every simulation, 0.6 MW and 0.3 MW respectively, and since METIS allows for only one lower hybrid system, they are combined into a single heating system providing 0.9 MW with given power and current deposition profiles into the plasma at constant plasma current and density. The control actuators are the LHCD power at 4.6 GHz and the ICRH power at 33 MHz and their feedforward components are constant at 2 MW and 0.32 MW, respectively, as in the reference discharge. The time constants for β_p and ι prefilters are respectively 0.04 s and 0.4 s, whose initial states are respectively 1.0282 ($\beta_{p,0}$) and $[0.9200, 0.9032, 0.9745, 0.9901, 0.7892, 0.6195, 0.4602, 0.3383, 0.2496, 0.1866]$

($\iota_{i,0}, i = 0, 0.1, 0.2, ..., 0.9$) corresponding to the counterparts at 3.1 s in shot #62946. The time constant and initial state for the low-pass filter in the feedback component are 1 s and 0, respectively. The actuated powers are the 4.6 GHz LHCD spreading between 0 and 3 MW and the 33 MHz ICRH from 0 to 1.5 MW.

3.1.3.1 Tracking of q-profile and β_p

Separate control of β_p and the core ι profile The simplest control evaluation case is the nominal control of β_p, with the safety factor control relaxed as shown in Fig. 3.5. There are totally 6 setpoints which are required to be achieved, sequentially 1.5, 2, 3, 1.9, 2.3 and 2.8. It is obvious that the combination of fast β_p and slow β_p controllers is able to track β_p with good control performance, e.g. the averaged rise time $\langle t_{r,\beta_p} \rangle$ at 132 ms, very small overshoots ($\langle l_{os,\beta_p} \rangle = 3.2$ %) and negligible steady-state errors under the condition that the powers of ICRH and LHCD are not saturated. In each control phase, the averaged relative error for β_p, i.e. $\langle J_{\beta_p} \rangle$, initially increases due to the sudden change of its regulation point, and then decreases substantially to around 10^{-7}. This allowed extensive closed-loop simulations to be performed in a reasonable time despite the complexity of the METIS code, and also provided realistic simulations of the closed-loop experiments on EAST, in which the sampling time has to match the requirements of the real-time magnetic reconstruction. This sampling time is adequate for the slow β_p controller (the characteristic time of the slow model is τ_{mag} = 0.4s), but discrepencies between the (ideal) continuous dynamics and the discrete ones due to sampling may influence the fast control of β_p (the characteristic time of the fast model is τ_{kin} = 0.04s). Since the rise time $\langle t_{r,\beta_p} \rangle$ is around six times the sampling interval and 3.5 τ_E, this influence appears to be insignificant. Concerning the evolution of the ι values at different radii, we note that the plasma temperature increases when the ICRH power and β_p increases, which makes the LHCD deposition more off-axis and also drives more bootstrap current, thus leading to the increase of the core safety factor profile.

The second case is the nominal control of ι values at normalized radius x = 0, 0.1, 0.2, ..., 0.5 with the β_p feedback control relaxed. Three sets of setpoints were prescribed, with the first setpoint globally positive magnetic shear, the second one being weakly negatively sheared in the plasma core, and the third being strongly centrally negatively sheared. As shown in Fig. 3.6, the setpoints are achieved with the averaged rise time $\langle t_{r,\iota} \rangle = 607$ ms and the averaged overshoots $\langle l_{os,\beta_p} \rangle = 1.4$ %. In each control phase, the averaged relative error for ι, i.e. $\langle J_\iota \rangle$, initialy increases due to its limited control bandwidth, and then decreases exponentially to around 10^{-6}. Since the plasma pressure is not actively controlled, in other words, the fast and slow β_p controllers are not switched on, the β_p value remains at around 1.5 due to very small variations of the ICRH power. It indicates that, as expected, the LHCD system is more suitable for ι control than for β_p control, while the ICRH system is just in reverse. In addition, small variations of β_p indicate that the control of ι points in the plasma core via LHCD does not obviously impact the value of plasma pressure.

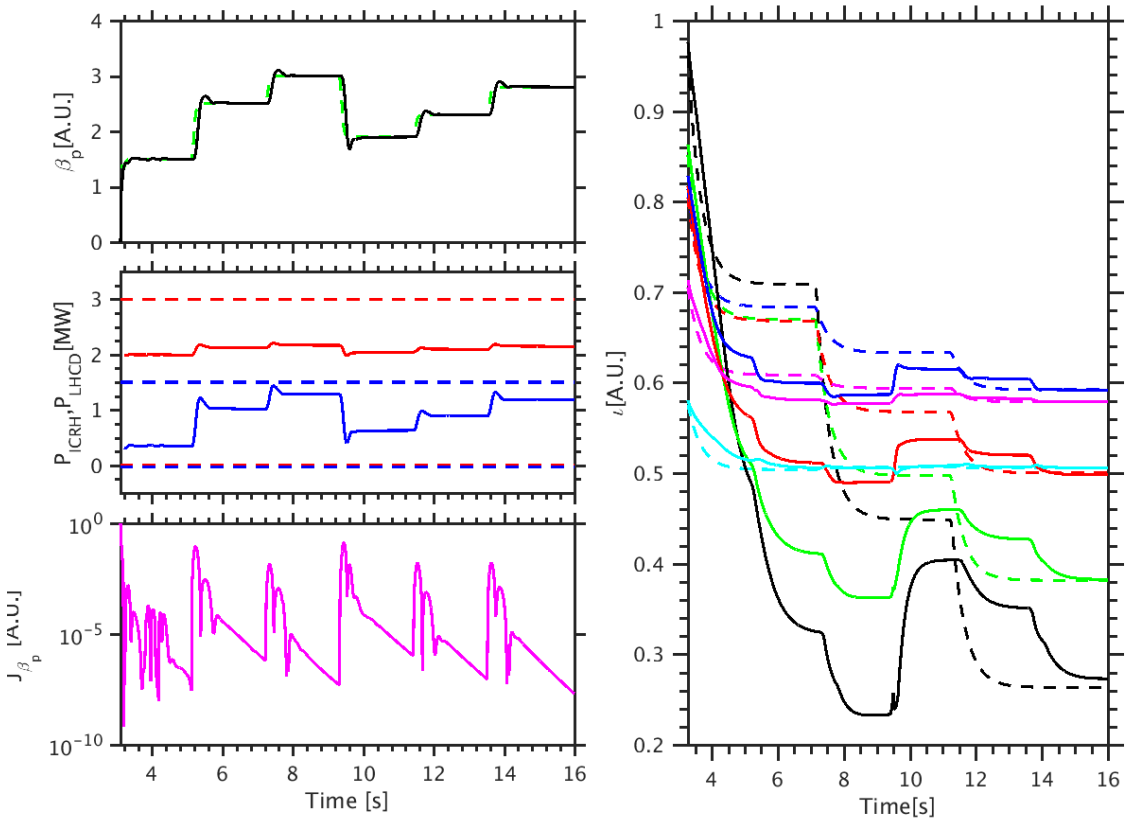

Figure 3.5: Tracking β_p. Left-top panel: time traces of β_p setpoints (green dashed) and evolutions (black) with β_p feedback control. Left-middle panel: time traces of actuated powers P_{ICRH} (blue) and P_{LHCD} (red), as well as the ICRH (blue dashed) and LHCD (red dashed) power limits. Left-bottom panel: time traces of the relative error index for β_p. Right panel: time traces of ι setpoints (dashed) and evolutions (solid) at x = 0 (black), 0.1 (green), 0.2 (red), 0.3 (blue), 0.4 (magenta), 0.5 (cyan) with ι control relaxed.

Simultaneous control of β_p and the core ι profile The nominal control of both ι and β_p is shown in Fig. 3.7. Three β_p setpoints, namely 2, 2.5 and 3 are prescribed, i.e. 2 in the time interval [3.1, 7.1] s, 2.5 in [7.2, 11.2] s and 3 in [11.3, 15.6] s. Likewise, three groups of setpoints for ι at 0, 0.1,..., 0.4 are specified, i.e. positive central magnetic shear between 3.1 s and 7.1 s, weakly central negative shear from 7.2 s to 11.2 s and strongly central negative shear in [11.3, 15.6] s. Clearly, all the targets are achieved using only the limited LHCD and ICRH powers, with the averaged rise time vector $(\langle t_{r,\beta_p}\rangle, \langle t_{r,\iota}\rangle)$ at (0.113, 1.11) s, the averaged overshoot vector $(\langle l_{os,\beta_p}\rangle, \langle l_{os,\iota}\rangle)$ at (1.44, 3.47) %. In each regulation window, J_ι evolves from 10^{-3} to 10^{-5} and J_{β_p} decreases from 10^{-2} to approximately 10^{-9}.

The corresponding evolutions of q-profile, the bootstrap current profile, electron and ion temperature profiles are depicted in Fig. 3.8. With the decrease of the central magnetic shear and the β_p increase, the bootstrap current was increased due to the increase of electron temperatures and their gradients and the LH-driven current was increased as well via actuating

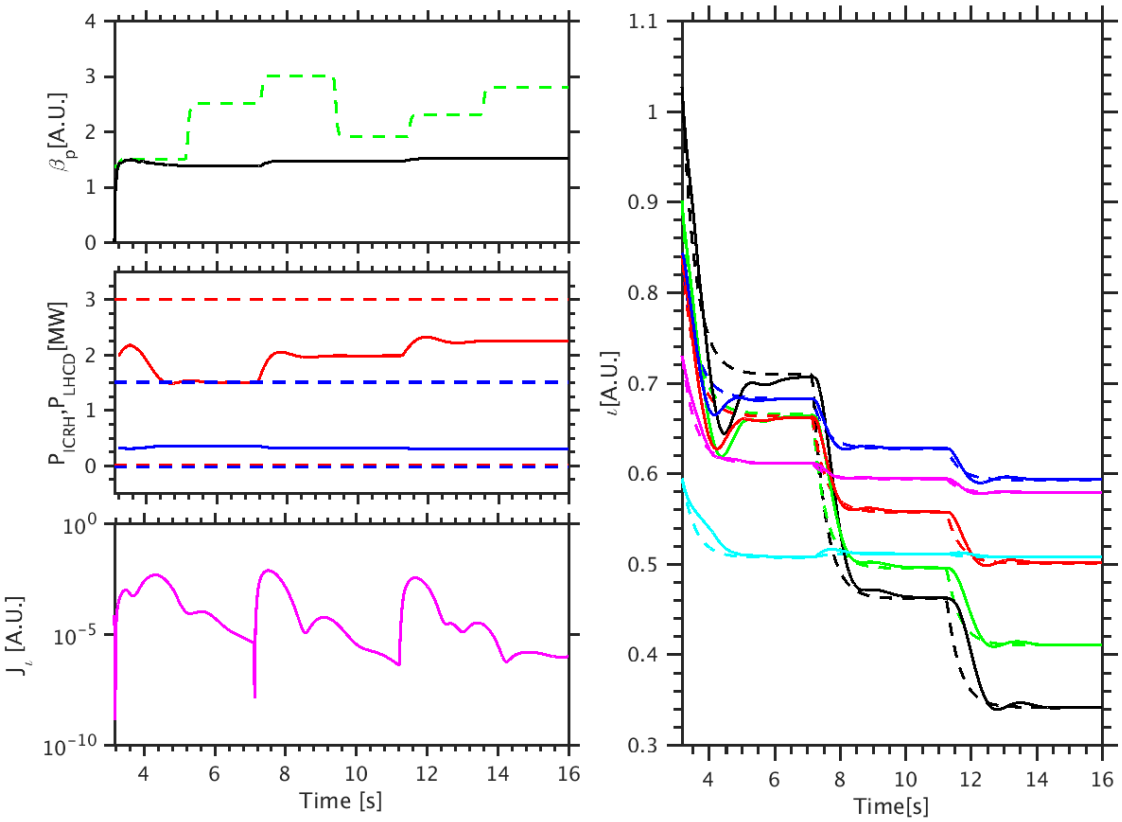

Figure 3.6: Tracking ι points at 0, 0.1, 0.2, ...,0.4. Left-top panel: time traces of β_p setpoints (green dashed) and evolutions (black) with β_p control relaxed. Left-middle panel: time traces of actuated powers P_{ICRH} (blue) and P_{LHCD} (red), as well as the ICRH (blue dashed) and LHCD (red dashed) power limits. Left-bottom panel: time traces of the averaged relative error index for ι. Right panel: time traces of ι setpoints (dashed) and evolutions (solid) at x = 0 (black), 0.1 (green), 0.2 (red), 0.3 (blue), 0.4 (magenta), 0.5 (cyan) with ι feedback control.

more LHCD power. An internal transport barrier was formed on the electron channel as one can notice a strong increase of T_e and J_{boot} in the center. However, the increase of electron temperatures implies the reduction of the electron-ion collision frequency (proportionally to $T_e^{-1.5}$), hence the ions could not be heated by electrons. Taking the ion radiation and power loss into account, the ions temperature dropped slightly. The EAST tokamak is a superconducting tokamak which is suitable for the long-pulse steady-state plasma operation. The second case involves the simulatenous control of β_p and ι in H-mode steady state operational scenarios. In order to design appropriate ι and β_p setpoints for H-mode steady-state plasma control, we perform trial simulations by regulating one set of ι values via the proposed ι controller and tracking β_p to different levels via the proposed β_p controller. The pair of ι and β_p values associated with zero surface loop voltage are selected as setpoints. Note that U_{loop} is not an actuator, and the condition of the zero loop voltage with the constant total plasma current is satified by appropriately coordinating the values of ι and β_p. With the procedure,

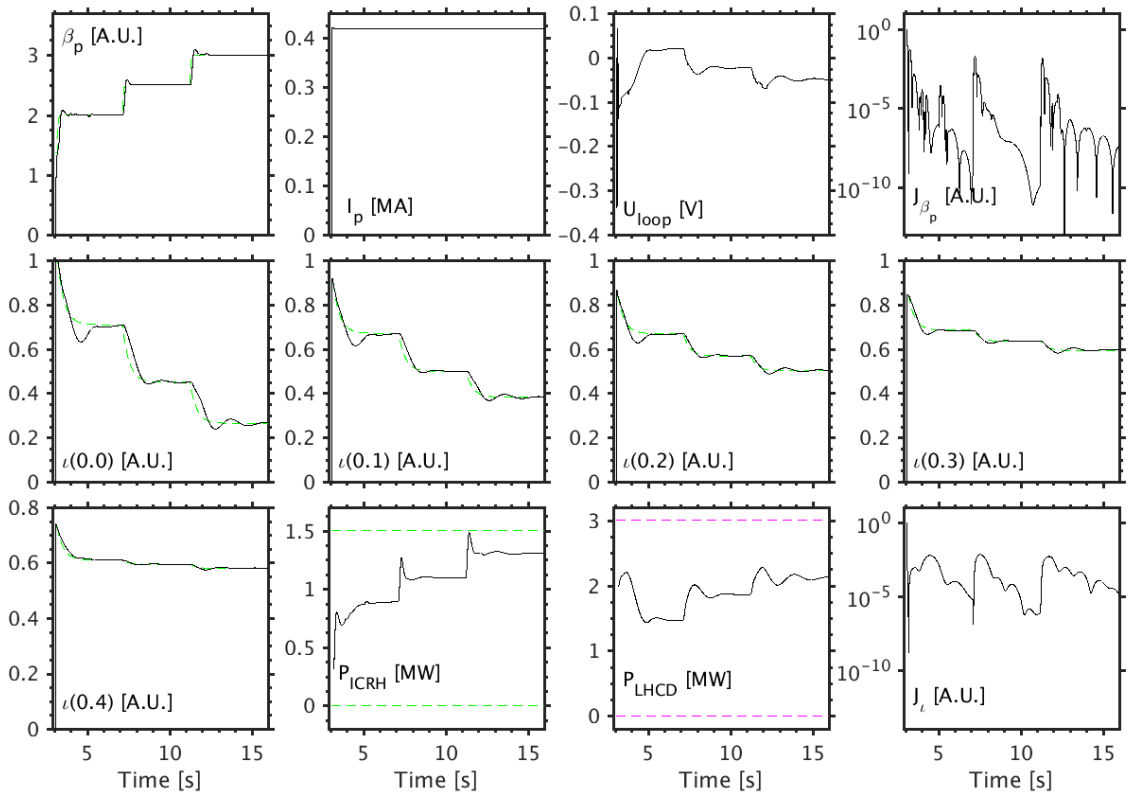

Figure 3.7: Tracking ι points at 0, 0.1, 0.2, ..., 0.4 and β_p simultaneously. Top panels from left to right: time traces of plasma poloidal pressure β_p, plasma current I_p, the loop voltage U_{loop}, the averaged relative error for β_p, $\langle J_{\beta_p} \rangle$. Middle panels from left to right: time traces of the ι septpoints (green dashed) and evolutions (black solid) at x = 0, 0.1, 0.2, 0.3. Bottom panels: time traces of the ι setpoints (green dashed) and evolutions (black solid) at x = 0.4, the actuated ICRH power P_{ICRH} (black solid) associated with its power limits (green dashed), the ICRH power P_{LHCD} (black solid) associated with its power limits (magenta dashed), and the averaged relative error for ι, $\langle J_\iota \rangle$.

three pairs of setpoints for ι and β_p are therefore designed. The tracking of these designed setpoints using the proposed control scheme is then performed with the results shown in Fig. 3.9. In each regulation window, the setpoints are reached with the averaged rise time vector $(\langle t_{r,\beta_p} \rangle, \langle t_{r,\iota} \rangle)$ at (0.146, 1.34) s, the averaged overshoot vector at $(\langle l_{os,\beta_p} \rangle, \langle l_{os,\iota} \rangle)$ at (2.13, 3.86) %, small steady state errors, and meanwhile, with the loop voltage approaching zero.

More interesting physical results are illustrated in Fig. 3.10. It seems that the increase of the absolute value of central magnetic shear combined with the β_p decrease can ensure the sum of bootstrap current and LH driven current approximately kept at a level so that the ohmic current would not play a role. With the decrease of the ICRH power, β_p drops from 2.8 to 2.2, associated with the global reduction of the electron temperature. The decrease of electron temperatures results in the growth of the collision frequency between electrons and ions, thus

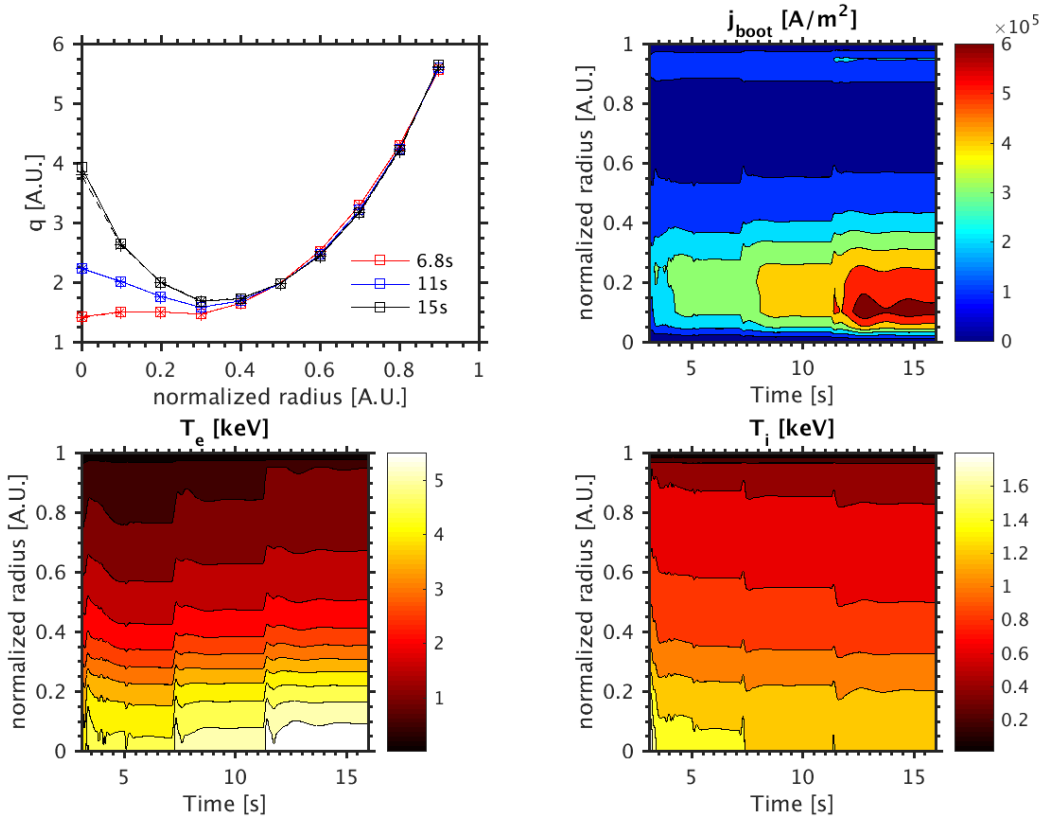

Figure 3.8: Simulation of a hybrid scenario. Left-top panel: typical q-profile setpoints (asterisk and dashed) and evolutions (square and solid) at 6.8 s (red), 11 s (blue) and 15 s (black). Right-top panel: contour plot of the bootstrap current j_{boot} evolution. Left-bottom panel: contour plot of the electron temperature profile T_e evolution. Right-bottom panel: contour plot of the ion temperature profile T_i evolution.

the ion temperatures globally increased via acquiring the energy from electrons. The two obvious bulbs for the loop voltage evolution, shown in Fig. 3.10, between scenario transition are attributed to the sudden decrease of the bootstrap current arising from the sudden decrease of electron temperatures and their gradients due to the decrease of the ICRH power. In order to compensate for the loss of the bootstrap current and keep the plasma current constant, the ohmic current increases in response to the loop voltage, U_{loop} (See [Wesson and Campbell, 2011] for its definition), delivered by the plasma current controller. Therefore, U_{loop} transiently increases before it is reduced to about 0 on a longer time scale due to the growth of P_{LHCD} and of the associated LH driven current, which leads to an increase of the central safety factor and shear reversal. Even though it plays a negligible role in the steady state scenarios, the ohmic current can be used transiently after setpoint changes or plasma disturbances considering the different time scales in which various parameters such as the bootstrap current or the LH driven current evolve.

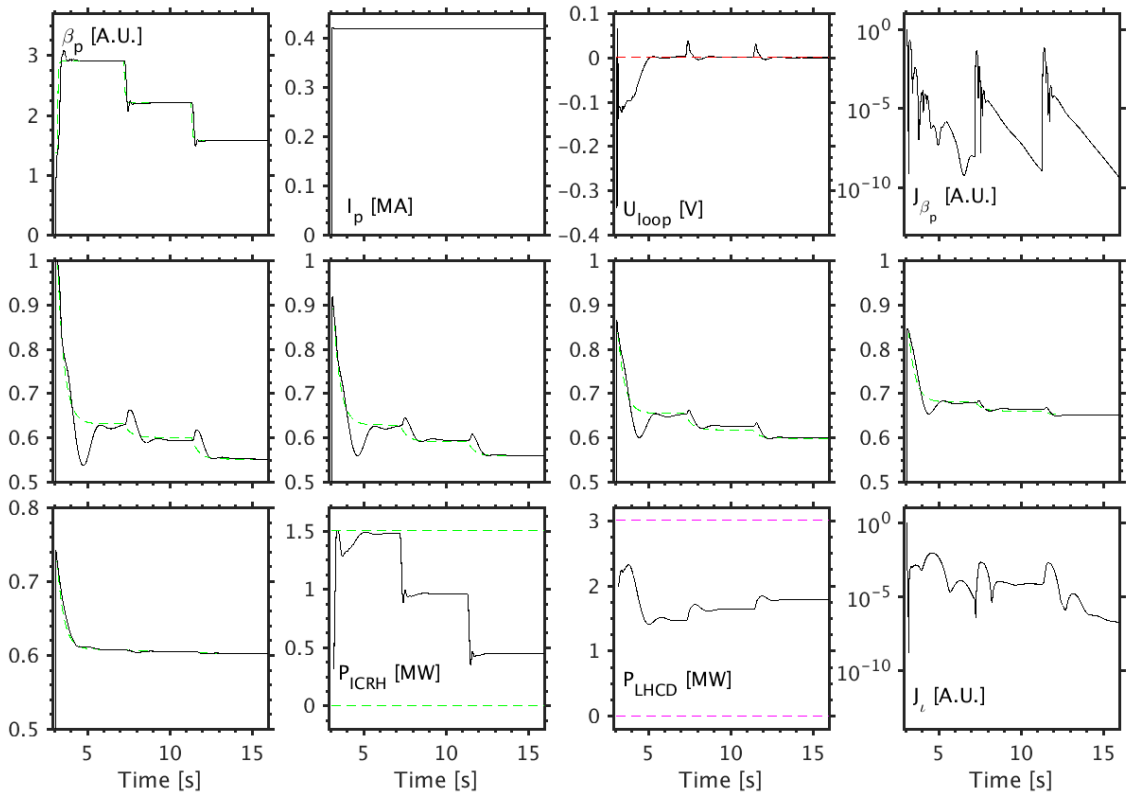

Figure 3.9: Tracking of ι points at 0, 0.1, 0.2, ..., 0.4 and β_p simultaneously. Top panels from left to right: time traces of plasma poloidal pressure β_p, plasma current I_p, the loop voltage U_{loop} (black solid) with the zero loop voltage line (red dashed) , the averaged relative error for β_p, $\langle J_{\beta_p} \rangle$. Middle panels from left to right: time traces of the ι setpoints (green dashed) and evolutions (black solid) at x = 0, 0.1, 0.2, 0.3. Bottom panels from left to right: time traces of the ι setpoints (green dashed) and evolutions (black solid) at x = 0.4, the actuated ICRH power P_{ICRH} (black solid) associated with its power limits (green dashed), the LHCD power P_{LHCD} (black solid) associated with its power limits (magenta dashed), and the averaged relative error for ι, $\langle J_\iota \rangle$.

3.1.3.2 Tracking with moderate time delays and power saturations

In this section, we first present the METIS simulation results with different levels of time delays. Then comparison of the simulations with and without the control conditioning module is provided to highlight the importance of online control conditioning for the feedback controller in attenuating the negative effects from time delays and power saturations.

Basically, the tokamak operation system is a time delay system, in which the time delays may arise from the PCS sampling, filtering, communication with the associated systems, the actuator systems, the diagnostic systems and the real-time equilibrium reconstruction algorithm. For time delay systems, the effects from time delays can be neglected if they

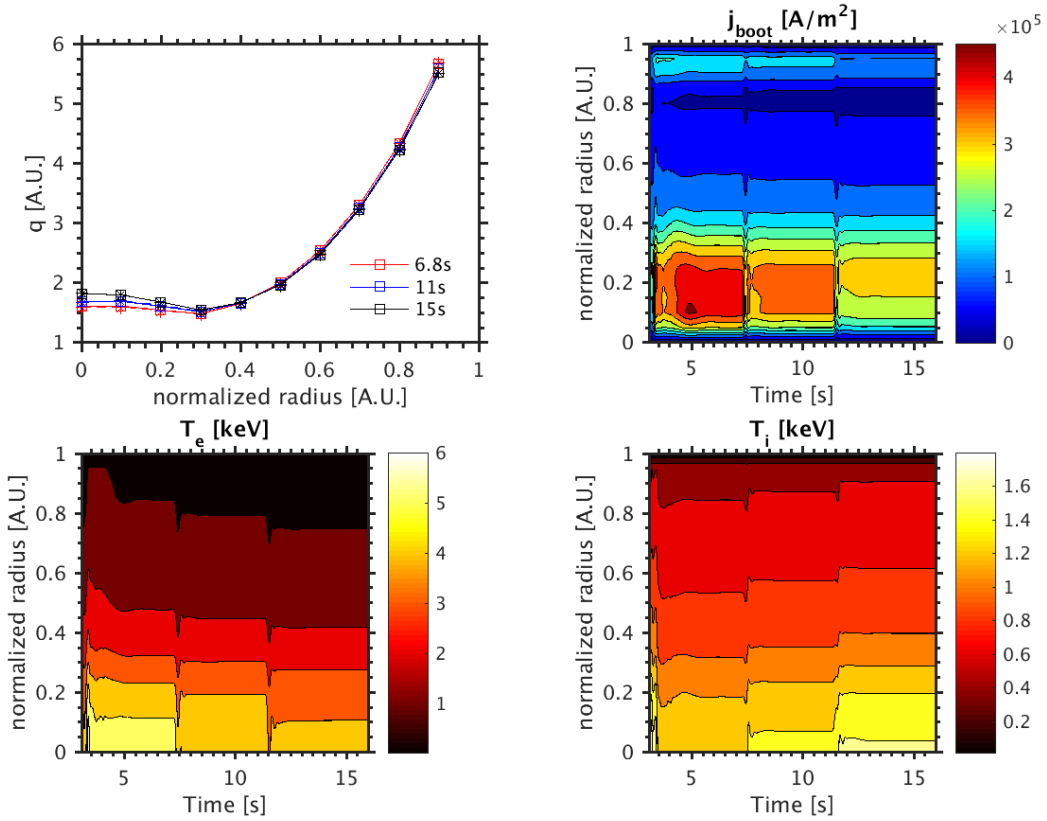

Figure 3.10: Simulation of a steady-state scenario. Left-top panel: typical q-profile setpoints (asterisk and dashed) and evolutions (square and solid) at 6.8 s (red), 11 s (blue) and 15 s (black). Right-top panel: contour plot of the bootstrap current j_{boot} evolution. Left-bottom panel: contour plot of the electron temperature profile T_e evolution. Right-bottom panel: contour plot of the ion temperature profile T_i evolution.

are under a particular threshold. However, exceeding the threshold may result in undesirable oscillations, sometimes even inducing closed-loop instability. Since the profile control sampling time is fixed at 20 ms, the time delays that appear in the discrete profile controller should be a multiple of the profile control sampling time. The actuation and measurement time delays can be as small as 1 ms because their sampling frequencies are much larger, e.g. 1000 Hz. The PCS profile control algorithm and the equilibrium reconstruction algorithm with larger sampling time at 20 ms thus constitute a primary source of time delays, which may cause time delays as large as 20 ms, 40 ms and even 60 ms. In this study, we evaluate the performance of the controller under the time delay environment by artificially varying the time delays in the actuation dynamics at 20 ms, 40 ms and 60 ms, respectively. The simulation results are illustrated in Fig. 3.11. By comparing the evolution of β_p and ι values in the plasma core with the actuation time delays at 20 ms, 40 ms and 60 ms, we can conclude that the control performance is not obviously damaged with the increase of time delays, which is beneficial from the online control conditioning for the controller states using the values of the control commands provided by the controller and of the actual powers provided by the ICRH and

LHCD power systems.

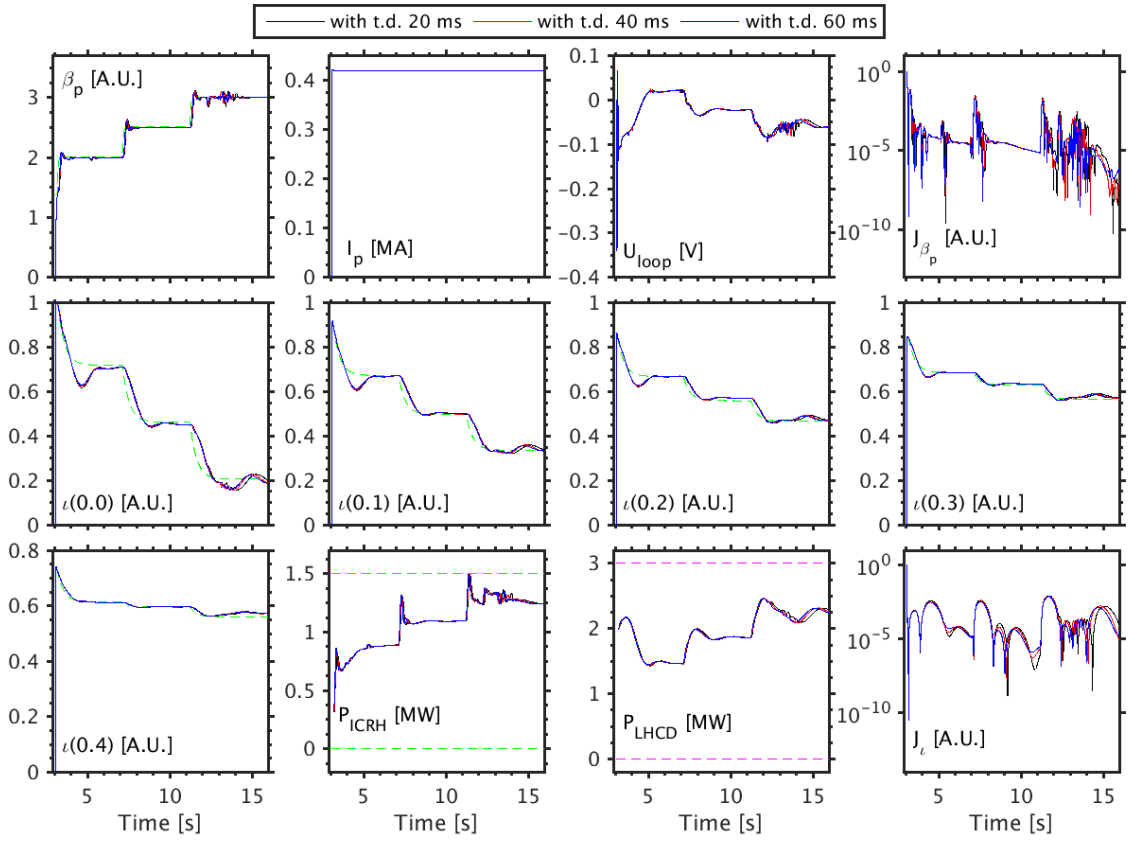

Figure 3.11: Tracking with time delays (t.d.) at 20 ms (black), 40 ms (red) and 60 ms (blue). Top panels from left to right: time traces of plasma poloidal pressure β_p, plasma current I_p, the loop voltage U_{loop}, the β_p performance index J_{β_p}. Middle panels from left to right: time traces of the ι points at x = 0, 0.1, 0.2, 0.3. Bottom panels from left to right: time traces of the ι point at x = 0.4, the actuated ICRH power P_{ICRH}, the LHCD power P_{LHCD}, and the ι performance index J_ι. The reference trajectories for ι and β_p are denoted by green dashed lines, the power limits for the ICRH and LHCD are indicated by blue and magenta dashed lines, respectively.

Normally, under ideal circumstances if the reference trajectories are properly prescribed, the magnitude and power rate limits of the ICRH and LHCD systems are never violated. However, unpredictable disturbances in tokamak plasmas could drive the plasma to abnormal states, which can probably cause power saturations, sometimes accompanied with time delays. In order to identify whether the controller with online control conditioning can effectively attenuate the effects from both the power saturations and time delays, control performance with and without the anti-windup module are compared in Fig. 3.12. In the scenario without control conditioning imposed, there are obvious oscillations of the β_p evolution at the beginning, which is caused by oscillations of the ICRH power mainly due to 60 ms time delays (i.e. 3 T_s). At 7.1 s, the β_p setpoints are increased from 2.0 to 3.5 exponentially. However, since the highest ICRH power that can be provided can not support the achievement of β_p at 3.5, the

ICRH power is saturated until 11.2 s. Then the reference trajectory starts to decrease from 3.5 to 3.0: one can notice that the β_p value immediately follows the reference trajectory for the scenario with control conditioning, but the scenario without control conditioning can not respond accordingly for as long as 4 s. As for ι one can notice that at the beginning the relative errors, i.e. $J_\iota[k]$, for two scenarios are approximately consistent, because the ι controller does not respond to the high frequency references/disturbances. After the saturation is relaxed, the relative error for ι with control conditioning is obviously much smaller than the one without control conditioning.

To sum up, using the controller outputs and the actual power measurements, we can calculate the actuation errors due to power saturations or time delays with respect to the control commands based on the two-time-scale plasma model. Then these errors are fed back to the controller for control states conditioning. This technique can attenuate negative effects from long time delays, e.g. 60 ms, and from the evolution after the power saturations are relaxed.

3.1.3.3 Tracking with varying weighting functions

The objective of this section is to compare the closed-loop simulation results using the feedback controller tuned with various weighting functions. Six simulation scenarios were evaluated, whose results are listed in Table 3.3. All the simulation scenarios have achieved the simultaneous control of q-profile and β_p, implying the potential robustness of the feedback controller to the weighting function parameters.

In the scenarios a-c, all three local controllers are tuned with the weighting functions as listed in the option I of Table 3.3. The tuning parameters M and A are respectively kept at 2 and 10^{-5}, and the desired closed-loop bandwidths are increased from the scenario a to c. Results show that the performance indexes $\langle\vec{t_r}\rangle$ and $\langle\vec{J}\rangle$ are gradually descreased for both β_p and ι tracking, which is accompanied with the increase of the overshoot index $\langle\vec{l}_{os}\rangle$. In the scenarios d-f, the fast β_p controller is tuned with the weighting functions in the Option I, while the slow β_p and ι controllers are tuned with the weighting functions in the Option II. Likewise, the tuning parameter M is fixed at 2 for all the weighting functions, while the desired closed-loop bandwidths and the low frequency tuning parameters are varied. Results imply that with the increase of the desired closed-loop bandwidths, the transient control performance is improved because the performance indexes $\langle\vec{t_r}\rangle$ and $\langle\vec{J}\rangle$ are decreased gradually and the overshoot index $\langle\vec{l}_{os}\rangle$ is increased in the scenarios d-f. In addition, statistics show that the averaged rise time $\langle t_{r,\beta_p}\rangle$, lies in 90-132 ms, i.e. (2.25-3.3) τ_E and also 4.5-6.6 times the sampling interval, which is physically reasonable and is a tradeoff between the control performance and robustness. The robustness performance to parameter disturbances will be evaluated in the next section.

Comparing the scenarios a-f, we conclude that when using the option II for control design, the ι control can be improved slightly, but the β_p control performance is damaged. To sum up, the tuning of the desired closed-loop bandwidths is essential for the control performance,

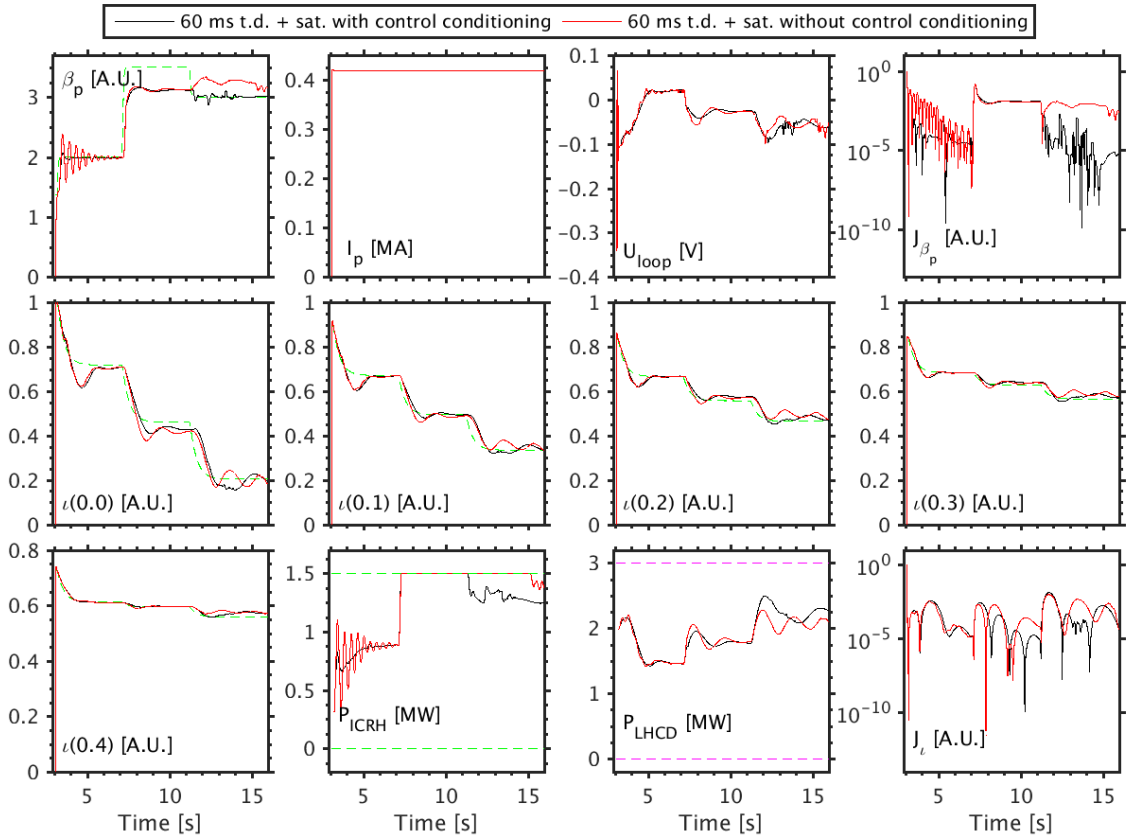

Figure 3.12: Comparison of tracking with 60 ms of time delays (t.d.) plus power saturations with (black solid) and without (red solid) online control conditioning. Top panels from left to right: time traces of plasma poloidal pressure β_p, plasma current I_p, the loop voltage U_{loop}, the β_p performance index J_{β_p}. Middle panels from left to right: time traces of the ι points at x = 0, 0.1, 0.2, 0.3. Bottom panels from left to right: time traces of the ι point at x = 0.4, the actuated ICRH power $\mathrm{P_{ICRH}}$, the ICRH power $\mathrm{P_{LHCD}}$, and the ι performance index J_ι. The reference trajectories for ι and β_p are denoted by green dashed lines, the power limits for the ICRH and LHCD are indicated by blue and magenta dashed lines respectively.

which should be carefully considered. In addition, the tuning parameter A should be made small, for example, at 10^{-5} to guarantee small tracking errors.

3.1.3.4 Robustness to plasma parameter uncertainties

In tokamak experiments, there are numerous parameters/profiles that were assumed to be constant but possibly vary and influence, in different degrees, the values of safety factors and plasma pressures. For example the line averaged density $\langle \bar{n}_e \rangle$, the confinement enhancement factor $H_{98}(y, 2)$ and the ion effective charge number Z_{eff} are among the most important ones. Hence, we consider those quantities as the sources of typical disturbances that occur in the course of the simulation and evaluate the robustness of the closed-loop system. Plasma current

Table 3.3: Weighting functions for the local controllers design and performance indexes.

Option	Index	$\omega_{B,\beta_{p,F}}$	$\omega_{B,\beta_{p,S}}$	$\omega_{B,\iota}$	$A_{\beta_{p,F}}$	$A_{\beta_{p,S}}$	A_ι	-	-	-	-	$\langle\vec{t_r}\rangle$ [s]	$\langle\vec{l}_{os}\rangle$ [%]	$\langle\vec{J}\rangle\times 10^4$ [A.U.]
	a	2π	π	π	10^{-5}	10^{-5}	10^{-5}	-	-	-	-	(0.107,0.808)	(4.02,3.43)	(9.78,14.0)
I	b	3π	1.5π	1.5π	10^{-5}	10^{-5}	10^{-5}	-	-	-	-	(0.0933,0.771)	(5.12,3.80)	(9.09,13.0)
	c	4π	2π	2π	10^{-5}	10^{-5}	10^{-5}	-	-	-	-	(0.100,0.752)	(6.19,4.12)	(8.94,12.0)
		$\omega_{B,\beta_{p,F}}$	$\omega_{p,\beta_{p,S}}$	$\omega_{u,\iota}$	$\omega_{p,3}$	$\omega_{u,\iota}$	$A_{\beta_{p,F}}$	$A_{p,\beta_{p,S}}$	$A_{u,\beta_{p,S}}$	$A_{p,\iota}$	$A_{u,\iota}$			
	d	2π	$10^{-0.3}$	1	$10^{-0.3}$	1	10^{-5}	$10^{-4.5}$	$10^{0.1}$	$10^{-4.5}$	$10^{0.1}$	(0.113,1.11)	(1.44,3.47)	(9.96,30.0)
II	e	3π	$10^{-0.15}$	1.2	$10^{-0.15}$	1.2	10^{-5}	$10^{-5.25}$	$10^{0.1}$	$10^{-5.25}$	$10^{0.1}$	(0.0933,0.906)	(3.33,4.46)	(9.12,26.0)
	f	4π	$10^{-0.10}$	1.5	$10^{-0.3}$	1.5	10^{-5}	10^{-6}	$10^{0.2}$	10^{-6}	$10^{0.2}$	(0.0933,0.885)	(4.69,5.18)	(9.01,26.0)

NOTE: $\langle\vec{t_r}\rangle \stackrel{\text{def}}{=} (\langle t_{r,\beta_p}\rangle, \langle t_{r,\iota}\rangle)$, $\langle\vec{l}_{os}\rangle \stackrel{\text{def}}{=} (\langle l_{os,\beta_p}\rangle, \langle l_{os,\iota}\rangle)$, $\langle\vec{J}\rangle \stackrel{\text{def}}{=} (\langle J_{\beta_p}\rangle, \langle J_\iota\rangle)$.

Table 3.4: List of the parameter variations.

β_p	$\delta\bar{n}_e$ [%], T.I. [s]	$\delta H_{98}(y,2)$[%], T.I. [s]	δZ_{eff} [%], T.I. [s]
2	+30 %, [3.7, 4.2]	+30%, [11.26, 11.76]	+30%, [12.26, 12.76]
	-30 %, [19.82, 20.32]	-30%, [4.7, 5.2]	-30%, [14.78, 15.28]
2.5	+30%, [6.22, 6.72]	+30%, [13.78, 14.28]	+30%, [17.30, 17.80]
	-30%, [22.34, 22.84]	-30%, [7.22, 7.72]	-30%, [18.82, 19.32]
3	+30%, [8.74, 9.24]	+30%, [16.30, 16.80]	+30%, [21.34, 21.84]
	-30%, [24.86, 25.36]	-30%, [9.74, 10.24]	-30%, [23.86, 24.36]

disturbances are not taken into account in this study because the plasma current is tightly regulated separately through a dedicated controller.

Simulation results of disturbance rejection by the β_p controller are depicted in Fig. 3.13, where 18 squared wave disturbances emerge in separate periods of the whole simulation as listed in Table 3.4. Specifically, the value of the averaged density is increased by 30% at 3.6 s (β_p at 2), 6.22 s (β_p at 2.5) and 8.74 s (β_p at 3) respectively and remains constant for 0.5 s before it returns to the original value. The value of the averaged density is decreased by 30% suddenly at 19.82 s (β_p at 2.0), 22.34 s (β_p at 2.5) and 24.86 s (β_p at 3) and remains the same for 0.5 s before returning to the initial value. The H factor is artificially decreased by 30% in the time periods [4.7, 5.2] s, [7.22, 7.72] s and [9.74, 10.24] s, while in the time periods [11.26, 11.76] s, [13.78, 14.28] s and [16.30, 16.80] s it grows by 30%. During the time intervals [12.26, 12.76] s, [17.30, 17.80] s and [21.34, 21.84] s we respectively increase the effective charge number by 30% while during the time intervals [14.78, 15.28] s, [18.82, 19.32] s and [21.34, 21.84] s the effective charge number is decreased by 30 %. We can conclude from our simulations that, in addition to good reference tracking, the fast and slow controllers are as well able to reject the 30% changes of $\langle\bar{n}_e\rangle$, $H_{98}(y,2)$ and Z_{eff} with a response time at around 0.25 s when the ICRH power is not saturated. We note that if the upper limit of the ICRH power is 1.5 MW, it is not possible to reject the 30% decrease of $H_{98}(y,2)$ when β_p is over 2.5 and also it cannot reject 30 % decrease of $\langle\bar{n}_e\rangle$ and Z_{eff} when β_p is at 3. The reason is that under those conditions the available ICRH power is not able to compensate the reduced part of β_p arising from the decrease of $H_{98}(y,2)$, $\langle\bar{n}_e\rangle$ and/or Z_{eff}. Importantly, we highlight that among all three parameters, $H_{98}(y,2)$ is the most important parameter that can significantly affect β_p.

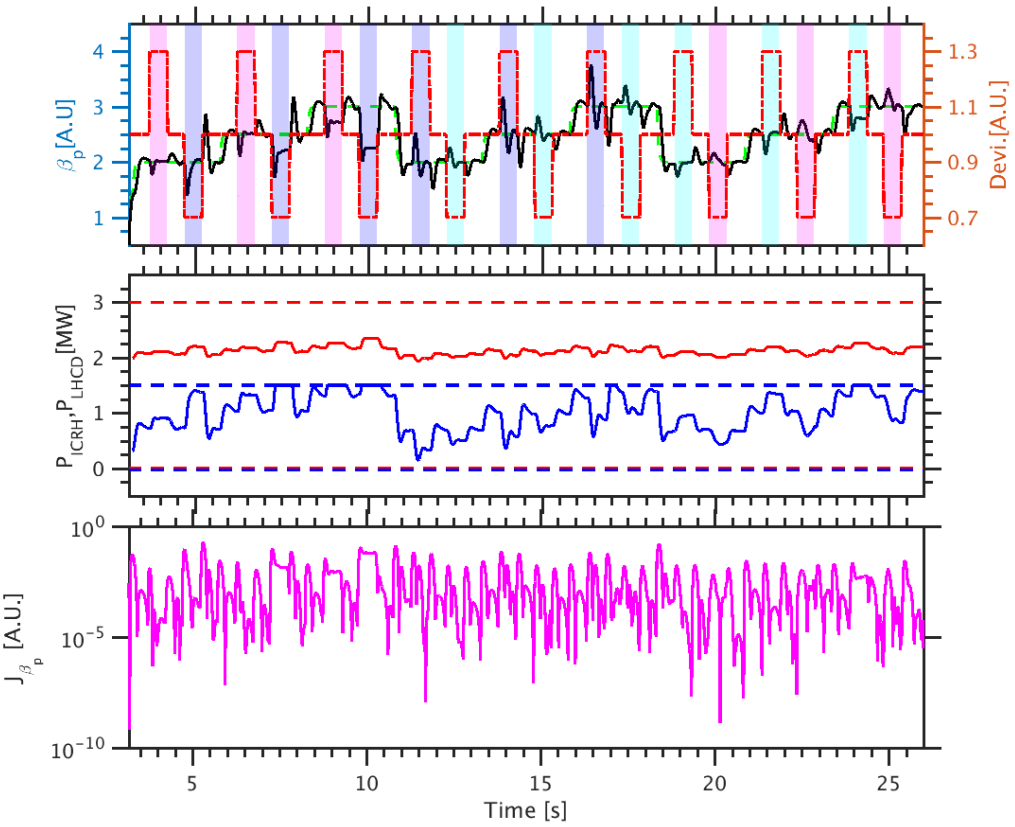

Figure 3.13: Disturbance rejection of β_p control. Top panel: time traces of β_p setpoints (green dashed) and evolutions (black solid), with the associated parameter variation intervals: magenta areas indicate that $\bar{n}_e$ is activated as a parameter disturbance, while $H_{98}(y,2)$ corresponds to the light purple areas and Z_{eff} is linked with cyan areas. The red dotted line represents the relative variation of each activated disturbance parameter. Middle panel: time traces of actuated powers P_{ICRH} (blue solid) and P_{LHCD} (red solid), as well as power ranges of ICRH (blue dashed) and LHCD (red dashed). Bottom panel: time traces of the relative error for β_p, i.e. J_{β_p}.

The robustness test of the ι controller against typical squared wave disturbances is presented in Fig. 3.14. In this case, three squared wave disturbances are imposed in the periods of [4, 4.5] s (30 % increase of $\langle\bar{n}_e\rangle$), [8, 8.5] s (30 % increase of $H_{98}(y,2)$)and [12, 12.5] s (30% increase of Z_{eff}). Even though the simulation experienced large and sudden disturbances in the first two phases, two groups of setpoints are finally reached without exceeding the limits of ICRH and LHCD powers. As for the third phase, since the model mistmatches are enlarged with strongly negative magnetic shear due to nonlinearity, the setpoints are reached after a few oscillations.

The simultaneous control of ι at 0, 0.1, 0.2, ..., 0.5 and β_p with typical disturbances is shown in Fig. 3.15. There are three squared wave disturbances with the amount of 30% growth occurring in the time intervals [4, 4.5] s (for averaged density), [8, 8.5] s (for H factor)

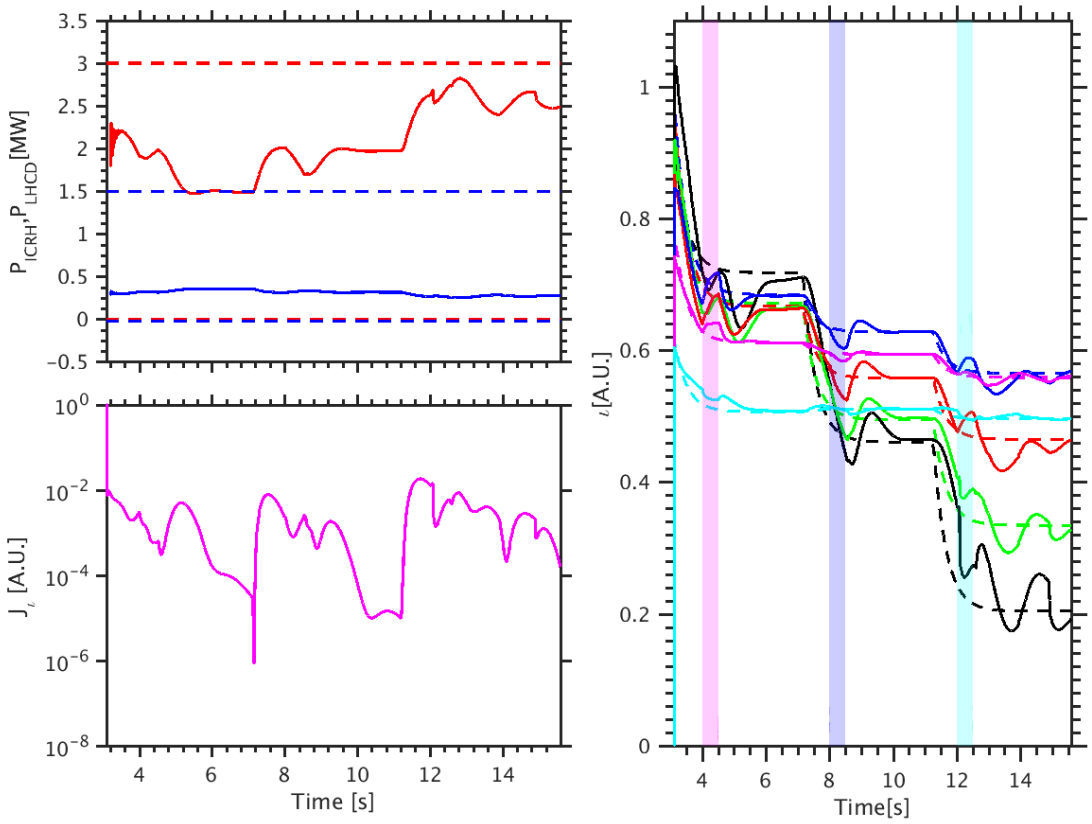

Figure 3.14: Disturbance rejection of ι control. Left-top panel: time traces of actuated powers P_{ICRH} (blue) and P_{LHCD} (red), power ranges of ICRH (blue dash) and LHCD (red dash). Left-bottom panel: time traces of the averaged relative error index for ι. Right panel: time traces of ι values (solid) and setpoints (dashed) at x = 0 (black), 0.1 (green), 0.2 (red), 0.3 (blue), 0.4 (magenta), 0.5 (cyan) with ι feedback control. Magenta, light purple and cyan areas are respectively indicating 30 % increase of $\bar{n}_e$, $H_{98}(y, 2)$ and Z_{eff}.

and [12, 12.5] s (for effective charges). In addition to reference tracking, β_p is well regulated against the three sudden and large disturbances with a response time of 0.2 s. The ι controller is able to reject the disturbances of both H factor and plasma density and finally reaches the targets. For the strongly negative shear case, it takes more time to achieve the target since the model mismatches are much larger, but it is nevertheless approached as closely as possible. Note that when β_p is at 3.0, a large amount of ICRH power is needed to sustain this value and only a limited amount of power is left to reject the disturbance, thus the ICRH power is saturated between 12 s and 12.5 s.

3.1.4 Conclusion of Section 3.1

In this work, a new $\mathcal{H}_\infty$ robust controller has been developed for the tracking of q-profile and β_p, based on a two-time-scale data-driven model. The model is divided into 3 sub-models for

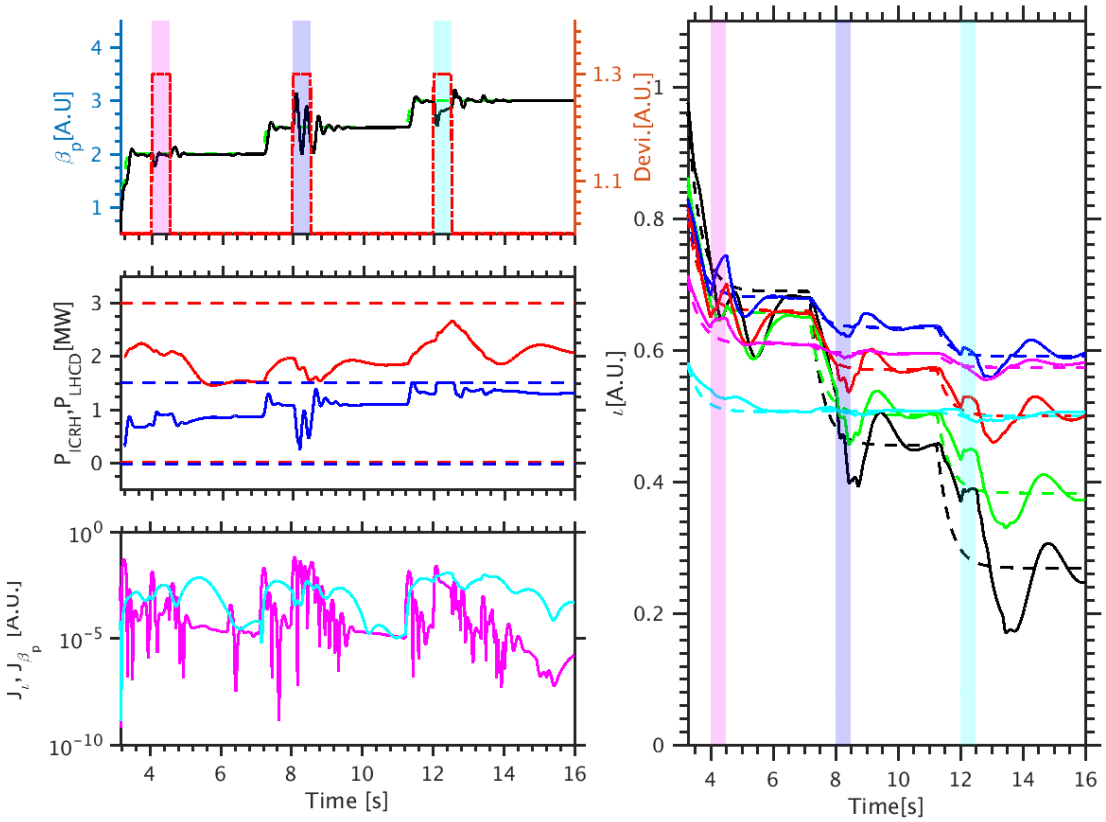

Figure 3.15: Disturbance rejection of simultaneous ι and β_p control. Left-top panel: time traces of β_p setpoints (green dashed) and evolutions (black), with magenta, light purple and cyan areas respectively indicating 30 % increase of $\bar{n}_e$, $H_{98}(y,2)$ and Z_{eff}. Left-middle panel: time traces of actuated powers P_{ICRH} (blue solid) and P_{LHCD} (red solid), power limits of ICRH (blue dashed) and LHCD (red dashed). Left-bottom panel: time traces of the relative error for $\iota(x)$ (cyan solid) on x and β_p (magenta solid). Right panel: time traces of ι values (solid) and setpoints (dashed) at x = 0 (black), 0.1 (green), 0.2 (red), 0.3 (blue), 0.4 (magenta), 0.5 (cyan) with ι feedback control.

separate control synthesis and eventually all the local controllers are combined for composite feedback control. In order to attenuate the negative effects from power saturations and time delays, a controller states conditioning loop is utilized to compensate for the actuation errors due to power saturation and time delays. Meanwhile, to avoid undesirable bumps, overshoots and power saturations at the control initialization, some pre-configurations on the setpoints and pre-filters are carefully made. The control tunings and relevant control performance have been evaluated numerically to provide some indications on experimental control tunings for the robust feedback controller. Importantly, extensive nonlinear closed-loop simulations with the METIS code show that using LHCD@4.6GHz and ICRH@33MHz systems as control actuators the proposed controller can successfully achieve and regulate the monotonic q-profile and reversed magnetic shear with high β_p in H-mode steady-state scenarios on EAST. Robustness tests indicate that it is possible to maintain the states by rejecting the disturbances of up to

different levels of plasma density variation, H-factor variation and effective charge variation separately.

In the future, the implementation of the control algorithms into the EAST PCS is expected and experimental tests on EAST are foreseen to further validate the effectiveness of the proposed control scheme. Furthermore, a series of extensions can be made based on the proposed controller. Firstly, control adaptivity can be imposed on the feedback controller (treated as a central controller) to enhance its control performance, for example, reducing the overshoots and steady-state errors, especially for the fast timescale kinetic control and the central safety factor control. In addition, a plant model-based feedforward can be combined with the feedback controller to not only actively control the response time but also optimally reduce the transient errors between measurements/estimations and setpoints, while the disturbance model-based feedforward can be implemented to deal with typical disturbances at the timescale beyond the control bandwidth of the fast controller. It is also interesting to explore the high plasma current, high plasma pressure, high bootstrap current fraction steady-state scenarios with the inclusion of NBIs and ECCDs as control actuators for the integrated control of q-profile, ion temperature and plasma rotation profiles and MHD instabilities.

3.2 Robust real-time feedback alternatives for kinetic control

In recent years, various control schemes have been proposed for tailoring plasma magnetic and kinetic parameters/profiles. Nonetheless, we find that performance comparison of different feedback controllers, even in a specific operational scenario, rarely appears in the literature. For the sake of routine tokamak plasma operation, it is interesting to have comprehensive knowledge of the characteristics of these feedback control schemes such that one can immediately select an optimal controller from a set of alternative ones for a specific control objective. In this section, we make the first attempt to provide practical and valuable designs along this line. Specifically, we develop a set of popular finite-dimensional kinetic controllers based on the same LTI data-driven model, and then evaluate and compare their performance and robustness by carrying out nonlinear closed-loop simulations and dedicated plasma experiments. A two-layer two-time-scale kinetic control scheme is thus developed for the comparative study, including an inner-layer with a low sampling frequency aimed at plasma kinetic control, whilst the high sampling frequency outer-layer deals with measurement preprocessing and actuation tracking. Four alternative finite-dimensional feedback controllers are introduced, namely $\mathcal{H}_\infty$ robust control, LQI control and the observer-based IMC for plasma kinetic tracking and the SIMC PI for kinetic/actuation tracking. In addition, the plasma parameters of interest, experimentally reconstructed or measured by the GPU-accelerated real-time equilibrium code, P-EFIT [Huang et al., 2020], using magnetic measurements, as well as coupled power measurements are handled by a set of average horizon filters in real-time for noise removal. Next, we present a compact LSS model for plasma feedback controller design. A two-layer two-time-scale kinetic control scheme is subsequently proposed, including a number of alternative kinetic control algorithms, measurement preprocessing module and cascade actuation controllers. The performance of the feedback control scheme is assessed, discussed and compared numerically

with the METIS plasma simulator [Artaud et al., 2018]. Afterwards, the initial experimental results achieved on the EAST tokamak are reported. Finally, we draw the conclusions and outline possible extensions.

3.2.1 Plasma dynamic model for control

In this section, we first revisit a linear two-time-scale model structure to approximate the plasma kinetic dynamics in an H-mode scenario on EAST. Subsequently, a model reduction technique based on the input lowpass filtering and SVD is employed onto this model for integrated feedback controller design.

3.2.1.1 Two-time-scale plasma model

The dynamic evolutions of plasma kinetic parameters with respect to control actuators, e.g. the LHCD power, in medium-sized or large tokamaks can be characterized by a lumped-parameter LTI two-time-scale model structure as demonstrated in [Moreau et al., 2008,Moreau et al., 2011,Moreau et al., 2013,Moreau et al., 2015]. This dynamic model comprises a slow sub-model illustrating the slow responses of plasma kinetic parameters with respect to the poloidal magnetic fluxes as:

$$\begin{aligned} \dot{X}_{\Psi}(t) =& A_{\mathrm{S}} X_{\Psi}(t) + B_{\mathrm{S}} U_{\mathrm{S}}(t) \\ \Xi_{\mathrm{S}}(t) =& C_{\mathrm{S}} X_{\Psi}(t) + D_{\mathrm{S}} U_{\mathrm{S}}(t) \end{aligned} \tag{3.25}$$

and a fast sub-model depicting the fast plasma kinetic evolutions possibly arising from plasma temperature profile variations as:

$$\begin{aligned} \dot{X}_{\mathrm{F}}(t) &= A_{\mathrm{F}} X_{\mathrm{F}}(t) + B_{\mathrm{F}} U_{\mathrm{F}}(t) \\ \Xi_{\mathrm{F}}(t) &= C_{\mathrm{F}} X_{\mathrm{F}}(t) + D_{\mathrm{F}} U_{\mathrm{F}}(t) \end{aligned} \tag{3.26}$$

in which

$$\begin{aligned} & U(t) = U_S(t) + U_F(t), \Xi(t) = \Xi_S(t) + \Xi_F(t) \\ & U(t) \overset{\text{def}}{=} U_0(t) - \bar{U}(t), \Xi(t) \overset{\text{def}}{=} \Xi_0(t) - \bar{\Xi}(t) \end{aligned} \tag{3.27}$$

Here, $U(t)$ is defined as a perturbing vector of the control inputs $U_0(t)$ around their input reference $\bar{U}(t)$, with its slow and fast components denoted by $U_{\mathrm{S}}(t)$ and $U_{\mathrm{F}}(t)$, respectively. Analogously, $\Xi(t)$ is defined as a perturbing vector of the plasma kinetic parameters of interest $\Xi_0(t)$ around their reference $\bar{\Xi}(t)$, comprising its slow part as Ξ_S and its fast part as Ξ_{F}. $X_{\Psi}(t)$ represents a perturbing vector of the poloidal magnetic fluxes against their reference values, while $X_F(t)$ is a perturbed kinetic state vector. The state-space matrices $(A_{\mathrm{S}}, B_{\mathrm{S}}, C_{\mathrm{S}}, D_{\mathrm{S}})$ and $(A_{\mathrm{F}}, B_{\mathrm{F}}, C_{\mathrm{F}}, D_{\mathrm{F}})$ contain the model coefficient matrices, which can either be identified by using subspace and prediction-error approaches [Ljung, 1995] or be obtained by performing linearization and discretisation on the sophisticated PDEs governing the plasma transport evolution. The approaches to obtaining these model coefficient matrices are beyond the scope of this part and interested readers can refer to Chapter 2 and [Moreau et al., 2008, Ljung, 1995] for more details.

3.2.1.2 Model reduction for integrated kinetic control design

We are now in a position to show that the linear two-time-scale plasma model [Moreau et al., 2008] with Eqs. (3.25) – (3.27) can be transformed into a compact form suitable for integrated feedback controller design. Involving a low-pass filter on the perturbed control inputs $U(t)$ with its characteristic time τ_c satisfying $\tau_{kin} \ll \tau_c \ll \tau_{mag}$, where τ_{kin} and τ_{mag} represent the kinetic and magnetic characteristic times, respectively. After some algebraic manipulations, the two-time-scale plasma model is therefore augmented into a state-space form as:

$$G = \left[\begin{array}{c|c} A & B \\ \hline C & D \end{array}\right] \tag{3.28}$$

where

$$A = \begin{bmatrix} A_S & 0 & B_S \\ 0 & A_F & -B_F \\ 0 & 0 & C_f A_f C_f^{-1} I \end{bmatrix}, B = \begin{bmatrix} 0 \\ B_F \\ C_f B_f I \end{bmatrix}, C = \begin{bmatrix} C_S & C_F & D_S \end{bmatrix}, D = 0 \tag{3.29}$$

Here, (A_f, B_f, C_f, D_f) is a state-space realization of the lowpass filter $G_f = \frac{1}{\tau_c s+1}$, in which s is a Laplace operator.

When the controlled degrees of freedom are greater than the number of control actuators, the system is called an underactuated system [Reyhanoglu et al., 1999], which is usually the case for tokamak plasma kinetic control. In this regard, minimizing the tracking error to zero may not be possible unless the given reference targets are located in an achievable region. Before synthesizing a feedback controller for an underactuated system, it is necessary to examine which output and input directions are most influential [Barton et al., 2012]. We therefore perform SVD [Skogestad and Postlethwaite, 2007] on the steady-state gain matrix of the model $G(s)$ to extract the most influential input and output control channels. In particular, to weigh the importance of each controlled outputs and manipulated inputs, symmetric positive definite matrices Q and R are first multiplied to the output and input of the model $G(s)$, generating a weighted dynamic model $G_w = Q^{\frac{1}{2}} G(s) R^{\frac{1}{2}}$. Subsequently, we perform SVD on the steady-state gain matrix of the weighted model, yielding $G_w(0) = U_0 \Sigma_0 V_0^T$. $\Sigma_0 = \text{diag}\{\Sigma_I, \Sigma_{II}\}$ is a diagonal matrix with the singular values in a descending order as $\sigma_1 \geq \sigma_2 \geq ... \geq \sigma_{n_I} \gg \sigma_{n_I+1} \gg ... \gg \sigma_{n_d}, n_d = \min\{n_y, n_u\}$, with n_y and n_u respectively denoting the number of outputs (controlled kinetic variables) and inputs (control actuators). Σ_I contains the largest n_I singular values while Σ_{II} contains the remaining insignificant ones. The left singular vectors $U_0 = [U_I, U_{II}] \in \mathbb{R}^{n_y \times n_u}$ are divided into the level I and II vector spaces, in which the level I singular vectors represent the most controllable output directions. Likewise, $V_0 = [V_I, V_{II}] \in \mathbb{R}^{n_u \times n_u}$ have the first n_I columns retained, as they correspond to the most influential input directions V_I. We remark that Q and R are the weighting gain matrices that can be iteratively adjusted to reach various control objectives. The decision on the restricted number of retained control channels n_I is heuristic, which can empirically be determined by following the condition $\sigma_{n_I+1} \leq 0.1\sigma_1$. With such a procedure, the integrated plasma model $G(s)$ can thus be transformed into a reduced one, which is proper, stabilizable and detectable. The reduced model is therefore given by $G_r(s) = M_y^T G(s) M_u$, where

$M_y = U_{\mathrm{I}}^T$ and $M_u = V_{\mathrm{I}}\Sigma_{\mathrm{I}}^{-1}$, and its state-space form can be expressed as:

$$G_r(s) = \left[\begin{array}{c|c} A_r & B_r \\ \hline C_r & D_r \end{array}\right] \tag{3.30}$$

3.2.2 Robust linear feedback algorithms

Having obtained a control-oriented state-space plasma dynamic model, alternative real-time kinetic feedback control algorithms can immediately be synthesized. We first present an overall control architecture for plasma kinetic control. Next, a set of alternate kinetic feedback algorithms are designed based on a given kinetic model, along with some beneficial techniques for measurement preprocessing and control actuation tracking.

3.2.2.1 Two-layer cascade kinetic control framework

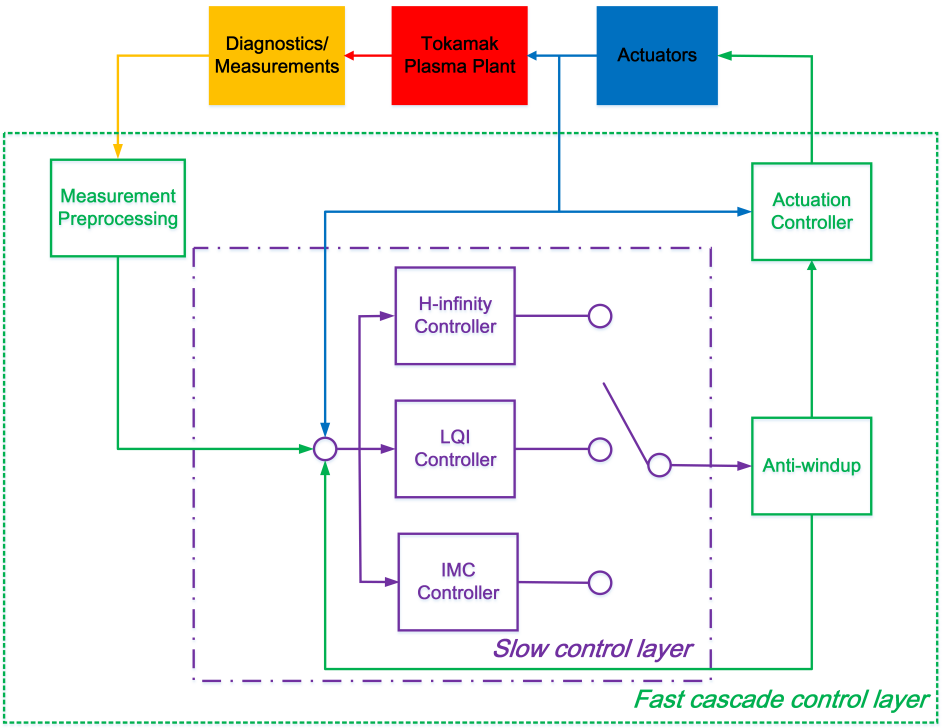

Figure 3.16: Layout of the two-layer cascade kinetic control framework.

As shown in Fig. 3.16, the overall kinetic feedback control framework for the EAST tokamak comprises two control layers that differ in the sampling frequency. The inner control layer, within the dashed purple frame, has a low sampling frequency at 50 Hz. It contains a set of alternate kinetic controllers such as the $\mathcal{H}_\infty$ robust control, the LQI control and the IMC control, along with a switch for real-time controller selection. Details on the design of these alternate kinetic controllers are given in Sections 3.2.4.2-3.2.4.4. The outer control layer,

within the green frame but outside of the purple frame, has a higher sampling frequency at 1000 Hz. It is primarily devoted to two separate tasks: 1). to preprocess the measured actuations from relevant actuator sensors and the real-time estimates of the plasma parameters of interest after the magnetic equilibrium reconstruction from, for instance, magnetic probes and polarimeter/interferometer diagnostics [Ferron et al., 1998, Baylor et al., 2004, Liu et al., 2014]; 2). to track the actuator commands requested by a selected inner-layer kinetic controller. Cascaded with an inner-layer kinetic controller, the actuation controller is designed for actuation tracking, as illustrated in Section 3.2.4.5. In the measurement preprocessing module, a set of simple average horizon filters [Ljung, 1995] are used to handle the high-frequency measurement noise. Following the same technique as in [Wang et al., 2020], the anti-windup modules are designed to mitigate the effects from the actuator saturations. We remark that the idea of the two-layer kinetic control framework originates from the following facts: 1). The time constant of the actuator dynamics such as the LHCD system is much smaller than the energy confinement time on EAST. 2). Plasma model uncertainties located in the high frequency domain beyond τ_E are not likely to damage the tracking performance if we properly prescribe the inner-layer sampling time to the level a few times smaller than τ_E [Ljung, 1995]. 3). The inner-layer kinetic controller can greatly benefit from the precise tracking of the requested commands enabled by the outer-layer actuation controller within one inner-layer sampling interval.

3.2.2.2 $\mathcal{H}_\infty$ robust kinetic control design

$\mathcal{H}_\infty$ robust control is a popular feedback control technique whose synthesis combines $\mathcal{H}_\infty$ robust stabilization with loop-shaping [Skogestad and Postlethwaite, 2007]. Basically, the design procedure is composed of two steps: 1). to augment the pre- and post-compensators on an open-loop system plant to acquire expected singular value shaping in the frequency-domain; 2). to synthesize a feedback controller by make the augmented system plant robust against model uncertainties via the $\mathcal{H}_\infty$ norm optimization. Thanks to its simplicity and robustness properties, it has already been applied to real-time magnetic and kinetic control in tokamak plasmas. In [Barton et al., 2012], the robust synthesis based on a first-principle-driven dynamic model for q-profile control was experimentally tested in L-mode plasmas on DIII-D. In [Nouailletas et al., 2019], $\mathcal{H}_\infty$ robust control was applied to plasma coil current and shape control on WEST experimentally. In [Wang et al., 2021], the performance of a decentralized $\mathcal{H}_\infty$ robust controller for the q-profile and β_p tracking on EAST is assessed numerically. In the present study, we adopt the similar synthesis method used in [Wang et al., 2021], but extend its application scope to multiple kinetic parameters and experimental setup. Another subtle difference is that in the present work, a single $\mathcal{H}_\infty$ robust controller is designed based on an integrated kinetic model containing both the fast and slow kinetic dynamics.

Our $\mathcal{H}_\infty$ robust control problem is to synthesize a feedback controller using the reduced model $G_r(s)$ derived in Eq. (3.30) via the mixed-sensitivity $\mathcal{H}_\infty$ norm optimization [Skogestad and Postlethwaite, 2007, Wang et al., 2021]. First of all, assuming the to-be-designed controller as $K_{r,\mathrm{HINF}}(s)$, we calculate the sensitivity function $S_r(s) = (I + G_r(s)K_{r,\mathrm{HINF}}(s))^{-1}$, which maps the control errors from the reference setpoints or the output disturbances. Next,

we design the proper weighting matrices $W_{\mathrm{HINF,S}}(s)$ and $W_{\mathrm{HINF,KS}}(s)$ to shape the sensitivity function $S_r(s)$ and $K_{r,\mathrm{HINF}}(s)S_r(s)$, respectively. Then, using the LMIs optimization technique [Wang et al., 2021] and the YALMIP toolbox [Lofberg, 2004] for MATLAB, the controller $K_{r,\mathrm{HINF}}(s)$ for $G_r(s)$ is synthesized by minimizing the $\mathcal{H}_\infty$ norm of the mixed-sensitivity function $T_{zw,\mathrm{HINF}} = \begin{bmatrix} W_{S,\mathrm{HINF}}S_r & W_{KS,\mathrm{HINF}}K_{r,\mathrm{HINF}}S_r \end{bmatrix}$. After the inverse singular vector transformation, the $\mathcal{H}_\infty$ robust feedback controller for the plant $G(s)$ is expressed as $K_{\mathrm{HINF}}(s) = M_u K_{r,\mathrm{HINF}}(s) M_y$. Therefore, the feedback ouputs are computed as $u_{\mathrm{fb},\mathcal{H}_\infty} = K_{\mathrm{HINF}}(s)(y_{\mathrm{m}} - y + y_{\mathrm{aw}}), u_{\mathrm{fb}} \in \mathbb{R}^{n_u}, y_{\mathrm{m}}, y, y_{\mathrm{aw}} \in \mathbb{R}^{n_y}$, where u_{fb} are the feedback outputs, y denotes the measured controlled variables and y_{aw} are the anti-windup components [Wang et al., 2021]. Combining constant feedforwards u_m and the feedback outputs yields the kinetic control inputs as $u_{\mathcal{H}_\infty} = u_{\mathrm{fb}\mathcal{H}_\infty} + u_{\mathrm{m}}$.

3.2.2.3 LQI kinetic control design

LQI control, a linear optimal control technique [Skogestad and Postlethwaite, 2007], extends the traditional linear quadratic regulator (LQR) to involve the penalization of the control error integral in the cost function, with the goal of achieving a zero steady-state tracking error under constant disturbances. This technique was first proposed in [Young and Willems, 1972], which has then been applied to many industrial and physical control problems [Anderson and Moore, 2007, Hassen et al., 2009, ElMadany and Abduljabbar, 1999, Gurung et al., 2017]. The merits of this technique are that it can be employed systematically for MIMO systems and that the controller performs satisfactorily in attenuating system disturbances. Notably, LQI has found its applications in many tokamak plasma control problems. In [Moreau et al., 2013], LQI was used to track the poloidal flux profile and β_N simultaneously in H-mode plasmas on DIII-D. In [Boyer et al., 2013], experimental tests have confirmed the performance of an LQI controller in tailoring q-profile in an L-mode plasma on DIII-D. In [Vail et al., 2019], the snowflake divertor configuration is achieved numerically by an LQI controller on NSTX–U.

In the present work, we design an LQI controller using the reduced model $G_r(s)$, and compare its performance with the other controllers. The LQI control objective is to minimize a combination of state errors and the control error integrals using minimum actuations. This control algorithm consists of a feedforward controller to estimate the input and state references, a Luenberger observer to estimate system states and a static feedback controller to compute the actuation commands.

Feedforward design The state reference x_{m} and the input reference u_{m} are obtained by solving the reduced model $G_r(s)$ at steady-state, i.e., $0 = A_r x_{\mathrm{m}} + B_r u_{\mathrm{m}}, y_{\mathrm{m}} = C_r x_{\mathrm{m}}$, as:

$$\begin{bmatrix} x_{\mathrm{m}} \\ u_{\mathrm{m}} \end{bmatrix} = \begin{bmatrix} A_r & B_r \\ C_r & 0 \end{bmatrix}^{-1} \begin{bmatrix} 0 \\ I \end{bmatrix} y_{\mathrm{m}} \tag{3.31}$$

where y_{m} represents the controlled output reference.

Luenberger observer The LQI control requires the knowledge of system states that may not be measurable in plasma experiments. However, an observer can be designed to estimate them if the system is observable. In our study, a simple Luenberger observer is employed as:

$$\dot{\hat{x}} = A_r\hat{x} + B_r u + L(y - C_r\hat{x}) \tag{3.32}$$

where u, y and $\hat{x}$ are the measured inputs, the measured outputs and the state estimates, respectively. L is a tuning gain matrix chosen to artificially place the eigenvalues of the estimation error dynamics such that the state estimates can converge exponentially faster than the system evolution.

Feedback design The LQI feedback commands $u_{\mathrm{fb,LQI}}$ are computed by minimizing a cost function $J_{\mathrm{fb,LQI}}$ that penalizes both the state errors, the output error integrals and the control inputs as:

$$\arg\min_{u_{\mathrm{fb,LQI}}} J_{\mathrm{fb,LQI}} = \frac{1}{2}\int_{t_0}^{\infty} (e_a^T Q e_a + u_{\mathrm{fb,LQI}}^T R u_{\mathrm{fb,LQI}})dt \tag{3.33}$$

where $Q^T = Q \geq 0$ is a weighting matrix for the state errors $x_{\mathrm{err}} = x_{\mathrm{m}} - \hat{x}$ and the output error integrals $z = \int_0^t (y_{\mathrm{m}} - y)dt$. $R^T = R > 0$ is a weighting matrix for the control inputs. $e_a = [x_{\mathrm{err}}^T, z^T]^T$ and $u_{\mathrm{fb,LQI}}$ represents the optimal feedback commands, parameterized as $u_{\mathrm{fb,LQI}} = -K_{\mathrm{fb,LQI}} e_a$. The feedback synthesis objective is to obtain an optimal gain matrix $K_{\mathrm{fb,LQI}}$ that minimizes Eq. (3.33). To compute $K_{\mathrm{fb,LQI}}$, we first augment the plasma plant with a vector of additional states z as:

$$\begin{bmatrix} \dot{x} \\ \dot{z} \end{bmatrix} = M_A \begin{bmatrix} x \\ z \end{bmatrix} + M_B u + M_W y_{\mathrm{m}} \tag{3.34}$$

where

$$M_A = \begin{bmatrix} A & 0 \\ -C & 0 \end{bmatrix}, M_B = \begin{bmatrix} B \\ 0 \end{bmatrix}, M_W = \begin{bmatrix} 0 \\ I \end{bmatrix} \tag{3.35}$$

Given the augmented system matrices, the optimal gain matrix is then expressed as $K_{\mathrm{fb,LQI}} = -R^{-1}M_B^T P$, where P is a symmetric positive-definite matrix that satisifies an algebraic Riccati equation [Skogestad and Postlethwaite, 2007] as:

$$PM_A + M_A^T P - PM_B R^{-1} M_B^T P + Q = 0 \tag{3.36}$$

The optimal feedback commands are thus calculated as $u_{\mathrm{fb,LQI}} = K_{\mathrm{fb,LQI}}(y_{\mathrm{m}} - y + y_{\mathrm{aw}}), u_{\mathrm{fb,LQI}} \in \mathbb{R}^{n_u}, y_{\mathrm{m}}, y, y_{\mathrm{aw}} \in \mathbb{R}^{n_y}$, where y_{aw} are the anti-windup compensated components [Wang et al., 2021]. Combining the feedforward u_{m} and feedback commands $u_{\mathrm{fb,LQI}}$, the LQI control inputs are $u_{\mathrm{LQI}} = u_{\mathrm{fb,LQI}} + u_{\mathrm{m}}$.

3.2.2.4 Observer-based IMC kinetic control design

IMC is a robust control technique first proposed in [Garcia and Morari, 1982]. The key idea of IMC resides in the internal model principle, stating that control can be achieved only if the

control system involves, either implicitly or explicitly, some representation of the controlled process [Saxena and Hote, 2012]. IMC has a simple design procedure providing a tradeoff between closed-loop performance and robustness to model inaccuracies with a single tuning parameter, which explains why it has found widespread applications [Harnefors and Nee, 1998, Narayanan et al., 1997, Yazdanian and Mehrizi-Sani, 2014]. The concept of IMC has already been used in tokamak plasma control, in which a typical example is the design of an anti-windup compensator to handle the actuator saturations [Wang et al., 2021]. Nonetheless, a pivotal drawback of the standard IMC lies in its restrictive applicability to an internally stable system, implying that control of unstable plasma phenomena such as vertical instability [Qiu et al., 2016, Gruber et al., 1993] using IMC seems unfeasible. Inspired by [Pannocchia and Heath, 2020, Heath et al., 2017], we develop an offset-free IMC control algorithm based on a PI observer for plasma kinetic tracking, which can potentially be adapted to control unstable and marginally stable plasma dynamics. The design of the observer-based IMC controller is composed of three steps: First, we use a Luenberger observer to estimate the states and disturbances. Second, we design a state feedback controller to stabilize the system dynamics. Third, a standard IMC control is adopted to achieve desirable control performance.

State and disturbance estimation To estimate the system states and disturbances, we assume constant system disturbances, i.e. $\dot{d} = 0$ [Pannocchia and Heath, 2020], and extend the reduced model Eq. (3.30) as:

$$\begin{aligned} \dot{x} =& A_r x + B_r u + B_d d \\ \dot{d} =& 0 \\ y =& C_r x + C_d d \end{aligned} \tag{3.37}$$

where $x \in \mathbb{R}^{n_x}, u \in \mathbb{R}^{n_u}, d \in \mathbb{R}^{n_d}, y \in \mathbb{R}^{n_y}$ are respectively the states, the inputs, the disturbances and the outputs. B_d and C_d are coefficient matrices to be determined. To guarantee the detectability of the augmented plasma model, we must prescribe the matrices (B_d, C_d) to satisfy the condition $\operatorname{rank} \begin{bmatrix} A & B_d \\ C & C_d \end{bmatrix} = n_x + n_d$. By setting $B_d = 0, C_d = I$, the disturbances at the output are observed, while by prescribing $B_d = B_p, C_d = 0$, the disturbances at the input are estimated. In this study, we choose the former setup, i.e. $B_d = 0, C_d = I$.

Combining the states x and the disturbances d into a state vector, i.e. $X = [x^T, d^T]^T$, we formulate the extended model in a compact form as:

$$\begin{aligned} \dot{X} =& A_e X + B_e u \\ y =& C_e X \end{aligned} \tag{3.38}$$

where $A_e = \begin{bmatrix} A_r & B_d \\ 0 & C_d \end{bmatrix}$, $B_e = \begin{bmatrix} B_r \\ 0 \end{bmatrix}$, $C_e = \begin{bmatrix} C_r & C_d \end{bmatrix}$.

The Luenberger observer is then expressed as:

$$\begin{aligned} \dot{\hat{X}} &= A_e \hat{X} + B_e u + L(y - \hat{y}) \\ \hat{y} &= C_e \hat{X} \end{aligned} \tag{3.39}$$

where $\hat{X} = [\hat{x}^T, \hat{d}^T]^T$ represents the estimate of X while $\hat{y}$ denotes the estimate of y. L is a gain matrix that can be tuned by placing the eigenvalues of A_e.

State feedback stabilization With the given observer, the states and disturbances can therefore be estimated in real-time. To stabilize the plasma plant, we use the reduced model to design a state feedback controller, parameterized as $u_{\mathrm{sf}} = -F_{\mathrm{sf}}\hat{x}$. F_{sf} is a static gain matrix to place the system poles to desirable stable region (with negative real eigenvalues), which is a crucial trick for control of unstable or marginally stable plasma dynamics [Pannocchia and Heath, 2020].

Offset-free internal model control The offset-free IMC control inputs comprise the standard IMC control component u_{sIMC} for disturbance rejection, the state feedback component u_{sf} for state stabilization and the preset feedforward component u_{m}, which reads:

$$u_{\mathrm{IMC}} = u_{\mathrm{sIMC}} - u_{\mathrm{sf}} + u_{\mathrm{m}} \tag{3.40}$$

where $u_{\mathrm{sIMC}} = Q(s)(r - M\hat{d})$, in which the to-be-designed terms include a stable transfer matrix $Q(s)$ and a static gain matrix M. To design them, we formulate the stabilized plasma dynamic model $G_{\mathrm{sf}}(s)$ and the disturbance dynamic model $G_{\mathrm{dist}}(s)$ as:

$$G_{\mathrm{sf}}(s) = \left[\begin{array}{c|c} A_r - F_{\mathrm{sf}}B_r & B_r \\ \hline C_r & 0 \end{array}\right], G_{\mathrm{dist}}(s) = \left[\begin{array}{c|c} A_r - F_{\mathrm{sf}}B_r & B_d \\ \hline C_r & C_d \end{array}\right] \tag{3.41}$$

IMC requires the steady-state gain of the open-loop transfer matrix to be an identity matrix, i.e. $G_{\mathrm{sf}}(0)Q(0) = I$. For simplicity, we design $Q(s) = F(s)G_{\mathrm{sf}}(0)^{\dagger} = -F(s)\left(C_r\left(A_r - F_{\mathrm{sf}}B_r\right)^{-1}B_r\right)^{\dagger}$, where $\dagger$ represents the pseudoinverse. The lowpass filter transfer matrix $F(s)$ is expressed as $F(s) = \mathrm{diag}\left(f_1(s), \ldots, f_{n_u}(s)\right), f_k(s) = \frac{1}{(\lambda_k s+1)}, k = 1, 2, \ldots, n_u$, in which λ_i are free parameters to be tuned [Pannocchia and Heath, 2020]. The static gain matrix M is designed as $M = G_{\mathrm{dist}}(0) = -C_r(A_r - F_{\mathrm{sf}}B_r)^{-1}B_d + C_d$.

3.2.2.5 SIMC PI actuation control design

In order to characterize the experimental conditions for H&CD actuation in tokamak plasma operation, actuator dynamics are considered to develop a set of actuator controllers to track the commands requested by an inner-layer kinetic controller. We assume that the additional heating power dynamics can be modelled as a set of first-order transfer functions with time-delay as:

$$G_{\mathrm{outer},i}(s) = \frac{k_i}{\tau_i s + 1} e^{-\theta_i s}, i \in \{\mathrm{ICRH}, \mathrm{LHCD}\} \tag{3.42}$$

where i is an indicator for an H&CD actuator, k_i denoting the steady-state gain for the i-th actuator, τ_i the characteristic time for the i-th actuator, while θ_i represents the time delay for the i-th actuator. $G_{\mathrm{outer},i}(s)$ is a transfer function for the i-th actuator determined by

three model parameters, i.e. k_i, τ_i and θ_i. These model parameters can easily be identified from the observed input-output data in dedicated plasma experiments using the subspace and prediction-error methods [Ljung, 1995].

Once the actuator dynamics are characterized by a simple model structure as shown in Eq. (3.43), we can then use a tuning rule based on the internal model principle to design an outer-layer PI actuator controller [Skogestad and Postlethwaite, 2007] . We define $u_{\text{inner},i}(t)$ as the command requested by the inner-layer kinetic controller for the i-th actuator controller and $u_{\text{mea},i}(t)$ as the corresponding measured actuation for the i-th actuator. The actuation tracking error $e_{\text{outer},i}$ is thus computed as $e_{\text{outer},i} = u_{\text{inner},i}(t) - u_{\text{mea},i}(t)$. The commands requested by the actuator controller for each H&CD systems $u_{\text{outer},i}(t)$ are then expressed as:

$$u_{\text{outer},i}(t) = -K_{\text{p,i}} e_{\text{outer},i} - K_{\text{I,i}} \int_0^t e_{\text{outer},i} dt + u_{\text{offset},i}, i \in \{\text{ICRH}, \text{LHCD}\} \tag{3.43}$$

in which

$$K_{p,i} = \frac{\tau_i}{k_i(\tau_{c,i} + \theta_i)}, K_{I,i} = \frac{K_{p,i}}{\tau_{I,i}}, \tau_{I,i} = \min\{\tau_i, (\tau_{c,i} + \theta_i)\} \tag{3.44}$$

where $K_{p,i}$ and $K_{I,i}$ are the proportional and integral gains for the i-th actuator, respectively. $u_{\text{offset},i}$ denotes the i-th reference value around which the actuator model $G_{\text{outer},i}(s)$ is identified. $\tau_{c,i}$ is a tuning parameter for the i-th actuator, which provides a trade-off between control performance and robustness against disturbances. More precisely, increasing $\tau_{c,i}$ can result in the growth of the response time but the control robustness can thus be improved, and it is suggested to have $\tau_{c,i} \geq \theta_i$. We emphasize that, in order to guarantee the actuation tracking performance, the sampling time for the actuator controllers (typically at 1 ms on EAST) should be smaller than the characteristic time for each H&CD systems and far less than that for the kinetic controller ($\sim \tau_E$).

3.2.3 Simulation results

We now demonstrate the effectiveness of the two-layer kinetic control scheme and compare the performance and robustness of the alternate real-time kinetic controllers on EAST using the METIS code [Artaud et al., 2018]. First, we show the performance of nominal tracking of three essential plasma kinetic parameters, namely the poloidal beta β_p, the average toroidal angular rotation velocity Ω_ϕ and the central electron temperature $T_{e,0}$ by actuating the ion ICRH power P_{IC} and the LHCD power P_{LH}, enabled by three optional kinetic controllers, i.e. $\mathcal{H}_\infty$ robust, LQI and the observer-based IMC, and two SIMC PI power controllers for ICRH and LHCD, respectively. Second, the robustness tests, under the variations of the line-averaged electron density $\langle \bar{n}_e \rangle$ and effective ion charge Z_{eff}, are conducted and compared.

3.2.3.1 METIS simulation setup and control configuration

The two-layer cascade control architecture is first developed and implemented in the MATLAB/Simulink environment, which is then coupled with METIS [Artaud et al., 2018], for

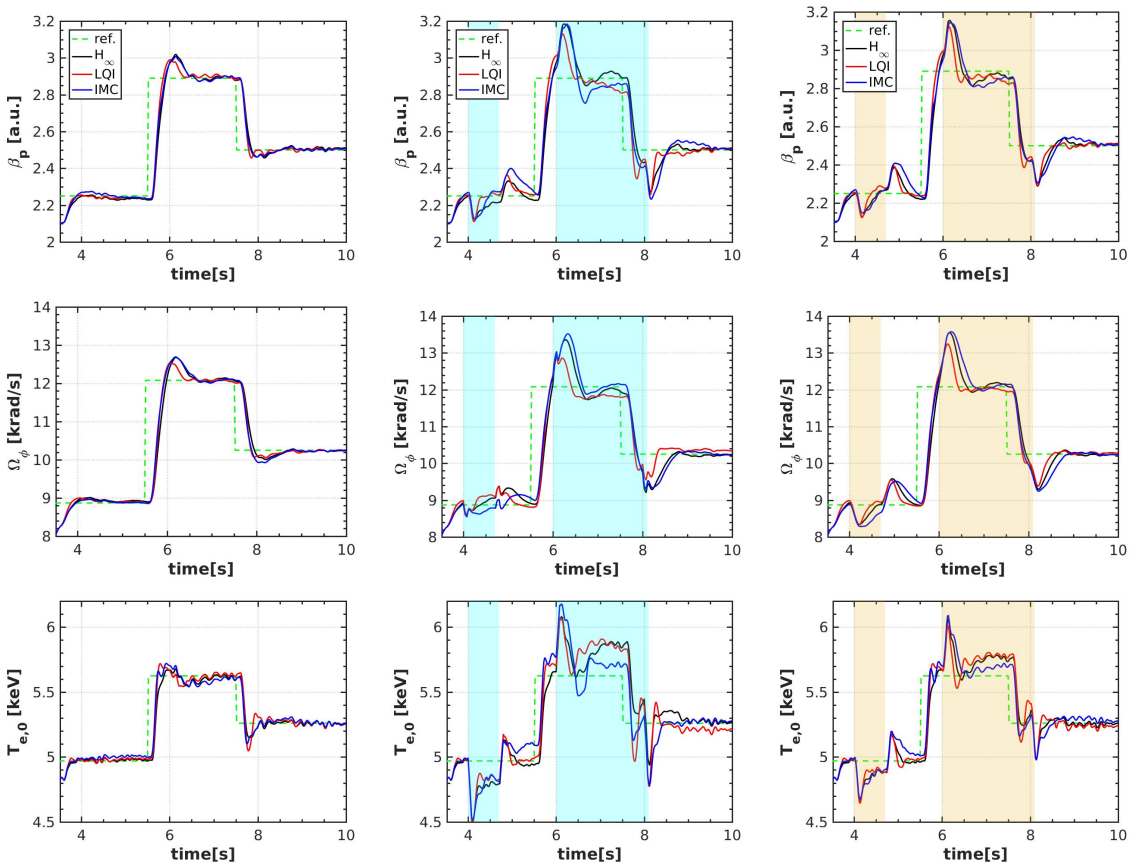

Figure 3.17: Tracking of plasma kinetic parameters with three alternative real-time feedback algorithms. (a)-(c): tracking of (a) β_p, (b) Ω_ϕ and (c) $T_{e,0}$ values in the nominal case. (d)-(f): tracking of (d) β_p, (e) Ω_ϕ and (f) $T_{e,0}$ values by perturbing $\langle\overline{n_e}\rangle$. (g)-(i): tracking (g) β_p, (h) Ω_ϕ and (i) $T_{e,0}$ values by perturbing Z_{eff}.

closed-loop control assessments. The reference scenario around which the model is identified is a steady state, fully non-inductive single-null H-mode discharge in the EAST tokamak, i.e. shot #62946, with the toroidal magnetic field $B_T = 2.5$ T, the central electron density $n_{e0} \approx 3.5 \times 10^{19}$ m^{-3} and plasma current $I_p = 0.42$ MA. More details about the METIS setup is given in Section 1 of the chapter. The three alternative kinetic feedback control algorithms are designed and implemented based on a LSS model identified from extensive dedicated simulations via the subspace and predition-error methods given in Chapter 2. The actuators, the ICRH and LHCD powers, are allowed to vary in the ranges of $[0, 1.5]$ MW and $[0, 3.0]$ MW, respectively. As illustrated in Fig. 3.17, the plasma kinetic control scheme is separated into two control layers with two timescales: in the outer layer, the powers coupled to the plasma, from the ICRH and LHCD systems, are tracked in the fast timescale with the sampling frequency at 1kHz; in the inner layer, the kinetic parameters are controlled simultaneously by an alternate kinetic controller in the slow timescale with the sampling frequency at 50 Hz (larger than $\frac{1}{\tau_E}$). The actuator dynamics for the ICRH and LHCD systems are modelled by two separate first-order time-delay transfer functions, respectively. Guided by the experimental data on

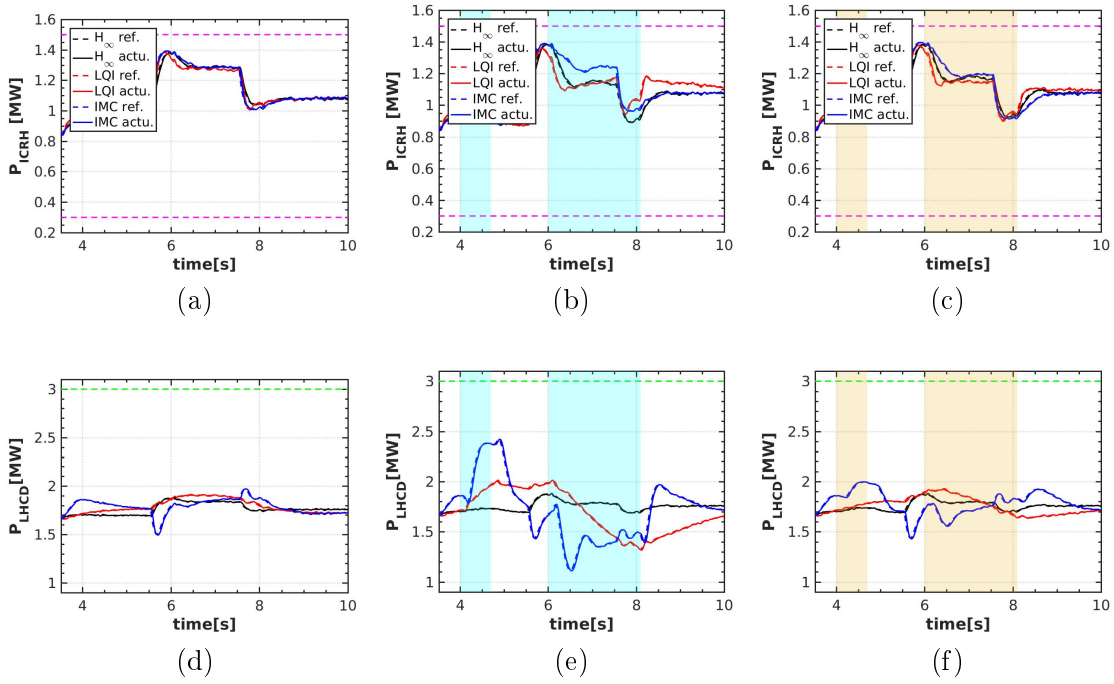

Figure 3.18: Tracking of the powers coupled to the plasma from the additional heating & current drive systems. (a)-(c): time traces of the ICRH power request (dashed) and the actuated ICRH power (solid) with the $\mathcal{H}_\infty$ (black), LQI (red) and IMC (blue) controllers in the nominal case (a), the $\langle\overline{n_e}\rangle$ perturbing case (b) and the Z_{eff} perturbing case. (d)-(f): time traces of the LHCD power request (dashed) and the actuated LHCD power (solid) with the $\mathcal{H}_\infty$ (black), LQI (red) and IMC (blue) controllers by perturbing Z_{eff}.

EAST, the actuation time constants for the ICRH and LHCD systems are chosen to be 5 ms, and the effective time delay for the actuators is uniformly set at 2 ms, while the steady-state gains are prescribed to be 1. With the actuator dynamics models, two separate SIMC PI power controllers are thus synthesized, with $\tau_{c,i} = 0.005$ s and $\theta_i = 0.002$ s for both actuators ($i \in \{\text{ICRH}, \text{LHCD}\}$). Note that the actuator control parameters can be adjusted according to the specific control requirements. In order to mimick the experimental conditions, white noise with power magnitude at 10^{-6} is imposed onto the measured powers obtained from the simple actuator dynamics models. The noise is thus handled by a moving average filter with the time horizon at 10 ms. Three alternative kinetic controllers were designed with the same linear state-space model. For the $\mathcal{H}_\infty$ controller, a desired closed-loop bandwidth is prescribed to be 0.15π, and the parameters A and M are respectively set at 2 and 10^{-6}. For the LQI controller, the weighting gains for the states, controlled variables and manipulated variables are optimized to achieve the desired control performance. For the IMC controller, the tuning parameter, the time constant, in the low pass filter τ_{IMC}, is prescribed at 0.08 s.

3.2.3.2 Nominal tracking in the current flat-top phase

The three alternative control schemes were used to track β_p, Ω_ϕ and $T_{e,0}$ simultaneously by actuating the ICRH and LHCD powers. All the feedback controllers are activated at 3.5 s in the current flattop phase. Three sets of reference setpoints for β_p, Ω_ϕ and $T_{e,0}$ are prescribed to be tracked. Fig. 2(a)-(c) shows the comparison of the kinetic parameter evolutions with three alternative control algorithms. It is evident that all the kinetic controllers based on the same data-driven model are capable of tracking the plasma parameters of interest effectively and comparable control performance has been obtained. One can notice that there are some small oscillations even at steady-state for $T_{e,0}$, primarily due to the measurement noise imposed on P_{ICRH} and P_{LHCD}. Compared with the other kinetic parameters, the evolution of $T_{e,0}$ is very sensitive to the evolution of additional heating powers. The requested (dashed) and actuated (solid) powers by these control schemes are shown in Fig. 3(a) and 3(d). We find that the SIMC PI power feedback controller can satisfactorily track the requested powers by the inner-layer kinetic controllers in three different cases. The requested powers are at similar levels in all the control schemes for the ICRH system, but differ in the LHCD system, implying that the ICRH system plays the dominant role in the kinetic control for parameters that do not depend strongly on the current density profile such as β_p, Ω_ϕ and $T_{e,0}$.

3.2.3.3 Robustness to plasma parameter uncertainties

In order to further evaluate the robustness of each controllers, we perform closed-loop METIS simulations with the control algorithms in which we perturbed a number of important plasma parameters at selected time intervals. Fig. 2(d)-(f) shows comparison of the kinetic parameter evolutions with the $\mathcal{H}_\infty$, LQI and IMC controllers under the perturbation of the averaged electron density. Particularly, in the time interval [4.0, 4.65]s, the value of $\langle \bar{n}_e \rangle$ is increased by a fraction of 10 %, which leads to the decrease of β_p, Ω_ϕ and $T_{e,0}$. In order to attenuate the disturbances, the feedback controllers request more powers on the ICRH and/or LHCD systems as shown in Fig. 3(b)-3(e). Within 0.3 s the disturbances on β_p are fully compensated while the disturbances on Ω_ϕ and $T_{e,0}$ are attenuated effectively. After 4.65 s, $\langle \bar{n}_e \rangle$ returns to the initial value, which results in the increase of β_p, Ω_ϕ and $T_{e,0}$. These new disturbances are successfully attenuated by the $\mathcal{H}_\infty$ and LQI controllers, but not with the IMC controller. In the time interval [6.0,8.1]s, $\langle \bar{n}_e \rangle$ is artificially decreased by 10 %, leading to the increase of the plasma parameters of interest. These $\langle \bar{n}_e \rangle$-driven disturbances on the controlled parameters are attenuated by decreasing the ICRH power except $T_{e,0}$, possibly arising from the considerable model mismatch and the variation of the achievable control region in $T_{e,0}$. After 8.1 s, $\langle \bar{n}_e \rangle$ returns to the intial value, the disturbances on β_p, Ω_ϕ and $T_{e,0}$ are successfully rejected by all the proposed control schemes.

Comparison of the kinetic parameter evolutions with the proposed control algorithms under the perturbation of the effective ion charge are shown in Figs. 2(g) - (i). Analogously, in the time interval [4.0,4.65]s, Z_{eff} is artificially increased by 10 %, which makes all the kinetic control variables drop. Results indicate that all the control schemes are capable of rejecting the disturbances arising from the Z_{eff} increase by adjusting the ICRH and LHCD powers (See

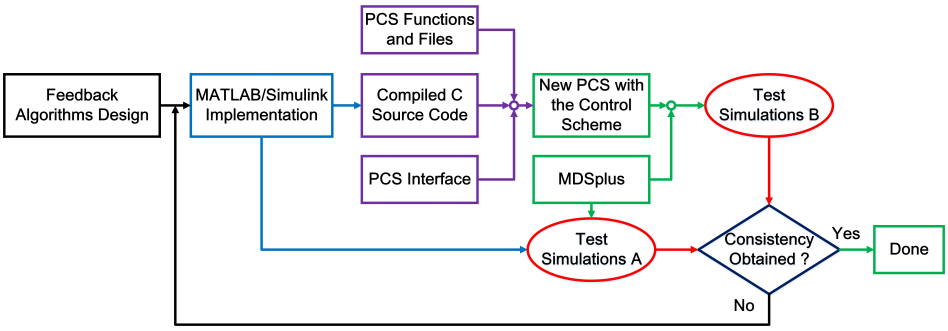

Figure 3.19: Diagram showing the procedure for the kinetic control algorithm implementation into the PCS.

Fig. 3(c)-(f)). In the time interval [6.0,8.1], Z_{eff} is artificially reduced by 10 %, which makes all the kinetic control variables grow. Similarly, results suggest that all the controllers can fairly attenuate the disturbances caused by the Z_{eff} decrease.Similarly, the attenuation of $T_{e,0}$ disturbance driven by the Z_{eff} variation is not satisfactory in the period [6,8] s, which may be explained by the enhanced model mismatch.

3.2.4 EAST experiments

In order to further evaluate and compare the performance of the proposed kinetic control scheme and algorithms, dedicated experiments have been performed in an H-mode operational scenario on the EAST tokamak, with the goal of tracking β_p, li and P_{LHCD} by adjusting the LHCD power command in real-time.

3.2.4.1 Control algorithm implementation in the PCS

Fig. 4 shows a procedure on how real-time feedback control algorithms can be implemented into the EAST plasma control system (PCS). We first develop the kinetic control algorithms in the MATLAB/Simulink environment, which are subsequently transformed into the C/C++ programming language using the embedded MATLAB coder (EMC) toolbox. Afterwards, the generated code is coupled with the PCS and jointly compiled for real-time application. The effectiveness of the algorithm implementation can be verified by performing test simulations via the EAST data simserver. Specifically, by feeding the same real-time EFIT estimates from a typical EAST plasma discharge to both versions of the kinetic control scheme, one implemented in MATLAB/Simulink and the other being coupled with the EAST PCS, the simulated outputs from both versions should be consistent with each other. This was checked, proving that no issues have appeared in the course of the control algorithm implementation in the PCS.

3.2.4.2 Diagnostics, actuators and experimental setup

Plasma parameters/profiles such as β_p and li are estimated by the GPU-accelerated real-time equilibrium reconstruction code, P-EFIT [Huang et al., 2020]. The POlarimeter-INTerferometer (POINT) diagnostic measures the plasma electron density [Qian et al., 2016, Liu et al., 2016b], regulated in real-time by a dedicated PID controller in the PCS. Due to reliability issues with the polarimeter diagnostic, the internal poloidal field measurements are not available for the P-EFIT reconstruction. Plasma current, position and shape are regulated by a set of feedback control algorithms in the PCS [Yuan et al., 2013]. The controlled parameters, β_p, li and the coupled power P_{LHCD}, are fed to the kinetic control scheme every 1 ms (outer-layer sampling time) to generate a power command for a control actuator, in which the kinetic control algorithms are activated every 20 ms (inner-layer sampling time). The measurement noise is handled by a moving average filter with a time horizon of 10 ms [Ljung, 1995]. The control actuator is the LHCD system at 4.6 GHz with coupled powers between 1.0 MW and 2.5 MW, tracked in real-time by a SIMC PI power feedback controller. We note that the minimum LHCD power is preset at 1.0 MW to guarantee that the plasma maintains in H-mode, without any H-L/L-H transitions in the course of control. The LHCD power dynamics at 4.6GHz is approximated by a first-order time-delay transfer function (See Eq. (D.1)) with its model coefficients identified from typical experimental data on EAST. Given the model coefficients, a SIMC PI rule is then adopted, resulting in a set of actuator feedback control coefficients as $K_{\mathrm{p,LHCD}} = 0.41$, $K_{\mathrm{I,LHCD}} = 343.69$, $u_{\mathrm{offset,LHCD}} = -0.45$, together with a static feedforward $K_{\mathrm{ff}} = 1.38$ to enhance the transient performance. The LHCD power actuation time delays are dealt with by a Smith predictor, with the prediction model as $G(z) = \frac{0.4141}{z-0.4307}$, where z refers to the Z-transform, and the estimated pure time delay at 2 ms. The PCS power command to the LHCD system is restricted to the range from 1 V to 3 V. Hence, an anti-windup module [Wang et al., 2021] is used to compensate the LHCD power command saturation. All the control references and coefficients are prescribed offline and loaded into the PCS before performing the experiments.

In the experimental study, the current flat-top phase of a pure radio-frequency (RF) upper-single-null (USN) H-mode plasma discharge is considered as the reference scenario, particularly with the toroidal field at 2.5 T, the plasma current at 350 kA, the central electron density at $\sim 4.2 \times 10^{19}$ m^{-3} and the central electron temperature at ~ 4 keV. In addition to the 4.6 GHz LHCD power, some LHCD power is injected at 2.45 GHz for current drive in the ramp-up phase, specifically 0.6 MW in the period [0.95, 2.25] s. Moreover, 0.9 MW of ECRH power is actuated during the current flat-top phase (in the time interval [1.98, 7.91] s) from two gyrotrons at 140 GHz to heat the plasma and maintain it in H-mode. The ICRH system is not available during the entire experiments.

The kinetic feedback control experiments are divided into two stages: first, the identification experiment is carried out to collect a set of sampled data for identification of a plasma dynamic model used for feedback control design; second, the performance of the real-time control algorithms is demonstrated experimentally.

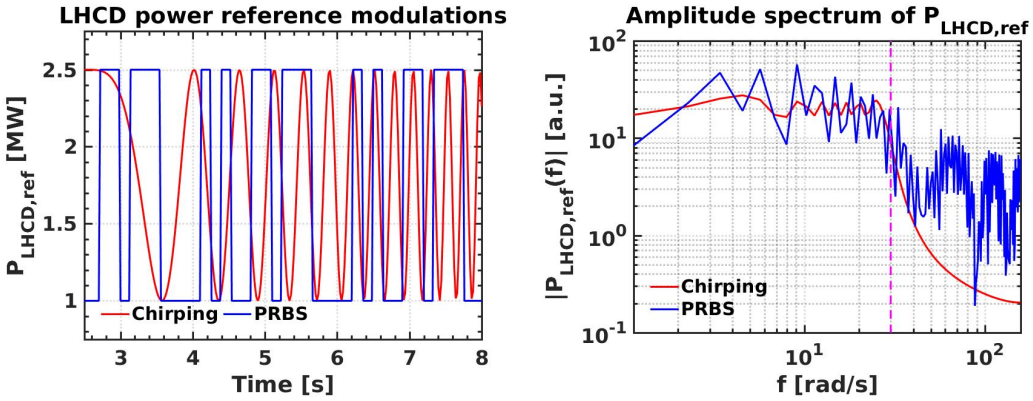

Figure 3.20: Design of LHCD power reference modulations to excite the dominant plasma eigenmodes. Upper panel: comparison of the $P_{\text{LHCD,ref}}$ modulations in chirping (red) and PRBS (blue) signals. Bottom panel: comparison of the amplitude spectra of the $P_{\text{LHCD,ref}}$ modulations in chirping (red) and PRBS (blue) signals.

3.2.4.3 Plasma identification experiment

Since the LHCD power at 4.6 GHz is allowed to vary in real-time ranging from 1.0 MW to 2.5 MW and the dominant plasma kinetic eigenmode, $\sim \frac{1}{\tau_E}$, is estimated to be around 25 s^{-1}, the goal now is to design LHCD power reference waveforms that maximally excite the dominant magnetic and kinetic eigenmodes, as shown in Fig. 5, including the chirping and PRBS power modulations. Since the expected τ_E is around 0.04 s, the designed frequency bandwidth of the LHCD power references in both signals is therefore restricted to be less than 30 rad/s, as shown in Fig. 5(b). Using the SIMC PI power feedback controller as given in Section 5.2, the open-loop power modulation experiment has been carried out on the EAST tokamak, with the results depicted in Fig. 6. Evidently, the chirping power reference, ranging from 1.0 MW to 2.5 MW, for the LHCD system was satisfactorily tracked in shot #93297 (See Fig. 6(a)), with the plasma parameters of interest β_p, li and ι_0 sufficiently responsive as shown in Fig. 6(b). In particular, β_p ranges from 1.5 to 1.9, li spreading from 0.9 to 1.2, while ι_0 lies in the interval [0.3, 0.5]. It is found that both li and ι_0 exhibit linear downward drifts, probably because of the transmission of the magnetic probing faults mounted at the plasma boundary to the P-EFIT equilibrium reconstruction. We remark that in the interval [2.5, 3.5] s, the LHCD system at 4.6 GHz made an actuation fault, which explains why the LHCD power reference cannot be well tracked in this period. Fig. 4(c)-4(d) shows another plasma power modulation discharge, with the PRBS power reference tracked using the same power feedback controller. One can notice that the responses of β_p, li and ι_0 with respect to the LHCD power are persistently exciting for model identification, and the systematic linear downward drifts occurring in li and ι_0 should bring some issues on their feedback control.

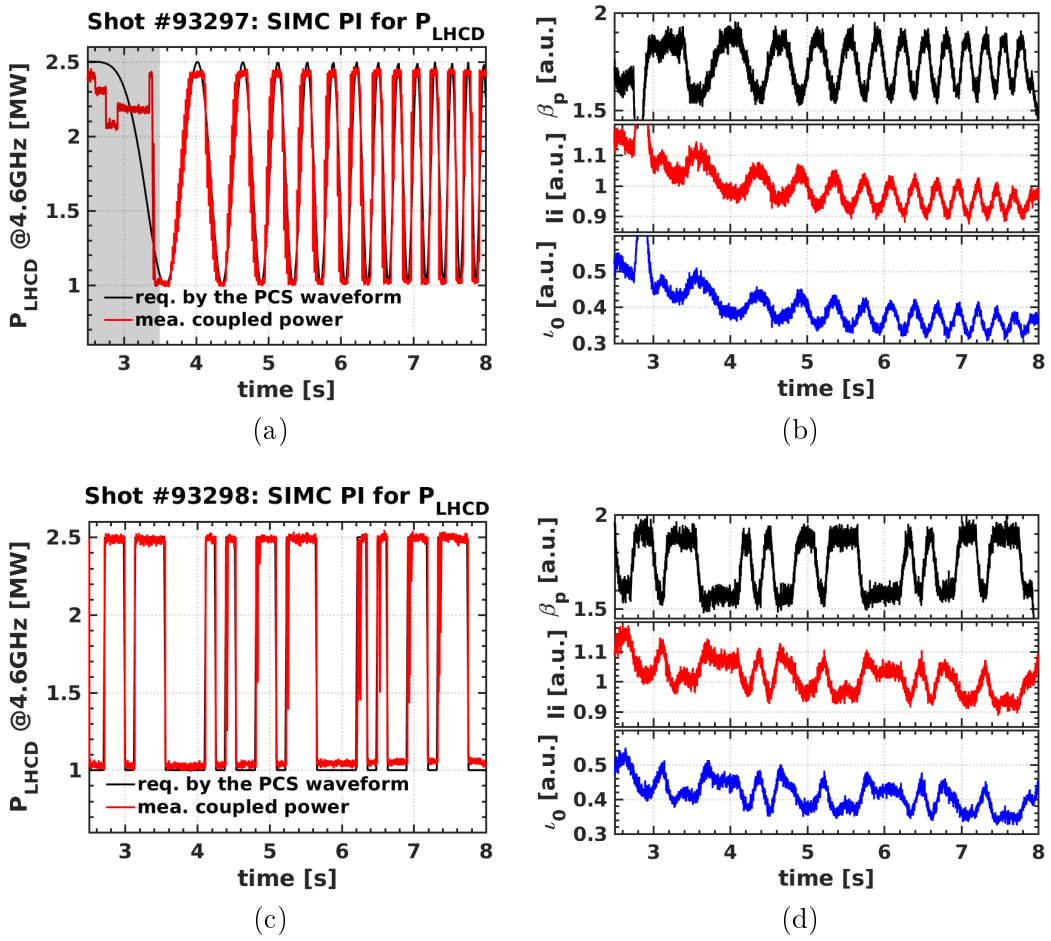

Figure 3.21: Plasma identification experiment showing the responses of β_p, li and ι_0 to the $P_{\mathrm{LHCD@4.6GHz}}$ modulations on EAST. Upper panels: time traces of the (a) $P_{\mathrm{LHCD@4.6GHz}}$ modulations in a chirping frequency waveform, tracked by a SIMC PI power controller, and of (b) β_p (top), li (middle) and ι_0 (bottom) estimates by P-EFIT. Lower panels: time traces of the $P_{\mathrm{LHCD@4.6GHz}}$ modulations in a PRBS waveform and of (d) β_p (top), li (middle) and ι_0 (bottom) estimates by P-EFIT. Shaded gray region indicates that the LHCD system made faults and saturated.

3.2.4.4 Control assessment with the ARTAEMIS plasma simulator

By adopting the system identification methodology used in [Moreau et al., 2008,Moreau et al., 2011], a two-time-scale data-driven model that describes the responses of β_p, li and ι_0 to the LHCD power has been identified from the power modulation data, containing five slow eigenmodes and one fast eigenmode. More precisely, the characteristic times for the slow τ_{S} and fast τ_{F} dynamics are 1.05 s and 0.017 s, respectively. The identified two-time-scale model was then transformed into a standard linear state-space (LSS) model by inserting a lowpass filter with $\tau_{\mathrm{filt}} = 0.1$ s at the control input. After model reduction, three alternative controllers described in Appendices are therefore designed using the reduced model. Table 1

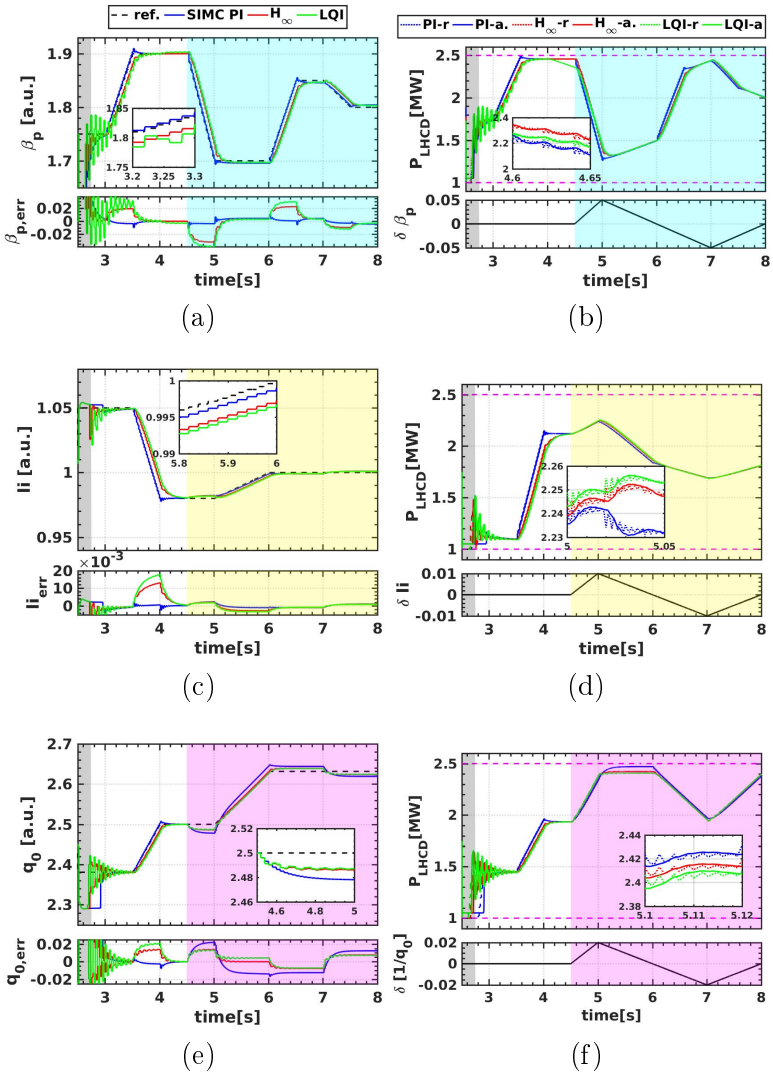

Figure 3.22: Simulated tracking of β_p, li and q_0 by actuating P_{LHCD} using the ARTAEMIS plasma simulator [Moreau et al., 2011]. Top panels: time evolutions of (a-top) β_p and (a-bottom) its tracking error $\beta_{p,\mathrm{err}}$, and of (b-top) the LHCD power P_{LHCD} and (b-bottom) vitual β_p disturbance, $\delta\beta_p$. Middle panels: time evolutions of (c-top) li and (c-bottom) its tracking error $\mathrm{li}_{\mathrm{err}}$, and of (d-top) the LHCD power P_{LHCD} and (d-bottom) li disturbance, δli. Bottom panels: time evolutions of (e-top) q_0 and (e-bottom) its tracking error $q_{0,\mathrm{err}}$, and of (f-top) the LHCD power P_{LHCD} and (f-bottom) q_0 disturbance, denoted as $\delta[\frac{1}{q_0}]$. Shade regions imply the existence of disturbances. All feedback algorithms were activated at 2.75 s. The blue, red and green lines correspond to the simulation results of the SIMC PI, $\mathcal{H}_\infty$ and LQI control, respectively. On the left, dashed black lines denote control targets. On the right, the dotted lines represent the LHCD power targets requested by a kinetic controller, while the solid lines are the achieved LHCD powers by a SIMC PI power controller.

lists the tuning parameters used for the kinetic controller design. The design of the SIMC

PI controller for each plasma kinetic parameters is performed separately by transforming the reduced model into a first-order transfer function with time delay ($\theta = 20$ ms). Prescribing the tuning parameter $\tau_c = 4\theta$, we therefore obtain the feedback coefficients K_p and K_i for β_p, li and ι_0, respectively. The feedforward gain G_{FF} is computed by simply inverting the model coefficient k_i as given in Eq. (D.1). The design of the $\mathcal{H}_\infty$ kinetic controller for each parameters is conducted subsequently, the weighting function $K_{\mathrm{S}} = \frac{s/M+w_b}{s+w_bA}$ is adjusted to shape the sensitivity functions, where the tuning of the closed-loop bandwidth ω_b is essential to balance the control performance and robustness. Finally, the design of the LQI kinetic controller for β_p, li and ι_0 is carried out, in which the tuning parameters Q_{s}, $Q_{\mathrm{o,int}}$ and R weigh the importance of the states, the output error integrals and the controlled inputs in the cost function $J_{\mathrm{fb,LQI}}$ as defined in Eq. (B.3), respectively. One can notice that the primary weights are put on the output error integrals to enable the transient control performance.

With the given control setup, the performance of each kinetic controllers is assessed using the identified linear two-time-scale model, simply called the ARTAEMIS model [Moreau et al., 2013], as a plasma simulator. The simulation results are shown in Fig. 7, indicating that all the controllers can achieve the effective tracking of β_p, li, $q_0(=\frac{1}{\iota_0})$ and P_{LHCD}, despite the presence of artificially prescribed disturbances. In the nominal cases, the performance of the SIMC PI controller outperforms that of the LQI and $\mathcal{H}_\infty$ controllers in both β_p, li and q_0 tracking, because its design primarily focusses on the fast integral control. In situations with disturbances, SIMC PI has the best robustness in β_p and li tracking due to its fast integral control, while LQI and $\mathcal{H}_\infty$ exhibit better robustness than SIMC PI in q_0 tracking because their designs account for the effect of slow plasma eigenmodes.

3.2.4.5 Closed-loop feedback control experiment

In the closed-loop control experiment, the performance of the two-time-scale cascade kinetic control scheme is further evaluated by tracking a plasma kinetic parameter and the coupled LHCD power simultaneously on the EAST tokamak.

The control of β_p using the SIMC PI tuning rule was performed experimentally in EAST shot #95195, with the feedforward and feedback gains shown in Table 1. A total of 5 targets, consistent with those used in ARTAEMIS simulations, were required to be achieved, sequentially 1.75, 1.90, 1.70, 1.85 and 1.80. Fig. 5(a)-(b) depict the evolution of β_p and the coupled LHCD power. Evidently, all the targets for β_p and P_{LHCD} were achieved using the cascade two-time-scale kinetic control scheme, despite the presence of the large measurement noise in β_p, except during the period [3.6, 4.8] s, when the LHCD actuator had an exceptional fault and was saturated to an upper limit lower than the expected value 2.5 MW. The control of β_p using the $\mathcal{H}_\infty$ kinetic controller was carried out in shot #95197, whose tuning parameters are listed in Table 1. The same SIMC PI power feedback controller was cascaded with the $\mathcal{H}_\infty$ kinetic controller while the same set of β_p targets were prescribed. The evolution of β_p and P_{LHCD} are shown in Fig. 5(c)-(d). Although all the targets were achieved, β_p exhibits an oscillatory trend and the tracking performance is not as good as in shot #95195, bacause of the β_p measurement noise and the LHCD power saturation. Comparing these two discharges,

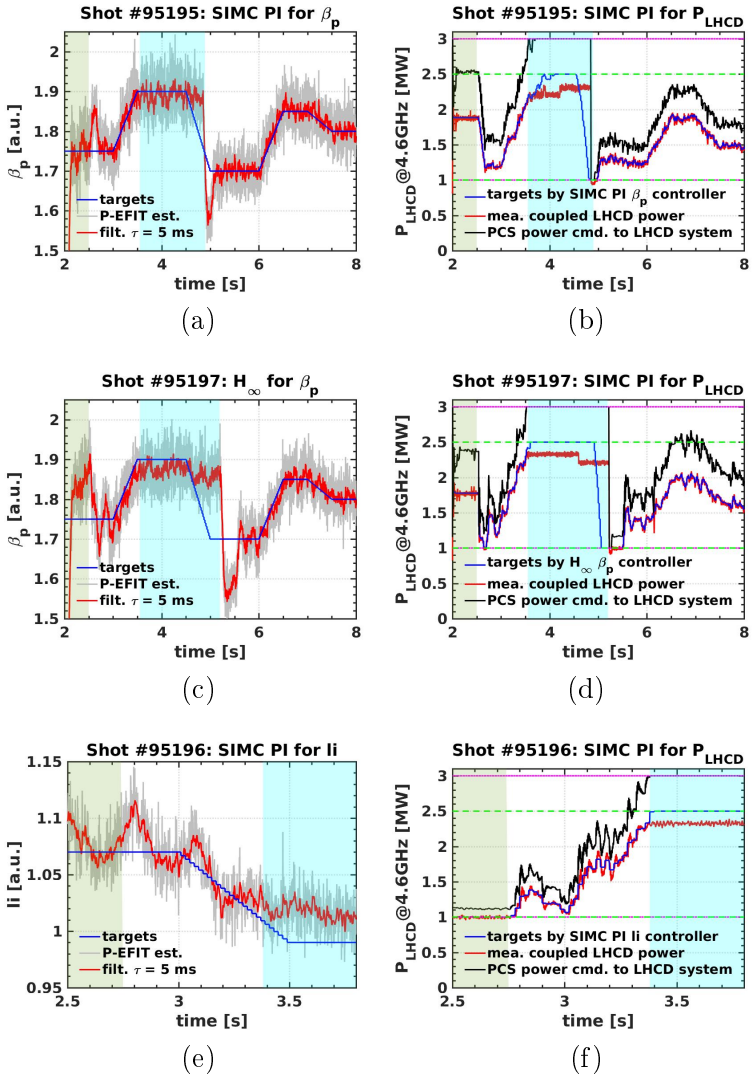

Figure 3.23: Plasma control experiments showing the tracking of β_p and li using the LHCD@4.6GHz power command on EAST. Upper and middle panels: time traces of (a, c) β_p targets (blue), P-EFIT estimate (gray) and lowpass filtered P-EFIT estimate (red), and of (b, d) the requested $P_{\mathrm{LHCD@4.6GHz}}$ (blue), the measured $P_{\mathrm{LHCD@4.6GHz}}$ (red) and the PCS power command to the LHCD system (black). β_p feedback was activated after 2.5 s right after the shaded light brown region. Bottom panels: time traces of li targets (blue), P-EFIT estimate (gray) and lowpass filtered P-EFIT estimate (red) and of the requested $P_{\mathrm{LHCD@4.6GHz}}$ (blue) and the measured $P_{\mathrm{LHCD@4.6GHz}}$(red) and the PCS power command to the LHCD system (black). li feedback started from 2.75 s right after the shaded light brown region. Shaded cyan region indicates the LHCD power was saturated. Magenta dotted lines represent the power command limits of the LHCD power controller, while green dashed lines denote the power request limits of the kinetic controller.

one can conclude that the SIMC PI controller performs slightly better than the $\mathcal{H}_\infty$ controller in the noise-corrupted experimental environment, consistent with the ARTAEMIS simulation result.

The control of li using the SIMC PI controller was performed in shot #95196, where two targets were prescribed, i.e. 1.07 and 0.99 and the SIMC PI kinetic controller gains for li are listed in Table 1. The same LHCD power feedback control algorithm and measurement preprocessing were configured. The evolution of li and P_{LHCD} are shown in Fig. 5(e)-(f). Analogous to β_p control, the signal-to-noise ratio (SNR) on li is still very large and the use of the moving average filter on li and P_{LHCD} turns out to be effective. As shown in Fig. 5(e), the first target was achieved with some oscillations, due to the presence of measurement noise and model uncertainties. Between 3.0 s and 3.5 s, the reference trajectory linearly dropped from 1.07 to 0.99 and the li controller was able to track the reference trajectories with some oscillations, until the LHCD power saturated at 2.3 MW. After 3.38 s, due to the power saturation, the second target could not be reached. As shown in Fig. 5(f), the LHCD power was precisely tracked via the inner-loop SIMC PI power feedback controller. One can notice that the attractive domain for li control is fairly narrow if only involving the LHCD power as the control actuator for li tracking. In addition, the measurement fault of the magnetic probes mounted at the plasma boundary is responsible for the unphysical linear drift of li, thus leading to the enhanced control difficulty. Involving more actuators such as the NBI systems is likely to broaden the attractive control region for li. Furthermore, it is anticipated that the removal of the measurement drift arising from the magnetic probing fault should make the li control more tractable.

3.2.5 Conclusion of Section 3.2

A two-layer kinetic control scheme has been proposed for plasma kinetic control in advanced tokamak scenarios. This control scheme is composed of an inner-layer with a set of alternate controllers to track plasma kinetic parameters of interest, and an outer-layer to preprocess the equilibrium measurements, compensate actuation saturations and track the requested additional heating powers. Taking advantage of the timescale separation property of the kinetic and additional power dynamics evolutions on the EAST tokamak, the kinetic control scheme uses two sampling frequencies, with the inner-layer at 50 Hz and the outer-layer at 1000 Hz. Even though the design of all these real-time kinetic feedback algorithms is based on a linear model identified from the sampled simulation/experimental data, the techniques can straightforwardly be extrapolated to cover those linear models obtained from the first-principles plasma theory. For comparison, three alternative kinetic controllers, the $\mathcal{H}_\infty$, LQI and observer-based IMC, are synthesized from the same reduced model, which are subsequently evaluated and compared in closed-loop METIS simulations. These nonlinear simulation results suggest that the proposed kinetic controllers can achieve the prescribed control targets of β_p, Ω_ϕ and $T_{e,0}$ using P_{IC} and P_{LH} simultaneously with comparable levels of performance and robustness, which are intimately related to the tuning parameters of each algorithms. This new control scheme has then been implemented into the EAST PCS using the EMC toolbox. Preliminary experiments on the EAST tokamak show that β_p, li and P_{LH} can successfully be tracked with

two simple kinetic controllers, SIMC PI and $\mathcal{H}_\infty$, with a 10 ms time-horizon moving average filter and a cascade SIMC PI power tracker. We conclude, from our simulations and initial experiments, that for an intrinsically stable SISO plasma control problem, it is advisable to start with a SIMC PI controller, as it is proven effective and easy to be designed, implemented and tuned experimentally; for an uncertain MIMO plasma control problem, the $\mathcal{H}_\infty$ robust kinetic controller is suggested because its design primarily focuses on enabling sufficient robustness against model uncertainties and meanwhile, its tuning is not very complicated.

In the future, extensive experimental tests on EAST are anticipated by involving more actuators and measurements, for example, the co-current NBI systems and the polarimeter/interferometer diagnostics. It would also be interesting to adopt adaptive laws to refine the control coefficients in real-time based on the observed input-output measurements. Furthermore, coordinating a set of local kinetic controllers for different operating points using gain scheduling can be explored easily under the proposed kinetic control scheme.

3.3 Summary of Chapter 3

In this chapter, robust control of q-profile and kinetic parameters in advanced tokamak scenarios based on linear data-driven models has been investigated. It consists of two major parts: the first part shows that simultaneous control of q-profile and β_p in an H-mode steady-state scenario on EAST can be achieved by a decentralized $\mathcal{H}_\infty$ control scheme synthesized from a two-time-scale data-driven model. A systematic feedback control synthesis is proposed and beneficial control implementation techniques are elaborated. Extensive closed-loop nonlinear METIS simulations have demonstrated the validity of the proposed control scheme. The second part primarily focusses on the comparison of the performance and robustness of three linear kinetic control algorithms, namely $\mathcal{H}_\infty$, LQI and IMC. In order to enhance actuation tracking, cascade actuator controllers based on the SIMC PI tuning rule are designed and implemented, running in a much faster timescale and proving effective in both METIS simulations and EAST experiments. Future works entail the development of robust control schemes synthesized from a nonlinear dynamic model such as a PNLSS model as depicted in Chapter 2. More extensive experiments on EAST are foreseen to sort out an optimal control scheme among a set of candidates for routine tokamak plasma operation. In Chapter 4, some contributions will be made regarding the use of online parametric adaptation for the characterization and compensation of plasma model uncertainties with a series of adaptive control laws.

Chapter 4

Adaptive Control

Contents

The confinement performance of a tokamak plasma is characterized by a variety of magnetic and kinetic parameters, many of which can be controlled in feedback by launching the associated actuator systems. However, nonlinear multi-scale disturbing phenomena such as microturbulence [Yoshizawa et al., 2003, Wesson and Campbell, 2011], MHD instabilities [Zohm, 2015] and impurity accumulation [Vershkov and Mirnov, 1974], are likely to play a detrimental role in the course of tokamak plasma operation by rendering the plasma to an unfavorable status. With the occurrence of large plasma uncertainties, the LSS model-based feedback controller may behave poorly, even with a risk of control instability. In Chapter 3, we have shown, both numerically and experimentally, that linear models identified from the sampled data can

conveniently be applied for a number of robust control designs to track certain plasma parameters/profiles around a certain operating point in advanced tokamak scenarios on EAST. Nonetheless, like the majority of the proposed control schemes for plasma control, the design of linear feedback controllers is based on an implicit assumption that they should at least work effectively around a specific operating point, for instance, in a given plasma scenario.

To proceed a step further, one interesting question is whether it is feasible to enable a feedback controller to run effectively in a broader operating space. In order to find a solution, in this chapter, we shall develop adaptive control algorithms emerging in the control community to tracking plasma parameters of interest in advanced tokamak scenarios. Adaptive control, a control methodology assuming the known model (controller) structure but with unknown parameters slowly time-varying or time-invariant, is capable of dealing with uncertain systems to achieve desirable control performance [Tao, 2014, Hou and Jin, 2013]. There is a rich literature regarding the techniques for design, analysis, performance and applications [Ioannou and Sun, 1996], which can be roughly divided into model-free and model-based adaptive control techniques. Among the model-free adaptive techniques, typical examples include ESC [Ariyur and Krstic, 2003], the dynamic linearization based adaptive control [Hou and Jin, 2013], fuzzy adaptive control [Chen et al., 2007] and the neural networks based adaptive control [Fu and Chai, 2007]. Model-based adaptive controllers comprise adaptive backstepping control [Krstic et al., 1995], MRAC [Tao, 2014, Ioannou and Sun, 1996], adaptive pole placement control [Lozano and Zhao, 1994], robust adaptive control [Ioannou and Sun, 1996, Landau et al., 2011] and gain scheduling control [Leith and Leithead, 2000].

As the first part of this chapter, we focus on the application of the ESC algorithms for plasma kinetic optimization in advanced tokamak scenarios. ESC is a model-free adaptive online optimization approach [Ariyur and Krstic, 2003], which slowly drives a system to an optimum where the cost function reaches a local minimum or maximum. This approach was first proposed in [Leblanc, 1922], which has found many industrial applications in various disciplines, including aerospace and propulsion control [Binetti et al., 2003], combustion instability control [Banaszuk et al., 2004], flow control [Wang et al., 2000] and robot control [Kumar et al., 2019]. The first rigorous assessment of the stability of ESC is given in [Wang and Krstic, 2000], which has later been extended to multivariate LTI Newton-based ESC (NESC) control [Ghaffari et al., 2012]. As an alternate, the time-varying NESC control is proposed in [Keating and Alleyne, 2017] and applied to the online optimization of vapor compression systems. For more recent achievements on ESC, interested readers are referred to [Dürr et al., 2013, Guay and Dochain, 2017,Guay and Atta, 2018,Dürr et al., 2017,Yin et al., 2018] and the fundamentals of ESC are illustrated in [Ariyur and Krstic, 2003]. Notably, ESC has also found its applications in tokamak plasma control, specifically in the control of MHD instabilities and the kinetic optimization. In [Ou et al., 2008], the feedforward optimization for the current profile control is achieved by using the standard multivariable ESC. In [Paley et al., 2009], ESC is used to maximize the sawteeth period by actuating the ECCD system in real-time on TCV. In [Bolder et al., 2012], the performance of ESC on the sawtooth period control is improved by replacing a lowpass filter with a moving average filter for the gradient estimation in conjection with a sliding mode optimizer. In [Wehner and Schuster, 2012], combined with the magnetic island width estimate, ESC allows for the minimization of the island-beam misalignment and the

time required for NTM stabilization on DIII-D. In [Lanctot et al., 2016], the toroidal angular momentum is maximized experimentally by actuating the error field coil currents based on the standard ESC. In this chapter, we are dedicated to optimizing plasma parameters of interest online using the multivariable NESC method. In contrast to the standard ESC scheme, the NESC enables the online estimation of the Hessian and Hessian inverse of a cost function (performance index) with respect to manipulated inputs. The evident benefit is that the control convergence rate can thus be assigned artificially, which is however not feasible with the standard ESC. More precisely, a decoupling technique with an extra closed-loop is used to estimate the Hessian and its inverse while the same technique that inherits from the standard ESC is for the gradient estimation. The performance of the NESC and standard ESC schemes are evaluated and compared via closed-loop METIS simulations in H-mode plasma scenarios on EAST and ITER.

The second and third parts of this chapter present the model reference adaptive control (MRAC) of plasma kinetic parameters in advanced tokamak scenarios. MRAC is an adaptive control strategy that has been extensively studied and its theory and design methodologies have been systematically established [Tao, 2014]. The essential characteristic of MRAC is that the closed-loop system dynamics are forced to match with a reference model system, through the cancellation of the system zeros that are assumed stable. We first study a SISO case, where the direct and indirect MRAC (dMRAC and iMRAC) control schemes are pursued in parallel. In particular, the dMRAC scheme assumes a stationary controller structure and updates the controller coefficients in real-time based on a set of adaptive laws. As a dual approach, the iMRAC scheme assumes a stationary model structure, whose coefficients are estimated in real-time by adopting adaptive laws before being used for updating the controller coefficients by following the model-matching conditions. With the similar idea, we then extend the dMRAC scheme into a MIMO version using the combination of the adaptive laws, driven by the normalized estimation errors (NEEs), and the LDS decomposition [Tao, 2014]. Nonlinear METIS simulations performed on EAST demonstrate the effectiveness of the proposed MRAC algorithms.

The *main achievements* of the chapter are listed below:

- Development of the NESC and ESC algorithms to achieve the online optimization of plasma kinetic parameters in H-mode scenarios on EAST and ITER.
- Development of the dMRAC and iMRAC schemes for tracking of essential plasma kinetic parameters in H-mode scenarios on EAST.
- Development of a MIMO dMRAC scheme for the simultaneous tracking of q_0 and β_p in H-mode scenarios on EAST.
- Demonstrating the effectiveness of the proposed ESC and MRAC algorithms via nonlinear closed-loop METIS simulations.

The remainder of the chapter is organized as follows. In Section 1, we formulate the kinetic control problem, sketch the essentials of the ESC approach and describe the LTI NESC

scheme. We then evaluate the control performance via nonlinear METIS simulations on EAST and ITER. In Section 2, we develop the dMRAC and iMRAC schemes for tracking of β_p, Ω_ϕ and $T_{e,0}$ and assess their validity via nonlinear METIS simulations on EAST. In Section 3, we consider a MIMO dMRAC scheme for tailoring q_0 and β_p by actuating ICRH and LHCD powers simultaneously and evaluate their performance via nonlinear METIS simulations on EAST. In Section 4, we draw conclusions and outline possible improvements.

4.1 ESC optimization of plasma kinetic parameters

In this section, we present the ESC and NESC algorithms to optimize plasma kinetic parameters online in H-mode plasma scenarios, without resorting to any plasma response models. First, we introduce the control objectives, outline the modelling of the to-be-optimized kinetic parameter evolutions and formulate the kinetic control problem. Subsequently, the NESC algorithm is illustrated in great detail. Nonlinear METIS simulations are finally carried out to assess the performance of the proposed ESC and NESC schemes.

4.1.1 Optimization problem formulation

Since ESC is a model-free adaptive optimization technique, it is intrinsically generic and can potentially be applied to the kinetic optimization of any simulated and experimental plasmas. Nonetheless, in order to discuss the control tuning procedure and evaluate the performance of the ESC technique, a simple fluid model combined with a number of scaling laws [Artaud et al., 2018] is employed as a plasma simulator to reveal the essential physics of kinetic parameter evolutions. Before formulating the kinetic optimization problem, we first briefly describe the modelling of the to-be-optimized kinetic parameters, i.e., plasma poloidal beta β_p, the average toroidal rotation angular speed Ω_ϕ and the α particle power P_α.

4.1.1.1 Modelling of plasma kinetic parameters

The plasma parameters of interest, β_p, Ω_ϕ and P_α are global indicators of the plasma confinement performance in tokamaks, which evolve on the timescale of the energy confinement time τ_E. β_p is a ratio between the total plasma kinetic energy and the energy stored in the poloidal magnetic field, expressed as:

$$\beta_p = \frac{4W_{th}(1+\kappa^2)}{3\mu_0 a R I_p^2} \tag{4.1}$$

where W_{th} represents the thermal plasma energy content, κ the elongation, μ_0 the magnetic permeability in vacuum space, a the plasma minor radius, R the plasma major radius, I_p the plasma current. W_{th} is obtained by solving a first-order ODE as:

$$\frac{dW_{th}}{dt} = -\frac{W_{th}}{\tau_E} + P_{heat} - P_{rad} \tag{4.2}$$

Here, τ_E is computed by using scaling laws. In L-mode, the ITERL-96P(th) scaling law reads:

$$\tau_{e,L} = 0.023 I_p^{0.96} B_t^{0.03} (\frac{n}{10^{20}})^{0.4} P_{in}^{-0.73} R^{1.83} \kappa^{0.64} \epsilon^{-0.06} A^{0.2} \tag{4.3}$$

where I_p is the plasma current, B_t the toroidal magnetic field, n the average electron density, P_{in} the input power, R the major radius, κ the elongation, ϵ the aspect ratio, A the atomic mass of the ions. In H-mode, the ITERH-98(y,2) scaling law writes:

$$\tau_{e,H} = 0.0562 I_p^{0.93} B_t^{0.15} (\frac{n}{10^{20}})^{0.41} P_{loss}^{-0.69} R^{1.97} \kappa^{0.78} \epsilon^{0.58} A^{0.19} \tag{4.4}$$

Here, $P_{loss} = P_{heat} - P_{rad}$, where P_{heat} and P_{rad} are respectively the total heating power and the radiation power, expressed as:

$$\begin{aligned} P_{heat} &= P_\Omega + P_\alpha + P_{IC} + P_{LH} + P_{EC} + P_{NBI} \\ P_{rad} &= P_{brem} + P_{cyclo} + \lambda_{line} P_{line} \end{aligned} \tag{4.5}$$

where P_Ω denotes the total ohmic power, and P_α the total α particle power generated from D-T reactions. P_{IC}, P_{LH}, P_{EC}, P_{NBI} are respectively the total deposited powers arising from the ICRH, LHCD, ECRH and NBI systems. P_{brem}, P_{cyclo} and P_{line} are the bremsstrahlung radiative power, the power lost by synchrotron radiation and the total radiative power due to line radiation, respectively. We note that λ_{line} indicates the fraction of the line radiation coming from the core plasma region. P_α is the total power arising from the generated α particles due to D-T reactions, which is derived as $P_\alpha = \int_0^1 p_{\alpha,th}(t,\rho) d\rho$, where $p_{\alpha,th}(t,\rho)$ is the α power density profile, computed as:

$$p_{\alpha,th}(t,\rho) = e E_{\alpha,T(d,n)He_4} n_D(t,\rho) n_T(t,\rho) \langle \sigma \upsilon \rangle_{T(d,n)He_4} [T_i(t,\rho)] \tag{4.6}$$

where e is the unit of electric charge, $E_{\alpha,T(d,n)He_4} = 3.5$ MeV, n_D and n_T are respectively the deuterium and tritium density profile. $\langle \sigma \upsilon \rangle_{T(d,n)He_4} [T_i(t,\rho)]$ is the D-T fusion reaction cross section closely related to the ion temperature profile. The ion temperature profile is inferred from the electron temperature profile by conserving both the total energy and charge. More details on the modelling of the other power sources and of the electron and ion temperature profile evolutions are given in [Artaud et al., 2018].

The modelling of the average toroidal rotation angular speed is performed mainly in order to account for the NBI effects and the intrinsic plasma rotation. The effects of magnetic field ripple losses, fast ion losses and fast ion momentum transport cannot be described by simple models, but they can be neglected. Nevertheless, a simple model is adequate to characterize the NBI-dominated plasmas, even for a fusion reactor such as ITER. The volume-averaged toroidal momentum is defined as:

$$R_{tot} = \int_0^1 \sum_{k=1}^{N_{ion}} m_p A_k n_k R \upsilon_{\phi,k} V' d\rho \tag{4.7}$$

where N_{ion} represents the total number of ion species, m_p the proton mass, A_k the number of the nucleons in the k-th ion species, n_k the average density of the k-th ion species, R the major radius, $\upsilon_{\phi,k}$ is the toroidal velocity of the ion species k, V' the derivative of the plasma volume

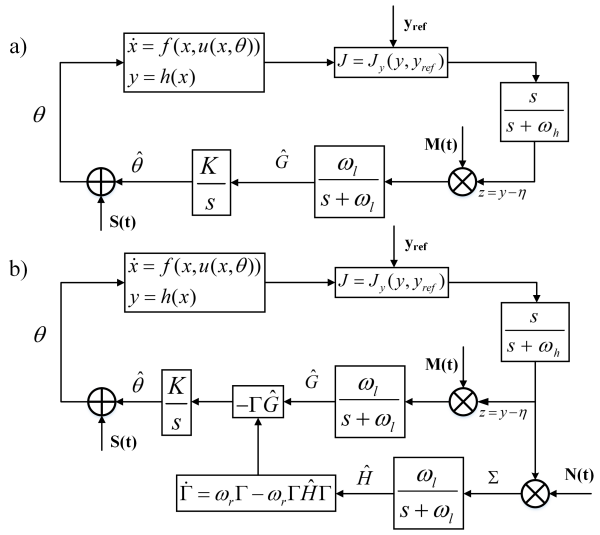

Figure 4.1: Schematic of a) the standard ESC and b) the NESC schemes.

enclosed in a magnetic surface with respect to the normalised minor radius ρ. Analogous to the thermal energy computation, the volume-averaged toroidal momentum is modelled as:

$$\frac{dR_{tot}}{dt} = -\frac{R_{tot}}{\tau_\phi} + \sum_{k=1}^{N_{NBI}} S_{\phi,NBI,k} + S_{\phi,intrinsic} + S_{\phi,RF} + S_{\phi,E_\parallel} + S_{\phi,ripple} + F_{n,0} \tag{4.8}$$

where τ_ϕ is the toroidal rotation confinement time, defined as $\tau_\phi = f_{\tau,rot}\min(\tau_E, \tau_{ii})$, where $f_{\tau,rot}$ is an adjustable factor with the order $O(1)$, τ_{ii} the ion confinement time. $S_{\phi,NBI,k}$ is the rotation source due to the k-th NBI injection, N_{NBI} the number of NBI injectors, $S_{\phi,intrinsic}$ the intrinsic toroidal rotation, $S_{\phi,RF}$ the rotation source due to the radiofrequency (RF) heating, $S_{\phi,E_\parallel}$ the rotation source due to the parallel electric field, $S_{\phi,ripple}$ the toroidal rotation source arising from the magnetic ripple effects. $F_{n,0}$ the rotation source due to the friction with cold neutrals. More details concerning these source terms are given in [Artaud et al., 2018].

4.1.1.2 Description of the kinetic optimization problem

A conceptual scheme of the kinetic parameter optimization using ESC is illustrated in Fig. 4.1(a). The objective is to optimize the control actuations online using the sampled input-output data such that the cost function penalizing the kinetic parameter deviations reaches a local minimum. The control actuators used in this study include the ICRH, LHCD and NBI system powers, though other actuators such as plasma current and density can also be involved for real-time optimization if necessary. The to-be-optimized kinetic parameters are the plasma poloidal beta, β_p, the average toroidal rotation angular speed, Ω_ϕ, the electron temperature on axis, $T_{e,0}$, and the α particle power, P_α, for ITER burning plasmas. We remark that β_p can be estimated via the real-time EFIT code [Lao et al., 1985, Ferron et al., 1998] by fitting the Grad-Shafranov equation with the boundary and internal magnetic diagnostics as constraints;

Ω_ϕ may be measured by the main-ion charge exchange recombination spectroscopy (MICER) in NBI-heated plasmas [Haskey et al., 2018]; $T_{e,0}$ may be measured by Thomson scattering and electron cyclotron emission (ECE); P_α can be inferred from the plasma density and ion temperature measurements, for example, Thomson scattering, interferometry and charge exchange recombination spectroscopy (CXRS) [Wesson and Campbell, 2011].

The extremum-seeking optimizer has two sets of inputs, one of which are the real-time estimates of plasma parameters of interest, while the others are their corresponding references, which are allowed to be time-varying. The evident merit of the ESC optimizer is that it does not rely on any *a priori* knowledge of plasma dynamics. An important constraint is that the ESC optimizer should operate in a slower timescale than that of the to-be-optimized plasma parameter evolutions such that a stable static input-output map, a sufficient condition for the stability of ESC, can be obtained [Ariyur and Krstic, 2003]. In our studied plasma scenarios, for example, on the ITER tokamak the energy confinement time τ_E is approximately in the order of 1 s, and the pulse duration can reach 1000 s. Hence, the use of the ESC optimizer is theoretically feasible thanks to the long-pulse duration and the real-time capability of the H&CD systems.

4.1.1.3 The optimization problem formulation using the ESC framework

The kinetic models described in Section 4.1.1.1 can be formulated as:

$$\dot{x} = f(x, \theta), J = h(x) \tag{4.9}$$

Here, $x \in R^n$ represents the states where n is the number of states, $\theta \in R^p$ the inputs, where p is the number of control actuators. $J \in R$ is a cost function which is defined as the weighted norm of all the state errors. $f : R^n \times R^p \rightarrow R^n$ and $h : R^n \rightarrow R$ are nonlinear smooth functions. More specifically, in an H-mode burning plasma scenario on ITER, our objective is to optimize β_p, Ω_ϕ and P_α to their desired targets $\beta_{p,\mathrm{ref}}$, Ω_{ref}, $P_{\alpha,\mathrm{ref}}$, respectively, by actuating P_{NBI1} and P_{IC} in real-time, with the other three actuators P_{NBI2}, P_{EC} and P_{LH} remaining at a constant level. We define β_p, Ω_ϕ and P_α as the kinetic parameter estimates while $\beta_{p,\mathrm{ref}}$, Ω_{ref}, $P_{\alpha,\mathrm{ref}}$ as their references. In this case, $n = 3, p = 5, \theta = [P_{\mathrm{NBI1}}, P_{\mathrm{NBI2}}, P_{\mathrm{EC}}, P_{\mathrm{IC}}, P_{\mathrm{LH}}]^T, x = [\tilde{\beta}_p, \tilde{\Omega}, \tilde{P}_\alpha]^T$, where $\tilde{\beta}_p$, $\tilde{\Omega}$ and $\tilde{P}_\alpha$ are defined as $\tilde{\beta}_p = \beta_p - \beta_{p,\mathrm{ref}}$, $\tilde{\Omega}_\phi = \Omega_\phi - \Omega_{\phi,\mathrm{ref}}$ and $\tilde{P}_\alpha = P_\alpha - P_{\alpha,\mathrm{ref}}$, respectively. In order to formulate the ESC optimization problem, we make the following assumptions about the plasma kinetic system [Ariyur and Krstic, 2003]:

1) There is a smooth function $l : R^n \rightarrow R^p$ such that $f(x, \theta) = 0$ if and only if $x = l(\theta)$;

2) For each $\theta \in R^n$, the equilibrium $x = l(\theta)$ of the system $\dot{x} = f(x, \theta)$ is locally exponentially uniformly stable in θ;

3) There exists $\theta^* \in R^n$ such that $\frac{\partial}{\partial \theta}(h \circ l)(\theta^*) = 0$ and $\frac{\partial^2}{\partial \theta^2}(h \circ l)(\theta^*) < 0$.

Our objective is to develop a feedback mechanism that drives the cost function J to its minimum without requiring the knowledge of either θ^* or the mapping functions f, l and h. As shown in Fig. 4.1(a), the standard ESC controller perturbs the estimate $\hat{\theta}$ with a periodic

signal $S(t)$ such as $a\sin(\omega t)$, which should be slow enough such that the plant (4.9) advances in a static map. The benefit of using the perturbation signal is to force the cost function J to respond periodically and then to extract the cost function gradient $\hat{G} = \frac{dJ}{d\theta}$. A highpass filter is first employed on J to remove the low-frequency uncorrelated component ($\omega_h < \omega$) and obtain z that is approximately sinusoidal. In order to estimate the cost function gradient $\hat{G}$, a lowpass filter is imposed on the product of two sinusoids z and $M(t)$, e.g. $\frac{2}{a}\sin(\omega t)$. Using an integrator, the actuation estimate $\hat{\theta}$ is then derived, where K is an adaptive gain to control the convergence rate. We emphasize that the cutoff frequency for the lowpass filter ω_l should be lower than the perturbing frequency ω, and to guarantee local stability, the perturbation amplitudes a and the adaptation gain matrix K need to be kept small. Hence, in the standard ESC scheme, there are three separate timescales: (1) fast (plasma kinetic evolutions), (2) medium (periodic perturbation) and (3) slow (gradient estimate).

4.1.2 NESC approach

Inspired by [Ghaffari et al., 2012], we develop an NESC scheme to optimize plasma kinetic parameters online, as depicted in Fig. 4.1(b). Basically, we can divide the NESC scheme into six components: 1). diagnostics/measurements to estimate plasma parameters of interest, e.g. β_p, Ω_ϕ, P_α; 2). define a proper cost function J to penalize the optimized kinetic parameter deviations; 3). estimate the Hessian $\hat{H}$ and Hessian inverse Γ for the gradient prediction; 4). estimate the gradient $\hat{G} = \frac{\partial J}{\partial \theta}$; 5). optimize the control inputs $\hat{\theta}$ using an integrator; 6). launch the control actuators, e.g. the ICRH system, for real-time actuation. We remark that Components 1 and 6 rely on the associated diagnostics and actuators, while the remaining components constitute the main NESC algorithm, which should be implemented into a PCS before experimental application [Snipes et al., 2017]. The rest part of this section presents the NESC design in more detail.

4.1.2.1 Cost function

The goal of the NESC optimizer for plasma kinetic parameters is to find optimal beam and radiofrequency actuations to minimize a cost function that penalizes both the parameter deviations and the control efforts, expressed as:

$$J = (x_{\text{ref}} - x_{\text{mea}})^T \Lambda (x_{\text{ref}} - x_{\text{mea}}) + (\theta_{\text{ref}} - \theta_{\text{sat}})^T \Delta (\theta_{\text{ref}} - \theta_{\text{sat}}) \tag{4.10}$$

where x_{ref} represents the references of plasma kinetic parameters, whilst x_{mea} denotes the estimates of plasma kinetic parameters. θ_{ref} is a vector of the requested actuations while θ_{sat} denotes the amount of the actuations that have passed through the saturation limits. Λ and Δ are two weighting matrices that weigh the importance of each input and output elements. We note that the references are allowed to be time-varying, but the settling time of the reference trajectories should be aproximately an order smaller than τ_E to guarantee the timescale separation between the plasma kinetic dynamics and the optimizer dynamics. The involvement of the second term in the cost function aims to attenuate the negative effects from actuator saturations [Mu et al., 2017].

4.1.2.2 Estimator

In this subsection, we estimate the gradient, the Hessian, the Hessian inverse of the cost function with respect to the control actuations.

Estimating the gradient Re-formulating equation (4.10) as $J = Q(\hat{\theta} + S)$ and using the Taylor expansion at $\hat{\theta}$ yield:

$$J = Q(\hat{\theta} + S) = Q(\hat{\theta}) + S^T \frac{\partial Q}{\partial \hat{\theta}} + R(S^T S) \tag{4.11}$$

To extract the term $\frac{\partial Q}{\partial \hat{\theta}}$ and attenuate the first term $Q(\hat{\theta})$, a highpass filter is imposed on J, yielding $J_f = Q_f(\hat{\theta}) + S^T \frac{\partial Q}{\partial \hat{\theta}} + R(S^T S)$. Multiplying the periodic signals $M(t)$ on both sides of Eq. (4.11) and averaging it in the period Π, we thus obtain:

$$\begin{aligned} \frac{1}{\Pi}\int_{t_0}^{t_0+\Pi} \hat{G} dt &= \frac{1}{\Pi}\int_{t_0}^{t_0+\Pi} M(t) y_f d\sigma \\ &= \frac{1}{\Pi}\int_{t_0}^{t_0+\Pi} M(t) Q_f(\hat{\theta}(t)) dt + \frac{1}{\Pi}\int_{t_0}^{t_0+\Pi} M(t) S(t)^T \frac{\partial Q}{\partial \hat{\theta}} dt + \\ &\quad \frac{1}{\Pi}\int_{t_0}^{t_0+\Pi} M(t) R(S^T S) dt \end{aligned} \tag{4.12}$$

Here, $Q_f(\hat{\theta})$ is a low-frequency component, and we assume that $Q_f(\hat{\theta}) = Q(t_0)$ when $t \in [t0, t0 + \Pi]$. Then the first term is transformed to $\frac{Q(t_0)}{\Pi}\int_{t_0}^{t_0+\Pi} M(t) dt$, which is 0. For the third term, since $R(S^T S)$ is an order smaller than the second term, it can be neglected. We assume that $\frac{\partial Q}{\partial \hat{\theta}}$ is constant during the interval $[t_0, t_0 + \Pi]$, which is then transformed to $\frac{1}{\Pi}\int_{t_0}^{t_0+\Pi} M(t) S(t)^T dt \frac{\partial Q}{\partial \hat{\theta}}$. Because $\frac{1}{\Pi}\int_{t_0}^{t_0+\Pi} M(t) S(t)^T dt$ is a unit matrix, we consequently have $\frac{1}{\Pi}\int_{t_0}^{t_0+\Pi} \hat{G} dt = \frac{\partial Q}{\partial \hat{\theta}}$.

Estimating the Hessian According to the assumptions made in Section 4.1.1.3, we infer that at the steady state $J = h(l(\theta))$, $\theta = \hat{\theta} + S(t)$ and $\hat{\theta} = \theta^* + \tilde{\theta}$. Due to the smoothness properties on f and h, we thus have $J = Q(\theta^* + \tilde{\theta} + S(t))$. Using the Taylor series expansion, J is then expressed as:

$$J = Q(\theta^* + \tilde{\theta} + S(t)) = J(\theta^*) + \frac{1}{2}(\tilde{\theta} + S(t))^T H(\tilde{\theta} + S(t)) + R(\tilde{\theta} + S) \tag{4.13}$$

We note that $\frac{\partial J(\theta^*)}{\partial \theta^*} = 0$ and the term $R(\tilde{\theta} + S)$ is a high order of $\tilde{\theta} + S$, which is negligible. In order to decouple the Hessian H in an average sense, the cost function is multiplied by a carefully designed time-varying matrix $N(t)$ [Ghaffari et al., 2012], which is given by:

$$N_{i,j} = \begin{cases} \frac{16}{a_i^2}\left(\sin(\omega_i t)^2 - \frac{1}{2}\right), \text{if} & i = j \\ \frac{4}{a_i a_j}\sin(\omega_i t)\sin(\omega_j t), \text{if} & i \neq j \end{cases} \tag{4.14}$$

where a_i and a_j are dither amplitudes, while ω_i are dither frequencies. Hence, the integral average of $N(t)J$ in the common period of the probing frequencies $\Pi = 2\pi \times \mathbf{LCM}\{\frac{1}{\omega_i}\}, i = 1, 2, ..., n$ (LCM is short for the least common multiple) yields:

$$\frac{1}{\Pi}\int_0^{\Pi} N(t)Jd\sigma = H + \frac{1}{\Pi}\int_0^{\Pi} R(\tilde{\theta} + S)d\sigma \tag{4.15}$$

To approximate the Hessian in an average sense, a lowpass filter is employed as:

$$\dot{H} = -w_r H + w_r \hat{H} \tag{4.16}$$

where w_r is a cut-off frequency on the timescale of Π and the state H converges to $\hat{H}$.

Estimating the Hessian inverse We assume Γ as the inverse of H, which means that $\Gamma H = I$. Differentiating the equality yields $\dot{\Gamma}H + \Gamma\dot{H} = 0$, which is right-multiplied by Γ on both sides, resulting in $\dot{\Gamma} = \Gamma\dot{H}\Gamma$. Combined with equation (4.16), the Hessian inverse is consequently obtained as a differential Riccati equation:

$$\dot{\Gamma} = w_r\Gamma - w_r\Gamma\hat{H}\Gamma \tag{4.17}$$

This equation has two equilibria, i.e., $\Gamma = 0$ and $\Gamma = \hat{H}^{-1}$. Further analysis indicates $\Gamma = 0$ is an unstable equilibrium, thus Γ should converge to $\hat{H}^{-1}$.

4.1.2.3 Optimizer

The objective of the optimizer is to use the estimates of the gradient and/or Hessian inverse to compute the optimal control actuations such that the cost function can be minimized or maximized. As shown in Fig. 4.1, the adaptive gains K_g and K_n scale the convergence rate of the ESC and NESC optimizers, respectively. In the standard ESC scheme, only the gradient estimate is used for optimization while, in the NESC scheme, both the gradient and Hessian inverse estimates are involved. As an integrator, the optimizer can thus be expressed as:

$$\dot{\hat{\theta}}(t) = \begin{cases} -K_g\frac{\partial Q}{\partial\hat{\theta}}, k = 0 \\ -K_n\Gamma\frac{\partial Q}{\partial\hat{\theta}}, k = 1 \end{cases} \tag{4.18}$$

where $k = 0$ represents the standard ESC scheme, while $k = 1$ indicates the NESC scheme. $\hat{\theta}$ represents the optimal control actuations. After integration, $\theta(t) = \hat{\theta}(t) + S(t)$ are output for the actuators, where $S(t)$ represents the dither signals.

4.1.2.4 Stability analysis

Assume that θ^* represents the optimal powers, and define the estimate error $\tilde{\theta} = \hat{\theta} - \theta^*$. We then formulate the NESC control system in a nonlinear state-space form as:

$$\frac{d}{dt}\begin{bmatrix} x \\ \tilde{\theta} \\ \tilde{G} \\ \tilde{\Gamma} \\ \tilde{H} \\ \tilde{\eta} \end{bmatrix} = \begin{bmatrix} f(x, \alpha(x, \theta^* + \tilde{\theta} + S(t))) \\ -K(\tilde{\Gamma} + H^{-1})\hat{G} \\ -\omega_l \tilde{G} + \omega_l (y - h \circ l(\theta^*) - \tilde{\eta}) M(t) \\ \omega_r (\tilde{\Gamma} + H^{-1})(I - (\tilde{H} + H)(\tilde{\Gamma} + H^{-1})) \\ -\omega_r (\tilde{H} - \omega_r H + \omega_l (y - h \circ l(\theta^* - \tilde{\eta}) N(t) \\ -\omega_h \tilde{\eta} + \omega_h (y - h \circ l(\theta^*)) \end{bmatrix} \tag{4.19}$$

where the closed-loop stability is illustrated by the following theorem:

Theorem 3. *Consider the feedback system (4.19) under Assumptions* 1−3. *There exists* $\bar{\omega} > 0$ *and for any* $\omega \in (0, \bar{\omega}) > 0$ *there exist* $\bar{\delta}, \bar{a} > 0$ *such that for the given* ω *and any* $a \in (0, \bar{a})$ *and* δ *there exists a neighborhood of the point* $(x, \hat{\theta}, \hat{G}, \Gamma, \hat{H}, \eta) = (l(\theta^*), \theta^*, 0, H - 1, H, h \circ l(\theta^*))$ *such that any solution of systems (4.19) from the neighborhood exponentially converges to an* $O(\omega + \delta + |a|)$*-neighborhood of that point. Furthermore,* $J(t)$ *converges to an* $O(\omega + \delta + |a|)$*-neighborhood of* $h \circ l(\theta)$.

Theorem 1 is demonstrated by using the averaging and singular perturbation analysis, details of which are given in [Ghaffari et al., 2012]. For the completeness, we hereby sketch the proof essentials. Compared to the controller dynamics, the system dynamics evolve much faster. The change of variable $\tau = \omega t$ formulates a standard singular perturbation system. First, we assume that $\omega = 0$, the singular perturbation system is degenerated into a reduced system, which can be demonstrated to have a unique exponentially stable periodic solution around its equilibrium. Second, the boundary layer model is studied, based on assumption 2, the equilibrium is locally exponentially uniformly stable in θ. The combination of the reduced system and the bounday layer system leads to the closed-loop exponential stability of the full system using the Tikhonov theorem [Khalil and Grizzle, 2002].

4.1.3 Simulation results

The ESC and NESC algorithms described in previous sections have been implemented into the MATLAB/Simulink framework, which are then coupled with the plasma simulator METIS [Artaud et al., 2018] for closed-loop control evaluations. We now present the nonlinear METIS simulation results regarding the ESC and NESC kinetic optimization on the EAST and ITER tokamaks.

4.1.3.1 ESC optimization of β_p, Ω_ϕ and $T_{e,0}$ by adjusting $P_{\mathbf{IC}}$ and $P_{\mathbf{LH}}$ on EAST

The first case consists in evaluating the performance of the ESC and NESC algorithms for the optimization of plasma kinetic parameters in a typical H-mode scenario on EAST via

nonlinear METIS simulations. The reference scenario for METIS simulations is consistent with the one used in Section 2 of Chapter 3. The objective is to track the poloidal beta β_p, the average toroidal rotation angular speed Ω_ϕ and the central electron temperature $T_{e,0}$ simultaneously by optimizing the ICRH and LHCD powers online using the ESC and NESC schemes. The ICRH and LHCD powers are allowed to vary in the ranges of [0, 1.5] MW and [0, 3.0] MW, respectively. The two candidate ESC optimizers were tuned using trial and error until the satisfactory performance was obtained. Table (4.1) lists the ESC tuning parameters for the ESC and NESC optimizers. The major difference between the standard ESC and NESC lies in whether the Hessian and Hessian inverse are estimated or not. In the standard ESC optimizer, the estimation is restricted to the gradient of the cost function with respect to control actuations, while in the NESC optimizer, the Hessian and its inverse are estimated by involving an additional loop as shown in Fig. 4.1(b). The dither frequency is computed as $\tau_{\text{dither}} = \frac{2\pi}{N_{\text{dither}}\hat{\tau}_E}$, where $\hat{\tau}_E$ represents the energy confinement time estimate (fixed at 0.04 s in this study) and N_{dither} is an integer ranging from 5-15 (fixed at 8 in this study). The dither magnitude should be set small at 0.05 MW. The time constant for the highpass filter, the gradient-oriented lowpass filter and the Hessian-oriented lowpass filter are respectively given by $\tau_h = \frac{1}{2}\tau_{\text{dither}}$,$\tau_l = \frac{1}{4}\tau_{\text{dither}}$ and $\tau_r = \frac{3}{20}\tau_{\text{dither}}$. The adaptive gains, weights and norms are chosen by trial and error. Increasing the adaptive gains can reduce the response time while it may have the risk of causing control instability. The norms are chosen to map the measured outputs and references to the interval of [-1,1]. Adjusting the weights on each control variables can make a trade-off on the importance of each variable in the cost function.

The optimization results for the two ESC optimizers are compared in Fig. 4.2, in which two sets of references are prescribed and the optimization is activated at 3.5 s. In particular, in the time period [3.5, 5] s, the β_p, Ω_ϕ and $T_{e,0}$ targets are 2.0, 8 krad/s and 4800 eV, respectively. From 5 s to 6 s, the targets for β_p, Ω_ϕ and $T_{e,0}$ are linearly increased to 2.25, 9 krad/s and 5000 eV, and this new kinetic equilibrium is requested to be sustained until 8 s. We can conclude from Fig. 4.2 that two groups of setpoints are achieved and maintained by both the standard ESC and NESC schemes, in which comparable optimization performance is obtained by these two candidate ESC optimizers. Nonetheless, one can still notice that slightly better tracking is acquired with the NESC optimizer, especially for β_p and Ω_ϕ. The time evolution of the optimized ICRH and LHCD powers are shown in Fig. 4.3. It is found that to achieve the first group of setpoints, the ICRH and LHCD powers are requested to be actuated at 0.75 MW and 1.75 MW respectively, while the second group of setpoints are reached by increasing the ICRH power to 0.95 MW and dropping the LHCD power to around 1.55 MW. The time evolution of the cost function and the gradient estimates for the two candidate ESC schemes are shown in Fig. 4.4. We can observe that between 5.6 s and 6.2 s, the cost function with the NESC optimizer is around half of that with the standard ESC optimizer, confirming that better transient tracking performance can be made with the NESC optimizer. The estimates of the Hessian inverse are depicted in Fig. 4.5, where the estimates are decreased suddenly from 5.5 s to 5.6 s and gradually increased from 5.6 s to 6.5 s, which results in the improved transient performance in the period of [5.6, 6.2] s for the NESC optimizer.

Table 4.1: The ESC and NESC tuning parameters used for METIS simulations on EAST.

Options	Parameters	Standard ESC		NESC	
	actuator	IC	LH	IC	LH
S	dither mag. [MW]	0.05			
	dither freq. τ_{dither} [rad/s]	19.6350			
	phase	0	$\pi/2$	0	$\pi/2$
M	dither mag. [MW]	20			
	dither freq. τ_{dither} [rad/s]	19.6350			
	phase	0	$\pi/2$	0	$\pi/2$
filters	highpass τ_h	9.8175			
	lowpass gradient τ_l	4.9087			
	lowpass Hessian τ_r	-		2.9452	
adaptive gains	K_g	0.0027		-	
	K_n	-		0.001	
weights	λ_{β_p}	4			
	λ_{Ω_ϕ}	3			
	$\lambda_{T_{e,0}}$	0.005			
norms	N_{β_p}	1000			
	N_{Ω_ϕ}	0.5			
	$N_{T_{e,0}}$	0.5			

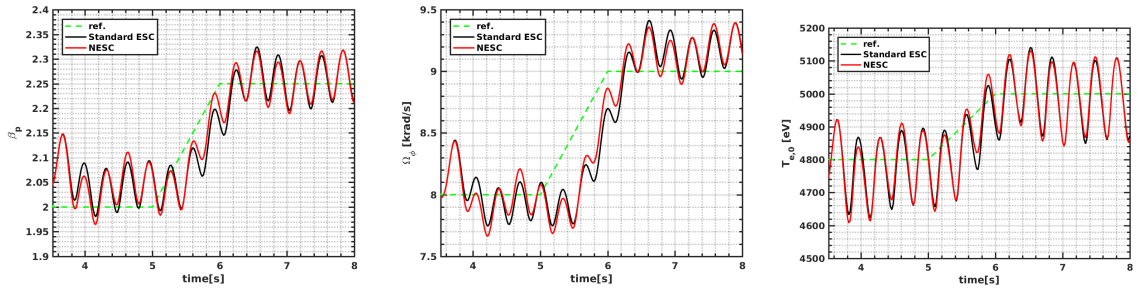

(a) (b) (c)

Figure 4.2: Comparison of plasma kinetic parameter optimization using the ESC and NESC schemes on EAST. Time traces of (a) the poloidal beta β_p, (b) the average toroidal rotation angular speed Ω_ϕ and (c) the central electron temperature $T_{e,0}$.

4.1.3.2 ESC optimization of β_p, Ω_ϕ and P_α by adjusting P_{NBI} and P_{IC} on ITER

The second case aims at extrapolating the ESC and NESC schemes on EAST to an H-mode burning plasma scenario on ITER. The reference scenario for METIS simulations on ITER is in line with the one studied in Section 1 of Chapter 2. The objective is to track the poloidal beta β_p, the average toroidal rotation angular speed Ω_ϕ and the α particle power P_α simultaneously by optimizing the co-current NBI and ICRH powers online. The first co-NBI

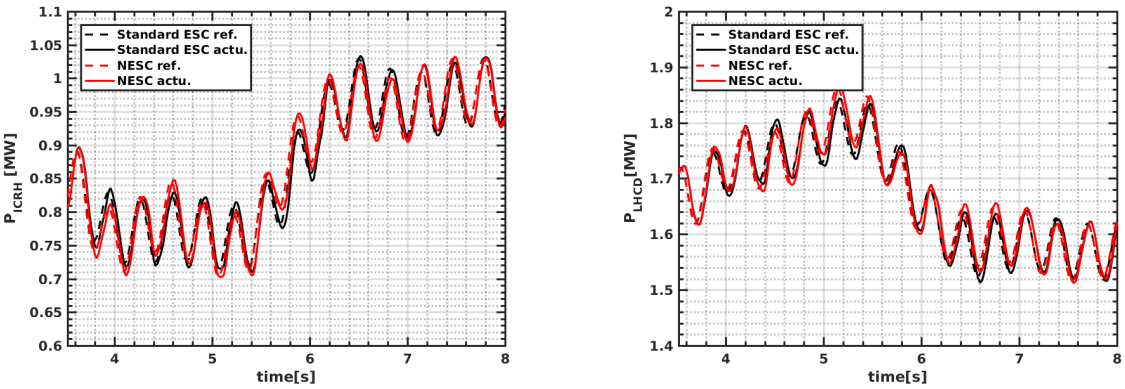

(a) (b)

Figure 4.3: Time traces of (a) the ICRH power and (b) the LHCD power on EAST.

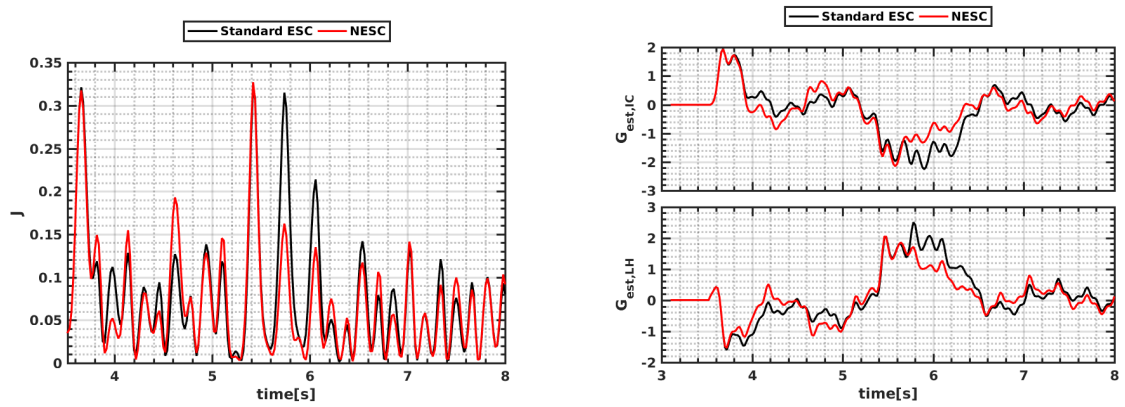

(a) (b)

Figure 4.4: Time traces of (a) the performance index and (b) the gradient estimates on EAST.

and ICRH powers are initialized with 10.3 MW and 12.5 MW, respectively, and are allowed to range in the interval of [5, 16.5] MW and [5, 20] MW. The other additional heating powers remain constant during the whole optimization process, specifically the second co-NBI at 10.3 MW, the ECRH at 12.5 MW and the LHCD at 25 MW. Two ESC schemes are coupled with the METIS code for closed-loop control evaluations using the MATLAB/Simulink framework. Similar to the first simulation case study, the tuning parameters for both ESC optimizers were tuned by trial and error until the satisfactory performance was obtained and Table 4.2 lists the used ESC tuning parameters for the following METIS simulations. As before, the dither frequency is determined by following the rule $\tau_{\text{dither}} = \frac{2\pi}{N_{\text{dither}}\hat{\tau}_E}$. In this case, N_{dither} is fixed at 12 and $\hat{\tau}_E$ is estimated to be 1.75 s. The dither magnitude is set at 0.4 MW and the dither phase for co-NBI and ICRH actuators are prescribed to be 0 and $\frac{\pi}{2}$, respectively. The time constant for the highpass filter, the gradient-oriented lowpass filter and the Hessian-oriented lowpass filter are respectively prescribed at $\tau_h = \frac{1}{2}\tau_{\text{dither}}$,$\tau_l = \frac{1}{4}\tau_{\text{dither}}$ and $\tau_r = \frac{1}{4}\tau_{\text{dither}}$. The

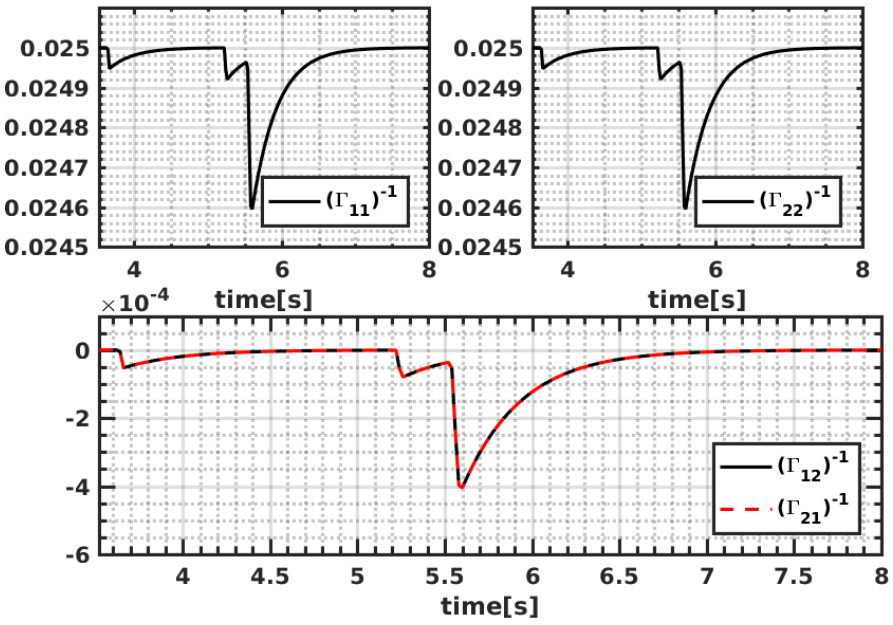

(a)

Figure 4.5: Time traces of the Hessian inverse estimates on EAST. Left-top panel: time traces of the first diagonal element estimate. Right-top panel: time traces of the second diagonal element estimate. Bottom panel: time traces of the off-diagonal element estimates.

adaptive gains, norms and weights for β_p, Ω_ϕ and P_α are set by trial and error.

The optimization results for the two candidate ESC optimizers are illustrated in Fig. 4.6. Two sets of targets for β_p, Ω_ϕ and P_α are preset to be followed and the optimization is activated at 300 s. In the interval [300, 400] s, the references for β_p, Ω_ϕ and P_α are 2.1, 12.4 krad/s and 58 MW. From 400 s to 600 s, the references linearly drop to 2.02, 12.2 krad/s and 54 MW. Simulation results indicate that both ESC and NESC optimizers can achieve effective tracking by adjusting the co-NBI and ICRH powers simultaneously. Fig. 4.7 shows the time evolution of the NBI and ICRH powers. Evidently, the optimized powers are mostly overlapped in the two ESC schemes. It appears that at the initial phase of optimization, the standard ESC scheme slightly outperforms the NESC scheme, which is further confirmed in Fig. 4.8(a). In the period [320, 350] s, the cost function J of the standard ESC is smaller than that of NESC, because of the difference in the gradient estimate in Fig. 4.8(b). For NESC, the Hessian inverse is also estimated as shown in Fig. 4.9. We remark that when the Hessian inverse is saturated to an identity matrix, NESC degenerates to a standard ESC scheme, which explains why the gradient and cost function of NESC overlaps with the standard ESC scheme in most occasions.

Table 4.2: The ESC and NESC tuning parameters used for METIS simulations on ITER.

Options	Parameters	Standard ESC		NESC	
	actuator	NBI	IC	NBI	IC
S	dither mag. [MW]	0.4			
	dither freq. [rad/s]	0.2992			
	phase	$\pi/2$	0	$\pi/2$	0
M	dither mag. [MW]	5			
	dither freq. [rad/s]	0.2992			
	phase	$\pi/2$	0	$\pi/2$	0
filters	highpass τ_h	0.1496			
	lowpass gradient τ_l	0.0748			
	lowpass Hessian τ_r	0.0748			
adaptive gains	K_g	0.0015		-	
	K_n	-		0.1	
weights	λ_{β_p}	1			
	λ_{Ω_ϕ}	1			
	λ_{P_α}	1			
norms	N_{β_p}	1000			
	N_{Ω_ϕ}	0.5			
	N_{P_α}	0.5			

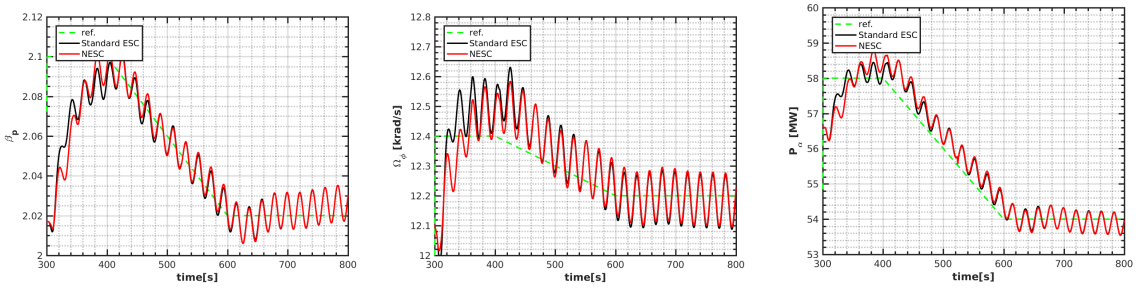

(a) (b) (c)

Figure 4.6: Comparison of plasma kinetic parameter optimization using the ESC and NESC schemes on ITER. Time traces of (a) the poloidal beta β_p, (b) the average toroidal rotation angular speed Ω_ϕ and (c) the α particle power generated from D-T reactions P_α.

4.1.4 Conclusion of Section 4.1

In this section, an NESC scheme has been developed and applied to the adaptive online optimization of plasma kinetic parameters in H-mode plasma scenarios on the EAST and ITER tokamaks via nonlinear METIS simulations. Compared with the standard ESC control, the NESC optimizer is able to estimate the Hessian and Hessian inverse of the cost function with respect to the control actuations, which makes the closed-loop convergence rate artificially-

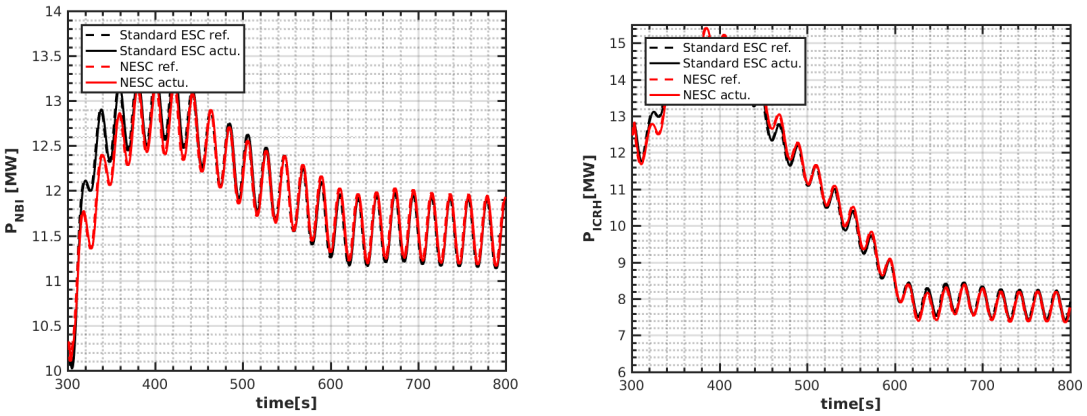

(a) (b)

Figure 4.7: Time traces of the additional heating and current drive powers on ITER, (a). the neutral beam injection power and (b). the ion cyclotron resonance heating power.

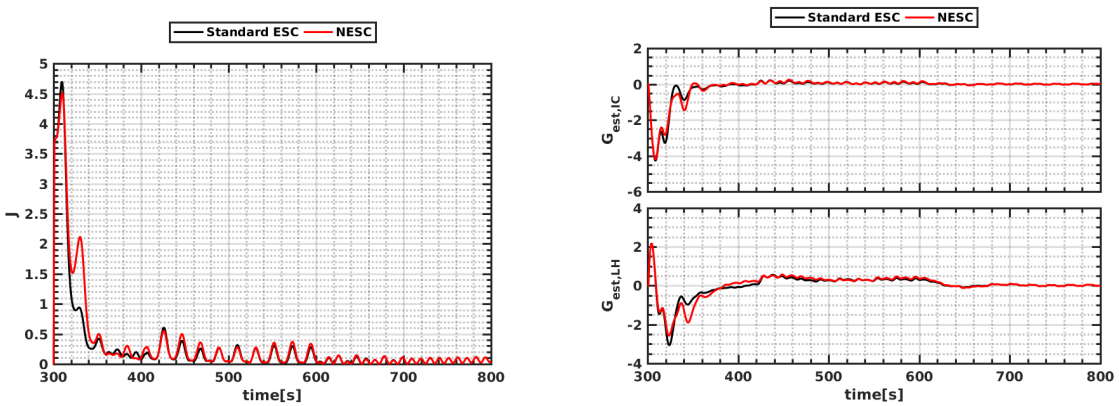

(a) (b)

Figure 4.8: Time traces of (a) the performance index and (b) the gradient estimates.

assignable. The drawback of this ESC optimization strategy is that it requires the actuation perturbations to extract the information of plasma dynamics and the optimization should be carried out in a much slower timescale than the characteristic time of plasma kinetic dynamics. Nonetheless, as an alternative method, it can potentially be applied to other plasma optimization problems where the plasma dynamics are highly nonlinear while the modelling is not possible or non-trivial, for instance, NTMs mitigation and suppression, ELMs suppression, the divertor heat flux and radiative power control.

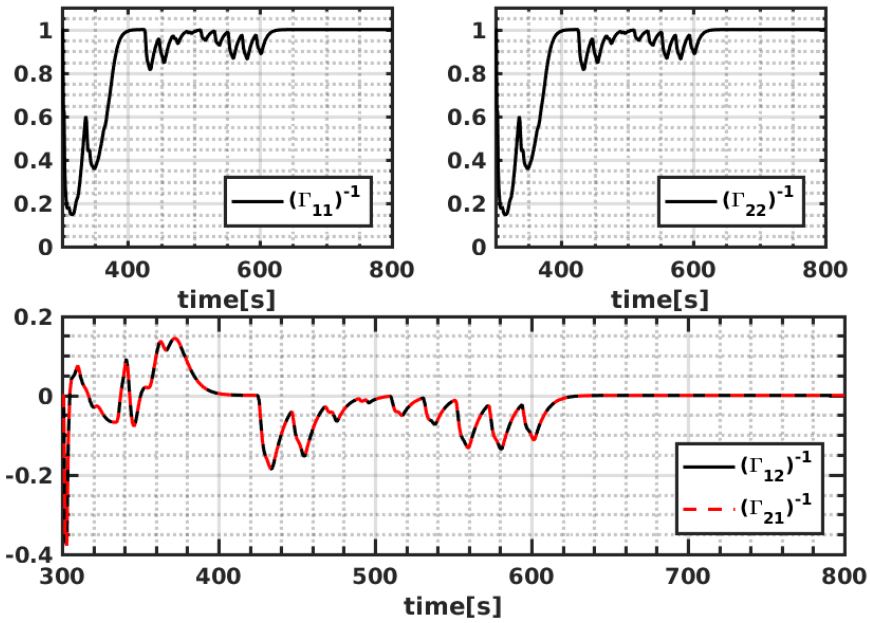

Figure 4.9: Time traces of the Hessian inverse estimates on ITER. Left-top panel: time traces of the first diagonal element estimate. Right-top panel: time traces of the second diagonal element estimate. Bottom panel: time traces of the off-diagonal element estimates.

4.2 MRAC control of plasma kinetic parameters: a SISO case

In this section, we investigate MRAC control of plasma kinetic parameters, including the poloidal beta β_p, the average toroidal rotation angular speed Ω_ϕ and the electron temperature on axis $T_{e,0}$ by actuating the ICRH power P_{ICRH} on EAST. First, the input-output transfer function structure is used to approximate the responses of plasma kinetic parameters with respect to the ICRH power. The adaptive control problem is then formulated by making a number of assumptions. Based on the given model structure and control assumptions, the dMRAC and iMRAC schemes are developed to track plasma kinetic parameters in a SISO setup, with the METIS simulation results demonstrating their effectiveness.

4.2.1 Control problem formulation

Our objective is to design a controller and parameter adjustment mechanism such that all the signals are bounded and the plant outputs track the desired plasma kinetic parameter reference as close as possible by actuating a control input [Ioannou and Sun, 1996]. The response of a kinetic parameter y_p with respect to a control actuator u_p can be expressed as an input-output transfer function:

$$y_p = G_p(s)u_p \tag{4.20}$$

with

$$G_p(s) = k_p \frac{Z_p(s)}{R_p(s)} \tag{4.21}$$

where $Z_p(s)$ and $R_p(s)$ are monic polynomials of degree $n_{p,z}$ and $n_{p,r}$, respectively and k_p is a constant named the high frequency gain. The reference model, which defines the desired control performance, is given by:

$$y_m = W_m(s)r \tag{4.22}$$

where y_m represents the desired trajectory to be tracked, r indicates the reference input, which is assumed to be uniformly bounded and piecewise continuous. $W_m(s)$ is the reference model which reads:

$$W_m(s) = k_m \frac{Z_m(s)}{R_m(s)} \tag{4.23}$$

where $Z_m(s)$ and $R_m(s)$ are monic polynomials of degree $n_{m,z}$ and $n_{m,r}$, respectively and k_m is a constant. In order to design a MRAC controller using only measured signals, i.e. without any differentiation involved, we make a number of assumptions on the plant and reference models as follows:

For the plant model (4.21):

- **P1**: $Z_p(s)$ is a monic Hurwitz polynomial.
- **P2**: An upper bound of the degree of the polynomial $R_p(s)$ is known to be n.
- **P3**: The relative degree $n^* = n_{p,r} - n_{p,z}$ is known.
- **P4**: The sign of the high frequency gain k_p is assumed to be known.

The assumption **P1** ensures that the plant transfer function $G_p(s)$ is minimum phase, which indicates that the plant should be detectable and stabilizable. **P2** allows the input-output filters designed for feedback control to be strictly proper. **P3** and **P4** are assumptions that can be relaxed by increasing the control complexity [Nussbaum, 1983, Morse, 1984].

For the reference model (4.23):

- **R1**: $Z_m(s)$ and $R_m(s)$ are both monic Hurwitz polynomials with the degree $n_{m,z}$ and $n_{m,r}$ and $n_{m,r} \leq n$.
- **R2**: The relative degree $n_m^* = n_{m,r} - n_{m,z}$ of $W_m(s)$ is the same as that of the plant $G_p(s)$, i.e. $n_m^* = n^*$.

In order to achieve the control objective, the dMRAC and iMRAC control schemes are considered based on the plant and reference model structures, respectively [Ioannou and Sun, 1996]. We first present the dMRAC scheme, which allows the controller structure to remain unchanged but with its control parameters directly adjusted according to the sampled input-output measurements by properly associating the model reference tracking errors with the control parameters. Then the iMRAC scheme is developed, which assumes a stationary model structure, and the controller parameters are calculated indirectly in two steps: the first step

consists in adapting the plant model parameters via the sampled input-output measurements, while the second step is to update the controller parameters by solving the reference model matching equations.

4.2.2 MRAC control: a direct approach

Based on the assumptions made for the plant and reference models, we now focus on the dMRAC design. In the first step, we assume that the plasma plant model is known, which may be identified from sampled simulations/experiments [Ljung, 1995] or obtained through the first-principles plasma theory [Artaud et al., 2018]. With the given plant and reference models, a model reference control (MRC) law [Morse, 1985] is thus derived by solving the reference-model matching equations. In the second step, we assume that the plasma plant model is not known exactly, and the certainty equivalence principle (CEP) [Ioannou and Sun, 1996, Landau et al., 2011] is thus used to develop adaptive laws for the control parameter adjustment.

4.2.2.1 Model reference control

Let us consider the following feedback controller structure as:

$$u_p = \theta_1^{*T}\frac{\alpha(s)}{\Lambda(s)}u_p + \theta_2^{*T}\frac{\alpha(s)}{\Lambda(s)}y_p + \theta_3^* y_p + c_0^* r \tag{4.24}$$

where

$$\alpha(s) = \begin{cases} [s^{n-2}, s^{n-3}, ..., s, 1]^T, & n \geq 2 \\ 0, & n < 2 \end{cases}$$

and $\theta_1^*, \theta_2^* \in \mathbb{R}^{n-1}, \theta_3^*, c_0^* \in \mathbb{R}$ are controller parameters to be designed, and $\Lambda(s)$ is an arbitrary monic Hurwitz polynomial of degree $n-1$ that contains $Z_m(s)$ as a factor $\Lambda(s) = \Lambda_0(s)Z_m(s)$, where $\Lambda_0(s)$ is a monic Hurwitz polynomial with the degree $n_0 = n - 1 - n_{m,z}$. u_p, y_p and r represent the measured input, the measured output and the reference, respectively. The control parameters can be expressed in a compact form as $\theta^* = [\theta_1^{*T}, \theta_2^{*T}, \theta_3^*, c_0^*]^T \in \mathbb{R}^{2n}$, which are designed to ensure that the transfer function from r to y_p is equal to the reference model $W_m(s)$.

Combining equations (4.20) and (4.24), the closed loop transfer function from r to y_p is computed as:

$$y_p = G_c(s)r = \frac{c_0^* k_p Z_p \Lambda^2}{\Lambda[(\Lambda - \theta_1^*)R_p - k_p Z_p(\theta_2^{*T}\alpha(s) + \theta_3^*\Lambda(s))]}r \tag{4.25}$$

The controller parameters θ^* can then be derived by solving the matching equation $G_c(s) = W_m(s)$, which writes as:

$$\frac{c_0^* k_p Z_p \Lambda^2}{\Lambda[(\Lambda - \theta_1^*)R_p - k_p Z_p(\theta_2^{*T}\alpha(s) + \theta_3^*\Lambda(s))]} = k_m\frac{Z_m(s)}{R_m(s)} \tag{4.26}$$

Choosing $c_0^* = \frac{k_m}{k_p}$ and $\Lambda(s) = \Lambda_0(s)Z_m(s)$, equation (4.26) is then transformed to an algebraic equation

$$\theta_1^{*T}\alpha(s)R_p(s) + k_p(\theta_2^*\alpha(s) + \theta_3^*\Lambda(s))Z_p(s) = \Lambda(s)R_p(s) - Z_p(s)\Lambda_0(s)R_m(s) \tag{4.27}$$

Multiplying $\frac{1}{R_p(s)}$ on both sides of equation (4.27), we obtain

$$\Lambda(s) - \theta_1^{*T}\alpha(s) - k_p\frac{Z_p(s)}{R_p(s)}\left(\theta_2^{*T}\alpha(s) + \theta_3^*\Lambda\right) = Z_p\left(Q(s) + k_p\frac{\Delta^*}{R_p}\right) \tag{4.28}$$

where $Q(s)$ and $k_p\Delta^*$ respectively represent the quotient and the remainder of $\frac{\Lambda_0 R_m}{R_p}$, i.e. $\frac{\Lambda_0 R_m}{R_p} = Q(s) + \frac{k_p\Delta^*}{R_p}$. We then obtain the control coefficients by solving the following equations

$$\begin{aligned} \theta_1^{*T}\alpha(s) &= \Lambda(s) - Z_p(s)Q(s) \\ \theta_2^{*T}\alpha(s) + \theta_3^*\Lambda(s) &= \frac{Q(s)R_p(s) - \Lambda_0(s)R_m(s)}{k_p} \end{aligned} \tag{4.29}$$

4.2.2.2 Adaptive controller parameter estimation

In this subsection, we assume that the plant model is not available, but the plant and reference models satisfy the assumptions **P1-P4** and **R1-R2**. The CEP is employed to design the dMRAC controller. The controller parameters θ^* are now replaced by their estimates $\theta(t)$ using an adaptive law, which is developed by relating the model tracking error with the controller parameters. The controller structure remains as:

$$u_p = \theta_1^{*T}\omega_1 + \theta_2^{*T}\omega_2 + \theta_3^* y_p + c_0^* r \tag{4.30}$$

Defining $\omega_1 = \frac{\alpha(s)}{\Lambda(s)}u_p$, $\omega_2 = \frac{\alpha(s)}{\Lambda(s)}y_p$, $\theta = [\theta_1^{*T}, \theta_2^{*T}, \theta_3^*, c_0^*]^T$ and $\omega = [\omega_1^T, \omega_2^T, y_p, r]^T$, the control law is expressed in a state-space form as:

$$\begin{aligned} \dot{\omega}_1 &= F\omega_1 + gu_p \\ \dot{\omega}_2 &= F\omega_2 + gy_p \\ u_p &= \theta^{*T}\omega \end{aligned} \tag{4.31}$$

where

$$F = \begin{bmatrix} -\lambda_{n-2} & -\lambda_{n-3} & -\lambda_{n-4} & \dots & -\lambda_0 \\ 1 & 0 & 0 & \dots & 0 \\ 0 & 1 & 0 & \dots & 0 \\ \vdots & \vdots & \ddots & \ddots & \vdots \\ 0 & 0 & \dots & 1 & 0 \end{bmatrix}, g = \begin{bmatrix} 1 \\ 0 \\ 0 \\ \vdots \\ 0 \end{bmatrix} \tag{4.32}$$

$\lambda_i, i = 0, ..., n-2$ are the coefficients of the monic Hurwitz polynomial:

$$\Lambda(s) = s^{n-1} + \lambda_{n-2}s^{n-2} + ... + \lambda_1 s + \lambda_0 = \det(sI_{n-1} - F) \tag{4.33}$$

Incorporating the control law (4.31) and the plant (4.21), we obtain the closed-loop system in a state-space form as:

$$\begin{aligned} \dot{Y}_c &= A_0 Y_c + B_c u_p, Y_c(0) = Y_0 \\ y_p &= C_c Y_c \end{aligned} \tag{4.34}$$

where the state vector Y_c is defined as $Y_c = [x_p^T, \omega_1^T, \omega_2^T]^T$ and

$$A_0 = \begin{bmatrix} A_p & 0 & 0 \\ 0 & F & 0 \\ gC_p^T & 0 & F \end{bmatrix}, B_c = \begin{bmatrix} B_p \\ g \\ 0 \end{bmatrix}, C_c = \begin{bmatrix} C_p & 0 & 0 \end{bmatrix}$$

Here, (A_p, B_p, C_p, D_p) is a state-space realization of the plant (4.21). Adding and subtracting the desired control input $B_c \theta^{*T} \omega$ yields $\dot{Y}_c = A_0 Y_c + B_c \theta^{*T} \omega + B_c(u_p - \theta^{*T} \omega)$. By a number of algebraic manipulations, we derive:

$$\begin{aligned} \dot{Y}_c &= A_c Y_c + B_c c_0^* r + B_c(u_p - \theta^{*T} \omega), Y_c(0) = Y_0 \\ y_p &= C_c Y_c \end{aligned} \tag{4.35}$$

where

$$A_c = \begin{bmatrix} A_p + B_p \theta_3^* C_p^T & B_p \theta_1^* & B_p \theta_2^{*T} \\ g\theta_3^* C_p^T & F + g\theta_1^* & g\theta_2^* \\ gC_p^T & 0 & F \end{bmatrix}$$

Considering the plant and reference model matching condition, the reference model is then given by:

$$\begin{aligned} \dot{Y}_m &= A_c Y_m + B_c c_0^* r, Y_c(0) = Y_0 \\ y_m &= C_c Y_m \end{aligned} \tag{4.36}$$

Subtracting equations (4.35) and (4.36), we obtain the error equation

$$\begin{aligned} \dot{X}_e &= A_c X_e + B_c(u_p - \theta^{*T} \omega) \\ e &= C_c X_e \end{aligned} \tag{4.37}$$

where $e = y_p - y_m$ and $X_e = Y_c - Y_m$. Considering $C_c(sI - A_c)^{-1} B_c c_0^* = W_m(s)$ and $u_p = \theta(t)^T \omega$, we can simplify equation (4.37) as $e = W_m(s)\rho^*(u_p - \theta^{*T} \omega)$. In order to construct adaptive laws, we define $u_f = W_m(s) u_p$ and $\phi = W_m(s)\omega$.

The gradient method with known sign of ρ^* ρ^* represents the direction of the control input on the control output. For example, β_p increases with P_{ICRH}, indicating that $\rho^* > 0$. ι_0 decreases with P_{LHCD}, implying that $\rho^* < 0$. If the sign of ρ^* is known, the error equation is given by:

$$e = \rho^*(u_f - \theta^{*T} \phi) \tag{4.38}$$

We assume the sign of the high frequency gain k_p is known and a gradient method is then employed to design the adaptive law. The error estimate $\hat{e}$ is expressed as $\hat{e} = \rho(t)\left(u_f - \theta(t)^T \phi\right)$,

where $\rho(t)$ and $\theta(t)$ are the estimates of ρ^* and θ^*. The normalized estimation error is then computed as $\epsilon = \frac{e-\hat{e}}{m^2}$, where $m^2 = 1 + n_s^2$ and $n_s^2 = \phi^T\phi + u_f^2$. Then we consider the cost function:

$$J(\rho, \theta) = \frac{\epsilon^2 m^2}{2} \tag{4.39}$$

Defining $\xi = \rho\left(u_f - \theta^T\phi\right)$, equation (4.39) is given by $J(\rho,\theta) = \frac{((e-\rho^*\theta^T\phi-\rho\xi+\rho^*\xi)-\rho^*u_f)^2}{2m^2}$. Because of the dependence of ξ on θ, $J(\rho,\theta)$ is not a convex function of ρ and θ. However, let us ignore the dependence and consider ξ as an independent variable. With the gradient method, we can then derive the adaptive laws for θ and ρ as:

$$\dot{\theta} = \Gamma_0\rho^*\epsilon\phi, \dot{\rho} = \gamma\epsilon\xi \tag{4.40}$$

where $\Gamma_0 = \Gamma_0^T > 0$ and $\gamma > 0$. ρ^* can be expressed $\rho^* = |\rho^*|\text{sign}(\rho^*)$. Since the term ρ^* is assumed to be constant and its sign is assumed to be known, the arbitrary adaptive gain matrix Γ_0 can be transformed to $\Gamma = \Gamma_0|\rho^*|$, which results in a set of implementable adaptive laws as:

$$\dot{\theta} = \Gamma\epsilon\phi\text{sign}(\rho^*), \dot{\rho} = \gamma\epsilon\xi \tag{4.41}$$

The gradient method with unknown sign of ρ^* If we do not know the sign of the gain ρ^*, we can develop adaptive laws using the Nussbaum gain. The estimate $\hat{e}$ of the tracking error e is expressed as:

$$\hat{e} = N(x)\rho(u_f - \theta^T\phi) \tag{4.42}$$

where the function $N(x)$ is referred to as the Nussbaum gain

$$N(x) = x^2 cos(x), x = \omega^2 + \frac{\rho^2}{2\gamma}, \dot{\omega} = \epsilon^2 m^2, w(0) = 0 \tag{4.43}$$

The adaptive laws are expressed as:

$$\dot{\theta} = -N(x)\Gamma\epsilon\phi, \dot{\rho} = N(x)\gamma\epsilon\xi \tag{4.44}$$

The Nussbaum gain is used to account for the unknown sign of ρ^* by changing the sign of the vector field of θ and ρ periodically with respect to the signal x.

4.2.3 MRAC control: an indirect approach

In this section, we develop an iMRAC scheme with normalization, based on the same assumptions used for the dMRAC design. The basic idea of the iMRAC controller is to develop adaptive laws to estimate the plant parameters of k_p, $Z_p(s)$ and $R_p(s)$, and these plant parameters are then used to compute the controller parameters by solving the model-matching equation.

4.2.3.1 Adaptive model parameter estimation

The plasma plant model is assumed to be a linear input-output transfer function model structure:

$$y_p = G_p(s)u_p = \frac{b_m s^m + b_1 s^{m-1} + b_2 s^{m-2} + ... + b_1 s + b_0}{s^n + a_{n-1}s^{n-1} + a_{n-2}s^{n-2} + ... + a_1 s + a_0} u_p \tag{4.45}$$

which can be then simplified into a linear regression form

$$z = \theta^{*T}\phi \tag{4.46}$$

where

$$z = \frac{s^n}{\Lambda_p(s)}, \theta^* = [0, 0, ..., 0, b_m, b_{m-1}, ..., b_0, a_{n-1}, ..., a_0]^T, \phi = \left[\frac{\alpha_{n-1}^T}{\Lambda_p(s)}u_p, -\frac{\alpha_{n-1}^T}{\Lambda_p(s)}y_p\right] \tag{4.47}$$

and $\Lambda_p(s) = s^n + \lambda_p^T \alpha_{n-1}$ is a Hurwitz polynomial, $\lambda_p = [\lambda_{n-1}, \lambda_{n-2}, \lambda_2, \lambda_1, \lambda_0]^T$. We note that the first $n - m - 1$ elements of θ^* are prescribed as 0.

The estimate of z is given by $\hat{z} = \hat{\theta}^T\phi$, where $\hat{\theta} = [0, 0, ..., 0, \hat{p}_1, \hat{p}_2]$, $\hat{p}_1 = [\hat{b}_{m-1}, ..., \hat{b}_0]$ and $\hat{p}_2 = [\hat{a}_{n-2}, ..., \hat{a}_0]$. The normalized error equation is expressed as $\epsilon = \frac{(z-\hat{z})}{m^2}$, where $z = y_p + \lambda_p^T\phi_2$, $m^2 = 1 + \phi^T\phi$, $\phi_2 = \frac{\alpha_{n-1}^T}{\Lambda_p(s)}y_p$. We then consider the cost function

$$J(p_1, p_2, k_p) = \frac{\epsilon^2 m^2}{2} \tag{4.48}$$

Using the gradient method, we can obtain the adaptive laws as

$$\dot{\hat{p}}_1 = \Gamma_1\bar{\phi}_1\epsilon, \dot{\hat{p}}_2 = \Gamma_2\phi_2\epsilon, \dot{\hat{k}}_p = \gamma\phi_{1m}\epsilon \tag{4.49}$$

where $\phi_1 = \alpha_{n-1}^T\Lambda_p(s)u_p$. Assuming the low bound of k_p is known, we can make the adaptive laws more robust by involving the projection technique

$$\dot{\hat{k}}_p = \begin{cases} \gamma\phi_{1m}\epsilon, & \text{if} \quad |\hat{k}_p| \gg k_0 \quad \text{or} \quad |\hat{k}_p| = 0 \quad \text{and} \quad \phi_{1m}\epsilon\text{sign}(k_p) \geq 0 \\ 0, & \text{otherwise} \end{cases} \tag{4.50}$$

4.2.3.2 Model reference control law

Once the plant parameters are estimated, we could immediately compute the appropriate control parameters by solving a matching equation which guarantees that the closed-loop transfer function is equal to the reference model transfer function. The plant parameters are replaced by their estimates based on the CEP. $c_0(t) = \frac{k_m}{\hat{k}_p}$, $\theta_1(t)$, $\theta_2(t)$ and $\theta_3(t)$ are computed by solving the following equations:

$$\begin{aligned} \theta_1(t)^T\alpha(s) &= \Lambda(s) - \hat{Z}_p(s)\hat{Q}(s) \\ \theta_2(t)^T\alpha(s) + \theta_3(t)\Lambda(s) &= \frac{\hat{Q}(s)\hat{R}_p(s) - \Lambda_0(s)R_m(s)}{\hat{k}_p} \end{aligned} \tag{4.51}$$

where $\hat{Z}_p = [\hat{k}_p, \hat{p}_1^T]\alpha_m(s)$, and $\hat{Q}$ is the polynomial quotient $\frac{\Lambda_0(s)R_m(s)}{\hat{R}_p(s)}$. The control law is therefore expressed as:

$$u_p = \theta^T(t)\omega \tag{4.52}$$

where

$$\theta(t) = [\theta_1^T, \theta_2^T, \theta_3, c_0]^T, \omega = [\omega_1^T, \omega_2^T, y_p, r]^T, \omega_1 = \frac{\alpha_{n-2}(s)}{\Lambda(s)}u_p, \omega_2 = \frac{\alpha_{n-2}(s)}{\Lambda(s)}y_p$$

4.2.4 Simulation results

The dMRAC and iMRAC schemes were implemented into the MATLAB/Simulink framework and coupled with the nonlinear plasma simulator, METIS [Artaud et al., 2018], for closed-loop control assessment. The closed-loop METIS simulations are based on the reference scenario in the current flattop phase of a fully non-inductive upper-single-null (USN) H-mode plasma discharge on the EAST tokamak. It has the toroidal magnetic field $B_T = 2.5$ T, the central electron density $n_{e0} \approx 3.5 \times 10^{19}$ m^{-3} and plasma current $I_p = 0.42$ MA. The discharge was obtained using LHCD (0.6 MW at 2.45 GHz and 2 MW at 4.6 GHz), 0.32 MW of ICRH at 33 MHz and 0.3 MW of ECRH at 140 GHz. The transition to H-mode occurred at 3.1 s with an H-mode enhancement factor $\mathrm{H}_{98}(y, 2) \sim 1.1$. The q-profile exhibited a small negative shear in the plasma core, with minimum q around 1.5 and $q_0 \sim 2$ on axis. The procedure for tuning the METIS code for interpretative simulations of advanced tokamak plasma discharges is described in [Moreau et al., 2015]. The objective is to assess the capabilities of the dMRAC and iMRAC schemes in tracking plasma magnetic kinetic parameters by adjusting the ICRH power and the controller parameters simultaneously. A number of simulation cases are presented to evaluate the performance and adaptivity of the proposed schemes.

4.2.4.1 Tracking of plasma kinetic parameters

It has been shown in Chapter 3 that the ICRH power is an effective actuator to track plasma kinetic parameters such as β_p, Ω_ϕ and $T_{e,0}$. Therefore, the first case consists in tracking β_p by actuating the ICRH power. Assuming that the response of β_p with respect to P_{IC} is approximated by a second-order transfer function as

$$G_{P_{IC},\beta_p}(s) = \frac{k_p s + k_z}{s^2 + k_{r,1}s + k_{r,2}} \tag{4.53}$$

The objective is to choose P_{IC} such that the behaviour of β_p follows the reference model $G_m(s) = \frac{20}{s+20}$. For the dMRAC controller, the controller model structure is given in equation (4.24). The ω_1 and ω_2 are computed by filtering the input $\tilde{P}_{\mathrm{ICRH}}$ and the output $\tilde{\beta}_p$ with a filter $\frac{1}{(s+2)}$. The controller parameters θ and the coefficient ρ are estimated using the adaptive laws as given in equations (4.42)-(4.44), in which the adaptive gains $\Gamma = 70I_4$ and $\gamma = 70$. The initial value of θ is set at 0, while the initial value of $\rho = 0$. For the iMRAC controller, the plasma plant model is estimated online first using the adaptive laws given in equations (4.49)-(4.50). Then the derived model parameters are used to update the control

parameters by solving the equations (4.51). The filtering term $\Lambda(s) = (s + 2)$ and the model parameters are initialized as $k_p = 18, k_z = 100, k_r = [22, 40]$. The β_p reference trajectories are designed to have two harmonics with frequency at 2 Hz and 1.25 Hz to satisfy the persistently exciting condition. Fig. 4.10 shows the closed-loop METIS simulation results, in which the controllers are activated at 3.5 s. It is found that both the dMRAC Nussbaum controller and the iMRAC controller can achieve the satisfactory tracking for β_p by adjusting the ICRH power in real-time. One can further notice that β_p cannot be tracked during the initial phase by the dMRAC Nussbaum control because the control parameters are prescribed to be 0, which assumes nothing about the model information. Because of the adaptive control estimation, after 1 s, the dMRAC Nussbaum controller starts to work effectively. The evolution of the controller parameters in dMRAC Nussbaum scheme is shown in Fig. 4.10(c). The positive sign of ρ indicates that β_p increases with P_{ICRH}. The reason why the iMRAC controller has good initial control performance is that the model used for the reference control design matches the plant well. Nonetheless, the model is not good enough, so that k_p and $p_{r,1}$ evolves a bit which leads to the variations of the controller parameters θ_1, θ_2 and c_0. To sum up, both dMRAC and iMRAC control schemes can achieve satisfactory tracking of β_p by actuating the power of the ICRH system. We emphasize that in order to achieve good control performance, two sets of parameters are important: 1) the adaptive gain used in the adaptive laws and 2) the initial setup of the model parameters in the iMRAC scheme and the controller parameters in the dMRAC Nussbaum scheme.

In order to further show the versatility of the MRAC schemes, we here use P_{ICRH} to track the toroidal rotation angular speed ω_ϕ and the central electron temperature $T_{e,0}$, separately. Analogously to the first case, the dMRAC and iMRAC schemes have been tested in parallel. The closed-loop METIS simulation results for the control of ω_ϕ are shown in Fig. 4.11. For the dMRAC control design, the adaptive laws with the Nussbaum gain described in equations (4.42)-(4.44) are employed to update the controller parameters $\theta(t)$ and the coefficient $\rho(t)$, with the adaptive gains $\Gamma = 1.75I_4$ and $\gamma = 1.75$. The initial value of θ and ρ are prescribed to be 0. For the iMRAC design, the plasma plant model, assumed to be a second-order transfer function, is estimated online using the adaptive laws provided in equations (4.49)-(4.50), with the adaptive gains prescribed as $\Gamma_{k_p} = 3200, \Gamma_{p_z} = 3200, \Gamma_{p_r} = 400I_2$. The filtering term $\Lambda = (s + 5)$, while the model parameters are initialized as $k_p = 80, k_z = 28, k_r = [22, 40]$. The reference trajectory has one harmonic at 1.5 Hz. As shown in Fig. 4.11(a), the tracking performance by the two considered adaptive schemes are satisfactory. The tracking errors of the two control schemes are illustrated in Fig. 4.11(b). One can notice that during the whole control phase, the iMRAC scheme outperforms the dMRAC Nussbaum scheme, because dMRAC Nussbaum scheme does not use any model information at the initial stage, which leads to the longer online tuning time. Although there is a model mismatch at the initial control stage, the iMRAC scheme is capable of self-tuning the model parameters to approximate the actual plasma dynamics, which generates better controller parameters and leads to the reduced tracking error.

The results of tracking the central electron temperature $T_{e,0}$ using P_{ICRH} are shown in Fig. 4.12. It is found that comparable tracking performance has been obtained by the two different MRAC schemes. In this case, the dMRAC Nussbaum controller performs slightly better, as

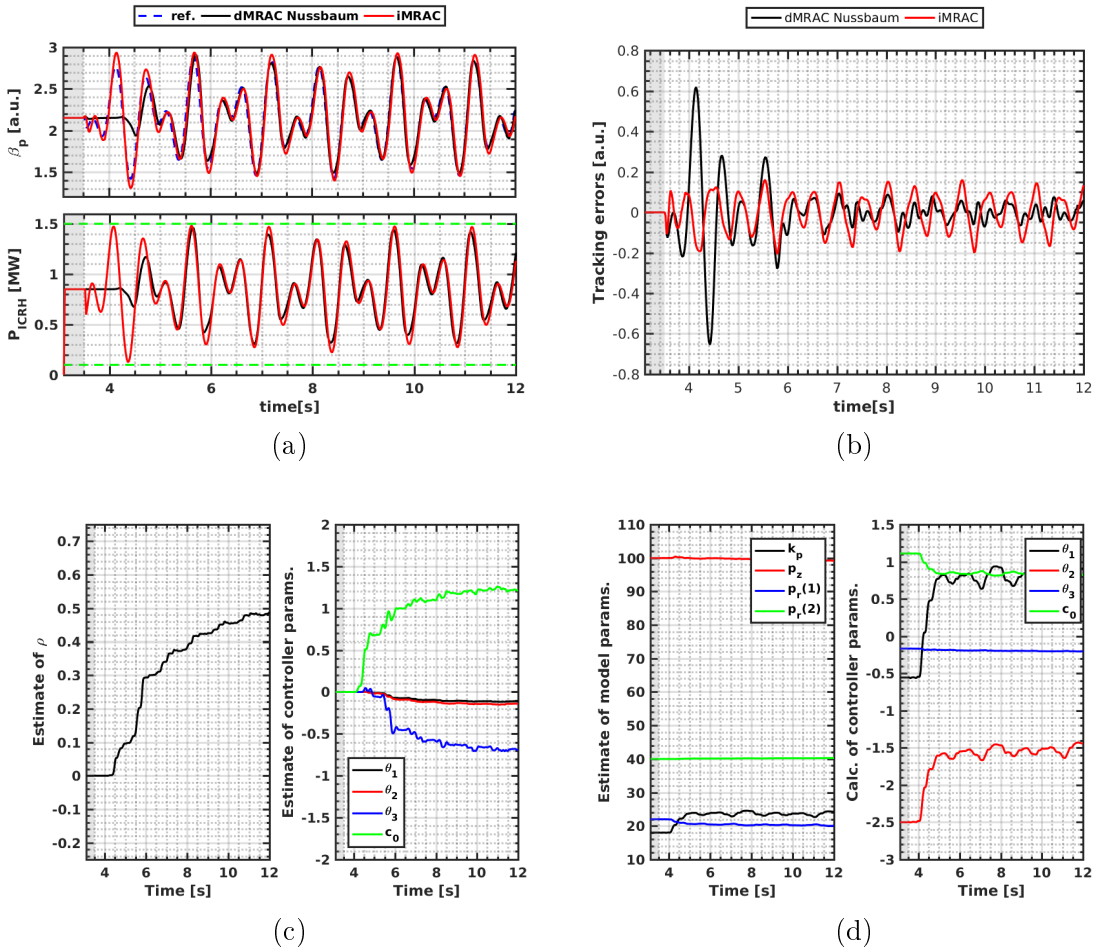

Figure 4.10: Tracking of β_p using P_{ICRH}. Upper frame of (a) : comparison of β_p references (blue dashed) and the achieved β_p values (black) by the direct MRAC Nussbaum controller, the achieved β_p values (red) by the indirect MRAC controller. Bottom frame of (a): time traces of the associated ICRH powers requested by the direct MRAC Nussbaum controller (black) and the indirect MRAC controller (red). Frame (b): time traces of β_p tracking errors by the dMRAC Nussbaum controller (black) and the iMRAC controller (red). Left frame of (c): time traces of the online estimate of ρ by the direct MRAC. Right frame of (c): time traces of the online estimate of the controller parameters for the direct MRAC. Left frame of (d): time traces of the online estimate of the model parameters by the indirect MRAC. Right frame of (d): time traces of the online update of the controller parameters by the indirect MRAC.

seen on Fig. 4.12(b) after 5 s.

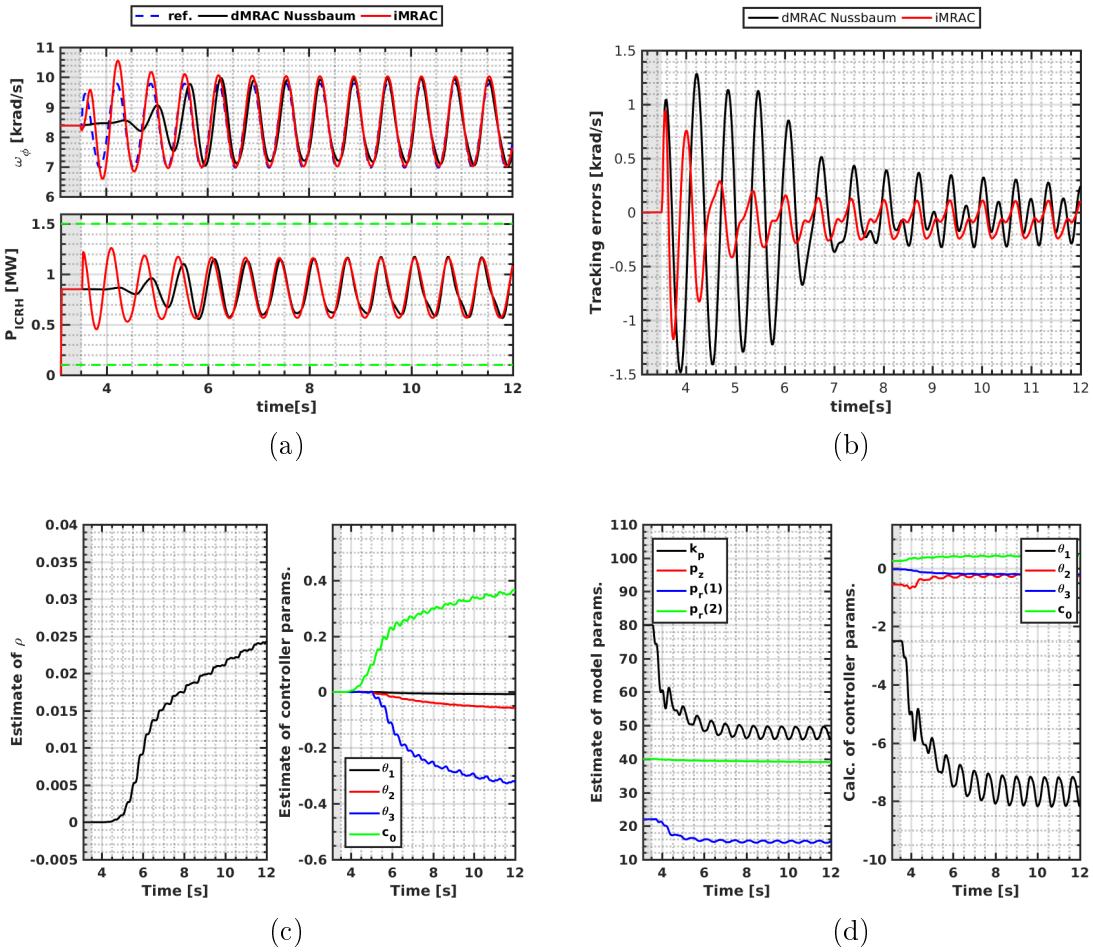

Figure 4.11: Tracking of ω_ϕ using P_{ICRH}. Upper frame of (a) : comparison of ω_ϕ references (blue dashed), the achieved β_p values (black) by the direct MRAC Nussbaum controller and the achieved ω_ϕ values (red) by the indirect MRAC controller. Bottom frame of (a): time traces of the associated ICRH powers requested by the direct MRAC Nussbaum controller (black) and the indirect MRAC controller (red). Frame (b): time traces of ω_ϕ tracking errors by the dMRAC Nussbaum controller (black) and the iMRAC controller (red). Left frame of (c): time traces of the online estimate of ρ by the dMRAC controller. Right frame of (c): time traces of the online estimate of the controller parameters for the dMRAC controller. Left frame of (d): time traces of the online estimate of the model parameters by the iMRAC controller. Right frame of (d): time traces of the online update of the controller parameters by the iMRAC controller.

4.2.4.2 Impact of the tuning parameters on tracking performance

The objective of this section is to investigate the impact of the tuning parameters used in the MRAC schemes on the control performance. In particular, three important tuning parameters are considered in great detail, including the adaptive gains, the control initialization and the

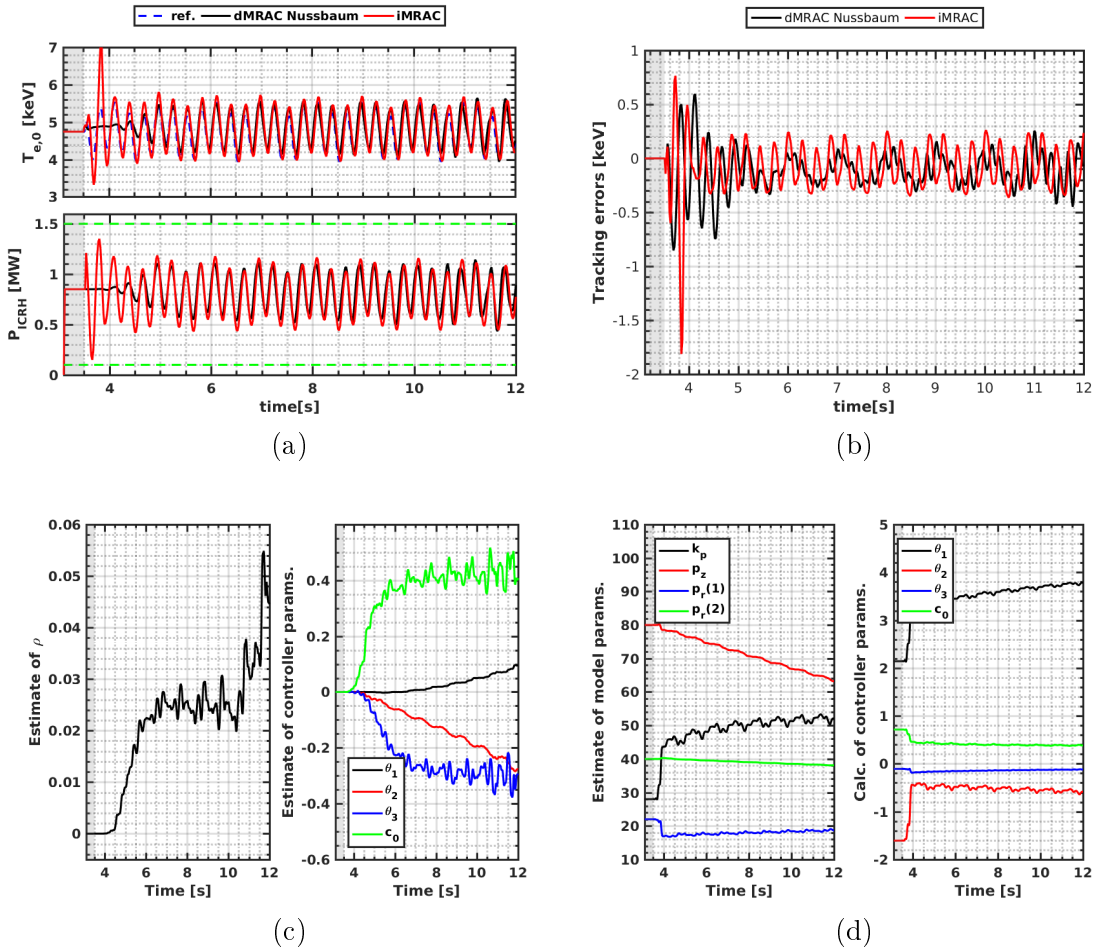

Figure 4.12: Tracking of $T_{e,0}$ using P_{ICRH}. Upper frame of (a): comparison of $T_{e,0}$ references (blue dashed), the achieved $T_{e,0}$ values (black) by the direct MRAC Nussbaum controller and the achieved $T_{e,0}$ values (red) by the indirect MRAC controller. Bottom frame of (a): time traces of the associated ICRH powers requested by the direct MRAC Nussbaum controller (black) and the indirect MRAC controller (red). Frame (b): time traces of $T_{e,0}$ tracking errors by the dMRAC Nussbaum controller (black) and the iMRAC controller (red). Left frame of (c): time traces of the online estimate of ρ by the dMRAC controller. Right frame of (c): time traces of the online estimate of the controller parameters for the dMRAC controller. Left frame of (d): time traces of the online estimate of the model parameters by the iMRAC controller. Right frame of (d): time traces of the online update of the controller parameters by the iMRAC controller.

plasma plant model order. The adaptive gains used in both dMRAC and iMRAC schemes are evaluated by scanning the adaptive gain values. Fig 4.13(a) shows the comparison of β_p tracking errors by actuating the ICRH power P_{ICRH} with the dMRAC controller. All the control parameters in the dMRAC Nussbaum controller are initialized as zero, which explains why the tracking errors are relatively large at the initial control phase. Due to the real-time

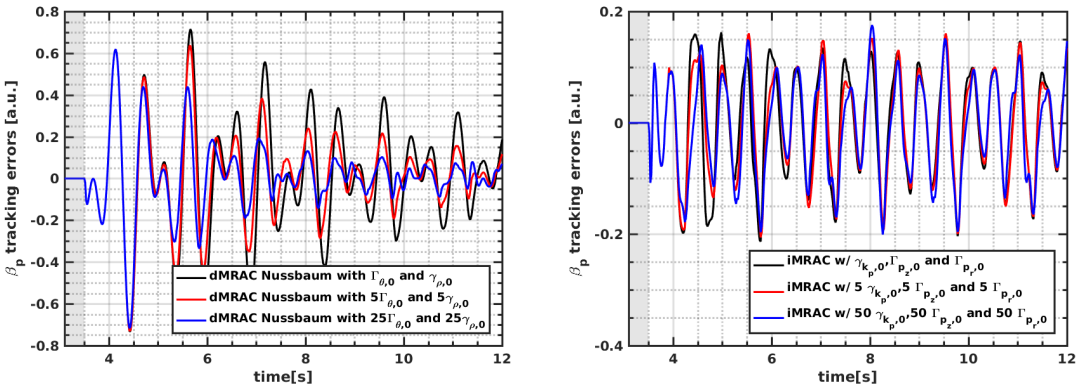

(a) (b)

Figure 4.13: Comparison of β_p tracking errors with different adaptive gains for (a) the direct MRAC Nussbaum controller, i.e. Γ_θ and γ_ρ and (b) the indirect MRAC controller, i.e. $\gamma_{k_p}, \Gamma_{p_z}$ and Γ_{p_r}.

control parameter adaptation, the tracking errors converge to a small value approaching 0. It is clear that the convergence rate grows with the increase of the adaptive gains for θ and ρ. With the adaptive gains fixed at $5\Gamma_{\theta,0}$ and $5\gamma_{\rho,0}$, the dynamic tracking errors are remarkably reduced to a small value in the interval [-0.05, 0.05]. The adaptive control gains were also scanned for the iMRAC scheme, and the METIS simulation results are shown in Fig. 4.13(b). One can notice that increasing the adaptive gains for the model coefficients k_p, p_z and p_r can only slightly reduce the tracking errors, implying that the initial model coefficients are close to the optimal values in the given plant model structure. Besides, we remark that the adaptive gains used for both dMRAC and iMRAC schemes should not be set large so as to avoid control instability issues.

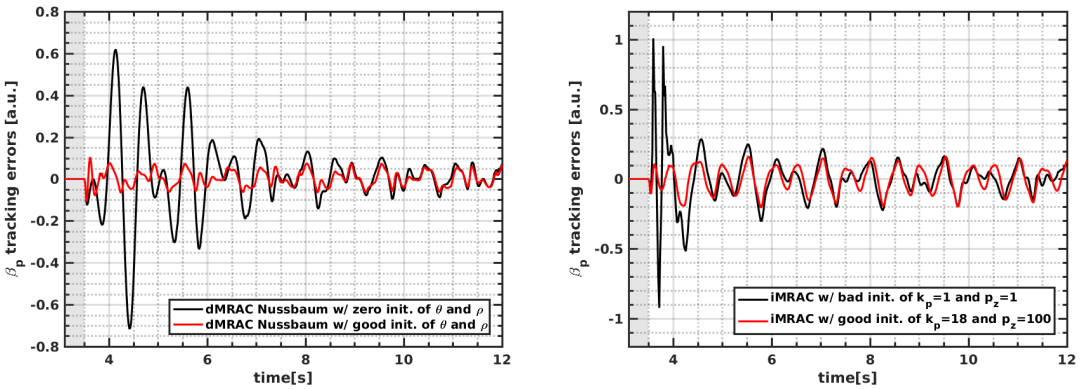

(a) (b)

Figure 4.14: Comparison of β_p tracking errors with different adaptive gains by (a) the direct MRAC Nussbaum controller and (b) the indirect MRAC controller.

The impact of control initialization on the tracking performance is evaluated by performing comparative simulations for the dMRAC and iMRAC controllers separately. The β_p tracking errors with zero control initialization are compared with those obtained with good control initialization for the dMRAC Nussbaum scheme, as shown in Fig. 4.14(a). It is clear that if the dMRAC Nussbaum controller is configured with good control initialization, the tracking errors at the initial phase of feedback control are remarkably smaller. It suggests that good control initialization is beneficial to the tracking performance at the initial control phase. Nonetheless, thanks to the adaptive laws, the tracking errors gradually converge to the same level with the controller that has been properly initialized. For the case of the iMRAC controller, we purposely initialize the model parameters k_p and k_z to be far away from the real values. The METIS simulation results are compared with the model parameters initialized properly in Fig. 4.14(b). As expected, at the initial control phase, the tracking errors are considerable, ranging from -1 to 1. Due to the model parameter adaptation, the tracking errors converge to the interval [-0.2,0.2], which is comparable with the case where the model parameters are properly initialized. Based on the comparative simulations for both the dMRAC and iMRAC schemes, we conclude that (1) control initialization is beneficial to the tracking performance at the initial adaptive control phase; (2) the controller can adaptively tune its parameters in a direct or indirect manner such that the tracking errors substantially decrease even with bad initialization of the controller parameters (dMRAC) and of the model parameters (iMRAC).

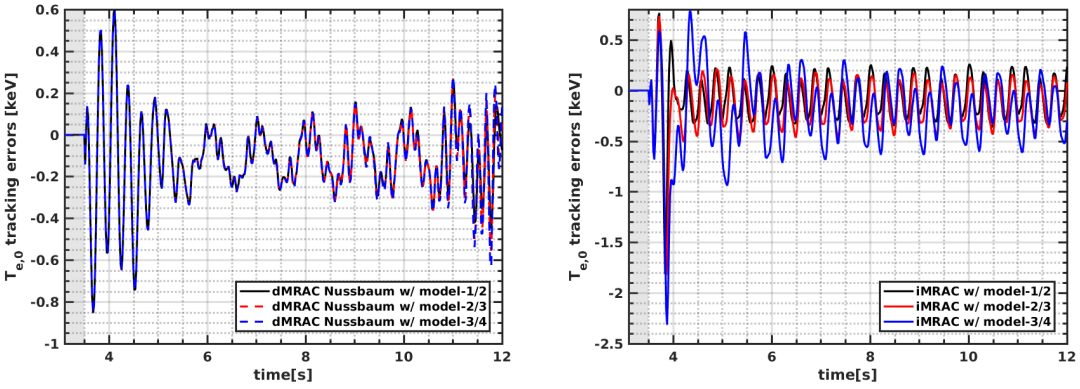

(a) (b)

Figure 4.15: Comparison of $T_{e,0}$ tracking errors with different model orders by (a) the dMRAC Nussbaum controller and (b) the iMRAC controller. Note that, in the legends, the symbol "model-i/j" represents the plant model with i zeros and j poles.

The impact of the model order on the tracking performance is evaluated via comparative simulations. The dMRAC controller for $T_{e,0}$ tracking was tested by assuming different model orders. The METIS simulation results are shown in Fig. 4.15(a) and no obvious differences were observed by using different model orders for the dMRAC controller. The model order on the control performance of an iMRAC scheme was also studied, with results shown in Fig. 4.15(b). We can see that the model-1/2 and model-2/3 seem to have comparable performance, and it appears that the tracking performance slightly descreases with the increase of the plasma

plant model order.

4.2.5 Conclusion of Section 4.2

In this section, two different MRAC schemes have been applied to tracking plasma kinetic parameters in tokamak plasmas by actuating the ICRH system. The first control scheme (dMRAC) assumes a stationary controller structure and updates the controller parameters, system inputs, references and outputs simultaneously. The controller parameters are estimated by a set of adaptive laws driven by a normalized estimation error. The use of a Nussbaum gain enables the effectiveness of the dMRAC control even when the sign of ρ is unknown. The second control scheme (iMRAC) assumes a stationary model structure, with the model parameters estimated online according to the sampled input-output data. Next, the controller parameters are derived by solving the model-matching equations aiming to approximate the reference model at best. Closed-loop METIS simulations performed on EAST suggest that these two MRAC control schemes can achieve the reference tracking effectively. Compared with iMRAC, the dMRAC Nussbaum controller does not require any model information in the course of control, though good control initialization can ensure better tracking performance at the initial control phase. However, the idea of iMRAC control is much more straightforward, and may be more suitable for the situation where the plasma plant model has sufficient quality.

4.3 MRAC control of plasma kinetic parameters: a MIMO case

In this section, the dMRAC scheme described in Section 4.2 is extended to a MIMO version for the tracking of plasma kinetic parameters in advanced tokamak scenarios. The MIMO extension of the output MRC is introduced first. Assuming unknown controller parameters, a MIMO version of dMRAC is then developed based on CEP, with simulation examples showing the effectiveness of the MIMO dMRAC scheme.

4.3.1 MRAC control: a direct approach

Let us assume the plasma dynamics to be a MIMO LTI transfer matrix with m inputs and m outputs:

$$y(t) = G(s)[u](t) \tag{4.54}$$

where $y(t) \in \mathbb{R}^m$ represents the system outputs containing the plasma parameters of interest, while $u(t) \in \mathbb{R}^m$ denotes the system inputs including the available control actuators. s is a Laplace transform variable or the differentiation operation. $G(s)$, an unknown and nonsingular transfer matrix, can be factorized as $G(s) = Z(s)P(s)^{-1}$, where $Z(s)$ and $P(s)$ are $m \times m$ coprime polynomial matrices, with $P(s)$ column proper.

We can then derive a left modified interactor matrix (LMI) [Tao, 2014] of $G(s)$ as $\xi_m(s)$:

$$\xi_m(s) = \begin{bmatrix} l_1(s) & 0 & 0 & ... & 0 \\ h_{21}^m(s) & l_2(s) & 0 & ... & 0 \\ h_{31}^m(s) & h_{32}^m(s) & l_3(s) & ... & 0 \\ ... & ... & ... & ... & ... \\ h_{m1}^m(s) & h_{m2}^m(s) & ... & ... & l_m(s) \end{bmatrix} \tag{4.55}$$

where $l_i(s), i = 1, 2, ..., m$ are monic Hurwitz polynomials, and $h_{ij}^m(s), i, j = 1, 2, ..., m$ are polynomials. Since the system is assumed to be proper and nonsingular, the LMI matrix has a stable inverse that indicates the zero structure of $G(s)$ at infinity. In addition, $\xi_m(s)$ is associated with the high frequency gain matrix (HFGM) of $G(s)$ in the following relation

$$K_p = \lim_{s \to \infty} \xi_m(s) G(s) \tag{4.56}$$

where $K_p \in \mathbb{R}^{m \times m}$ denotes the HFGM of $G(s)$ that is finite and nonsingular.

In order to achieve the MRAC control stability, we make the following assumptions on the plasma system dynamics:

(a) All zeros of $G(s)$ are stable;

(b) The upper bound of the observability index of $G(s)$ is known;

(c) The transfer matrix $G(s)$ is proper and nonsingular;

(d) The LMI matrix $\xi_m(s)$ of $G(s)$ is known;

(e) All the leading principle minors of the HFGM K_p are not zero whose signs are known.

Assumption **(a)** ensures that the plasma system is stabilizable and detectable; Assumption **(b)** is satisfied to design proper input-output filters; Assumption **(c)** and **(d)** are utilized to design a reference model; Assumption **(e)** is analogous to know the sign of the high frequency gain in a SISO case, which is satisfied to guarantee the correct convergent direction.

4.3.1.1 Reference model

The reference model refers to the desired system dynamics to be followed, expressed as:

$$y_m(t) = W_m(s)[r](t) \tag{4.57}$$

where $y_m(t) \in \mathbb{R}^m$ represents the desired output while $r(t)$ denotes the reference input which is assumed to be bounded and piecewise continuous. $W_m(s)$ is the reference model designed as the inverse of the LMI matrix, i.e. $W_m(s) = \xi_m^{-1}(s)$.

4.3.1.2 Control law

The controller structure is defined as:

$$u(t) = \Theta_1^T \omega_1(t) + \Theta_2^T \omega_2(t) + \Theta_{20} y(t) + \Theta_3 r(t) \tag{4.58}$$

where $\Theta_1 \in \mathbb{R}^{m(\bar{\nu}-1)\times m}$ and $\Theta_2 \in \mathbb{R}^{m(\bar{\nu}-1)\times m}$ are control parameters for the filtered inputs $\omega_1(t)$ and outputs $\omega_2(t)$, respectively. ν represents the upper bound of the observability index of $G(s)$. $\Theta_{20} \in \mathbb{R}^{m\times m}$ and $\Theta_3 \in \mathbb{R}^{m\times m}$ are the control parameters for the outputs and the reference inputs, respectively. Θ_1 can be further divided as $\Theta_1 = [\Theta_{11}, \Theta_{12}, ..., \Theta_{1\bar{\nu}-1}]$, where $\Theta_{1i} \in \mathbb{R}^{m\times m}, i = 1, 2, \ldots, \bar{\nu}-1$. Likewise, Θ_2 is expressed as $\Theta_2 = [\Theta_{21}, \Theta_{22}, ..., \Theta_{2\bar{\nu}-1}]$, where $\Theta_{2i} \in \mathbb{R}^{m\times m}, i = 1, 2, ..., \bar{\nu}-1$. ω_1 and ω_2 are filtered input-output signals:

$$\omega_1(t) = F(s)u(t), \omega_2(t) = F(s)y(t) \tag{4.59}$$

where

$$F(s) = \frac{I_0(s)}{\Lambda(s)}, I_0(s) = [I_m, sI_m, ..., s^{\bar{\nu}-1}I_m]^T$$

where $\Lambda(s)$ is a monic Hurwitz polynomial of degree $\bar{\nu}-1$.

First, we assume the plant model is known, which can be identified from sampled input-output data using the system identification methodology described in Chapter 2. We can then choose $\Theta_3^* = K_p^{-1}$ and the control parameters Θ_1^*, Θ_2^* and Θ_{20}^* are computed by solving the following matching equation:

$$\Theta_1^{*T} I_0(s)P(s) + (\Theta_2^{*T} I_0(s) + \Theta_{20}\Lambda(s))Z(s) = \Lambda(s)(P(s) - \Theta_3^* \xi_m(s)Z(s)) \tag{4.60}$$

We first divide $\Lambda(s)$ on the both sides of equation (4.60) and then post-multiply by $P(s)^{-1}$, which yields:

$$I_m - \Theta_1^{*T} F(s) - \Theta_2^{*T} F(s)G(s) - \Theta_{20}^* y(t) = \Theta_3^* W_m^{-1}(s)G(s) \tag{4.61}$$

Then post-multiplying by $u(t)$ on both sides of equation (4.61), we obtain

$$u(t) - \Theta_1^* \omega_1(t) - \Theta_2^* \omega_2(t) - \Theta_{20} y(t) = \Theta_3^* W_m^{-1}(s)[y](t) \tag{4.62}$$

Subtracting $\Theta_3^* r$ on both sides, and using the relation $W_m(s) = \xi_m^{-1}(s)$ and $\Theta_3^* = K_p^{-1}$, we then derive

$$K_p(u(t) - \Theta_1^{*T}\omega_1(t) - \Theta_2^{*T}\omega_2(t) - \Theta_{20}^* y(t) - \Theta_3^* r(t)) = \xi_m(s)[y - y_m](t) \tag{4.63}$$

Assume that we obtain the true control parameters, i.e. $u(t) = \Theta_1^{*T}\omega_1(t) + \Theta_2^{*T}\omega_2(t) + \Theta_{20}^* y(t) + \Theta_3^* r(t)$. Then equation (4.63) becomes $\xi_m(s)[y - y_m](t) = 0$. Due to the nonsingularity of $\xi_m(s)$, it implies that $\lim_{t\to\infty}(y - y_m) = 0$. In other words, if the true control parameters are utilized for output feedback control, the output y converges to the reference y_m asymptotically.

4.3.1.3 Adaptive law

In this section, we assume that the plasma plant model parameters are unknown, which motivates us to develop adaptive laws that estimate the appropriate control parameters online. Consider the same controller structure as equation (4.58) and define the true and unknown control parameters as

$$\Theta^* = [\Theta_1^{*T}, \Theta_2^{*T}, \Theta_{20}^*, \Theta_3^*] \tag{4.64}$$

Since we do not know the exact values of the true control parameters Θ^*, the CEP [Tao, 2014] is used to replace the true control parameters by their estimates

$$\Theta = [\Theta_1^T(t), \Theta_2^T(t), \Theta_{20}(t), \Theta_3(t)] \tag{4.65}$$

Defining the estimation error as $\tilde{\Theta} = \Theta(t) - \Theta^*$, the associated regressor is expressed as:

$$\omega(t) = [\omega_1^T(t), \omega_2^T(t), \omega_{20}, \omega_3]^T \tag{4.66}$$

Decomposition of the HFGM K_p Assumption (d) indicates that K_p has all non-zero leading principle minors, and K_p can be non-uniquely decomposed as $K_p = LDS$, where $L, D, S \in \mathbb{R}^{m\times m}$, L represents a lower triangular matrix, S is a symmetric positive definite matrix, $S = S^T > 0$, and

$$D = \text{diag}\left\{\text{sign}\left(\Delta_1\right)\gamma_1, \text{sign}\left(\frac{\Delta_2}{\Delta_1}\right)\gamma_2, ..., \text{sign}\left(\frac{\Delta_m}{\Delta_{m-1}}\right)\gamma_m\right\} \tag{4.67}$$

Substituting the gain matrix $K_p = LDS$ into equation (4.63), we obtain

$$DS\left(u(t) - \Theta_1^{*T}\omega_1(t) - \Theta_2^{*T}\omega_2(t) - \Theta_{20}^* y(t) - \Theta_3^* r(t)\right) = L^{-1}\xi_m(s)[y - y_m](t) \tag{4.68}$$

Parameterizing the control law $u(t) = \Theta^T(t)\omega$, and the tracking error $e(t) = y(t) - y_m(t)$, we obtain $L^{-1}\xi_m(s)[e](t) = DS\tilde{\Theta}^T\omega$. Next, introducing a new matrix $\Lambda^* = L^{-1} - I_m$, one has

$$\Lambda^* = \begin{bmatrix} 0 & 0 & 0 & \dots & 0 \\ \lambda_{2,1}^* & 0 & 0 & \dots & 0 \\ \lambda_{3,1}^* & \lambda_{3,2}^* & 0 & \dots & 0 \\ \vdots & \vdots & \vdots & \ddots & 0 \\ \lambda_{m,1}^* & \lambda_{m,2}^* & \dots & \lambda_{m,m-1}^* & 0 \end{bmatrix} \tag{4.69}$$

Replacing L^{-1} by Λ^* yields

$$\xi_m(s)[e](t) + \Lambda^*\xi_m(s)[e](t) = DS\tilde{\Theta}^T\omega \tag{4.70}$$

Parameterizing Λ^* with $m-1$ column vectors

$$\begin{aligned}
\lambda_2^* &= \lambda_{2,1}^* \in \mathbb{R} \\
\lambda_3^* &= [\lambda_{3,1}^*, \lambda_{3,2}^*]^T \in \mathbb{R}^2 \\
\vdots &= \vdots \\
\lambda_{m-1}^* &= [\lambda_{m-1,1}, \lambda_{m-1,2}, ..., \lambda_{m-1,m-2}] \in \mathbb{R}^{m-2} \\
\lambda_m^* &= [\lambda_{m,1}, \lambda_{m,2}, ..., \lambda_{m,m-1}] \in \mathbb{R}^{m-1}
\end{aligned} \tag{4.71}$$

where $\lambda_{i,j}$ represents the estimate of the Λ^* elements, while λ_i^{*T} denotes the estimate of the row vectors of Λ^*.

We then define a monic Hurwitz polynomial $f(s)$, with its degree equal to the maximum degree of $\xi_m(s)$, and design a stable filter with $h(s) = \frac{1}{f(s)}$ and impose $h(s)$ on the equation (4.70), we obtain

$$\xi_m(s)h(s)[e](t) + \Lambda^*\xi_m(s)h(s)[e](t) = DSh(s)\tilde{\Theta}^T\omega \tag{4.72}$$

Defining the first term on the left side of equation (4.72) as

$$\underline{e} = \xi_m(s)h(s)[e](t) \tag{4.73}$$

where $\underline{e} = [\underline{e}_1, \underline{e}_2, ..., \underline{e}_m]^T$ and $\underline{e}_i \in \mathbb{R}, i = 1, 2, ..., m$. Then we create the regressors $\eta_i, i = 2, ..., m$, which are given by $\eta_i(t) = [\underline{e}_1, \underline{e}_2, ..., \underline{e}_{i-1}]^T \in \mathbb{R}^{i-1}$. Then the second term on the left side of equation (4.72) is expressed as

$$e_L^* = \Lambda^*\xi_m(s)h(s)[e](t) = [0, \lambda_2^{*T}\eta_2, ..., \lambda_m^{*\,T}\eta_m] \tag{4.74}$$

Denoting $\Upsilon(t)$ as the estimate of $\Upsilon^* = DS$, $\zeta(t) = h(s)[\omega](t)$ and $\xi(t) = \Theta^T(t)\zeta(t) - h(s)[\Theta^T\omega](t)$, and defining the estimate of e_L^* as $e_L(t) = [0, \lambda_2^T\eta_2, ..., \lambda_m^T\eta_m]$, we then relate the estimation error to the parameteric error

$$\epsilon(t) = \underline{e}(t) + e_L(t) + \Upsilon(t)\xi(t) \tag{4.75}$$

Combining equations (4.72)-(4.75), the estimate error equation is given by

$$\epsilon(t) = \tilde{e}_L(t) + \tilde{\Upsilon}\xi(t) + DS\tilde{\Theta}^T\zeta(t) \tag{4.76}$$

where $\tilde{e}_L(t) = [0, \tilde{\lambda}_2^T\eta_2, ..., \tilde{\lambda}_m^T\eta_m]^T$, and $\tilde{\Upsilon} = \Upsilon(t) - \Upsilon^*$. Equation (4.76) thus completes associating the tracking error $\epsilon(t)$ with the parameter errors. Next, we start developing adaptive laws to estimate the unknown parameters online.

Adaptive parameter estimation We define the parameter errors as

$$\tilde{\Theta} = \Theta(t) - \Theta^*, \tilde{\Upsilon} = \Upsilon(t) - \Upsilon^*, \tilde{\lambda}_i = \lambda_i(t) - \lambda_i^*, i = 2, 3, ..., m \tag{4.77}$$

Since we assume that the unknown parameters are constant, the derivatives of the unknown parameters are given by

$$\dot{\hat{\Theta}}(t) = \dot{\Theta}, \dot{\hat{\Upsilon}}(t) = \dot{\Upsilon}, \dot{\hat{\lambda}}_i(t) = \dot{\lambda}_i, i = 2, 3, ..., m \tag{4.78}$$

By using the gradient estimate technique, the adaptive laws are expressed as

$$\dot{\Theta} = -\frac{D\epsilon\zeta}{s^2}, \dot{\Upsilon} = -\frac{\Gamma_\Upsilon \epsilon \xi^T}{s^2}, \dot{\lambda}_i = -\frac{\Gamma_{\lambda,i}\epsilon_i\eta_i}{s^2} \tag{4.79}$$

where s is a normalized value, $s^2 = 1+\zeta^T(t)\zeta(t)+\xi^T(t)\xi(t)+\sum_{i=2}^{m}\eta_i(t)^T\eta_i(t)$ and $\Gamma_\Upsilon \in \mathbb{R}^{m\times m}$ and $\Gamma_{\lambda,i} \in R^{(i-1)\times(i-1)}$ are both the adaptive gain matrices, which satisfy $\Gamma_\Upsilon = \Gamma_\Upsilon^T > 0, \Gamma_{\lambda,i}^T = \Gamma_{\lambda,i} > 0, i = 2, 3, ..., m$.

4.3.2 Simulation results

The MIMO dMRAC scheme described in Section 4.3.1 was first implemented into the MATLAB/Simulink framework, which was then coupled with METIS for closed-loop control evaluation. The METIS simulations are based on the same reference scenario used in Section 4.2.4. The objective is to track β_p and ι_0 simultaneously by actuating P_{ICRH} and P_{LHCD} on EAST using the MIMO dMRAC scheme. To do so, we first make a number of assumptions: all the zeros of the transfer matrix $G(s)$ mapping β_p and ι_0 from the ICRH and LHCD powers are stable, the upper bound of the observability index is 2, and $G(s)$ is proper and nonsingular. After some trial and error, the LMI matrix ξ_m is defined as $\begin{bmatrix} 0.05s+1 & 0 \\ 0 & (0.05s+1)^2 \end{bmatrix}$. In addition, we assume that all the leading principle minors of the HFGM K_p are not zero. Based on the physical intuition, it is found that increasing the ICRH power leads to the growth of β_p and rising the LHCD power results in the drop of ι_0. Hence, we have $\text{sign}(\Delta_1) = 1$ and $\text{sign}\left(\frac{\Delta_2}{\Delta_1}\right) = -1$. The adaptive gains for Θ, Υ and λ_i are prescribed by trial and error. In this case, we find that $\text{DD} = \begin{bmatrix} 8\times10^4 & 0 \\ 0 & -4\times10^3 \end{bmatrix}$, $\Gamma_\Upsilon = \begin{bmatrix} 10^6 & 0 \\ 0 & 10^6 \end{bmatrix}$ and $\lambda_i = 10^6$ yields good tracking performance. The controller parameters are initialized as

$$\Theta|_{t=t_0} = \begin{bmatrix} -0.0873 & -0.0152 & 0.0549 & 0.0283 & -1.1420 & 0.3359 & 0.8505 & 0.3518 \\ 0.0018 & -0.0043 & -0.0018 & 0.0045 & -0.0247 & 0.0408 & -0.0257 & -0.0274 \end{bmatrix}^T$$

$\Upsilon|_{t=t_0} = \begin{bmatrix} 0.1909 & 0.0002 \\ -0.0046 & -0.0263 \end{bmatrix}$ and $\lambda|_{t=t_0} = \begin{bmatrix} 0 & 0.0024 \\ 0 & 0 \end{bmatrix}$,where t_0 is the initial time when the controller is switched on. The filter $h(s)$ is $\frac{1}{(s+10)^2}$ and the lowpass filter for the observed input and output are $\frac{1}{(s+1)}$.

With this configuration, the MIMO dMRAC scheme has been tested through the closed-loop METIS simulations. The simultaneous tracking results are shown in Fig. 4.16. In order to test the controller with a time-varying reference input, a harmonic reference with the frequency at 1 Hz is prescribed for β_p, while another slower harmonic reference with the frequency at

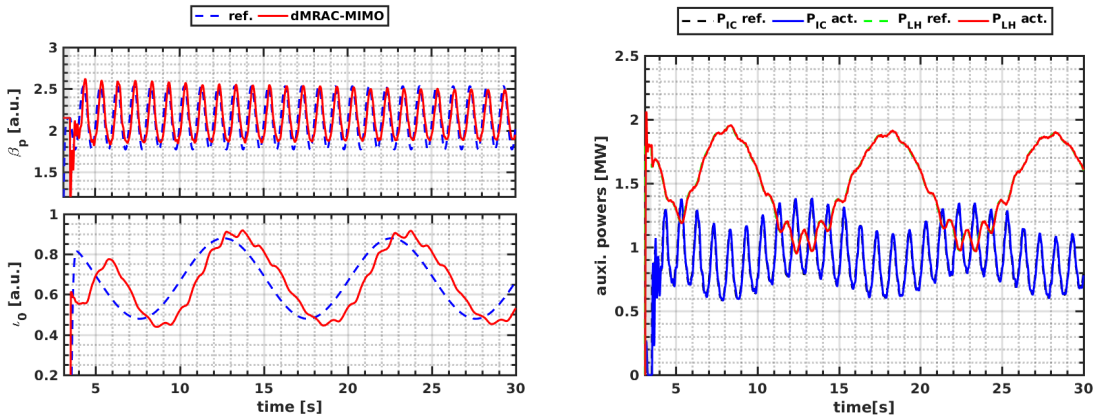

(a) (b)

Figure 4.16: Simultaneous tracking of β_p and ι_0 using the ICRH and LHCD powers. (a) Time traces of the reference trajectories and the achieved values of β_p (top) and ι_0 (bottom). (b) Time traces of the requested and achieved auxiliary heating and current drive powers.

0.1 Hz is prescribed for ι_0. The references for β_p and ι_0 are tracked with the ICRH and LHCD powers fairly well. In particular, the MIMO dMRAC controller automatically favors the LHCD power to track ι_0 and the ICRH power to track β_p according to the adaptive laws driven by the observed input-output data. Fig. 4.17-4.18 shows the evolution of the estimated elements of λ and Υ, respectively, while Fig. 4.19-4.21 illustrates the evolution of the estimated elements of Θ. These results demonstrate the adaptivity of the MIMO dMRAC scheme in the simultaneous tracking of β_p and ι_0.

4.3.3 Conclusion of Section 4.3

In this section, a MIMO dMRAC control scheme is proposed for the simultaneous control of β_p and ι_0 in advanced tokamak scenarios on EAST. This control approach manifests itself as a MIMO extension of the dMRAC scheme described in Section 4.2. Similar to the idea of the SISO dMRAC scheme, the MIMO dMRAC scheme assumes a stationary multivariable controller structure and updates the controller parameters adaptively, driven by the normalized estimation errors. The LDS decomposition of the HFGM allows for the available information about the plasma dynamics to be minimum, enabling the system stability and the asymptotic output tracking, despite the occurrence of system parameter uncertainties. Dedicated METIS simulations on EAST have numerically demonstrated the validity of the proposed MIMO dMRAC scheme. Future efforts entails the implementation of this control algorithm into the EAST PCS for experimental validation. It is also interesting to explore the impact of the tuning parameters on the control performance and to seek a systematic tuning procedure for this scheme.

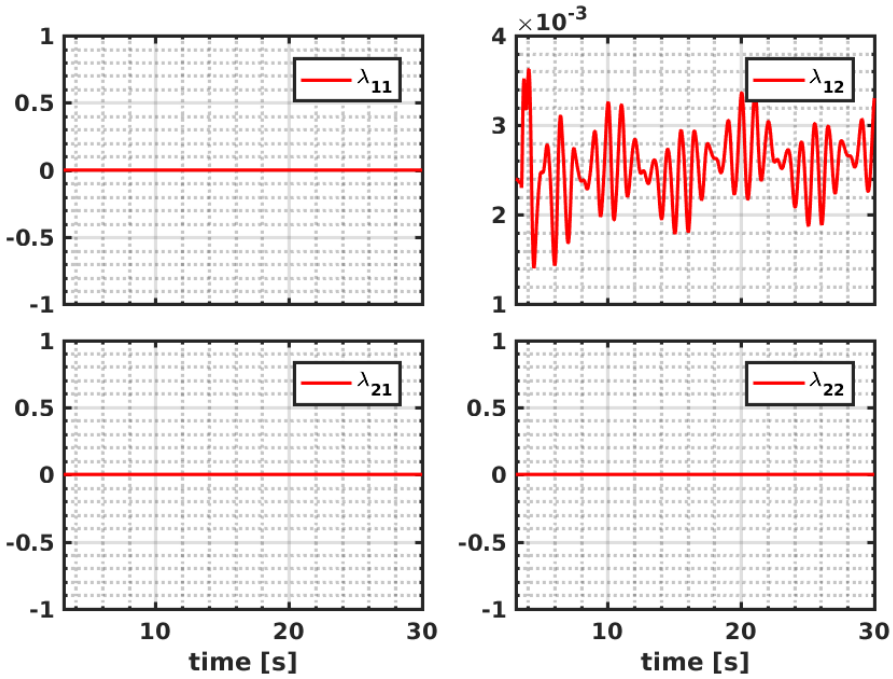

Figure 4.17: Time evolution of the estimated elements of λ.

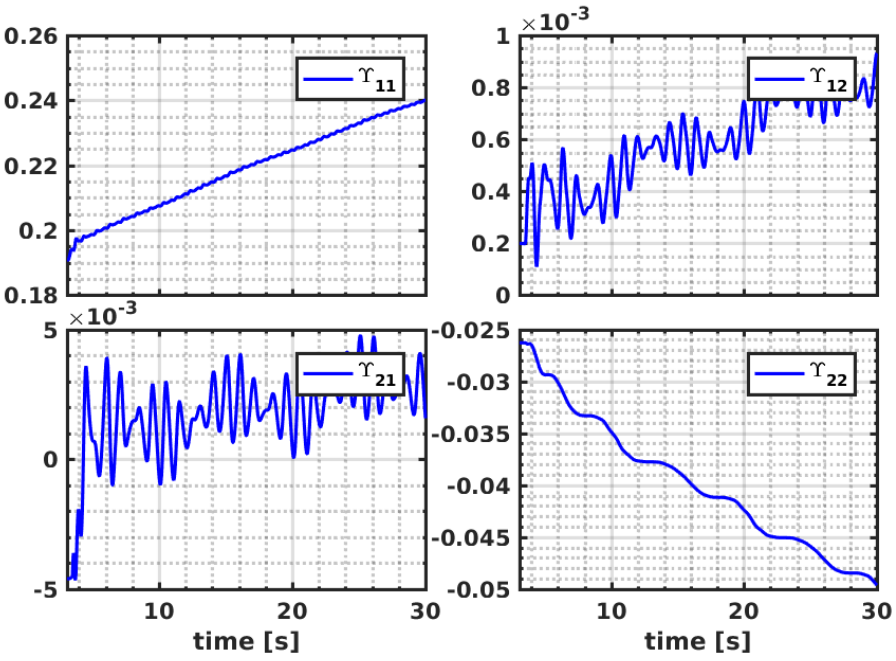

Figure 4.18: Time evolution of the estimated elements of Υ.

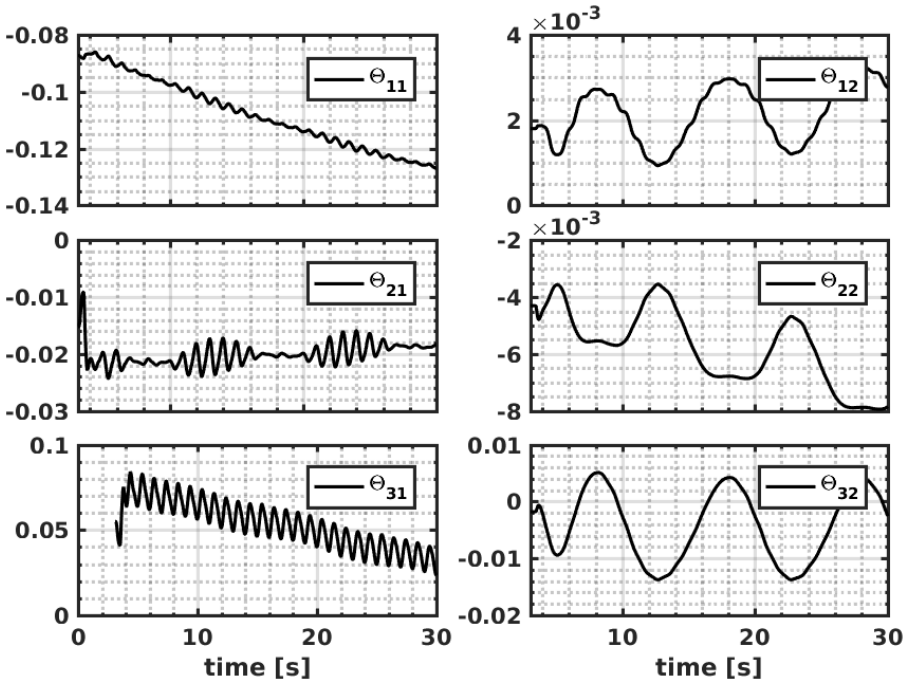

Figure 4.19: Time evolution of the estimated elements of Θ from Θ_{11} to Θ_{32}.

4.4 Summary of Chapter 4

In this chapter, adaptive control of essential plasma kinetic parameters in advanced tokamak scenarios has been investigated numerically, which is divided into three parts: The first part shows that the NESC scheme can be applied for the adaptive online optimization of plasma kinetic parameters in advanced tokamak scenarios. The benefit of NESC is that in addition to the gradient estimate, the Hessian and Hessian inverse can be estimated as well, making the closed-loop convergence rate artificially-assignable. Nonlinear METIS simulations performed on EAST and ITER indicate that comparable optimization performance can be obtained with the NESC and standard ESC schemes. Compared with other controller schemes, for instance, LQI and $\mathcal{H}_\infty$ controllers, the apparent drawback of ESC lies in its long response time. Nonetheless, the ESC optimization results can be used as the feedforward baseline trajectories. Furthermore, ESC may prove to be more effective than other linear feedback controllers for the real-time optimization of strong nonlinear dynamics, for instance, the ELM suppression with the resonant magnetic perturbations (RMP). The second and third parts deal with the application of the MRAC algorithms for plasma magnetic kinetic control in advanced tokamak scenarios. For the SISO case, two different MRAC schemes (dMRAC and iMRAC) are proposed and tested with nonlinear METIS simulations. Results indicate that both dMRAC and iMRAC schemes can successfully be applied for the adaptive tracking of kinetic parameters by actuating the ICRH power, which may broaden the attractive control region of linear controllers proposed in Chapter 3. For the MIMO case, a dMRAC scheme has been considered and tested with nonlinear METIS simulations. We can infer, from our simulations, that the MIMO dMRAC scheme is capable of tracking plasma magnetic and

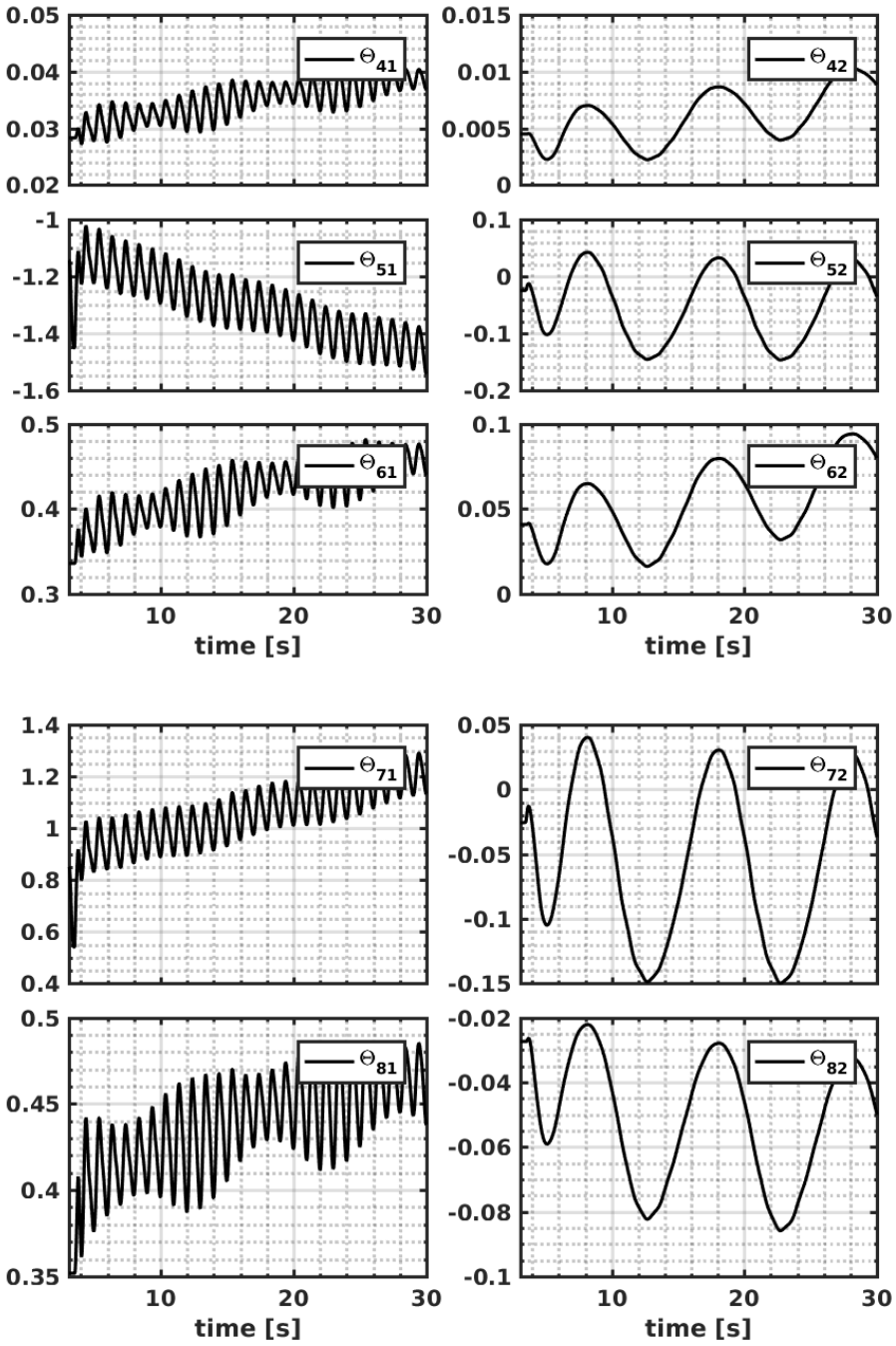

Figure 4.20: Time evolution of the estimated elements of Θ from Θ_{41} to Θ_{62}.

kinetic parameters simultaneously with multiple control actuators. In the future, the proposed adaptive control algorithms should be implemented into a PCS for experimental evaluations. Meanwhile, possible improvements towards an optimization of the MIMO MRAC scheme can be made. In the next chapter, another powerful control technique will be introduced and evaluated for the simulatenous control of q-profile and β_p in H-mode plasmas on EAST, the

offset-free MPC scheme.

Chapter 5

Model Predictive Control

Contents

Simultaneous magnetic and kinetic plasma control based on extremely simple LSS models identified using a two-time-scale approximation has been developed in recent years and the models used in Chapter 3 were based on this approximation [Moreau et al., 2011]. Ideally, first-principles plasma transport models could be preferred as they should have a universal domain of validity, but despite their increasing complexity, they still depend on many uncertain parameters and their accuracy cannot be widely assessed, even in their linearized version for real-time control applications. So the idea here is to free oneself from the complexity of such models and to reduce the control computational cost, at the expense of a more restricted applicability (e.g. to a given device, actuator set and operation scenario). In the so-called ARTAEMIS two-time-scale models [Moreau et al., 2011] and in the associated control algorithms, the fast component of the kinetic plasma dynamics, including in particular momentum and thermal diffusion, is considered as a singular perturbation of a quasi-static equilibrium, which itself is governed on the resistive timescale by the flux diffusion equation. The system identification problem is thus made tractable by the partial decoupling of the slow and fast dynamics. Combined with linear-quadratic optimal control theory, the effectiveness of this approach to simultaneously control the plasma poloidal flux profile and the normalized pressure parameter, in non-inductive, high-β_N discharges was demonstrated experimentally on

the DIII-D tokamak [Moreau et al., 2013]. Using the same approach, simultaneous control of the safety factor profile, $q(x)$, and plasma pressure was also achieved in closed-loop nonlinear plasma transport simulations [Moreau et al., 2015]. However, in such simulations the desired steady-state q-profiles were obtained either much too slowly, or after a large undershoot of the safety factor in the plasma core with respect to its target value and a damped oscillation. A non-monotonic approach of the q-profile to its target profile is not desirable, as it may lead to MHD instabilities during the build up of the plasma equilibrium. In this regard, the model predictive control (MPC) [Maciejowski, 2002], an alternate control approach combined with the ARTAEMIS plasma dynamic model, is expected to achieve enhanced control performance for the tracking of plasma magnetic and kinetic parameters/profiles in tokamaks.

The control of plasma magnetic and kinetic parameters in tokamaks using MPC has already been investigated [Ouarit et al., 2011,Maljaars et al., 2015,Maljaars et al., 2017,Wehner et al., 2016]. MPC control solves a receding-horizon optimization problem where an unconstrained/constrained cost function that penalizes both predictive errors and control efforts in a prescribed time horizon is minimized online to find an optimal control actuation [Garcia et al., 1989]. In [Ouarit et al., 2011], control of q-profile via MPC was initiated and its effectiveness was verified in Tore Supra plasma simulations. In [Maljaars et al., 2015], first-principle-driven (FPD) models linearized around a set of operating points are treated as predictive models and nonlinear RAPTOR simulations [Felici et al., 2011] have demonstrated the validity of MPC in q-profile tracking on ITER. The similar technique was then extended to track q-profile and plasma β simultaneously in L-mode plasmas, whose effectiveness has been validated experimentally on the TCV tokamak [Maljaars et al., 2017]. In [Wehner et al., 2016], the FPD-MPC control of q-profile and the stored energy for high performance steady-state operation has been pursued on DIII-D experimentally. In [Moreau et al., 2018], using a two-time-scale data-driven model, the offset-free MPC [Borrelli and Morari, 2007,Maeder et al., 2009,Maeder and Morari, 2010] for the q-profile and β_p tracking was first demonstrated in an H-mode steady-state scenario on EAST via nonlinear closed-loop METIS simulations. The validity of this approach has recently been confirmed through dedicated plasma experiments on the EAST tokamak [Moreau et al., 2021]. This chapter presents the METIS simulation and experimental results reported in [Moreau et al., 2018,Moreau et al., 2021].

MPC is a form of control in which the current actuation is obtained by solving a finite-horizon optimal control problem at each sampling instant with the current plant state as the initial state, which yields an optimal sequence of future actuations. The first actuator values of each sequence are applied to the plant [Mayne et al., 2000]. In the literature, the applications of MPC were initiated in the works [Cutler and Ramaker, 1980,Prett and Gillette, 1980,Rachael et al., 1978]. The state-space interpretation of MPC is first proposed in [Lee et al., 1994], and the stability of constrained MPC is proved in [Rawlings and Muske, 1993]. Interested readers are referred to [Mayne et al., 2000] for a complete survey of MPC control and to [Maciejowski, 2002,Alamir, 2013] for tutorials. In order to deal with system disturbances, an offset-free MPC technique was proposed and proved to be effective [Borrelli and Morari, 2007,Maeder et al., 2009,Maeder and Morari, 2010,Morari and Maeder, 2012]. The benefits of MPC are that it can easily handle multivariable cases, system constraints, model uncertainties as well as nonlinearities in an intuitive way. On the other hand, its high computational burden

is considered as an apparent disadvantage over other control strategies such as LQI control and $\mathcal{H}_\infty$ robust control. This chapter is dedicated to developing an offset-free MPC by using a data-driven two-time-scale plasma response model for the tracking of q-profile and β_p in H-mode scenarios on the EAST tokamak. Both numerical simulations and experiments are investigated.

The *main achievements* of the chapter are summarised as follows:

- Developing an offset-free MPC control scheme, based on a two-time-scale plasma response model [Moreau et al., 2011, Moreau et al., 2013, Moreau et al., 2015] for tracking of q-profile and β_p in H-mode scenarios on EAST.
- Coupling the offset-free MPC controller with the plasma simulator METIS [Artaud et al., 2018], and numerically evaluating the control performance on EAST.
- Implementing the offset-free MPC controller into the EAST PCS and experimentally demonstrating its effectiveness by tracking β_p and q_0 in H-mode scenarios on EAST.

The rest of the chapter is organized as follows: In Section 1, we review the two-time-scale model structure and formulate the offset-free MPC control problem. The PI Luenberger observer for states and disturbances estimation using the linear two-time-scale model is elaborated. Closed-loop METIS simulation results are shown to confirm the effectiveness of the control algorithm in Section 2. The first, proof-of-principle model predictive kinetic control experiments performed on EAST are reported in Section 3. Finally, we draw conclusions and outline the future plans.

5.1 Offset-free MPC approach

In this section, the predictive model used in MPC for q-profile and β_p control is first revisited, based on which a PI Luenberger observer is designed to estimate plasma states and modelling errors online. Afterwards, the offset-free MPC control problem is formulated using the predictive model, state and disturbance estimates, prescribed references and actuation constraints. The controller output requests are solved by a quadratic programming optimizer.

5.1.1 Predictive model

The ARTAEMIS model [Moreau et al., 2011] used in the present work describes the coupled time evolution of $\psi(x,t) = \psi(x,t) - \psi_b(t)$ where x is a normalized radial coordinate defined below, $\psi(x,t)$ is the poloidal magnetic flux profile in Weber and $\psi_b(t)$ its value at the plasma boundary, of $\iota(x,t) = \frac{1}{q(x,t)}$, and of the slow (quasi-static) and fast components of $\beta_p(t)$ ($\beta_{p,S}$ and $\beta_{p,F}$, respectively), with $\beta_p(t) = \beta_{p,S}(t) + \beta_{p,F}(t)$. Details concerning this approximation and the identification of a two-time-scale plasma dynamic model from sampled experimental

or simulated data are given in references [Moreau et al., 2011, Moreau et al., 2013, Moreau et al., 2015] and in the previous chapters. The general structure of the model is postulated from the projection onto radial basis functions (cubic splines) of a set of coupled plasma response equations that only depend on x and t, and which stem from the linearized flux-averaged plasma transport equations. A lumped-parameter LTI control-oriented model is thus obtained, in which all distributed variables and unknown operators reduce to finite dimension vectors and matrices. It combines a slow dynamic model, which couples ψ and β_p as:

$$\begin{aligned} \dot{X}_S(t) &= A_S X_S(t) + B_S U_S(t) \\ \psi(t) &= C_\psi X_S(t) \\ \beta_{p,S} &= C_S X_S(t) + D_S U_S(t) \end{aligned} \tag{5.1}$$

and a fast dynamic model,

$$\begin{aligned} \dot{X}_F(t) &= A_F X_F(t) + B_F U_F(t) \\ \beta_{p,F}(t) &= C_\beta X_F(t) \end{aligned} \tag{5.2}$$

where A_S and A_F are regular matrices with negative eigenvalues. The vector U, containing the actuator inputs, is also splitted into a slow and a fast component ($U = U_S + U_F$). The q-profile is controlled through its inverse as:

$$\iota(x,t) = \frac{1}{q(x,t)} = -\frac{\partial \psi(x,t)}{\partial x} \left(\frac{\partial \Phi(x,t)}{\partial x} \right)^{-1} \tag{5.3}$$

where $\Phi(x,t)$ is the toroidal magnetic flux in Weber, $\Phi_{max} = \Phi(x=1)$ is its value at the plasma boundary, which is assumed constant, and $x = \left(\frac{\Phi}{\Phi_{max}} \right)^{\frac{1}{2}}$. After linearization around the reference plasma equilibrium and projection of $\psi(x,t)$ and of $\iota(x,t)$ on the radial basis functions, the vector $\iota(t)$ can therefore be related to the vector $\psi(t)$ through a linear output equation as:

$$\iota(t) = \Gamma_\iota \psi(t) = C_\iota X_S(t) \tag{5.4}$$

In order to identify the various matrices in the ARTAEMIS model corresponding to the selected operation scenario on EAST, a large number of nonlinear simulations were performed using the METIS plasma simulator tuned for the reference discharge #62946, until a fair agreement with experimental data and interpretative TRANSP simulation results was obtained. This procedure was previously used for DIII-D and is described in [Moreau et al., 2011]. The resulting datasets were then used in the ARTAEMIS prediction-error system identification algorithm. The reference scenario around which the linear response model was identified was a steady state, fully non-inductive single-null H-mode discharge, at a toroidal magnetic field, $B_T = 2.5$ T, central electron density, $n_{e0} \approx 3.5 \times 10^{19}$ m^{-3}, and plasma current, $I_p = 0.42$ MA. The discharge had been obtained using LHCD (0.6 MW at 2.45 GHz and 2 MW at 4.6 GHz), 0.32 MW of ICRH at 33 MHz and 0.3 MW of ECRH at 140 GHz. The transition to H-mode occurred at 3.1 s with an H-factor, $H_{98(y,2)} \sim 1.1$. The steady state poloidal β and internal inductance parameters were $\beta_p = 1.3$ and $l_i = 1.2$, respectively, and the q-profile exhibited a small negative shear in the plasma core, with a minimum q around

1.5 and $q_0 \sim 2$ on axis. The plasma parameter profiles are obtained from EFIT magnetic equilibrium reconstructions, which are available in real-time using magnetic and kinetic measurements, including interfero-polarimetry data from the POINT diagnostic [Huang et al., 2017, Liu et al., 2016b]. Two important parameters characterizing the identified models are the largest (negative) eigenvalues of A_S and A_F, found as -1.19 and -24.8 s^{-1}, which correspond to time constants $\tau_S = 0.840$ s and $\tau_F = 0.040$ s for the resistive (slow model) and thermal (fast model) diffusion timescales, respectively.

5.1.2 State and disturbance estimation

In order to make the controller robust against uncertainties, the identified model is augmented with an output disturbance model to estimate the mismatch between measured and predicted outputs [Borrelli and Morari, 2007]. Hence, at each time step, an observer provides an estimate of the system states and output disturbances, and the controller uses the augmented model to predict the behavior of the system over a future prediction horizon, assuming the mismatch is constant. In its continuous time version, the augmented model reads:

$$\begin{cases} \dot{X}_S &= A_S X_S(t) + B_S U_S(t) \\ \dot{X}_F &= A_F X_F(t) + B_F U_F(t) \\ \dot{d}_\iota &= 0 \\ \dot{d}_\beta &= 0 \\ \iota &= C_\iota X_S(t) + d_\iota(t) \\ \beta_p &= C_S X_S(t) + D_S U_S(t) + C_\beta X_F(t) + d_\beta(t) \end{cases} \tag{5.5}$$

where $d_\iota(t)$ and $d_\beta(t)$ are disturbance vectors representing the errors on $\iota(t)$ and $\beta_p(t)$, respectively. $U_S(t)$ is obtained through a simple lowpass filter and $U_F(t) = U(t) - U_S(t)$. The filter cutoff frequency, $f_{filt} = \frac{1}{\tau_{filt}}$, is chosen during the model identification and is such that $\tau_F \ll \tau_{filt} \ll \tau_S$. The filter states that allow $U_S(t)$ and $U_F(t)$ to be computed in the observer at time t, are transmitted to the controller with the estimated system states and disturbances and with the real-time measurements of the controlled variables, $\iota_m(t)$ and $\beta_{p,m}(t)$.

The state and disturbance estimator is a PI observer based on the augmented system above, and is designed as follows:

$$\begin{cases} \dot{\hat{X}}_S(t) = & A_S \hat{X}_S(t) + B_S U_S(t) + K_{11}\left(-\iota_m(t) + C_\iota \hat{X}_S + \hat{d}_\iota(t)\right) + \\ & K_{12}\left(-\beta_{p,m}(t) + C_S \hat{X}_S(t) + D_S U_S(t) + C_\beta \hat{X}_F(t) + \hat{d}_\beta(t)\right) \\ \dot{\hat{X}}_F(t) = & A_F \hat{X}_F(t) + B_F U_F(t) + K_{21}(-\iota_m(t) + C_\iota \hat{X}_S(t) + \hat{d}_\iota(t)) + \\ & K_{22}\left(-\beta_{p,m}(t) + C_S \hat{X}_S(t) + D_S U_S(t) + C_\beta \hat{X}_F(t) + \hat{d}_\beta(t)\right) \\ \begin{bmatrix} \dot{\hat{d}}_\iota(t) \\ \dot{\hat{d}}_\beta(t) \end{bmatrix} = & K_{31}\left(-\iota_m(t) + C_\iota \hat{X}_S(t) + \hat{d}_\iota(t)\right) + K_{32}\left(-\beta_{p,m}(t) + C_S \hat{X}_S(t) + \right. \\ & \left. D_S U_S(t) + C_\beta \hat{X}_F(t) + \hat{d}_\beta(t)\right) \end{cases} \tag{5.6}$$

where symbols with a hat represent the estimates of the system states and disturbances, and the $K_{i,j}$ matrices are chosen so that $[K_{31}, K_{32}]$ is non-singular, and the estimator is stable

and converges rapidly. The observer then tracks the measurements without steady-state error ($\dot{\hat{d}}_\iota = 0, \dot{\hat{d}}_\beta = 0$). In addition, by definition, the fast variables U_F, X_F and $\beta_{p,F}$ vanish in steady-state, and the observer therefore satisfies (the ∞ symbol indicates steady-state):

$$\hat{X}_{S,\infty} = -A_S^{-1} B_S U_\infty \tag{5.7}$$

and

$$K_S U_\infty = \begin{bmatrix} \iota_{m,\infty} - \hat{d}_{\iota,\infty} \\ \beta_{p,m,\infty} - \hat{d}_{\beta,\infty} \end{bmatrix} \tag{5.8}$$

with

$$K_S = \begin{bmatrix} -C_\iota A_S^{-1} B_S \\ -C_S A_S^{-1} B_S + D_S \end{bmatrix} \tag{5.9}$$

The controller objective is to make $\iota_{m,\infty}$ and $\beta_{p,m,\infty}$ equal to ι_{target} and $\beta_{p,target}$, respectively (offset-free control), or as close as possible if the dimension of the image space of K_S, spun by the actuators is smaller than the number of controlled variables. In order to avoid combinations of actuators which would lead to unnecessary actuation cost, an SVD of K_S is used and the allowed actuator space will be limited to the first n_{svd} singular vectors of K_S, i.e. $U = T_{svd} V$, where n_{svd} (the dimension of V) is a free parameter. At each time step, the MPC algorithm then solves a quadratic programming (QP) problem using the predicted evolution of the augmented system over a time horizon τ_H, which is chosen of the order of τ_S, or smaller. A long time horizon may not be meaningful because the prediction is made with the assumption that the estimated error at time t will be constant between t and $t + \tau_H$. The QP problem to be solved at time t reads as follows:

For $t \leq t' \leq t + \tau_H$, find $V(t')$ that minimizes:

$$\begin{aligned} I_H(t) = &\int_t^{t+\tau_H} \left\{ \int_0^1 dx \mu(x)^2 \left[\iota(x,t') - \iota_{target}(x) \right]^2 \right\} dt' + \int_t^{t+\tau_H} \left\{ \lambda_{kin}^2 \left[\beta_p(t) - \beta_{p,target} \right]^2 \right\} dt' \\ &+ \int_t^{t+\tau_H} \left\{ \lambda_{fast}^2 X_F(t)^2 + R \left[U(t') - U_\infty \right]^2 \right\} dt' \end{aligned} \tag{5.10}$$

with $U(t') = T_{svd} V(t')$, subject to the actuator constraints, $LU(t') \leq M$, while $X_S(t')$, $X_F(t')$, $\iota_(t')$, $\beta_p(t')$, $d_\iota(t')$ and $d_\beta(t')$ evolve according to the augmented system, with the initial conditions: $X_S(t' = t) = \hat{X}_S(t)$, $X_F(t' = t) = \hat{X}_F(t)$, $d_\iota(t' = t) = \hat{d}_\iota(t)$ and $d_\beta(t' = t) = \hat{d}_\beta(t)$. In order to keep the computation time small, the elements of $V(t')$ are constrained to be a piecewise constant functions with only n_{nodes} independent unknowns equidistributed over the horizon τ_H. The free parameters $\mu(x)$ and λ_{kin} are weights given to the various variables to be controlled, λ_{fast} is a weight given to the fast model states that can moderate the kinetic control response time, and R is a positive matrix that can moderate the controller actuation effort. Once the QP problem has been solved, the first sample $U(t' = t)$ is used for the actuator commands at time t. The minimized cost function penalizes, with appropriate weights, the deviations of the predicted controlled outputs from their targets, as well as the actuator power if $R \neq 0$. Another way to moderate the actuation effort and avoid overshoots and oscillations is to reshape the targets waveforms in $I_H(t)$ so that they approach the setpoints exponentially from their current values $\iota_m(t)$ and $\beta_{p,m}(t)$, with a time constant, τ_{target}, of the order of τ_S [Maciejowski, 2002].

5.2 Simulation results

To illustrate and validate the new ARTAEMIS MPC control algorithm presented above, we shall now describe the results of nonlinear closed-loop simulations in a high-β_p non-inductive scenario on EAST. The simulations were performed by inserting the METIS code at the output of the controller in a MATLAB/Simulink model, and feeding the appropriate METIS outputs back into the controller. Many plasma parameters or profiles such as the plasma shape, B_t, n_{e0}, will be assumed independent of the actuators and were fixed external inputs to the code, together with all the chosen METIS options for modeling the various physical phenomena. The time evolution of these parameters and profiles was based on the actual experimental data from shot #62946 until $t = 3.2$ s when control was switched on. They were held constant afterwards. Also, constant feedforward LHCD at 2.45 GHz (0.6 MW) and ECRH (0.3 MW) were used in all simulations, as in the reference shot. For $t \geq 3.2$ s, at each time step (with a sampling time of 20 ms) the 4.6 GHz LHCD and 33 MHz ICRH actuator powers were prescribed by the controller and the evolution of all the plasma parameters and profiles that depend on the injected power (e.g. $I_p, V_{surf}, li, \beta_p, \Psi(x,t), q(x,t)$), temperature profiles, etc.) was simulated. The controller filter cutoff time constant and the number of nodes for the predictive horizon were chosen as $\tau_{filt} = 0.2s$ and $n_{nodes} = 2$, respectively, and have been unchanged for all the simulations presented below. The constraint matrices L and M were defined to bound the 4.6 GHz LHCD power to $0 \leq P_{LHCD} \leq 3$ MW and the ICRH power to $0 \leq P_{ICRH} \leq 1.5$ MW.

All the simulations were performed in the current control mode in which the surface loop voltage is used to track a given I_p waveform, as in the reference discharge. When the plasma state is relatively close to the required equilibrium, the controller can also be used in the voltage control mode [Moreau et al., 2013,Moreau et al., 2015] where V_{surf} can either be fixed to zero for non-inductive operation, or be used as a profile control actuator in addition to LHCD and ICRH. The plasma current is then allowed to vary within some bounds, but it is regulated through the control of the poloidal flux [Moreau et al., 2013] and of the safety factor [Moreau et al., 2015] across the entire plasma cross-section ($0 \leq x \leq 0.9$).

5.2.1 Control of q_0 with LHCD

The simplest test of the controller is to track a given target value of the safety factor at a given normalized radius, using the 4.6 GHz LHCD actuator only. In this case, offset-free MPC is possible with the controller synthesis, as proved in [Borrelli and Morari, 2007] when the number of controlled variables is equal to the number of actuators or smaller. At constant plasma current, the most sensitive area to control the $q(x)$ profile is the plasma core, and in particular the magnetic axis. An example is displayed on Fig. 5.1, where the controller was requested to track subsequently three different target values of $q_0 = q(x = 0)$, namely $q_{0,target}$ = 1.1, 3.5 and 1.7. The ICRH power was fixed (0.32 MW), and the controller parameters were chosen as $n_{svd} = 1$ (since there is only one actuator), $R = 0$, $\tau_{target} = \tau_H = \tau_S = 0.84$ s. The weight function, $\mu(x)$, was replaced by the Dirac distribution, $\delta(0) = 1$ and $\delta(x \neq 0) = 0$,

and $\lambda_{kin} = \lambda_{fast} = 0$ since there is no controlled kinetic variable. Fig. 5.1 also shows the time evolution of the minimum $q(x)$ across the plasma and of β_p. The tracking of the different q_0 targets in the time intervals 3.2 s$\leq t \leq$ 7.1 s, 7.2 s$\leq t \leq$ 13.1 s and 13.2 s$\leq t \leq$ 18 s, respectively, is performed in about 2 to 3 s, i.e. a few resistive times, and without steady-state offset. The time evolution of the minimum q-value (top frame, blue trace) indicates that the second q_0 target yields a q-profile with a strong negative shear in the plasma core (minimum value $q_{min} = 1.7$). The bottom frame shows the evolution of the 4.6 GHz LHCD power requested by the controller and of the constant feedforward ICRH, ECRH and 2.45 GHz LH powers. Distributed control of the q-profile can also be performed using piecewise linear weight

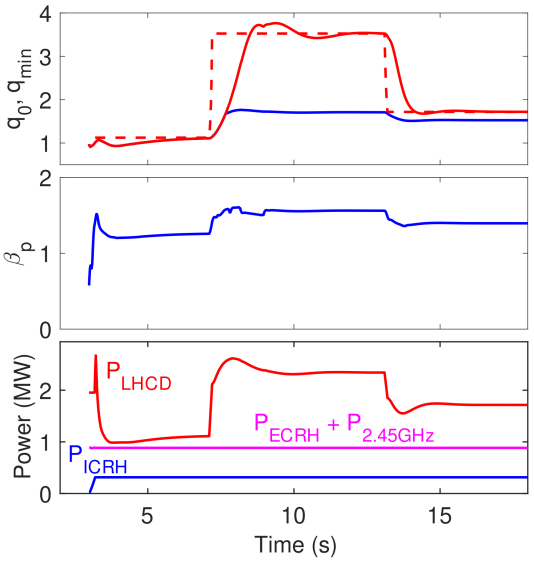

Figure 5.1: q_0 control with LHCD only. Top: $q_0(t)$ (red solid), $q_{0,target}(t)$ (red dashed) and $q_{min}(t)$ (blue) vs time. Middle: β_p vs time (not controlled). Bottom: 4.6 GHz LHCD actuator power (red) and feedforward powers: ICRH (blue) and ECRH plus 2.45 GHz LHCD (magenta).

functions, $\mu(x)$, defined and equal to 0 or 1 at the radial knots of the basis functions, $x_k = 0$, 0.1, 0.2, ..., 1. In this case, genuine offset-free control cannot be sought but the controller is designed to achieve a least-squares minimization of the radially integrated error signals, as can be seen in the definition of the cost function $I_H(t)$. When I_p is fixed, there is no need to control the safety factor in the outer edge of the plasma because it is directly related to I_p. However, it is important to select target profiles that are accessible (or nearly accessible) with the available actuators so that the least-squares approach is meaningful. In practice such profiles can be obtained offline from open loop simulations using a plasma simulator such as METIS, or using more sophisticated models. For comparison with the previous case, an example is shown in Fig. 5.2 with three different q-profile targets having the same values as in Fig. 5.1 but with $\mu(x_k) = 1$ for $0 \leq x_k \leq 0.5$. The target q-profiles were chosen from METIS simulations with powers different from the reference discharge, and are represented by diamond symbols. The other controller parameters, constraints and feedforward powers were the same as for the previous example. The q-profile at the start of control ($t = 3.2$ s) is

shown by the black curve on Fig. 5.2. The first target profile was a monotonic profile with $q_0 = q_{min} = 1.1$ (represented by magenta diamonds), and was tracked for 3.2 s$\leq t \leq$ 7.1 s. The profile represented by the magenta line is the achieved q-profile at $t = 7.1$ s, in steady state. It is achieved with no offset, showing that the chosen target is consistent with the family of plasma equilibria that can be obtained in this scenario with the available feedback and feedforward actuators. At this time, the target profile is suddenly changed into the negative shear safety factor profile with $q_0 = 3.5$ and $q_{min} = 1.7$ (red diamonds) until $t = 13.1$ s when the target profile is changed again to the weak shear profile with $q_0 = 1.7$ and $q_{min} = 1.6$ (blue diamonds). The controller behaves very similarly as in Fig. 5.1, but with a small steady state offset on axis, which is compensated by a better tracking of the target profile up to $x = 0.5$ (including the region of minimum q). The solid red and blue lines are the profiles achieved at $t = 13.1$ s and $t = 18$ s, respectively. For comparison, the dashed lines on Fig. 5.2 represent the profiles achieved in the previous case, i.e. with q_0 control only, at the same times.

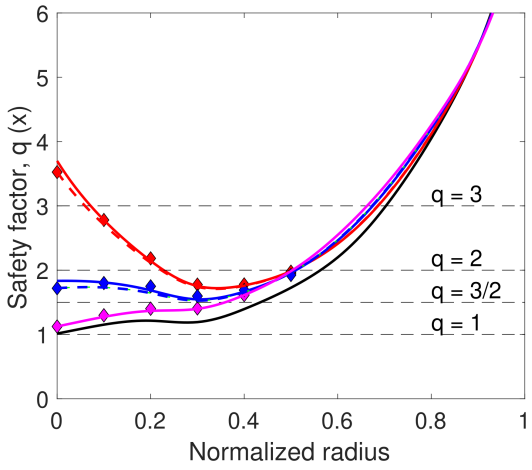

Figure 5.2: $q(x)$ control with $\mu(x) = 1$ for $0 \leq x \leq 0.5$ and with LHCD only. Achieved $q(x)$ at $t = 3.2$ s (black), 7.1 s (magenta), 13.1 s (red solid), and 18 s (blue solid). Target profiles are constant during these intervals (diamond symbols). Dashed lines are profiles achieved with q_0 control only (see Fig. 5.1).

5.2.2 Simultaneous control of $q(x)$ and β_p with LHCD and ICRH

The two-time-scale ARTAEMIS models describe the fast kinetic dynamics of the plasma as a singular perturbation of a quasi-static equilibrium, which is slowly evolving due to the coupling between the kinetic and magnetic plasma parameters. Local dependences of the plasma transport coefficients on the safety factor profile or on the magnetic shear are well-known examples of the various causes that lead to such coupled dynamics. When attempting to control simultaneously the safety factor profile and some other kinetic plasma parameters (e.g. β_p or β_N), it may be unnecessary or even sometimes undesirable to request changes of such parameters on a timescale that is too short compared to the resistive evolution of the plasma equilibrium. Restricting the model to the zero-order equations in the singular

perturbation analysis, i.e. to the slow model, will result in a slower kinetic control, but it may preserve a quasi-static equilibrium relationship between various plasma parameters during the transient evolution from an initial plasma state to the desired high performance steady state. Among other advantages, neglecting the fast model reduces the dimension of the QP problem to be solved and therefore alleviates the real-time computations at each time step. This would be mostly beneficial for the control of kinetic profiles (e.g. temperature, rotation) rather than of a scalar like β_p. An example of the simultaneous control of $q(x)$ and β_p on the

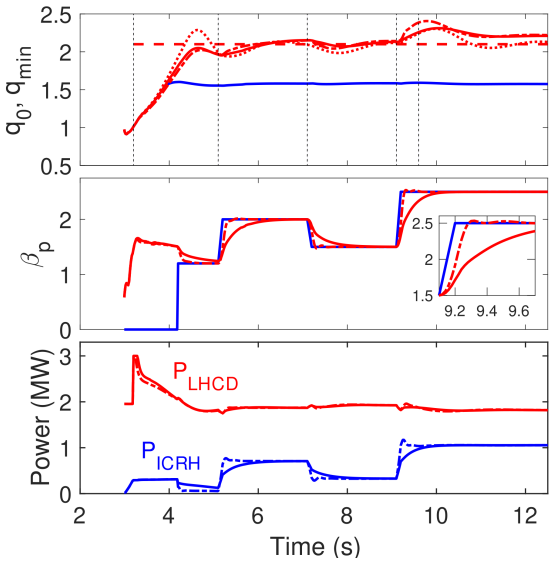

Figure 5.3: Distributed $q(x)$ control and slow β_p control with LHCD and ICRH. Top: $q_0(t)$ (red solid, the dotted red line is from discrete q_0 and β_p control for comparison), $q_{0,target}(t)$ (red dashed) and $q_{min}(t)$ (blue). Middle: $\beta_p(t)$ (red solid) and $\beta_{p,target}(t)$ (blue). Bottom: LHCD (red) and ICRH (blue) actuator powers. β_p control starts at 4.2 s while $q(x)$ control starts at 3.2 s. The dash-dot lines are from fast β_p control.

slow (resistive) timescale, with LHCD and ICRH, is depicted on Fig. 5.3 and Fig. 5.4. Four different β_p targets were tracked, $\beta_{p,target} = 1.2$ from $t = 4.2$ s to $t = 5.1$ s, and $\beta_{p,target} = 2$, 1.5 and 2.5 for 5.2 s $\leq t \leq$ 7.1 s, 7.2 s $\leq t \leq$ 9.1 s and $t \geq 9.2$ s, respectively. The q-profile is controlled from $t = 3.2$ s and between $x = 0$ and $x = 0.5$ ($\mu(x) = 1$ for $0 \leq x \leq 0.5$), and the target q-profile is constant while β_p changes. As before, $R = 0$ and $\lambda_{fast} = 0$ (no fast model), but here $\tau_{target} = \tau_H = \tau_S/2 = 0.42$ s and, for $t \geq 4.2$ s, $n_{svd} = 2$ and $\lambda_{kin} = 1$ (normalized variables are used in the controller). Fig. 5.3 shows the time evolution of q_0, q_{min}, the target and achieved β_p, and the actuator powers. Fig. 5.4 shows the achieved q-profiles at the start of the control phase and at the end of each constant $\beta_{p,target}$ phases, and the target q-profile. An additional profile is shown at $t = 9.6$ s, which corresponds to the largest transient q_0 offset during the transition to the $\beta_p = 2.5$ plasma equilibrium (Fig. 5.3). As mentioned before, the steady state offsets generally remain with distributed q-profile control due to the insufficient number of actuators. The q-profile offset is mostly apparent near the magnetic axis where the safety factor is highly sensitive to any perturbation. The steady-state q_0 offset disappears when only q_0 and β_p are controlled, as shown by the dotted red trace on Fig. 5.3 (top frame)

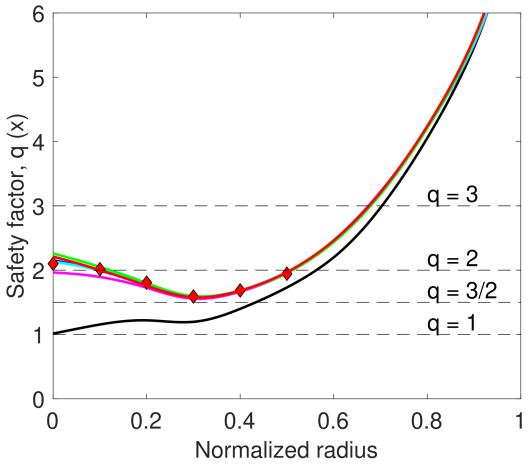

Figure 5.4: Combined distributed $q(x)$ control and slow β_p control with LHCD and ICRH. Achieved $q(x)$ at t =3.2 s (black), 5.1 s (magenta), 7.1 s (blue), 9.1 s (cyan), 9.6 s (green) and 12.5 s (red). These times are shown on Fig. 5.3 by vertical lines. The target q-profile is constant (diamond symbols) and $\mu(x) = 1$ for $0 \leq x \leq 0.5$. β_p control starts at 4.2 s while $q(x)$ control starts at 3.2 s.

at t = 7.1 s, 9.1 s and 12.5 s.

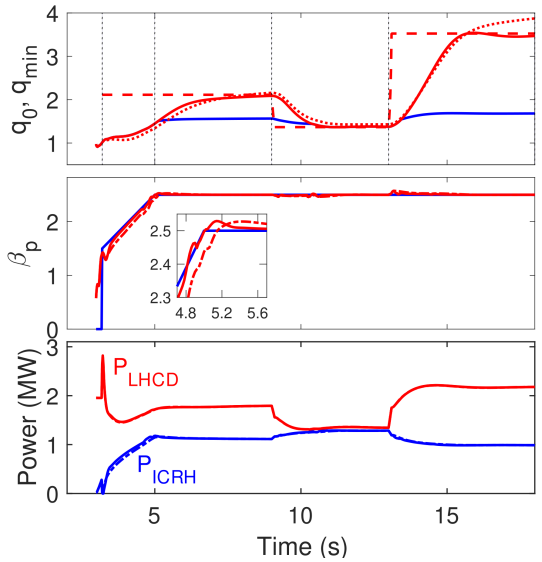

Figure 5.5: Combined q_0 and fast β_p control from t = 3.2 s with LHCD and ICRH. Top: $q_0(t)$ (red solid, the dotted red line is from distributed $q(x)$ and fast β_p control for comparison), $q_{0,target}$ (red dashed) and $q_{min}(t)$ (blue). Middle: $\beta_p(t)$ (red solid) and $\beta_{p,target}(t)$ (blue). Bottom: LHCD (red) and ICRH (blue) powers. The dash-dot lines are from slow β_p control.

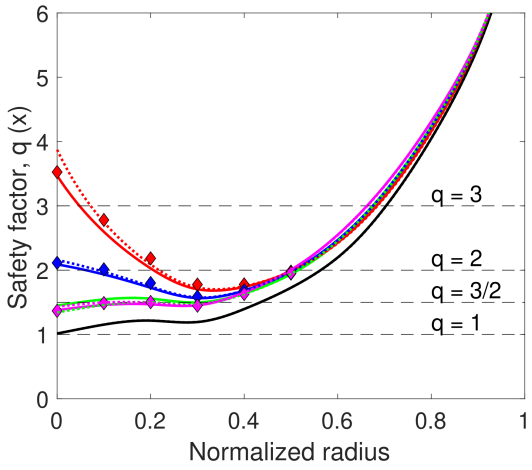

Figure 5.6: Combined q_0 and fast β_p control with LHCD and ICRH. Achieved profiles at t =3.2 s (black), 5 s (green), 9 s (blue), 13 s (magenta), and 18s (red). These times are shown on Fig. 5.5 by vertical lines. The dotted lines are from distributed $q(x)$ and fast β_p control for comparison. The $q(x)$ targets (diamond symbols) are held constant during these time intervals. β_p and $q(x)$ control starts at 3.2 s.

5.2.3 Faster control of β_p

To illustrate the combination of MPC with singularly perturbed dynamic models with two time scales, we describe now the simultaneous control of $q(x)$ and β_p including the first-order perturbation of the identified model, i.e. the fast model and states, in the control algorithm. The effect can be seen on Fig. 5.3 where we have superimposed the result of the fast βp control using $\lambda_{fast} = 1.5$ (dash-dot lines). Another example shown on Fig. 5.5 and Fig. 5.6 combines a β_p ramp request for 3.2 s $\leq t \leq$ 5 s up to $\beta_p = 2.5$, either with fast control ($\lambda_{fast} = 3$, solid lines) or without (dashed lines), followed by the tracking of three different q-profiles at constant β_p, either with distributed $q(x)$ control (dotted lines) or with discrete q_0 control (solid lines). Here $\tau_H = \tau_S = 0.84$ s, $\tau_{target} = 2\tau_S = 1.68$ s, $n_{svd} = 2$ and $\lambda_{kin} = 1$. The first q-profile target has $q_0 = 2.1$ and $q_{min} = 1.6$, the second one has $q_0 = q_{min} = 1.4$, and the last one has $q_0 = 3.5$ and $q_{min} = 1.7$ with a large negative magnetic shear over a broad region of the plasma ($x \leq 0.32$). Note that increasing τ_{target} to $2\tau_s$ results in a smooth approach to the various q_0 targets (Fig. 5.5).

Finally, in Fig. 5.7 and Fig. 5.8, combinations of four different values of $\beta_{p,target}$ = 1.5, 2, 2.5 and 3, and three different q-profiles are tracked successively using the same distributed $q(x)$ control as before, with $\tau_H = \tau_S = 0.84$ s, $\tau_{target} = 2\tau_S = 1.68$ s, $n_{svd} = 2$ and $\lambda_{kin} = 1$. Again, one can compare the results with fast control ($\lambda_{fast} = 3$, solid lines) and without (dashed lines). The q-profile targets are all reached in about 2.5 s ($\approx$ 3 resistive times) and the actuators adjust to reach the various $\beta_{p,target}$ within about 0.2 s ($\approx 5\tau_F$) with fast control and 0.4-0.5 s ($\geq 10\tau_F$ or $0.5\tau_S$) with slow control, while restoring the desired q-profile shape after each large β_p perturbation.

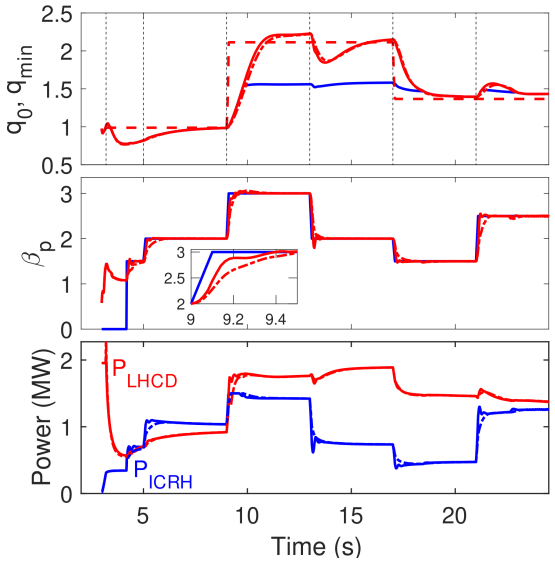

Figure 5.7: Distributed $q(x)$ and fast β_p control with LHCD and ICRH. Top: $q_0(t)$ (red solid), $q_{0,target}(t)$ (red dashed) and $q_{min}(t)$ (blue). Middle: $\beta_p(t)$ (red solid) and $\beta_{p,target}(t)$ (blue). Bottom: LHCD (red) and ICRH (blue) actuator powers. The dashed-dot lines are from slow β_p control.

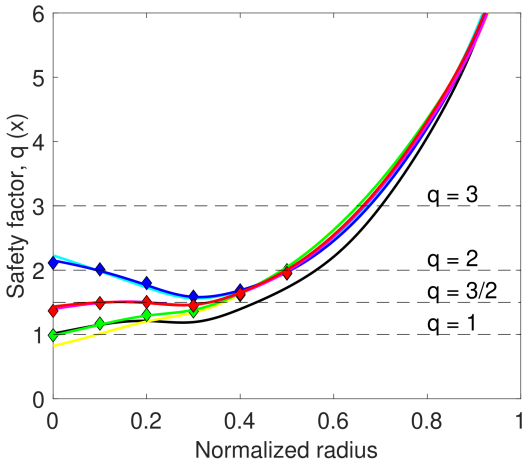

Figure 5.8: Distributed $q(x)$ and fast β_p control with LHCD and ICRH. Achieved $q(x)$ at $t = 3.2$ s (black), 5 s (yellow), 9 s (green), 13 s (cyan) and 17 s (blue), 21 s (magenta), 25 s (red). β_p and q-profile targets (diamond symbols) are held constant during these time intervals. $\mu(x) = 1$ for $0 \leq x \leq 0.5$.

5.3 EAST experiments

The effectiveness of the offset-free MPC control scheme in tracking of q-profile and β_p was demonstrated through extensive nonlinear METIS simulations in Section 2. In this section, we report on the first experiments using this new kinetic control algorithm in its simplest version

to track time-dependent targets for the central safety factor and for the poloidal pressure on the EAST tokamak. Here, the ARTAEMIS two-time-scale identification procedure was applied to EAST experimental data instead of simulated data in a typical H-mode scenario with ECRH and LHCD. When these identification experiments were performed, the only actuator available with enough real-time dynamics was the LHCD system at 4.6 GHz, with a coupled power between 1 MW and 2.5 MW. Additional LHCD power (0.5 MW) was injected at 2.45 GHz during the plasma current ramp-up, and 0.9 MW of ECRH power was injected during the 350 kA current flattop, from 2 gyrotrons at 140 GHz. The system identification data was obtained from a few discharges, with chirping frequency and PRBS modulations of the LHCD power, respectively (See Chapter 2). A linear state-space model with 9 eigenmodes was found to reproduce satisfactorily the coupled evolution of the poloidal-flux profile, $\psi(x,t)$, of the inverse of the safety factor profile, $\iota(x,t) = \frac{1}{q(x,t)}$ and of the slow and fast components ($\beta_{p,slow}$ and $\beta_{p,fast}$, respectively) of β_p, with $\beta_p(t) = \beta_{p,slow}(t) + \beta_{p,fast}(t)$.

In the first discharge, the target q_0 was set at 2.4 from $t = 2.7$ s to $t = 4.5$ s and was raised to $q_0 = 2.8$ at $t = 4.52$ s (the control cycle time was 20 ms). The evolution of q_0 and the LHCD command are shown on Fig. 5.9(a) and Fig. 5.9(b), respectively. The q_0 targets are reached in about 1 s. To cope with the nonlinear response of the LHCD actuator to the command, a PI actuator control module was added in cascade with the MPC module. The effectively coupled LHCD power is also shown on Fig. 5.9(b) (blue trace). In the second discharge, a piecewise linear β_p target waveform with $1.6 < \beta_p < 1.9$ was tracked. The evolution of β_p was perfectly under control, as shown on Fig. 10(a). The LHCD command and coupled power are shown on Fig. 5.10(b).

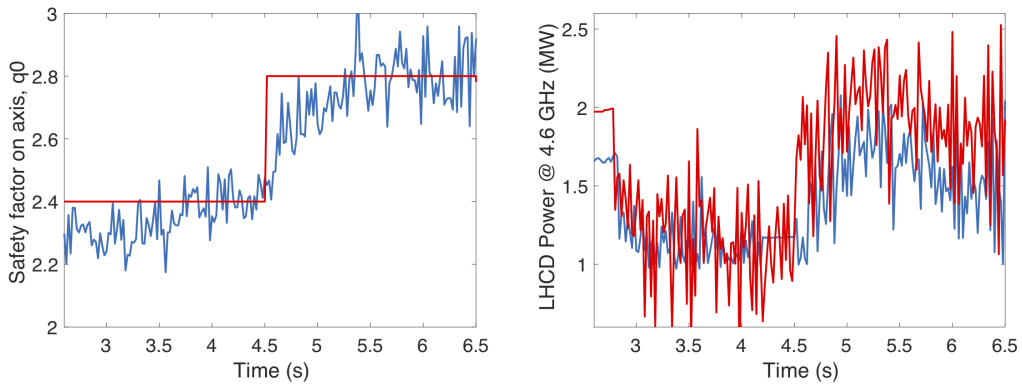

(a) (b)

Figure 5.9: (a). Safety factor on the magnetic axis from real-time EFIT equilibrium reconstruction (blue) and target waveform (red). (b). Coupled LHCD power (blue) and MPC command (red) after a PI actuator control module. Control starts at 2.7 s.

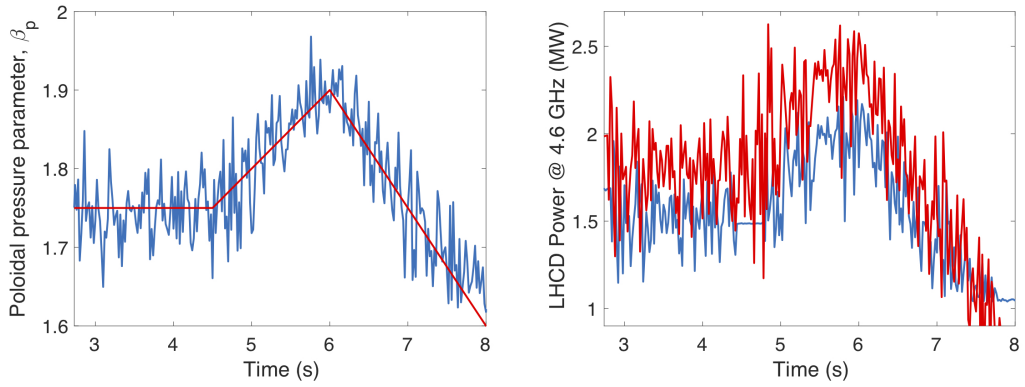

(a) (b)

Figure 5.10: (a). Poloidal pressure parameter, β_p, from real-time EFIT equilibrium reconstruction (blue) and target waveform (red). (b). Coupled LHCD power (blue) and MPC command (red) after a PI actuator control module. Control starts at t = 2.7 s.

5.4 Summary of Chapter 5

For complex systems with multiple timescales such as tokamak plasmas, MPC can be combined with singular perturbation theory to synthesize fast controllers based on extremely simple, data-driven, two-time-scale models. This has been demonstrated, for the first time, through extensive nonlinear closed-loop simulations and tokamak plasma experiments for the high β_p operation scenario in the EAST tokamak. Simultaneous control of q-profile and β_p was achieved using LHCD and ICRH actuators in closed-loop METIS simulations. The offset-free MPC algorithm used here includes a real-time estimation of the model errors and results in a much faster and robust control than was obtained previously using linear-quadratic optimal control, with similar models [Moreau et al., 2015]. In order to further evaluate the performance of this control strategy, dedicated experiments were initiated on the EAST tokamak. The first results obtained so far have shown the effectiveness in tracking q_0 and β_p using the LHCD system on EAST. In the future, the technique can be extended for the simultaneous control of the q-profile and other kinetic variables or profiles (e.g. ion or electron temperature, plasma rotation, or fusion reaction rate in burning plasmas). Furthermore, incorporating feedforward control, characterizing model uncertainties, and possibly using real-time adaptive model identification may result in further performance improvements.

Chapter 6

Conclusion and Perspectives

In the thesis, the data-driven modelling and active feedback control of q-profile and kinetic parameters in advanced tokamak scenarios are investigated. The main objectives are to approximate nonlinear plasma dynamics using a generic system identification approach, and develop robust and adaptive control schemes to enable enhanced control performance in magnetic and kinetic control. The plasma parameters used for feedback control comprise q-profile, the poloidal beta β_p, the internal inductance li, the average toroidal rotation angular speed Ω_ϕ, the electron temperature on axis $T_{\mathrm{e},0}$, the α particle power P_α, the coupled LHCD power P_{LHCD}, the coupled ICRH power P_{ICRH} and the coupled NBI power P_{NBI}. The control actuators include the ICRH system, the LHCD system and the NBI system. Two tokamak devices, namely the EAST and ITER tokamaks, have been accounted for in this thesis. Both nonlinear METIS simulations and dedicated experiments have been performed on the EAST tokamak to evaluate and compare the proposed identification and control algorithms, whilst these algorithms are numerically tested on ITER through METIS simulations.

The first part of the thesis presents the identification of a PNLSS plasma dynamic model using sampled simulation/experimental data. Two alternate linear identification methods handling data in the time- and frequency-domains are proposed. The first one uses the TD subspace and PEM identification methods to extract and refine an LSS model from data, based on which a PNLSS dynamic model is obtained via the LM optimization. The second method manipulates the observed data in the frequency-domain: first, the collected data is transformed into the frequency-domain and then an LSS model is identified using the FD subspace identification and PEM methods, and the PNLSS plasma model is subsequently derived via the LM optimization by initializing its linear coefficient matrices with the obtained LSS model. The validity and effectiveness of the nonlinear identification scheme has been confirmed, both numerically and experimentally, on the EAST and ITER tokamaks. Enhanced predictive performance regarding the PNLSS model over its LSS counterpart has been demonstrated.

The second part of the thesis concerns the robust control of q-profile and kinetic param-

eters in advanced tokamak scenarios on the EAST tokamak. First, a decentralized robust design is proposed based on a two-time-scale data-driven model, which takes full advantage of the powers of LMIs and timescale separation. The novelty of this control scheme contains the use of plasma timescale separation and a decoupling technique to acquire multi-functional capabilities, and of the internal model principle to absorb moderate time-delays and the actuation dynamics effects. Three general TD performance indexes are proposed to characterize q-profile control performance quantitatively for analysis and comparison. A procedure is given to efficiently design magnetic and kinetic references, enabling the accessibility of an H-mode steady-state scenario. Beneficial control implementation techniques are provided as well. Second, we compare three common robust control schemes, namely, $\mathcal{H}_\infty$ robust control, the LQI control and the IMC control. The performance of each control scheme is evaluated, discussed and compared both numerically and experimentally on the EAST tokamak. Extensive simulation and initial experimental results imply that, for the SISO control, it is advisable to start with the SIMC PI technique because of its simplicity, easy implementation and reasonable performance while, for the MIMO control, $\mathcal{H}_\infty$ robust control is preferred due to its simple tuning rule and robustness against model uncertainties. In addition, a cascade loop dedicated to the tracking of the requested actuations using the SIMC PI rule has been added to further enhance the kinetic control performance.

The third part of the thesis investigates the adaptive control of plasma magnetic and kinetic parameters in advanced tokamak scenarios. First, we have applied the NESC for the adaptive online optimization of plasma kinetic parameters, though this technique can generally be extended to other nonlinear plasma control problems, for example, the sawtooth period control, the NTM suppression, the error field correction. METIS simulation results on EAST and ITER indicate that comparable online optimization performance can be obtained by the standard ESC and NESC, but evidently more parameters, e.g. the Hessian and its inverse, can be estimated online by NESC. Second, we have, for the first time, introduced the MRAC algorithms for plasma kinetic control in advanced tokamak scenarios. More precisely, we first investigate a SISO case, where dMRAC and iMRAC schemes are explored in parallel. In view of dMRAC, we use a given LTF model to design an MRC controller, whose coefficients are updated online based on a set of adaptive laws driven by the NEE. The iMRAC algorithm updates the controller coefficients online by matching the model parameters, adaptively estimated using the real-time input-output measurements, with a given reference model. METIS simulation results on EAST suggest that both dMRAC and iMRAC schemes can achieve good reference tracking performance. In addition, it is found that control initialization and adaptive gains are important factors to influence the control performance in both schemes. Afterwards, we extend the dMRAC scheme to a MIMO version by adopting the LDS decomposition, whose effectiveness has been confirmed by closed-loop METIS simulations.

The fourth part of the thesis demonstrates the offset-free MPC control of q-profile and β_p in advanced tokamak scenarios on EAST. Different from the standard MPC, the offset-free MPC uses a PI Luenberger observer to estimate the states and disturbances in real-time, which are then fed to a quadratic optimizer for feedback computation. Assuming a constant output disturbance, the observer uses a linear two-time-scale model, identified from sampled simulations/experiments, to estimate model mismatches in real-time. The same model is

incorporated in the MPC optimizer, taking into account the actuation constraints. The effectiveness of this control scheme has been numerically confirmed in the simulatenous control of q-profile and β_p on EAST. Recent control experiments performed on the EAST tokamak have further demonstrated the validity of this control scheme in β_p and q_0 tracking.

Now, in the perspective of future research, there are a number of relevant topics that can be investigated:

• The proposed PNLSS identification scheme may be effective for the approximation of nonlinear plasma dynamics in the scrape-off-layer (SOL), the pedestal and plasma-wall interaction of advanced tokamak plasmas.

• Develop nonlinear optimal control algorithms based on the PNLSS model for kinetic control in tokamak plasmas to examine whether the control performance will be enhanced or not.

• Extend the LTI data-driven model to a linear-parameter-varying (LPV) version for enhanced model predictive performance.

• Extrapolate the proposed robust and adaptive control algorithms to other tokamak plasma control problems, for example, plasma position and shape control, vertical instability control, divertor detachment and heat flux control, plasma density and temperature profile control.

• The NESC algorithm may prove effective in other nonlinear plasma control problems such as sawtooth period control, NTM mitigation and suppression, error field correction.

• Experimental tests of the NESC and MRAC algorithms on the EAST tokamak are anticipated.

Bibliography

[Alamir, 2013] Alamir, M. (2013). *A pragmatic story of model predictive control: self-contained algorithms and case-studies*. CreateSpace Independent Publishing Platform.

[Albajar et al., 2001] Albajar, F., Johner, J., and Granata, G. (2001). Improved calculation of synchrotron radiation losses in realistic tokamak plasmas. *Nuclear fusion*, 41(6):665.

[Anderson and Moore, 2007] Anderson, B. D. and Moore, J. B. (2007). *Optimal control: linear quadratic methods*. Courier Corporation.

[Argomedo et al., 2013] Argomedo, F. B., Witrant, E., Prieur, C., Brémond, S., Nouailletas, R., and Artaud, J.-F. (2013). Lyapunov-based distributed control of the safety-factor profile in a tokamak plasma. *Nuclear Fusion*, 53(3):033005.

[Ariyur and Krstic, 2003] Ariyur, K. B. and Krstic, M. (2003). *Real-time optimization by extremum-seeking control*. John Wiley & Sons.

[Artaud et al., 2010] Artaud, J., Basiuk, V., Imbeaux, F., Schneider, M., Garcia, J., Giruzzi, G., Huynh, P., Aniel, T., Albajar, F., Ané, J., et al. (2010). The cronos suite of codes for integrated tokamak modelling. *Nuclear Fusion*, 50(4):043001.

[Artaud et al., 2018] Artaud, J., Imbeaux, F., Garcia, J., Giruzzi, G., Aniel, T., Basiuk, V., Bécoulet, A., Bourdelle, C., Buravand, Y., Decker, J., et al. (2018). METIS: a fast integrated tokamak modelling tool for scenario design. *Nuclear Fusion*, 58(10):105001.

[Åström et al., 2006] Åström, K. J., Hägglund, T., and Astrom, K. J. (2006). *Advanced PID control*, volume 461. ISA-The Instrumentation, Systems, and Automation Society Research Triangle ....

[Azizov, 2012] Azizov, E. A. (2012). Tokamaks: from A. D. Sakharov to the present (the 60-year history of tokamaks). *Physics-Uspekhi*, 55(2):190.

[Banaszuk et al., 2004] Banaszuk, A., Ariyur, K. B., Krstić, M., and Jacobson, C. A. (2004). An adaptive algorithm for control of combustion instability. *Automatica*, 40(11):1965–1972.

[Barton et al., 2015a] Barton, J. E., Besseghir, K., Lister, J., and Schuster, E. (2015a). Physics-based control-oriented modeling and robust feedback control of the plasma safety factor profile and stored energy dynamics in ITER. *Plasma Physics and Controlled Fusion*, 57(11):115003.

[Barton et al., 2012] Barton, J. E., Boyer, M. D., Shi, W., Schuster, E., Luce, T. C., Ferron, J. R., Walker, M. L., Humphreys, D. A., Penaflor, B. G., and Johnson, R. D. (2012). Toroidal current profile control during low confinement mode plasma discharges in DIII-D via first-principles-driven model-based robust control synthesis. *Nuclear Fusion*, 52(12):123018.

[Barton et al., 2015b] Barton, J. E., Boyer, M. D., Shi, W., Wehner, W., Schuster, E., Ferron, J. R., Walker, M. L., Humphreys, D. A., Luce, T. C., Turco, F., et al. (2015b). Physics-model-based nonlinear actuator trajectory optimization and safety factor profile feedback control for advanced scenario development in DIII-D. *Nuclear Fusion*, 55(9):093005.

[Baylor et al., 2004] Baylor, L. R., Burrell, K., Groebner, R., Houlberg, W. A., Ernst, D., Murakami, M., and Wade, M. R. (2004). Comparison of toroidal rotation velocities of different impurity ions in the DIII-D tokamak. *Physics of Plasmas*, 11(6):3100–3105.

[Binetti et al., 2003] Binetti, P., Ariyur, K. B., Krstic, M., and Bernelli, F. (2003). Formation flight optimization using extremum seeking feedback. *Journal of guidance, control, and dynamics*, 26(1):132–142.

[Blanken et al., 2019] Blanken, T., Felici, F., Galperti, C., Kudláček, O., Janky, F., Mlynek, A., Giannone, L., Lang, P., Treutterer, W., Heemels, W., et al. (2019). Model-based real-time plasma electron density profile estimation and control on ASDEX Upgrade and TCV. *Fusion Engineering and Design*, 147:111211.

[Bock et al., 2017] Bock, A., Fable, E., Fischer, R., Reich, M., Rittich, D., Stober, J., Bernert, M., Burckhart, A., Doerk, H., Dunne, M., et al. (2017). Non-inductive improved H-mode operation at ASDEX Upgrade. *Nuclear Fusion*, 57(12):126041.

[Bodin and Newton, 1980] Bodin, H. and Newton, A. (1980). Reversed-field-pinch research. *Nuclear fusion*, 20(10):1255.

[Bolder et al., 2012] Bolder, J., Witvoet, G., De Baar, M., Van De Wouw, N., Haring, M., Westerhof, E., Doelman, N., and Steinbuch, M. (2012). Robust sawtooth period control based on adaptive online optimization. *Nuclear Fusion*, 52(7):074006.

[Borrelli and Morari, 2007] Borrelli, F. and Morari, M. (2007). Offset free model predictive control. In *2007 46th IEEE Conference on Decision and Control*, pages 1245–1250. IEEE.

[Bosch and Hale, 1992] Bosch, H.-S. and Hale, G. (1992). Improved formulas for fusion cross-sections and thermal reactivities. *Nuclear fusion*, 32(4):611.

[Boyer et al., 2015] Boyer, M., Andre, R., Gates, D., Gerhardt, S., Goumiri, I., and Menard, J. (2015). Central safety factor and betaN control on NSTX-U via beam power and plasma boundary shape modification, using TRANSP for closed loop simulations. *Nuclear Fusion*, 55(5):053033.

[Boyer et al., 2017] Boyer, M., Andre, R., Gates, D., Gerhardt, S., Menard, J., and Poli, F. (2017). Feedback control design for non-inductively sustained scenarios in NSTX-U using TRANSP. *Nuclear Fusion*, 57(6):066017.

[Boyer et al., 2013] Boyer, M. D., Barton, J., Schuster, E., Luce, T. C., Ferron, J. R., Walker, M. L., Humphreys, D. A., Penaflor, B. G., and Johnson, R. D. (2013). First-principles-driven model-based current profile control for the DIII-D tokamak via LQI optimal control. *Plasma Physics and Controlled Fusion*, 55(10):105007.

[Boyer et al., 2014] Boyer, M. D., Barton, J., Schuster, E., Walker, M. L., Luce, T. C., Ferron, J. R., Penaflor, B. G., Johnson, R. D., and Humphreys, D. A. (2014). Backstepping Control of the Toroidal Plasma Current Profile in the DIII-D Tokamak. *IEEE Trans. Contr. Sys. Techn.*, 22(5):1725–1739.

[Boyer et al., 2019] Boyer, M. D., Erickson, K., Grierson, B. A., Pace, D. C., Scoville, J., Rauch, J., Crowley, B., Ferron, J. R., Haskey, S. R., Humphreys, D. A., et al. (2019). Feedback control of stored energy and rotation with variable beam energy and perveance on DIII-D. *Nuclear Fusion*.

[Braams and Stott, 2002] Braams, C. M. and Stott, P. E. (2002). *Nuclear fusion: half a century of magnetic confinement fusion research*. CRC Press.

[Bucalossi et al., 2014] Bucalossi, J., Missirlian, M., Moreau, P., Samaille, F., Tsitrone, E., Van Houtte, D., Batal, T., Bourdelle, C., Chantant, M., Corre, Y., et al. (2014). The WEST project: Testing ITER divertor high heat flux component technology in a steady state tokamak environment. *Fusion Engineering and Design*, 89(7-8):907–912.

[Challis, 2004] Challis, C. (2004). The use of internal transport barriers in tokamak plasmas. *Plasma physics and controlled fusion*, 46(12B):B23.

[Chen et al., 2007] Chen, B., Liu, X., and Tong, S. (2007). Adaptive fuzzy output tracking control of mimo nonlinear uncertain systems. *IEEE Transactions on Fuzzy Systems*, 15(2):287–300.

[Cordey et al., 2005] Cordey, J., Thomsen, K., Chudnovskiy, A., Kardaun, O., Takizuka, T., Snipes, J., Greenwald, M., Sugiyama, L., Ryter, F., Kus, A., et al. (2005). Scaling of the energy confinement time with β and collisionality approaching iter conditions. *Nuclear fusion*, 45(9):1078.

[Cutler and Ramaker, 1980] Cutler, C. R. and Ramaker, B. L. (1980). Dynamic matrix control?? A computer control algorithm. In *joint automatic control conference*, number 17, page 72.

[Denton et al., 1986] Denton, R. E., Drake, J., Kleva, R. G., and Boyd, D. (1986). Skin currents and compound sawteeth in tokamaks. *Physical Review Letters*, 56(23):2477.

[Dickson and Fanelli, 2013] Dickson, M. H. and Fanelli, M. (2013). *Geothermal energy: utilization and technology*. Routledge.

[Dreesen et al., 2015] Dreesen, P., Ishteva, M., and Schoukens, J. (2015). Decoupling multivariate polynomials using first-order information and tensor decompositions. *SIAM Journal on Matrix analysis and Applications*, 36(2):864–879.

[Dürr et al., 2017] Dürr, H.-B., Krstić, M., Scheinker, A., and Ebenbauer, C. (2017). Extremum seeking for dynamic maps using lie brackets and singular perturbations. *Automatica*, 83:91–99.

[Dürr et al., 2013] Dürr, H.-B., Stanković, M. S., Ebenbauer, C., and Johansson, K. H. (2013). Lie bracket approximation of extremum seeking systems. *Automatica*, 49(6):1538–1552.

[ElMadany and Abduljabbar, 1999] ElMadany, M. M. and Abduljabbar, Z. S. (1999). Linear quadratic gaussian control of a quarter-car suspension. *Vehicle System Dynamics*, 32(6):479–497.

[Eriksson and Porcelli, 2002] Eriksson, L.-G. and Porcelli, F. (2002). Toroidal plasma rotation induced by fast ions without external momentum injection in tokamaks. *Nuclear fusion*, 42(8):959.

[Fasoli et al., 2016] Fasoli, A., Brunner, S., Cooper, W., Graves, J., Ricci, P., Sauter, O., and Villard, L. (2016). Computational challenges in magnetic-confinement fusion physics. *Nature Physics*, 12(5):411–423.

[Felici et al., 2011] Felici, F., Sauter, O., Coda, S., Duval, B., Goodman, T., Moret, J., Paley, J., Team, T., et al. (2011). Real-time physics-model-based simulation of the current density profile in tokamak plasmas. *Nuclear Fusion*, 51(8):083052.

[Ferron et al., 2006] Ferron, J., Gohil, P., Greenfield, C., Lohr, J., Luce, T., Makowski, M., Mazon, D., Murakami, M., Petty, C., Politzer, P., et al. (2006). Feedback control of the safety factor profile evolution during formation of an advanced tokamak discharge. *Nuclear fusion*, 46(10):L13.

[Ferron et al., 1998] Ferron, J., Walker, M., Lao, L., John, H. S., Humphreys, D., and Leuer, J. (1998). Real time equilibrium reconstruction for tokamak discharge control. *Nuclear fusion*, 38(7):1055.

[Fisch, 1978] Fisch, N. J. (1978). Confining a tokamak plasma with RF-driven currents. *Physical Review Letters*, 41(13):873.

[Freidberg, 2008] Freidberg, J. P. (2008). *Plasma physics and fusion energy*. Cambridge university press.

[Fu and Chai, 2007] Fu, Y. and Chai, T. (2007). Nonlinear multivariable adaptive control using multiple models and neural networks. *Automatica*, 43(6):1101–1110.

[Garcia and Morari, 1982] Garcia, C. E. and Morari, M. (1982). Internal model control. a unifying review and some new results. *Industrial & Engineering Chemistry Process Design and Development*, 21(2):308–323.

[Garcia et al., 1989] Garcia, C. E., Prett, D. M., and Morari, M. (1989). Model predictive control: theory and practice—a survey. *Automatica*, 25(3):335–348.

[Gaye et al., 2011] Gaye, O., Moulay, E., Brémond, S., Autrique, L., Nouailletas, R., and Orlov, Y. (2011). Sliding mode stabilization of the current profile in tokamak plasmas. In *2011 50th IEEE Conference on Decision and Control and European Control Conference*, pages 2638–2643. IEEE.

[Ghaffari et al., 2012] Ghaffari, A., Krstić, M., and Nešić, D. (2012). Multivariable newton-based extremum seeking. *Automatica*, 48(8):1759–1767.

[Gong et al., 2019] Gong, X., Garofalo, A. M., Huang, J., Qian, J., Holcomb, C. T., Ekedah, A., Maingi, R., Li, E., Zeng, L., Zhang, B., et al. (2019). Integrated operation of steady-state long-pulse H-mode in Experimental Advanced Superconducting Tokamak. *Nuclear Fusion*, 59(8):086030.

[Goumiri et al., 2016] Goumiri, I., Rowley, C., Sabbagh, S., Gates, D., Gerhardt, S., Boyer, M., Andre, R., Kolemen, E., and Taira, K. (2016). Modeling and control of plasma rotation for NSTX using neoclassical toroidal viscosity and neutral beam injection. *Nuclear Fusion*, 56(3):036023.

[Goumiri et al., 2017] Goumiri, I., Rowley, C. W., Sabbagh, S., Gates, D., Boyer, M., Gerhardt, S., Kolemen, E., and Menard, J. (2017). Simultaneous feedback control of plasma rotation and stored energy on NSTX-U using neoclassical toroidal viscosity and neutral beam injection. *Physics of Plasmas*, 24(5):056101.

[Green et al., 2003] Green, B. et al. (2003). ITER: burning plasma physics experiment. *Plasma physics and controlled fusion*, 45(5):687.

[Gruber et al., 1993] Gruber, O., Lackner, K., Pautasso, G., Seidel, U., and Streibl, B. (1993). Vertical displacement events and halo currents. *Plasma physics and controlled fusion*, 35(SB):B191.

[Guay and Atta, 2018] Guay, M. and Atta, K. T. (2018). Dual mode extremum-seeking control via lie-bracket averaging approximations. In *2018 Annual American Control Conference (ACC)*, pages 2972–2977. IEEE.

[Guay and Dochain, 2017] Guay, M. and Dochain, D. (2017). A proportional-integral extremum-seeking controller design technique. *Automatica*, 77:61–67.

[Gurung et al., 2017] Gurung, N., Bhattarai, R., and Kamalasadan, S. (2017). Optimal linear-quadratic-integral controller design for doubly-fed induction generator. In *2017 IEEE Power & Energy Society General Meeting*, pages 1–5. IEEE.

[Hanus et al., 1987] Hanus, R., Kinnaert, M., and Henrotte, J.-L. (1987). Conditioning technique, a general anti-windup and bumpless transfer method. *Automatica*, 23(6):729–739.

[Harnefors and Nee, 1998] Harnefors, L. and Nee, H.-P. (1998). Model-based current control of ac machines using the internal model control method. *IEEE Transactions on Industry Applications*, 34(1):133–141.

[Haskey et al., 2018] Haskey, S., Grierson, B., Stagner, L., Chrystal, C., Ashourvan, A., Bortolon, A., Boyer, M., Burrell, K., Collins, C., Groebner, R., et al. (2018). Active spectroscopy measurements of the deuterium temperature, rotation, and density from the core to scrape off layer on the DIII-D tokamak. *Review of Scientific Instruments*, 89(10):10D110.

[Hassen et al., 2009] Hassen, S. S., Heurs, M., Huntington, E. H., Petersen, I. R., and James, M. (2009). Frequency locking of an optical cavity using linear–quadratic gaussian integral control. *Journal of Physics B: Atomic, Molecular and Optical Physics*, 42(17):175501.

[Heath et al., 2017] Heath, W., Polignano, M., and Pannocchia, G. (2017). Observer-based offset-free internal model control. *IFAC-PapersOnLine*, 50(1):898–903.

[Hinton and Hazeltine, 1976] Hinton, F. and Hazeltine, R. D. (1976). Theory of plasma transport in toroidal confinement systems. *Reviews of Modern Physics*, 48(2):239.

[Hou and Jin, 2013] Hou, Z. and Jin, S. (2013). *Model free adaptive control: theory and applications*. CRC press.

[Huang et al., 2020] Huang, Y., Luo, Z., Xiao, B., Lao, L., Mele, A., Pironti, A., Mattei, M., Ambrosino, G., Yuan, Q., Wang, Y., et al. (2020). Gpu-optimized fast plasma equilibrium reconstruction in fine grids for real-time control and data analysis. *Nuclear Fusion*, 60(7):076023.

[Huang et al., 2017] Huang, Y., Xiao, B., Luo, Z., Qian, J., Li, S., Chen, Y., Liu, H., Xu, L., Yuan, Y., and Yuan, Q. (2017). Development of real-time plasma current profile reconstruction with POINT diagnostic for EAST plasma control. *Fusion Engineering and Design*, 120:1–8.

[Huang et al., 2018] Huang, Z., Coda, S., et al. (2018). Dependence of density fluctuations on shape and collisionality in positive-and negative-triangularity tokamak plasmas. *Plasma Physics and Controlled Fusion*, 61(1):014021.

[Humphreys et al., 2015] Humphreys, D., Ambrosino, G., de Vries, P., Felici, F., Kim, S. H., Jackson, G., Kallenbach, A., Kolemen, E., Lister, J., Moreau, D., et al. (2015). Novel aspects of plasma control in ITER. *Physics of Plasmas*, 22(2):021806.

[Humphreys et al., 2006] Humphreys, D., Ferron, J., La Haye, R., Luce, T., Petty, C., Prater, R., and Welander, A. (2006). Active control for stabilization of neoclassical tearing modes. *Physics of Plasmas*, 13(5):056113.

[Ida and Fujita, 2018] Ida, K. and Fujita, T. (2018). Internal transport barrier in tokamak and helical plasmas. *Plasma Physics and Controlled Fusion*, 60(3):033001.

[Ioannou and Sun, 1996] Ioannou, P. A. and Sun, J. (1996). *Robust adaptive control*, volume 1. PTR Prentice-Hall Upper Saddle River, NJ.

[Joffrin, 2007] Joffrin, E. (2007). Advanced tokamak scenario developments for the next step. *Plasma Physics and Controlled Fusion*, 49(12B):B629.

[Joffrin et al., 2003] Joffrin, E., Crisanti, F., Felton, R., Litaudon, X., Mazon, D., Moreau, D., Zabeo, L., Albanese, R., Ariola, M., Alves, D., et al. (2003). Integrated scenario in JET using real-time profile control. *Plasma physics and controlled fusion*, 45(12A):A367.

[Kallenbach et al., 2015] Kallenbach, A., Bernert, M., Beurskens, M., Casali, L., Dunne, M., Eich, T., Giannone, L., Herrmann, A., Maraschek, M., Potzel, S., et al. (2015). Partial detachment of high power discharges in ASDEX Upgrade. *Nuclear Fusion*, 55(5):053026.

[Kallenbach et al., 2010] Kallenbach, A., Dux, R., Fuchs, J., Fischer, R., Geiger, B., Giannone, L., Herrmann, A., Lunt, T., Mertens, V., McDermott, R., et al. (2010). Divertor power load feedback with nitrogen seeding in ASDEX Upgrade. *Plasma Physics and Controlled Fusion*, 52(5):055002.

[Kallenbach et al., 2005] Kallenbach, A., Lang, P., Dux, R., Fuchs, C., Herrmann, A., Meister, H., Mertens, V., Neu, R., Pütterich, T., Zehetbauer, T., et al. (2005). Integrated exhaust control with divertor parameter feedback and pellet ELM pacemaking in ASDEX Upgrade. *Journal of nuclear materials*, 337:732–736.

[Kalogirou, 2013] Kalogirou, S. A. (2013). *Solar energy engineering: processes and systems*. Academic Press.

[Keating and Alleyne, 2017] Keating, B. and Alleyne, A. (2017). Time-varying newton based extremum seeking for optimization of vapor compression systems. In *2017 American Control Conference (ACC)*, pages 31–36. IEEE.

[Kessel et al., 1994] Kessel, C., Manickam, J., Rewoldt, G., and Tang, W. (1994). Improved plasma performance in tokamaks with negative magnetic shear. *Physical Review Letters*, 72(8):1212.

[Khalil and Grizzle, 2002] Khalil, H. K. and Grizzle, J. W. (2002). *Nonlinear systems*, volume 3. Prentice hall Upper Saddle River, NJ.

[Kim and Lister, 2012] Kim, S. and Lister, J. (2012). A potentially robust plasma profile control approach for ITER using real-time estimation of linearized profile response models. *Nuclear Fusion*, 52(7):074002.

[Kim et al., 1991] Kim, Y., Diamond, P., and Groebner, R. (1991). Neoclassical poloidal and toroidal rotation in tokamaks. *Physics of Fluids B: Plasma Physics*, 3(8):2050–2060.

[Kong et al., 2019] Kong, M., Blanken, T., Felici, F., Galperti, C., Maljaars, E., Sauter, O., Vu, T., Carpanese, F., Merle, A., Moret, J.-M., et al. (2019). Control of neoclassical tearing modes and integrated multi-actuator plasma control on TCV. *Nuclear Fusion*, 59(7):076035.

[Krivenski et al., 1985] Krivenski, V., Fidone, I., Giruzzi, G., Granata, G., Meyer, R., and Mazzucato, E. (1985). Improving current generation in a tokamak by electron cyclotron waves. *Nuclear fusion*, 25(2):127.

[Krstic et al., 1995] Krstic, M., Kokotovic, P. V., and Kanellakopoulos, I. (1995). *Nonlinear and adaptive control design*. John Wiley & Sons, Inc.

[Kumar et al., 2019] Kumar, S., Mohammadi, A., Quintero, D., Rezazadeh, S., Gans, N., and Gregg, R. D. (2019). Extremum seeking control for model-free auto-tuning of powered prosthetic legs. *IEEE Transactions on Control Systems Technology*.

[Labit et al., 2019] Labit, B., Eich, T., Harrer, G. F., Wolfrum, E., Bernert, M., Dunne, M. G., Frassinetti, L., Hennequin, P., Maurizio, R., Merle, A., et al. (2019). Dependence on plasma shape and plasma fueling for small edge-localized mode regimes in TCV and ASDEX Upgrade. *Nuclear fusion*, 59(8):086020.

[Laborde et al., 2004] Laborde, L., Mazon, D., Moreau, D., Murari, A., Felton, R., Zabeo, L., Albanese, R., Ariola, M., Bucalossi, J., Crisanti, F., et al. (2004). A model-based technique for integrated real-time profile control in the JET tokamak. *Plasma Physics and Controlled Fusion*, 47(1):155.

[Lanctot et al., 2016] Lanctot, M., Olofsson, K., Capella, M., Humphreys, D., Eidietis, N., Hanson, J., Paz-Soldan, C., Strait, E., and Walker, M. (2016). Error field optimization in DIII-D using extremum seeking control. *Nuclear Fusion*, 56(7):076003.

[Landau et al., 2011] Landau, I. D., Lozano, R., M'Saad, M., and Karimi, A. (2011). *Adaptive control: algorithms, analysis and applications*. Springer Science & Business Media.

[Landau and Zito, 2007] Landau, I. D. and Zito, G. (2007). *Digital control systems: design, identification and implementation*. Springer Science & Business Media.

[Lao et al., 1985] Lao, L., John, H. S., Stambaugh, R., Kellman, A., and Pfeiffer, W. (1985). Reconstruction of current profile parameters and plasma shapes in tokamaks. *Nuclear fusion*, 25(11):1611.

[Leblanc, 1922] Leblanc, M. (1922). Sur l'electrification des chemins de fer au moyen de courants alternatifs de frequence elevee. *Revue générale de l'électricité*, 12(8):275–277.

[Lee et al., 2001] Lee, G., Kwon, M., Doh, C., Hong, B., Kim, K., Cho, M., Namkung, W., Chang, C.-S., Kim, Y., Kim, J., et al. (2001). Design and construction of the KSTAR tokamak. *Nuclear Fusion*, 41(10):1515.

[Lee et al., 1994] Lee, J. H., Morari, M., and Garcia, C. E. (1994). State-space interpretation of model predictive control. *Automatica*, 30(4):707–717.

[Leith and Leithead, 2000] Leith, D. J. and Leithead, W. E. (2000). Survey of gain-scheduling analysis and design. *International journal of control*, 73(11):1001–1025.

[Lennart, 1999] Lennart, L. (1999). System identification: theory for the user. *PTR Prentice Hall, Upper Saddle River, NJ*, pages 1–14.

[Lin-Liu and Hinton, 1997] Lin-Liu, Y. and Hinton, F. (1997). Trapped electron correction to beam driven current in general tokamak equilibria. *Physics of Plasmas*, 4(11):4179–4181.

[Litaudon et al., 2013] Litaudon, X., Voitsekhovitch, I., Artaud, J., Belo, P., Bizarro, J. P., Casper, T., Citrin, J., Fable, E., Ferreira, J., Garcia, J., et al. (2013). Modelling of hybrid scenario: from present-day experiments towards ITER. *Nuclear Fusion*, 53(7):073024.

[Liu et al., 2012] Liu, F., Moreau, D., Artaud, J., Garcia, J., and Nouailletas, R. (2012). Model-based magnetic and kinetic control of ITER scenarios. In *Proc. 39th EPS Conf. on Plasma Physics (Stockholm, Sweden, 2–6 July 2012) P*, volume 1.

[Liu et al., 2016a] Liu, H., Jie, Y., Ding, W., Brower, D., Zou, Z., Qian, J., Li, W., Yang, Y., Zeng, L., Zhang, S., et al. (2016a). Internal magnetic field measurements by laser-based polarimeter-interferometer (POINT) system on EAST. *Journal of Instrumentation*, 11(01):C01049.

[Liu et al., 2014] Liu, H., Jie, Y., Ding, W., Brower, D. L., Zou, Z., Li, W., Wang, Z., Qian, J., Yang, Y., Zeng, L., et al. (2014). Faraday-effect polarimeter-interferometer system for current density measurement on EAST. *Review of Scientific Instruments*, 85(11):11D405.

[Liu et al., 2016b] Liu, H., Qian, J., Jie, Y., Ding, W., Brower, D., Zou, Z., Li, W., Lian, H., Wang, S., Yang, Y., et al. (2016b). Initial measurements of plasma current and electron density profiles using a polarimeter/interferometer (POINT) for long pulse operation in EAST. *Review of Scientific Instruments*, 87(11):11D903.

[Ljung, 1995] Ljung, L. (1995). *System identification toolbox: User's guide*. Citeseer.

[Ljung, 2010] Ljung, L. (2010). Perspectives on system identification. *Annual Reviews in Control*, 34(1):1–12.

[Ljung and Söderström, 1983] Ljung, L. and Söderström, T. (1983). *Theory and practice of recursive identification*. MIT press.

[Lofberg, 2004] Lofberg, J. (2004). YALMIP: A toolbox for modeling and optimization in MATLAB. In *2004 IEEE international conference on robotics and automation (IEEE Cat. No. 04CH37508)*, pages 284–289. IEEE.

[Lozano and Zhao, 1994] Lozano, R. and Zhao, X.-H. (1994). Adaptive pole placement without excitation probing signals. *IEEE Transactions on Automatic Control*, 39(1):47–58.

[Maciejowski, 2002] Maciejowski, J. M. (2002). *Predictive control: with constraints*. Pearson education.

[MacKay, 2008] MacKay, D. (2008). *Sustainable Energy-without the hot air*. UIT cambridge.

[Maeder et al., 2009] Maeder, U., Borrelli, F., and Morari, M. (2009). Linear offset-free model predictive control. *Automatica*, 45(10):2214–2222.

[Maeder and Morari, 2010] Maeder, U. and Morari, M. (2010). Offset-free reference tracking with model predictive control. *Automatica*, 46(9):1469–1476.

[Maljaars et al., 2017] Maljaars, E., Felici, F., Blanken, T., Galperti, C., Sauter, O., De Baar, M., Carpanese, F., Goodman, T., Kim, D., Kim, S., et al. (2017). Profile control simulations and experiments on TCV: a controller test environment and results using a model-based predictive controller. *Nuclear Fusion*, 57(12):126063.

[Maljaars et al., 2015] Maljaars, E., Felici, F., De Baar, M., van Dongen, J., Hogeweij, G., Geelen, P., and Steinbuch, M. (2015). Control of the tokamak safety factor profile with time-varying constraints using MPC. *Nuclear Fusion*, 55(2):023001.

[Manwell et al., 2010] Manwell, J. F., McGowan, J. G., and Rogers, A. L. (2010). *Wind energy explained: theory, design and application*. John Wiley & Sons.

[Marquardt, 1963] Marquardt, D. W. (1963). An algorithm for least-squares estimation of nonlinear parameters. *Journal of the society for Industrial and Applied Mathematics*, 11(2):431–441.

[Marques, 2010] Marques, J. (2010). Evolution of nuclear fission reactors: Third generation and beyond. *Energy Conversion and Management*, 51(9):1774–1780.

[Matthews et al., 1999] Matthews, G., Balet, B., Cordey, J., Davies, S., Fishpool, G., Guo, H., Horton, L., Von Hellermann, M., Ingesson, L., Lingertat, J., et al. (1999). Studies in JET divertors of varied geometry. II: Impurity seeded plasmas. *Nuclear fusion*, 39(1):19.

[Mavkov et al., 2017a] Mavkov, B., Witrant, E., and Prieur, C. (2017a). Distributed control of coupled inhomogeneous diffusion in tokamak plasmas. *IEEE Transactions on Control Systems Technology*, (99):1–8.

[Mavkov et al., 2018] Mavkov, B., Witrant, E., Prieur, C., Maljaars, E., Felici, F., Sauter, O., et al. (2018). Experimental validation of a Lyapunov-based controller for the plasma safety factor and plasma pressure in the TCV tokamak. *Nuclear Fusion*, 58(5):056011.

[Mavkov et al., 2017b] Mavkov, B., Witrant, E., Prieur, C., and Moreau, D. (2017b). Multi-experiment state-space identification of coupled magnetic and kinetic parameters in tokamak plasmas. *Control Engineering Practice*, 60:28–38.

[Mayne et al., 2000] Mayne, D. Q., Rawlings, J. B., Rao, C. V., and Scokaert, P. O. (2000). Constrained model predictive control: Stability and optimality. *Automatica*, 36(6):789–814.

[Mazon et al., 2003] Mazon, D., Litaudon, X., Moreau, D., Pericoli-Ridolfini, V., Zabeo, L., Crisanti, F., De Vries, P., Felton, R., Joffrin, E., Murari, A., et al. (2003). Active control of the current density profile in JET. *Plasma physics and controlled fusion*, 45(7):L47.

[McCracken et al., 2005] McCracken, G. M., McCracken, G., and Stott, P. (2005). *Fusion: the energy of the universe*. Academic Press.

[McKelvey et al., 1996] McKelvey, T., Akçay, H., and Ljung, L. (1996). Subspace-based multivariable system identification from frequency response data. *IEEE Transactions on Automatic Control*, 41(7):960–979.

[Morari and Maeder, 2012] Morari, M. and Maeder, U. (2012). Nonlinear offset-free model predictive control. *Automatica*, 48(9):2059–2067.

[Moreau et al., 2015] Moreau, D., Artaud, J., Ferron, J. R., Holcomb, C. T., Humphreys, D. A., Liu, F., Luce, T. C., Park, J. M., Prater, R., Turco, F., et al. (2015). Combined magnetic and kinetic control of advanced tokamak steady state scenarios based on semi-empirical modelling. *Nuclear Fusion*, 55(6):063011.

[Moreau et al., 2003] Moreau, D., Crisanti, F., Litaudon, X., Mazon, D., De Vries, P., Felton, R., Joffrin, E., Laborde, L., Lennholm, M., Murari, A., et al. (2003). Real-time control of the q-profile in JET for steady state advanced tokamak operation. *Nuclear Fusion*, 43(9):870.

[Moreau et al., 2008] Moreau, D., Mazon, D., Ariola, M., De Tommasi, G., Laborde, L., Piccolo, F., Sartori, F., Tala, T., Zabeo, L., Boboc, A., et al. (2008). A two-time-scale dynamic-model approach for magnetic and kinetic profile control in advanced tokamak scenarios on JET. *Nuclear Fusion*, 48(10):106001.

[Moreau et al., 2011] Moreau, D., Mazon, D., Walker, M., Ferron, J., Burrell, K., Flanagan, S., Gohil, P., Groebner, R., Hyatt, A., La Haye, R., et al. (2011). Plasma models for real-time control of advanced tokamak scenarios. *Nuclear Fusion*, 51(6):063009.

[Moreau et al., 2018] Moreau, D., Qian, J., Yuan, Q., Huang, Y., Ding, S., Du, H., Li, M., Luo, Z., Artaud, J., et al. (2018). Model-predictive kinetic control for steady state plasma operation scenarios on east. Technical report.

[Moreau et al., 2013] Moreau, D., Walker, M. L., Ferron, J. R., Liu, F., Schuster, E., Barton, J. E., Boyer, M. D., Burrell, K. H., Flanagan, S., Gohil, P., et al. (2013). Integrated magnetic and kinetic control of advanced tokamak plasmas on DIII-D based on data-driven models. *Nuclear Fusion*, 53(6):063020.

[Moreau et al., 2021] Moreau, D, W. S. Q. J. Y. Q. et al. (2021). Model predictive kinetic control experiments on EAST.

[Morse, 1984] Morse, A. (1984). An adaptive control for globally stabilizing linear systems with unknown high-frequency gains. In *Analysis and Optimization of Systems*, pages 58–68. Springer.

[Morse, 1985] Morse, A. (1985). A model reference controller for the adaptive stabilization of any strictly proper, minimum phase, linear system with relative degree not exceeding two. In *Proceedings of the 1985 MTNS Conference*.

[Mu et al., 2017] Mu, B., Li, Y., House, J. M., and Salsbury, T. I. (2017). Real-time optimization of a chilled water plant with parallel chillers based on extremum seeking control. *Applied energy*, 208:766–781.

[Narayanan et al., 1997] Narayanan, N. L., Krishnaswamy, P., and Rangaiah, G. (1997). An adaptive internal model control strategy for ph neutralization. *Chemical Engineering Science*, 52(18):3067–3074.

[Nilsson et al., 2013] Nilsson, E., Decker, J., Peysson, Y., Artaud, J.-F., Ekedahl, A., Hillairet, J., Aniel, T., Basiuk, V., Goniche, M., Imbeaux, F., et al. (2013). Comparative modelling of lower hybrid current drive with two launcher designs in the Tore Supra tokamak. *Nuclear Fusion*, 53(8):083018.

[Noël and Kerschen, 2017] Noël, J.-P. and Kerschen, G. (2017). Nonlinear system identification in structural dynamics: 10 more years of progress. *Mechanical Systems and Signal Processing*, 83:2–35.

[Nouailletas et al., 2014] Nouailletas, R., Nardon, E., and Brémond, S. (2014). Robust Vertical Plasma Stabilization of the future tungsten divertor configuration of Tore Supra. *IFAC Proceedings Volumes*, 47(3):1349–1354.

[Nouailletas et al., 2019] Nouailletas, R., Nardon, E., Moreau, P., Reux, C., et al. (2019). WEST magnetic control. In *2019 IEEE 58th Conference on Decision and Control (CDC)*, pages 3214–3219. IEEE.

[Nussbaum, 1983] Nussbaum, R. D. (1983). Some remarks on a conjecture in parameter adaptive control. *Systems & control letters*, 3(5):243–246.

[Ono et al., 2000] Ono, M., Kaye, S., Peng, Y.-K., Barnes, G., Blanchard, W., Carter, M., Chrzanowski, J., Dudek, L., Ewig, R., Gates, D., et al. (2000). Exploration of spherical torus physics in the NSTX device. *Nuclear Fusion*, 40(3Y):557.

[Ou et al., 2007] Ou, Y., Luce, T., Schuster, E., Ferron, J., Walker, M., Xu, C., and Humphreys, D. (2007). Towards model-based current profile control at diii-d. *Fusion Engineering and Design*, 82(5-14):1153–1160.

[Ou et al., 2008] Ou, Y., Xu, C., Schuster, E., Luce, T., Ferron, J., Walker, M., and Humphreys, D. (2008). Design and simulation of extremum-seeking open-loop optimal control of current profile in the DIII-D tokamak. *Plasma Physics and Controlled Fusion*, 50(11):115001.

[Ouarit et al., 2011] Ouarit, H., Brémond, S., Nouailletas, R., Witrant, E., and Autrique, L. (2011). Validation of plasma current profile model predictive control in tokamaks via simulations. *Fusion Engineering and Design*, 86(6-8):1018–1021.

[Paduart et al., 2012] Paduart, J., Lauwers, L., Pintelon, R., and Schoukens, J. (2012). Identification of a Wiener–Hammerstein system using the polynomial nonlinear state space approach. *Control Engineering Practice*, 20(11):1133–1139.

[Paduart et al., 2010] Paduart, J., Lauwers, L., Swevers, J., Smolders, K., Schoukens, J., and Pintelon, R. (2010). Identification of nonlinear systems using polynomial nonlinear state space models. *Automatica*, 46(4):647–656.

[Paley et al., 2009] Paley, J., Felici, F., Coda, S., Goodman, T., Team, T., et al. (2009). From profile to sawtooth control: developing feedback control using ECRH/ECCD systems on the TCV tokamak. *Plasma Physics and Controlled Fusion*, 51(12):124041.

[Pannocchia and Heath, 2020] Pannocchia, G. and Heath, W. P. (2020). Offset-free IMC with generalized disturbance models. *Automatica*, 122:109270.

[Park et al., 2017] Park, M., Na, Y.-S., Seo, J., Kim, M., and Kim, K. (2017). Effect of electron cyclotron beam width to neoclassical tearing mode stabilization by minimum seeking control in ITER. *Nuclear Fusion*, 58(1):016042.

[Petty et al., 2017] Petty, C. C., Nazikian, R., Park, J. M., Turco, F., Chen, X., Cui, L., Evans, T. E., Ferraro, N., Ferron, J. R., Garofalo, A. M., et al. (2017). Advances in the

steady-state hybrid regime in DIII-D—a fully non-inductive, ELM-suppressed scenario for ITER. *Nuclear Fusion*, 57(11):116057.

[Pfalzner, 2006] Pfalzner, S. (2006). *An introduction to inertial confinement fusion.* CRC Press.

[Pintelon and Schoukens, 2012] Pintelon, R. and Schoukens, J. (2012). *System identification: a frequency domain approach.* John Wiley & Sons.

[Pintelon et al., 2010] Pintelon, R., Schoukens, J., Vandersteen, G., and Barbé, K. (2010). Estimation of nonparametric noise and FRF models for multivariable systems—Part I: Theory. *Mechanical Systems and Signal Processing*, 24(3):573–595.

[Piras et al., 2009] Piras, F., Coda, S., Furno, I., Moret, J., Pitts, R., Sauter, O., Tal, B., Turri, G., Bencze, A., Duval, B., et al. (2009). Snowflake divertor plasmas on TCV. *Plasma Physics and Controlled Fusion*, 51(5):055009.

[Prett and Gillette, 1980] Prett, D. M. and Gillette, R. (1980). Optimization and constrained multivariable control of a catalytic cracking unit. In *Joint automatic control conference*, number 17, page 73.

[Qian et al., 2016] Qian, J., Lao, L., Liu, H., Ding, W., Zeng, L., Luo, Z., Ren, Q., Huang, Y., Huang, J., Brower, D., et al. (2016). East equilibrium current profile reconstruction using polarimeter-interferometer internal measurement constraints. *Nuclear Fusion*, 57(3):036008.

[Qiu et al., 2016] Qiu, Q., Xiao, B., Guo, Y., Liu, L., Xing, Z., and Humphreys, D. (2016). Simulation of east vertical displacement events by tokamak simulation code. *Nuclear Fusion*, 56(10):106029.

[Rachael et al., 1978] Rachael, J., Rault, A., Testud, J., and Papon, J. (1978). Model Predictive heuristic control: application to an Industrial Process. *Automatica*, 14(5):413–428.

[Rawlings and Muske, 1993] Rawlings, J. B. and Muske, K. R. (1993). The stability of constrained receding horizon control. *IEEE transactions on automatic control*, 38(10):1512–1516.

[Rebut et al., 1995] Rebut, P.-H. et al. (1995). ITER: the first experimental fusion reactor. *Fusion engineering and design*, 30(1-2):85–118.

[Relan et al., 2018] Relan, R., Tiels, K., Marconato, A., Dreesen, P., and Schoukens, J. (2018). Data driven discrete-time parsimonious identification of a nonlinear state-space model for a weakly nonlinear system with short data record. *Mechanical Systems and Signal Processing*, 104:929–943.

[Reyhanoglu et al., 1999] Reyhanoglu, M., van der Schaft, A., McClamroch, N. H., and Kolmanovsky, I. (1999). Dynamics and control of a class of underactuated mechanical systems. *IEEE Transactions on Automatic Control*, 44(9):1663–1671.

[Rice et al., 2007] Rice, J., Ince-Cushman, A., Degrassie, J., Eriksson, L.-G., Sakamoto, Y., Scarabosio, A., Bortolon, A., Burrell, K., Duval, B., Fenzi-Bonizec, C., et al. (2007). Inter-machine comparison of intrinsic toroidal rotation in tokamaks. *Nuclear Fusion*, 47(11):1618.

[Rybicki and Lightman, 2008] Rybicki, G. B. and Lightman, A. P. (2008). *Radiative processes in astrophysics*. John Wiley & Sons.

[Ryutov et al., 2012] Ryutov, D., Cohen, R., Rognlien, T., and Umansky, M. (2012). A snowflake divertor: a possible solution to the power exhaust problem for tokamaks. *Plasma Physics and Controlled Fusion*, 54(12):124050.

[Sauter et al., 1999] Sauter, O., Angioni, C., and Lin-Liu, Y. (1999). Neoclassical conductivity and bootstrap current formulas for general axisymmetric equilibria and arbitrary collisionality regime. *Physics of Plasmas*, 6(7):2834–2839.

[Saxena and Hote, 2012] Saxena, S. and Hote, Y. V. (2012). Advances in internal model control technique: A review and future prospects. *IETE Technical Review*, 29(6):461–472.

[Scherer et al., 1997] Scherer, C., Gahinet, P., and Chilali, M. (1997). Multiobjective output-feedback control via LMI optimization. *IEEE Transactions on automatic control*, 42(7):896–911.

[Schuster et al., 2017] Schuster, E., Wehner, W. P., Barton, J. E., Boyer, M. D., Luce, T. C., Ferron, J. R., Holcomb, C. T., Walker, M. L., Humphreys, D. A., Solomon, W. M., et al. (2017). Enhanced reproducibility of L-mode plasma discharges via physics-model-based q-profile feedback control in DIII-D. *Nuclear Fusion*, 57(11):116026.

[Skogestad and Postlethwaite, 2007] Skogestad, S. and Postlethwaite, I. (2007). *Multivariable feedback control: analysis and design*, volume 2. Wiley New York.

[Snipes et al., 2017] Snipes, J., Albanese, R., Ambrosino, G., Ambrosino, R., Amoskov, V., Blanken, T., Bremond, S., Cinque, M., De Tommasi, G., De Vries, P., et al. (2017). Overview of the preliminary design of the ITER plasma control system. *Nuclear Fusion*, 57(12):125001.

[Soukhanovskii et al., 2012] Soukhanovskii, V., Bell, R. E., Diallo, A., Gerhardt, S., Kaye, S., Kolemen, E., LeBlanc, B. P., McLean, A., Menard, J., Paul, S. F., et al. (2012). Snowflake divertor configuration studies in National Spherical Torus Experiment. *Physics of Plasmas*, 19(8):082504.

[Summers and O'Mullane, 2011] Summers, H. and O'Mullane, M. (2011). Atomic data and modelling for fusion: the adas project. In *AIP Conference Proceedings*, volume 1344, pages 179–187. American Institute of Physics.

[Tao, 2014] Tao, G. (2014). Multivariable adaptive control: A survey. *Automatica*, 50(11):2737–2764.

[Vail et al., 2019] Vail, P. J., Boyer, M. D., Welander, A. S., and Kolemen, E. (2019). Design and simulation of the snowflake divertor control for nstx–u. *Plasma Physics and Controlled Fusion*, 61(3):035005.

[Van der Zwaan, 2008] Van der Zwaan, B. (2008). Prospects for nuclear energy in Europe. *International Journal of Global Energy Issues*, 30(1-4):102–121.

[Velarde et al., 1992] Velarde, G., Ronen, Y., and Martínez-Val, J. M. (1992). *Nuclear fusion by inertial confinement: A comprehensive treatise*. CRC Press.

[Verdult and Verhaegen, 2002] Verdult, V. and Verhaegen, M. (2002). Subspace identification of multivariable linear parameter-varying systems. *Automatica*, 38(5):805–814.

[Verdult and Verhaegen, 2005] Verdult, V. and Verhaegen, M. (2005). Kernel methods for subspace identification of multivariable LPV and bilinear systems. *Automatica*, 41(9):1557–1565.

[Verhaegen and Verdult, 2007] Verhaegen, M. and Verdult, V. (2007). *Filtering and system identification: a least squares approach*. Cambridge university press.

[Vershkov and Mirnov, 1974] Vershkov, V. and Mirnov, S. (1974). Role of impurities in current tokamak experiments. *Nuclear Fusion*, 14(3):383.

[Vijvers et al., 2014] Vijvers, W., Canal, G. P., Labit, B., Reimerdes, H., Tal, B., Coda, S., De Temmerman, G., Duval, B. P., Morgan, T., Zielinski, J. J., et al. (2014). Power exhaust in the snowflake divertor for L-and H-mode TCV tokamak plasmas. *Nuclear Fusion*, 54(2):023009.

[Vu et al., 2016] Vu, N. M. T., Nouailletas, R., Lefèvre, L., and Felici, F. (2016). Plasma q-profile control in tokamaks using a damping assignment passivity-based approach. *Control Engineering Practice*, 54:34–45.

[VU et al., 2014] VU, N. T., Nouailletas, R., Lefèvre, L., Brémond, S., and Felici, F. (2014). Ida-pbc control for the coupled plasma poloidal magnetic flux and heat radial diffusion equations in tokamaks. *IFAC Proceedings Volumes*, 47(3):11398–11403.

[Vu et al., 2017] Vu, N. T., Nouailletas, R., Maljaars, E., Felici, F., Sauter, O., Team, T., et al. (2017). Plasma internal profile control using ida-pbc: Application to tcv. *Fusion Engineering and Design*, 123:624–627.

[Wakatani, 1998] Wakatani, M. (1998). *Stellarator and heliotron devices*, volume 95. Oxford University Press on Demand.

[Walker et al., 2020] Walker, M. L., De Vries, P., Felici, F., and Schuster, E. (2020). Introduction to Tokamak Plasma Control. In *2020 American Control Conference (ACC)*, pages 2901–2918. IEEE.

[Wang and Krstic, 2000] Wang, H.-H. and Krstic, M. (2000). Extremum seeking for limit cycle minimization. *IEEE Transactions on Automatic control*, 45(12):2432–2436.

[Wang et al., 2000] Wang, H.-H., Yeung, S., and Krstic, M. (2000). Experimental application of extremum seeking on an axial-flow compressor. *IEEE Transactions on Control Systems Technology*, 8(2):300–309.

[Wang et al., 2020] Wang, S., Witrant, E., and Moreau, D. (2020). Robust control of q-profile and βp using data-driven models on east. *Fusion Engineering and Design*, page 112071.

[Wang et al., 2021] Wang, S., Witrant, E., and Moreau, D. (2021). Robust control of q-profile and βp using data-driven models on east. *Fusion Engineering and Design*, 162:112071.

[Wehner et al., 2016] Wehner, W., Lauret, M., Schuster, E., Ferron, J. R., Holcomb, C., Luce, T. C., Humphreys, D. A., Walker, M. L., Penaflor, B. G., and Johnson, R. D. (2016). Predictive control of the tokamak q profile to facilitate reproducibility of high-q min steady-state scenarios at DIII-D. In *Control Applications (CCA), 2016 IEEE Conference on*, pages 629–634. IEEE.

[Wehner and Schuster, 2012] Wehner, W. and Schuster, E. (2012). Control-oriented modelling for neoclassical tearing mode stabilization via minimum-seeking techniques. *Nuclear Fusion*, 52(7):074003.

[Wesson and Campbell, 2011] Wesson, J. and Campbell, D. J. (2011). *Tokamaks*, volume 149. Oxford University Press.

[Westerhof et al., 2002] Westerhof, E., Sauter, O., Mayoral, M., Howell, D., Mantsinen, M., Nave, M., Alper, B., Angioni, C., Belo, P., Buttery, R., et al. (2002). Control of sawteeth and triggering of NTMs with ion cyclotron resonance frequency waves in JET. *Nuclear fusion*, 42(11):1324.

[Witrant et al., 2007] Witrant, E., Joffrin, E., Brémond, S., Giruzzi, G., Mazon, D., Barana, O., and Moreau, P. (2007). A control-oriented model of the current profile in tokamak plasma. *Plasma Physics and Controlled Fusion*, 49(7):1075.

[Wolf, 2002] Wolf, R. (2002). Internal transport barriers in tokamak plasmas. *Plasma Physics and Controlled Fusion*, 45(1):R1.

[Xiao et al., 2008] Xiao, B., Humphreys, D., Walker, M., Hyatt, A., Leuer, J., Mueller, D., Penaflor, B., Pigrowski, D., Johnson, R., Welander, A., et al. (2008). EAST plasma control system. *Fusion engineering and design*, 83(2-3):181–187.

[Yazdanian and Mehrizi-Sani, 2014] Yazdanian, M. and Mehrizi-Sani, A. (2014). Internal model-based current control of the rl filter-based voltage-sourced converter. *IEEE Transactions on Energy Conversion*, 29(4):873–881.

[Yin et al., 2018] Yin, C., Wu, S., Zhou, S., Cao, J., Huang, X., and Cheng, Y. (2018). Design and stability analysis of multivariate extremum seeking with newton method. *Journal of the Franklin Institute*, 355(4):1559–1578.

[Yoshizawa et al., 2003] Yoshizawa, A., Itoh, S. I., and Itoh, K. (2003). Plasma and fluid turbulence: theory and modelling.

[Young and Willems, 1972] Young, P. C. and Willems, J. (1972). An approach to the linear multivariable servomechanism problem. *International journal of control*, 15(5):961–979.

[Yu et al., 2019] Yu, C., Ljung, L., Wills, A., and Verhaegen, M. (2019). Constrained subspace method for the identification of structured state-space models. *IEEE Transactions on Automatic Control*.

[Yuan et al., 2013] Yuan, Q., Xiao, B., Luo, Z., Walker, M., Welander, A., Hyatt, A., Qian, J., Zhang, R., Humphreys, D., Leuer, J., et al. (2013). Plasma current, position and shape feedback control on EAST. *Nuclear Fusion*, 53(4):043009.

[Yuanxi et al., 2006] Yuanxi, W., Jiangang, L., Peide, W., et al. (2006). First engineering commissioning of EAST tokamak. *Plasma Science and Technology*, 8(3):253.

[Zohm, 2015] Zohm, H. (2015). *Magnetohydrodynamic stability of tokamaks*. John Wiley & Sons.

Résumé— Cette thèse étudie la modélisation basée sur les données et le contrôle du profil de courant du plasma et des paramètres cinétiques dans des scénarios de tokamak avancés. Une approche de modélisation nonlinéaire basée sur les données, à savoir l'identification du modèle Polynomial NonLinear State-Space (PNLSS), est proposée dans la thèse, pour la première fois, pour incorporer la dynamique nonlinéaire dans les plasmas de tokamak avancés, par exemple, les interactions d'ondes de plasma et les effets bootstrap. En utilisant des modèles linéaires basés sur les données, un certain nombre de schémas de contrôle avancés sont développés, par exemple, le contrôle robuste $\mathcal{H}_\infty$, le contrôle linéaire quadratique intégral (LQI), le contrôle interne du modèle (IMC) et le contrôle prédictif du modèle sans décalage (MPC). Des simulations METIS nonlinéaires et des expériences sur plasma ont été réalisées sur le tokamak EAST pour valider l'efficacité des schémas de contrôle proposés. Pour élargir la région de contrôle attrayante et permettre un espace opératoire plus large, des approches de contrôle adaptatif sont explorées, y compris le contrôle sans modèle de recherche d'extrémum (ESC) et le contrôle adaptatif de référence de modèle (MRAC). Ces nouveaux algorithmes de contrôle ont été implémentés et évalués numériquement via des simulations METIS nonlinéaires sur les tokamaks EAST et ITER.
Mots clés: Tokamak, Contrôle des Plasmas, Modélisation du Plasma Tokamak, Identification du Système, Contrôle Robuste, Contrôle Adaptatif, Contrôle Prédictif de Modèle

Abstract— This thesis investigates data-driven modelling and control of plasma current profile and kinetic parameters in advanced tokamak scenarios. A nonlinear data-driven modelling approach, namely the Polynomial NonLinear State-Space (PNLSS) model identification, is proposed in the thesis, for the first time, to incorporate nonlinear dynamics in advanced tokamak plasmas, for instance, plasma-wave interactions and bootstrap effects. Using linear data-driven models, a number of advanced control schemes are developed, for example, $\mathcal{H}_\infty$ robust control, linear-quadratic-integral (LQI) control, the internal model control (IMC) and the offset-free model predictive control (MPC). Both nonlinear METIS simulations and plasma experiments have been performed on the EAST tokamak to validate the effectiveness of the proposed control schemes. To broaden the attractive control region and enable broader operating space, adaptive control approaches are explored, including model-free extremum-seeking control (ESC) and model reference adaptive control (MRAC). These new control algorithms have been implemented and evaluated numerically via nonlinear METIS simulations on the EAST and ITER tokamaks.
Keywords: Tokamak, Plasma Control, Tokamak Plasma Modelling, System Identification, Robust Control, Adaptive Control, Model Predictive Control

GIPSA-lab, 11 rue des Mathématiques, Grenoble Campus BP46, F-38402
Saint-Martin-d'Hères, FRANCE